UNIVERSITA
DEGLI STUDI
FIRENZE

DOTTORATO DI RICERCA IN
SCIENZE CHIMICHE

CICLO XXXIV

COORDINATORE Prof. Piero Baglioni

Ab initio Analysis of Magnetic Systems: Structural and Magnetic Properties from the Bulk Phase to the Adsorption on Surface

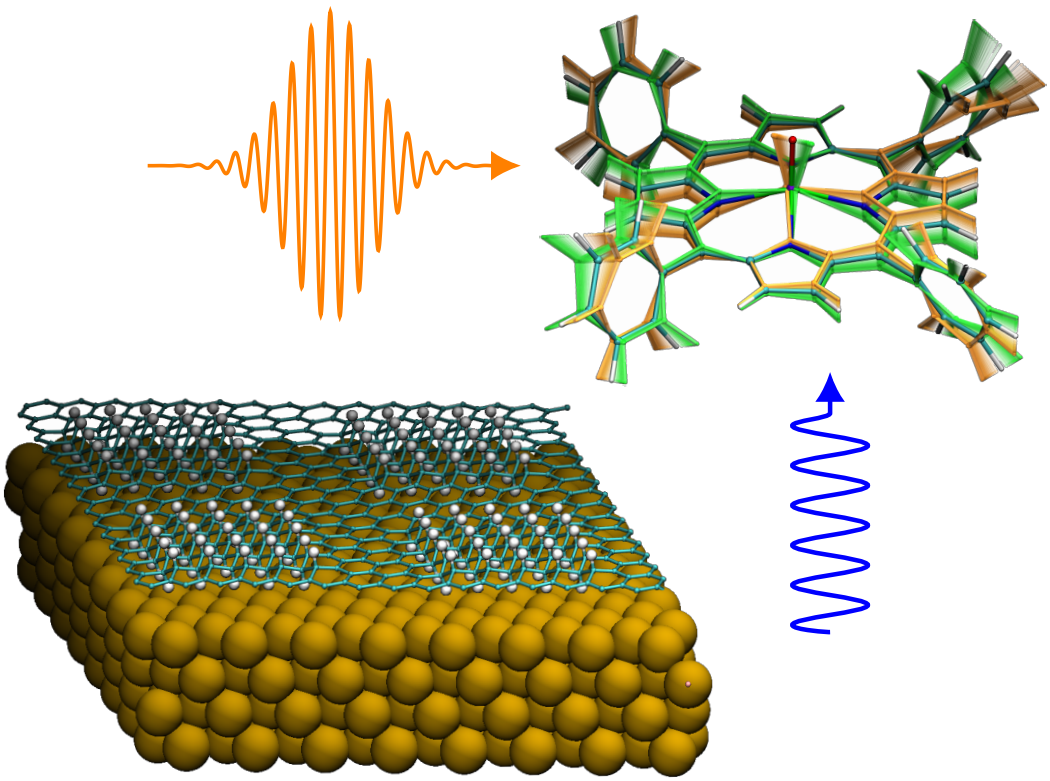

Dottorando:
Dott. Andrea Albino

Tutore:
Prof. Federico Totti

UNIVERSITA
DEGLI STUDI
FIRENZE

DOTTORATO DI RICERCA IN
SCIENZE CHIMICHE

CICLO XXXIV

COORDINATORE Prof. Piero Baglioni

Ab initio Analysis of Magnetic Systems: Structural and Magnetic Properties from the Bulk Phase to the Adsorption on Surface

Settore Scientifico Disciplinare CHIM/03

Dottorando:
Dott. Andrea Albino

Tutore:
Prof. Federico Totti

Coordinatore:
Prof. Piero Baglioni

Anni 2018/2021

Ai miei genitori

"If I have seen further it is by standing on the shoulders of Giants" [1]
Isaac Newton (1642-1727)

SCIENTIFIC ARTICLES

PUBLISHED PAPERS

• Albino, A.; Benci, S.; Atzori, M.; Chelazzi, L.; Ciattini, S.; Taschin, A.; Bartolini, P.; Lunghi, A.; Righini, R.; Torre, R.; Totti, F. & Sessoli, R. "The Temperature Dependence of Spin-Phonon Coupling in [$VO(acac)_2$]: a Computational and Spectroscopic Study" *J. Phys. Chem. C*, **2021**, 125(40) 22100–22110

• Santanni, F.; Albino, A.; Atzori, M.; Ranieri, D.; Salvadori E.; Chiesa, M.; Sorace, L.; Totti F.; Bencini, A. & Sessoli, R. "Probing Vibrational Symmetry Effects and Nuclear Spin Economy Principles in Molecular Spin Qubits" *Inorg. Chem.*, **2021**, 60(1) 140-151

• Albino, A.; Benci, S.; Tesi, L.; Atzori, M.; Torre, R.; Sanvito, S.; Sessoli, R. & Lunghi, A. "First-Principles Investigation of Spin–Phonon Coupling in Vanadium-Based Molecular Spin Quantum Bits" *Inorg. Chem.*, **2019**, 58(15), 10260–10268.

PAPERS NOT INCLUDED IN THIS THESIS

• Atzori, M.; Garlatti, E.; Allodi, G.; Chicco, S.; Chiesa, A.; Albino, A.; De Renzi R.; Salvadori, E.; Chiesa, M. & Sorace, L. "Radiofrequency to Microwave Coherent Manipulation of an Organometallic Electronic Spin Qubit Coupled to a Nuclear Qudit" *Inorg. Chem.*, **2021**, 60(15) 11273–11286

PAPERS IN PREPARATION

• Elena Garlatti; Alessandro Chiesa; Simone Chicco; Luigi Paolasini; Roberto Caciuffo; Claudio Mazzoli; Stefano Carretta; Fabio Santanni; Andrea Albino; Alessandro Lunghi; Federico Totti & Roberta Sessoli "Unveiling relaxation dynamics in a prototype molecular qubit by phonon mapping, *ab initio* simulation and Inelastic X-ray Scattering measurement"

• Anatoly R. Melnikov; Yaroslav V. Getmanov; Oleg A. Shevchenko; Stefano Benci; Fabio Santanni; Andrea Albino; Renato Torre; Lorenzo Sorace; Federico Totti; Alessandro Lunghi; Roberta Sessoli; Matvey V. Fedin & Sergey L. Veber "Spin dynamics in [VO(tpp)] under high-power THz radiation: insights into spin-phonon coupling"

• Andrea Albino; Francesco Buonocore; Massimo Celino; Nicola Lisi; Federico Totti & Roberta Sessoli "Are stable magnetic graphene derivatives attainable?"

ACKNOWLEDGMENTS

I am deeply indebted to the many colleagues of Laboratorio di Magnetismo Molecolare (LAMM) who have shared their knowledge, enthusiasm, expertise and good time with me in the past six years, from my Bachelor Thesis internship.

I particularly would like to acknowledge Professors Roberta Sessoli, Federico Totti, Lorenzo Sorace, Andrea Caneschi, Alessandro Lunghi, for their fruitful discussions and their constant support that inspired my work.

The work present in this Thesis have been supported by the EU Commission through the QuantERA Project SUMO, the FETOPEN project FATMOLS (GA 862893), by the "Ministero dell'Istruzione dell'Universitá e della Ricerca" (MIUR) through PRIN 2015 (Project HYFSRT), PRIN 2017 (Project 2017Z55KCW) and Progetto Dipartimenti di Eccellenza 2018-2022 (ref no. B96C1700020008), by the Fondazione Cassa di Risparmio di Firenze, by European Union's Horizon 2020 research and innovation program under grant agreement no. 871124 Laserlab-Europe, by the MOLSPIN COST action CA15128 project by the Science Foundation Ireland (Grant 14/IA/2624), and by AMBER (grant/12/RC/2278 P2).

The computing resources have been provided by CRESCO/ENEAGRID High Performance Computing infrastructure and its staff funded by ENEA, the Italian National Agency for New Technologies, Energy and Sustainable Economic Development, by the Trinity Centre for High Performance Computing and the Irish Centre for High-End Computing and by the in-house HPC facility "Lamm20".

ABSTRACT

Today, a steadily growing community of scientists is developing the tools of a new science that merges quantum physics and theoretical computer science, called quantum information science. Its basic constituent is the quantum analogue of the classical bit, say the qubit. In the development of spin-based quantum technologies it has become clear that molecules carrying a paramagnetic center represent particularly versatile building blocks as they can offer a high degree of tunability.

In this framework, the microscopic description of time dependent spin phenomena represents an aspect of paramount importance due to its broad impact in magnetism. The complete knowledge of the phonons' interaction with the spin system in potential solid state molecular qubits is a challenging task. Solve this question would mean being able to build molecular systems having the desired features, in particular long spin relaxation time even at high temperature. In this thesis a tailored computational protocol is proposed, able to reproduce magnetic, structural, and vibrational properties of transition metal complexes, in isolated environment or embedded in molecular crystals. Some theoretical attempts to analyze in detail the nature of the most relevant vibrational modes giving rise to spin relaxation have also been reported. They include the investigation of spin–phonon coupling and the identification of the local molecular vibrations that are more detrimental for coherence, so that they can be suppressed by chemical optimization. The importance of several factors influencing the vibrational degree of freedom is highlighted. Intrinsic effects are due to the chemical nature of the first coordination shell, and extrinsic effects are related to interaction with the lattice environment, i.e, the packing effects, crystal symmetry, etc. The results of these studies represent further pieces of the puzzle of the role played by vibrations in determining the relaxation properties of potential molecular qubits at the quantitative level.

A further investigation regarded the implantation of magnetic moments in graphene for spintronics applications. This computational study aims at sistematic and comprehensive understanding of structural and magnetic properties of graphene across its conformational space when covalently functionalized with hydrogen or fluorine atoms in different stoichiometries. The hydrogenated systems are then adsorbed on Au(111) crystal face or on a graphene buffer layer. A new strategy, based on non homogeneous graphene hydrogenation, is rationalized to build stable magnetic structures and maximize the magnetic moment per unit area.

CONTENTS

INTRODUCTION

The general subject of this thesis is the study of magnetic properties of molecular materials.

In the framework of molecular species bearing unpaired electrons, there is a long route the magnetochemistry community ran into [2], before the modern definition of Molecular Magnetism arose as one of the most straightforward applications of the quantum mechanisms. Since then, numerous and complex quantum phenomena, not obtainable with common extended magnetic crystals, have been observed [3–5], stimulating research of the physical laws governing the functioning of any device with sizes below 10 nm, where energy levels are quantized and quantum effects tend to become dominant.

The approaches followed during last decades comprise a wide variety of molecular species, e. g., the organic, inorganic and organometallic routes have been followed to develop the synthesis of molecular based magnetic materials [6, 7].

A broad class of magnetic molecules is constituted by multi-spin clusters [8–10], called Single Molecule Magnets (SMMs). These systems, below a critical temperature, behave like giant anisotropic spins, exhibiting spontaneous magnetization below a critical temperature, magnetic memory (hysteresis and coercive field) and quantum effects. The first application proposed for these *bistable* molecules was as magnetic memory devices because they can remain magnetized in one of two spin states, giving rise to a ”bit“ of memory [11–13], allowing to push the boundaries of high density storage toward the single molecule dimension physical limit. The initial strategy to observe a long relaxation time of the magnetization was that of synthesizing high-spin molecules, or clusters, with large spin S and large easy axis type magnetic anisotropy ($D < 0$) [10, 14, 15]. The seminal discovery of the first archetypes of SMMs opened up an entirely new field for scientists, towards nanotechnologies.

Further in-depth studies revealed new properties such as *quantum coherence* [16–18] and that, descending the hierarchy of complexity down to the bottom, magnetic molecules with single spin 1/2 centers - two-level quantum systems - showed long coherence times and Rabi oscillations [19–23]. Quantum coherence is an essential ingredient in quantum information processing. Coherence is an ideal property of waves that enables stationary (i.e. temporally and spatially constant) interference, it refers in quantum physics to the existence of a superimposed (or

entangled) states that haven't got a classical counterpart and constitute the great potential to be exploited in quantum technologies.

People in the magnetism community fight against the transient nature of the coherent quantum states, decaying in time due to *spin relaxation*. Someone would like to have the lifetime of quantum states as long as possible, as for SMMs; there are also use cases where a lifetime as short as possible is sought, as for contrast agents [24]. Our aim is to engineer molecular structures in a way that the T_1 fits the requirements for the application we have in mind: if too long it limits the speed of initialization of the qubit, whereas, if too short it induces a collapse of T_2, especially as the temperature increases.

Advanced molecular synthetic techniques allow a precise control and reproducibility of discrete molecular structures, a wide playground for employing chemistry to modulate the quantum physics of magnetic materials. It provides a realistic method for fine-tuning the properties of these molecular nanoscale materials, impacting in quantum information science fields such as quantum sensing, quantum information processing and molecular spintronics. The structural control gives in principle many possibilities to modulate the bulk electrical, magnetic, and optical properties towards two of the key open challenges in quantum-computing research, namely *coherence* and *scalability*. To address the real world most challenging problems, a quantum computer would require at least 200 fault-free qubits. In order to find a solution, quantum computers must scale up. The scalability is one of the challenges for which a chemistry-based bottom-up approach is best-suited and molecular qubits hold a great value in this purpose with respects to other systems, say, atoms or superconducting circuits.

Molecular spin systems can be easily coupled to each other and organized in quantum devices at the nanoscale, but still strongly suffer from the short lifetime of the quantum superposition of states due to uncontrolled interaction with the surrounding environment. The spin dynamics can be characterized by interaction with other magnetic dipoles moments or with other kinds of particles; when other spins are kept sufficiently far apart and the magnetic perturbation vanishes, the primarily perturbing source of "noise" are the atomic vibrations, or massless quasi-particles called *phonons*, that modulate spin energy levels in solids. This interaction is already active at few kelvin and becomes detrimental for quantum coherence when temperature is raised up to few tens of kelvin.

The present thesis work is theoretical in its approach, although the nature of experimental work in the treated subjects have influenced the selection of material to be investigated. Our efforts were devoted to the microscopic understanding of mechanisms underlying the relaxation processes that are responsible for short coherence times in $S = 1/2$ magnetic molecules. Quantum chemistry calculations are

a fundamental tool to unravel the electronic structure of the compounds, towards rational design of sophisticated systems with peculiar chemical and physical properties. The extension of combined analysis of both the molecular properties and solid-state properties of molecules in the lattice is hereafter pursued. The macroscopic properties of molecular materials turn to be determined also by interactions between the constituent molecules. The lacking of theoretical models able to explain the microscopic origin of the relaxation in chemical systems [25–27], anyway, is a critical factor for the enhancement of technologies that aim to exploit quantum properties of matter motivate us to further investigate and acquire a deeper knowledge to engineer molecular structures and create more efficient molecular magnets with long coherence times.

The thesis is organized in four chapters.

In Chapter 1 the basic concepts about qubits are presented, with a progressive focus on the molecular spin qubits and an introduction on spin relaxation concepts.

Chapter 2 describes experimental techniques and theoretical methods of magnetic resonance, together to the modern computational approaches to calculate magnetic properties and vibrational properties.

Chapter 3 presents the investigation of the interplay between spins and phonons, the different aspects investigated in several vanadium-based or copper-based molecular systems are illustrated. The results of this studies represent further pieces of the puzzle of the role played by vibrations in determining the relaxation properties of potential molecular qubits at the quantitative level. The results are integrated with further preliminary tests and comparison that led us to clarify queries at the interface between the fields of *solid-state chemistry* and *molecular chemistry*. The division of these two disciplines is not sharp [28], as in many other fields, the contributions coming from different backgrouns are very important and the language of modern solid-state physics [29], of band theory and lattice dynamics, mixes with the concepts familiar to chemists such as bonds, clusters, molecular patterns.

Chapter 4 is devoted to long range magnetically ordered system, seeking for stable implantation of magnetic moments in graphene derivative as a fruitfull material for spintronics applications.

1

THE ROUTE TO SINGLE ION 3*d* COMPLEXES AS QUBITS

1.1 QUANTUM COMPUTATION

One of the main motivations for research in quantum information science is that certain computational tasks might be executed exponentially faster on a quantum processor than on a classical one. Quantum information science has seen an explosive development in recent years, particularly within the past three decades [30]. Considerable technical progress was achieved [31], perhaps the most impressive has been in the area of proof-of-concept implementations [32–34]; first practical applications already appeared in literature, employing the first available quantum computers (5-qubit, 6-qubit and 20-qubit quantum hardwares by IBM) [35–37]. A key milestone to be achieved in this field will be the development of a fully featured large Quantum Computer (QC) overcoming the scalability challenge which comprises of integrating a large number of qubits and correcting quantum errors. Such a universal quantum computer, performing a computational task beyond the capability of any classical computer, would allow to achieve the last step of quantum technology capabilities, that is a goal known as *quantum supremacy* [38, 39].

The detailed theoretical apparatus concerning the quantum computation, ranging from the postulate of quantum mechanics to the theory of quantum measurements, passing through the fundamental concepts of quantum channels and fidelity of quantum information, is outside the scope of this work. Marvelous books are here referenced by the author of this thesis [40–42] and the main concepts are hereafter mentioned.

The key requirements for the practical purpose of building a real quantum device are known as Di Vincenzo criteria [43]are hereafter presented, highlighting the ones more closely discussed in further chapters.

1. A SCALABLE PHYSICAL SYSTEM WITH WELL CHARACTERIZED QUBITS

The bit is the fundamental concept of classical computation and classical information [44]. Quantum computation and quantum information are built upon an analogous concept, the quantum bit, or qubit for short (see Fig. 1.1). The difference between bits and qubits is that a qubit can be in a state other than $|0\rangle$ or $|1\rangle$. It is also possible to form linear combinations of states, often called superpositions:

$$|\psi\rangle = \alpha|0\rangle + \beta|1\rangle$$
$$|\psi\rangle = \cos\phi|0\rangle + \sin\phi e^{i\theta}|1\rangle \tag{1.1}$$

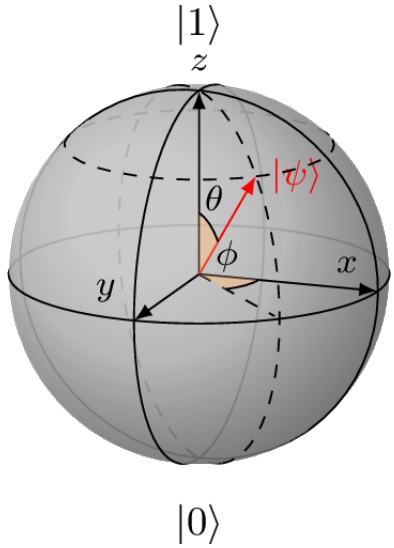

Figure 1.1: The Bloch sphere representation [45, 46]. It is a three dimensional mapping of a n level quantum system, with $n = 2$, also called "qubit" [40]. The 2^n states are spanned by the state vector $|\Psi\rangle$ in the whole solid angle. The orthogonal population vectors are spatially antiparallel and located on the z axis, while their linear superpositions have a component on the xy plane.

We can examine a bit to determine whether it is in the state 0 or 1. For example, computers do this all the time when they retrieve the contents of their memory. Rather remarkably, we cannot examine a qubit to determine its quantum state, that is, the values of α and β. This dichotomy between the unobservable state of a qubit and the observations we can make lies at the heart of quantum computation and quantum information.

2. THE ABILITY TO INITIALIZE THE STATE OF THE QUBITS TO A SIMPLE FIDUCIAL STATE, SUCH AS $|000\ldots\rangle$

This arises first from the straightforward computing requirement that registers should be initialized to a known value before the start of computation. The speed with which a qubit can be zeroed will eventually be a very important issue. The system can either be "naturally" cooled if the ground state of its Hamiltonian is the state of interest, or the standard state can be achieved by a measurement which projects the system either into the state desired or another state which can be rotated into it [47, 48].

3. LONG RELEVANT DECOHERENCE TIMES, MUCH LONGER THAN THE GATE OPERATION TIME

Decoherence times characterize the dynamics of a qubit (or any quantum system) in contact with its environment. The (somewhat overly) simplified definition of this time is that it is the characteristic time for a generic qubit state $|\psi\rangle = \alpha|0\rangle + \beta|1\rangle$ to be transformed into the mixture $\rho = |\alpha|^2|0\rangle\langle 0| + |\beta|^2|1\rangle\langle 1|$. Decoherence is very important for the fundamentals of quantum physics, as it is identified as the principal mechanism for the emergence of classical behavior.

Here comes the focus on the further discussions involving coordination chemistry: despite the advantage of chemical tunability of molecular systems with respect to classical inorganic materials, the short lifetime of the quantum superposition of states, represented by the spin–spin relaxation time T_2 or the phase memory time T_m [49], has up to now posed important limitations in their perspective use as qubits. Solving this issue deserves a solid grasp on the microscopic phenomena interfering with a optimal behaviour of molecules as quantum bits.

4. A "UNIVERSAL" SET OF QUANTUM GATES

A quantum algorithm is typically specified as a sequence of unitary transformations U_1, U_2, U_3; ..., each acting on a small number of qubits, typically no more than three. The most straightforward transcription of this into a physical system is to identify Hamiltonians which generate these unitary transformations, viz., $U_1 = e^{i\mathscr{H}_1 t/\hbar}, U_2 =$ ..., etc.; then, the physical apparatus should be designed so that $\mathscr{H}_1$ can be turned on from time 0 to time t_1, then, turned off and $\mathscr{H}_2$ turned on from time t_1 to time t_2, etc.

In some systems, like nuclear spin investigated in NMR [50], there are two-body interactions present which cannot be turned off, as well as others which are switchable. This would in general be fatal for quantum computation, but the particular form of the fixed interactions permit their effects to be annulled by particular "refocusing" sequences of the controllable interactions, and it has recently been discovered that these refocusing sequences can be designed and implemented efficiently.

5. A QUBIT-SPECIFIC MEASUREMENT CAPABILITY

For any process modifying the quantum states of qubits, the final measurement of those states is of fundamental importance when performing computations. Measurement techniques that are not 100% efficient are typically repeated to increase the success rate.

For computation alone, the five requirements above suffice. But the advantages of quantum information processing are manifest in many kinds of information-processing tasks [31], that involve more than just computation, and for which quantum technologies provide a unique advantage. Further criteria are added among the qubits requirements:

6. THE ABILITY TO INTERCONVERT STATIONARY AND FLYING QUBITS
7. THE ABILITY TO FAITHFULLY TRANSMIT FLYING QUBITS BETWEEN SPECIFIED LOCATIONS

Using this terms emphasizes that the optimal embodiment of qubits that are readily transmitted from place to place is likely to be very different from the optimal qubits for reliable local computation. The qubit encoded either in the polarization or in the spatial wavefunction of the photon is often addressed as promising kind of flying qubit corroborated by the well established technology of light transmission through optical fibers.

Several possible implementations of a digital QC have been proposed within a variety of physical frameworks[51].

These notably include photons, trapped ions [52], superconducting circuits [53], linear optics [54] and nuclear [50, 55] or electron spins. Different platforms can also be combined in new hybrid structures exploiting the advantages of the different components [56, 57].

Electron spins systems have been tested in many environments, from materials-based systems such as nitrogen vacancies in diamond [58, 59], doped semiconductor [60], quantum dots [61, 62], to mesoscopic spin clusters [63, 64] and molecular qubits [19, 65, 66].

1.2 MOLECULAR QUBITS

The study of molecular nanomagnets for the spin qubit application effectively began in 2007 with a seminal study by Ardavan et al. [67] with the determination of decoherence times in 8-membered heterometallic rings Cr_7M.

Moving on from bistable magnetic molecules to molecular spin qubits, means thinking in terms of quantum decoherence (T_2) instead of simply in terms of magnetic relaxation (T_1) [68, 69], as will be explained in Sec. 1.3.

A necessary condition for using an electron spin system as a qubit is the presence of two low-lying states in the molecule's energy spectrum (effective $S = 1/2$ pseudo-spin), which encode the qubit wavefunction. One can use a static magnetic field to tune the gap between the two levels, and pulsed magnetic fields resonant to this gap to perform rotations like with a true $S = 1/2$ electron or nuclear spin. It must be possible to manipulate the spin without significant decay of the wavefunction to other non-controllable (noncomputational) states, i. e., in a time much shorter than the decoherence time. Small decay rates (or leakage) of wavefunction requires that "noncomputational" states of the molecule, that is, quantum levels not to be employed to encode a qubit, are energetically well separated from the qubit levels in terms of the pulse's spectral width. This a not particularly restrictive condition on the spectrum considering the attainable pulse durations [65]. A consequence of dealing with an effective $S = 1/2$ spin is represented by the presence of excited spin states. The population leakage from the two lowest states, $|0\rangle$ and $|1\rangle$, to the excited states represent a possible source of error in the quantum algorithm if a direct control of these transition cannot be well addressed and controlled [70]. The presence of more than two controllable levels becomes although a value of molecular qubits, as shown below [48]. For these reasons, studies in this field focused on coordination complexes based on transition metal ions with a single unpaired electron [71]. These are the most obvious two-level quantum systems and promising candidates to fulfill the DiVincenzo criteria. In comparison to spin clusters, they represent quite a natural choice for the implementation of a quantum bit. They are "true" (as opposed to "effective") two-level systems. They lack of excited electron-spin levels, fostering the magnetic relaxation through excited spin levels when thermal population is raised. The orbital contribution L is largely quenched leading to a small magnetic anisotropy, giving access to higher coherence times.

In spite of their electronic structure simplicity, only very recently has the search for viable molecular qubit candidates turned to a single metal ion with an $S = 1/2$ ground state [20, 21].

A further important advantage of molecular systems is the possibility to go beyond a simple two-state system trough the hyperfine coupling with the metal

atom nucleus. The idea behind this necessity is the Quantum Error Correction (QEC) schemes application, encoding the quantum information into "logical qubits", objects with more than two possible energy levels, usually referred as *qudit*, a d-level system (with $d > 2$) [48, 72, 73]. The weak hyperfine coupling active between nuclear qudit and an electronic spin qubit is a common feature in transition metal complexes, the number of states is defined by spin multiplicity $(2S+1)(2I+1)$. Usually its detrimental effects on relaxation time, especially in moderate external field, is recorded [19, 71]. Recently, it was demonstrated that the qubit-qudit can be controlled, opening new avenues on the modelization of new multifrequency magnetic resonance experiments to manipulate quantum states. Thank to the very different energies involving electronic and nuclear resonant transitions, and given that their interaction is much smaller than the difference of excitation energies, the eigenstates are simple tensor products of the eigenstates of S_z and I_z, simplifying the implementation of the pulsed EPR experiment. electronic part by chemical design to "check" the trustworthiness of computational states of the logical qubit. Successful application of quantum error correction [48] protocols can be crucial to enhance the potentiality of molecular qubits in quantum information science.

The molecular approach proves to be uniquely suited both for chemical design and the processing of spins in solid matter. A major advantage of molecular spin qubits over other candidates stems from the power of chemistry for a tailored and inexpensive synthesis of systems for their experimental study. Molecular $S = 1/2$ qubits with large quantum coherences have been realized by chemically controlling many aspects of their molecular structure and environment: metal ion, ligands, donor atoms (ligand field), spin delocalization, the solvent, the counterion, the matrix (diamagnetic dilution), the covalent network (Metal Organic Frameworks, MOF) Fig. 1.2.

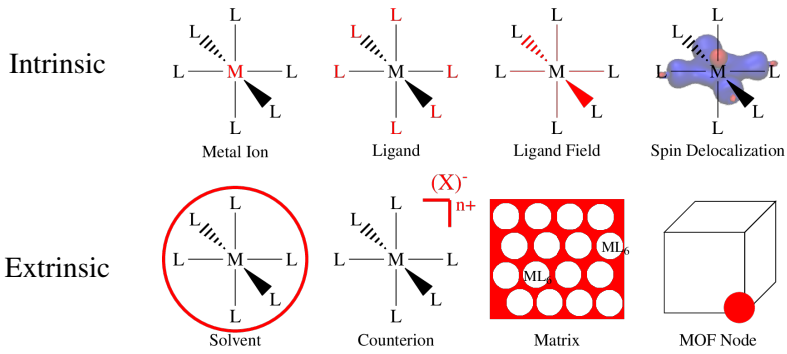

Figure 1.2: Intrinsic and extrinsic features that can be modulated to tune coherence properties.

1.3 RELAXATION PROCESSES

Among the experimental techniques to investigate magnetic materials, many methods are available that measure the response of the material to an external magnetic field [74], comprising magnetic susceptibility measurements in an oscillating field, EPR and NMR spectroscopies, etc. [4].

Constituent atoms or molecules of paramagnetic materials have permanent magnetic moments (dipoles), even in the absence of an applied field. The moment is due to the spin of unpaired electrons, carrying a spin $S = 1/2$. Spin-1/2 particles have two quantum levels, their associated dipoles do not interact with one another and are randomly oriented in the absence of an external field due to thermal agitation, resulting in zero net magnetic moment (Fig. 1.3 (**a**)). In other words, the occupation probabilities of the two available states (p_0 and p_1) are equal. When a static magnetic field **B** is applied, the magnetic moment of the spin aligns with the external field. Spin-1/2 may only be polarized either "up" (parallel to the external field) or "down" (anti-parallel to the external field). Usually, the two states are labeled $|0\rangle$ and $|1\rangle$ to recall the realm of bits that are two-level elementary carriers in information theory, the parallel configuration has a lower energy than the anti-parallel one. The real experiment is carried on macroscopic specimen, probing a large number of spins at the same time, usually called *ensemble*: a Boltzmann distribution occurs with the lower level of population greater than the upper level one, as showed in Fig. 1.3 (**b**). The macroscopic magnetization vector can be moved away from equilibrium, with rotations in the whole solid angle by pulsed or continuous magnetic fields. Observation of resonance absorption in magnetic resonance experiments is possible thank to the effect of an oscillating radiation field in the xy plane stimulating transitions between two spin states in a static magnetic field oriented along the z-axis. The radiation fields fall in the radiofrequency (RF) range of energies in NMR, and in the microwave (MW) range for EPR. Since the number of transitions which take place in unit time from a certain level is just equal to the population of that level multiplied by the transition probability, there is a net absorption of energy from the radiation field, resulting in an establishment of a macroscopic magnetization.

If the spin system were not coupled with its surrounding or weakly coupled to it, the microwave field acting continuously on the spin system (CW-EPR) would eventually equalize (Fig. 1.3 (**c**)) or invert (Fig. 1.3 (**d**)) the populations in the two levels and after a short time the absorption EPR signal would cease.

This behaviour is not observed because there is competition between relaxation phenomena and radiation field, and, if the latter is strong enough with respect to the spin–environment interaction, the EPR signal saturates, i. e. the population will be equalized as expected, but still an *energy absorption perdures*. The system is trying

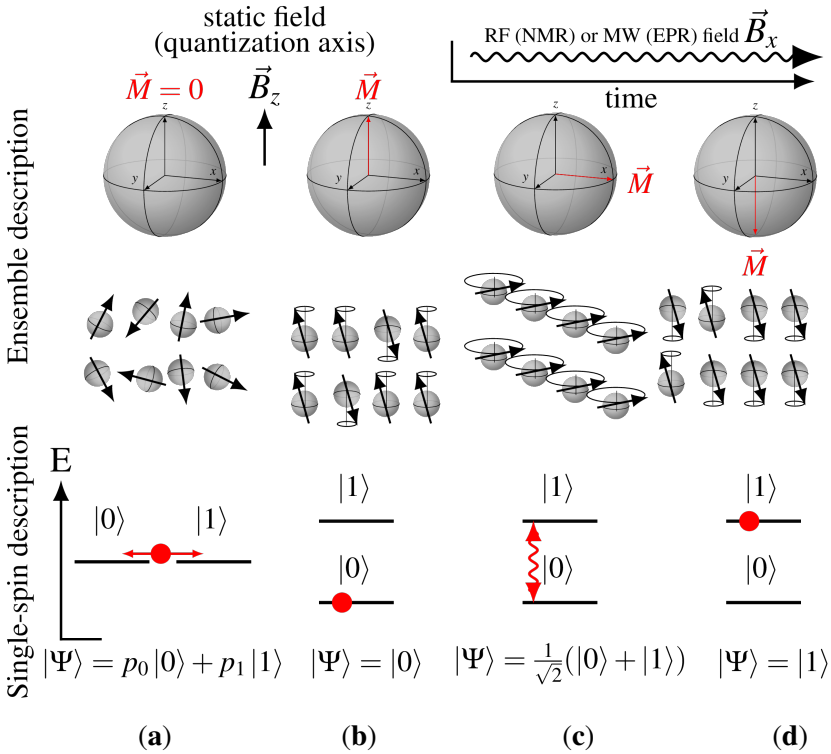

Figure 1.3: (**a**) Paramagnet in zero external field, net magnetization is zero. (**b**) Paramagnet in external field **B**, a population difference and a net magnetization is established. (**c**) When a 90° pulse is applied to the sample a coherent state of spins is generated, resulting in a in-plane magnetization rotating in the xy plane on the Bloch sphere at Larmor frequency. (**d**) A 180° pulse is generating a population inversion, with a higher population of spins polarized anti-parallel to the field **B**. Note that the ensemble description is intended in the rotating frame [49], while the single spins are represented in the static frame, the black circles represent the rotation of the spin at Larmor frequency.

to actually relax back to the original Boltzmann distribution, and, when the cause of the disturbance is removed, it drifts towards a thermodynamic equilibrium [75]. There must be so a process acting to restore equilibrium; such a process is called a “relaxation” [76, 77] – the relaxation phenomenon is found in many branches of physics, and occurs since a physical system will tend to reach its lowest possible energy configuration. Generally, several mechanisms contribute to the decay of polarization (Fig. 1.3 (**b**,**d**)) or coherence (Fig. 1.3 (**c**)) on a given transition [78–86]. The efficiency of a relaxation process is designated by the inverse of a relaxation

time, a relaxation rate, which is just a measure of the rate at which equilibrium would be regained if there were no opposing action. Hence the experimental accessible physical magnitude is the relaxation rate and it is the sum of the relaxation rates due to single microscopic mechanism acting in parallel on the spin. For consecutive steps in a given pathway the relaxation times and for parallel pathways the relaxation rates have to be added, each path acts like branches of parallel resistors in a simple electric problem. Conceptually the spin relaxation and current flow in parallel circuits are described with the same mathematical formalism, when one resistor (R_1) rises over a certain threshold the current flows exclusively through other available paths (say, R_2 and R_3), making R_1 an irrelevant part of the circuit.

The two relevant parameters that characterize the relaxation are the *longitudinal relaxation time*, T_1, which corresponds to the intrinsic lifetime of a population state that can assume either the $|0\rangle$ or the $|1\rangle$ value (Fig. 1.5 (**a**)), and the *transverse relexation time*, T_2, that is the characteristic time in which the precessing spins lose the coherence of the phase of the superposition state (Fig. 1.5 (**b**)) [87]. The coherent state is described by superimposed state of single-spin wavefunction (Fig. 1.5 (**c**)), the coherent superposition of a macroscopic number of spins is detectable as a net magnetization in the xy plane, normal to the external magnetic field. The terms longitudinal and transverse have to be intended relatively to the quantization axis, chosen as the external field direction.

Many models can be currently used to reproduce, explain and understand the magnetic resonance measurements outcomes.

In this chapter we began utilizing the bulk properties of a large ensemble of spins (i.e., the equations of the total magnetization M as derived by Bloch [45]), which removes quantum-mechanical uncertainties but does hide details of single-spin behavior.

So far the nature of the transition probabilities due to microscopic mechanisms was not specified, the box below defines the main parameters that can be measured and the underlying mechanisms involved in relaxation, in the classical description of relaxation we have two different relaxation-rate constants: T_1 and T_2, that shall be discussed in Ch. 3.

THE RELAXATION TIMES

T_1 Longitudinal, or spin-lattice, relaxation restores the thermal equilibrium value. T_1 relaxation changes the energy of the spin system with a *spin flip*. It is related to the mean lifetime of a given spin-orientation state. This lifetime limitation has an effect on the linewidth as explained by the following argument. All quantum-mechanical transitions have a limiting non-zero spectral width, called lifetime broadening, which arises from the finite lifetime of any excited state. Such non-zero frequency spread is attributed to the Heisenberg uncertainty principle. Briefly, the underlying principle is $T\delta E > \hbar$, where δE is the uncertainty in the energy of the system due to the non-zero transition probability Z per second of its decay and $T = Z^{-1}$ is its mean lifetime. The quantity $|\delta U| \sim \hbar/T$ is called the width of the energy level considered. For example, if $T_1 = 10^{-9}s$, then $|\delta E|10^{-25}J$ or $\Delta\nu 10^{8}s^{-1}$, corresponding to an EPR linewidth of about 6.0 mT. Lifetime broadening is one of the contributions to the *homogeneous* linewidth and defines the minimum linewidth for a given system. The type of transition probabilities are depicted in Fig. 3.2.

T_2^* Spin-spin, or pure dephasing, relaxation is an energy conserving *flip-flop* process of two spins is twice as effective as a single spin flip in destroying coherence. In such a flip-flop process, one of the spins changes from the α to the β state thereby providing the energy for a second spin to change from the β to the α state, a mechanism which is called spin-spin relaxation.

T_2 Transverse relaxation, $1/T_2 = 1/T_2^* + 1/2T_1$, leads to a decay of transverse magnetization towards zero. No change in energy, as in pure flip-flop mechanism. It does require some kind of an interaction with the environment, otherwise the dynamics of the spin system would be coherent. Note that a spin flip (T_1) which leads to longitudinal relaxation destroys the correlation of the precession phase between the affected spin and the other spins, hence it also contributes to transverse relaxation.

T_m The phase-memory time T_m is often a useful empirical parameter. It is usually associated with the decay of the primary echo [49] when time is between two pulses is increased. In some cases this decay is exponential. T_m corresponds to the inverse homogeneous line width and is sometimes simply called T_2 in literature. Note however that there may be contributions to T_m from instantaneous diffusion which do not correspond to spin relaxation and can, in principle, be refocused. There are also contributions to T_m other than lifetime broadening ($1/(2T_1)$) and spin-spin relaxation ($1/T_2$). For example, the local field at the excited A spins is influenced by dipolar couplings to surrounding B spins which are not excited. Also other mechanisms affect T_m spectral diffusion, instantaneous diffusion, inhomogeneities of the sample, chemical reactions or spin diffusion are some examples. For this last effect to be significant, dipolar couplings between A and B spins are required which are of the same order of magnitude as the difference in their respective resonance frequencies. The dipolar interaction mixes A and B spins, consequently polarization on an A-spin transition partially evolves to polarization on B-spin transitions.

Decoherence processes, that occur in molecular and solid state systems, can be described for an ensemble in the time domain with the dipole moment correlation function Fig. 1.4:

$$\langle \mu(0)\mu(t)\rangle = exp\left[-t\left(\frac{1}{2T_1}+\frac{1}{T_2^*}\right)\right] exp(-2\Delta^2 t^2) \tag{1.2}$$

$$\frac{1}{T_2} = \frac{1}{2T_1}+\frac{1}{T_2^*} \tag{1.3}$$

the first exponential Eq. 1.2 contains processes described in the box above and classified in two general categories: *i) spin-spin relaxation*, $T_2{}^*$, a through-space interaction of neighbouring spins – electronic and nuclear – within the qubit (Hyperfine interaction [88]) and between neighbouring qubits [89], and *ii) spin-lattice relaxation*, T_1, caused by interaction with thermal vibrations of the molecule and/or the lattice vibrations (phonons) within the material [90]. The second exponential in Eq. 1.2 takes into account the inhomogeneous broadening, corresponding to a Gaussian contribution to the linewidth in the frequency domain, it can be removed by using appropriately designed spin-echo sequences. These sequences would eliminate the contribution to decoherence resulting from inhomogeneous broadening of the spin ensemble [65].

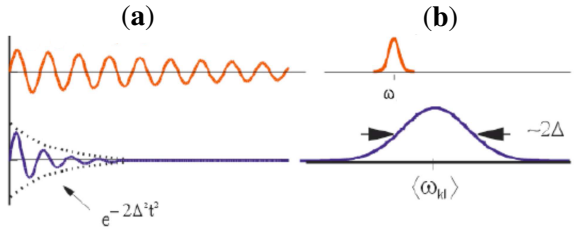

Figure 1.4: Dipole moment correlation function amplitude decay in the time domain (**a**) and its Fourier transform in the frequency domain (**b**). The orange signal is the decay due to T_1 and T_2, the blue signal contains the inhomogeneous broadening, too. Image adapted from [91]

The Bloch sphere representation [45, 46] plays a fundamental role to describe and visualize both the single spin (microscopic) or an ensemble of spins (macroscopic) dynamics. The single spin are governed and described by laws of quantum mechanics. The Bloch sphere is a mathematical tool that maps a n 1/2 partcles quantum system onto the 3D space, if $n = 2$ it is the representation of a "qubit" [40]. The 2^n states are spanned by the state vector $|\Psi\rangle$ in the whole solid angle. The orthogonal population vectors $|0\rangle$ and $|1\rangle$ representing *observable* states are

spatially antiparallel and located on the z axis while their linear superpositions representing *coherent* quantum states have a component on the xy plane.

The macroscopic description is accomplished by the Bloch equations: they can be represented in the Bloch sphere and describe the equations of motion of macroscopic magnetization ($\vec{\mathbf{M}}$) as a classical vector obtained by summing up all magnetic moments in the sample [45]. It is possible to represent the magnetization by a vector in the direction of the magnetic field. The magnetization vector is moved by an angle proportional to the length and intensity of the pulse. The vector can be actually moved along the sphere by application of magnetic field non-collinear with the external static field. If the vector is rotated by 90° or 180°, then the process is called a 90° pulse or 180° pulse, respectively (Fig. 1.3 (**c**-**d**)) [92].

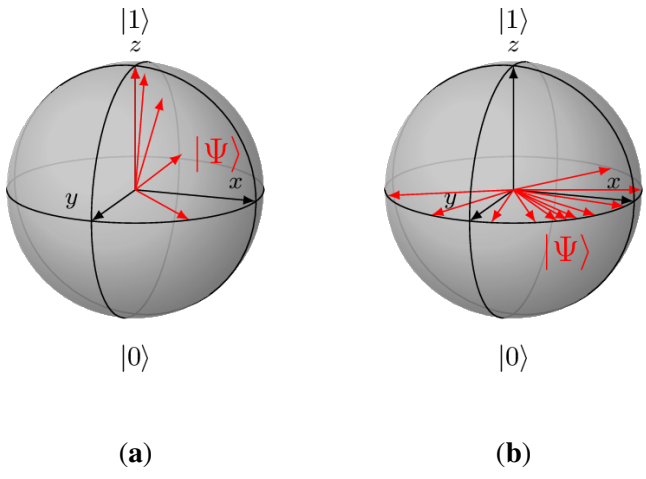

Figure 1.5: Relaxation processes denoted by T_1 (**a** and T_2 (**b**)) parameters occurring in a molecular spin qubit.

Successful electron spin qubits in both sensing and computing must have long coherence times relative to their characteristic Larmor precession frequency, which governs the limiting timescale at which the electron spin qubit can change its quantum state. Using X-band EPR ($\sim$ 9.5 GHz), this timescale is on the order of 10 ns. To maintain phase information adequate for fault-tolerant quantum computations, as mentioned in Sec. 1.1, the ratio of T_m over the time necessary for an individual quantum operation (a pulse length) has to be larger than 10^4 [43].

The terms coherence and decoherence are used interchangeably throughout the literature, with the former being the goal of a qubit interaction – the formation of a state of coherent superposition [93] (Fig. 1.3 **c**) – and the latter describing the decay or loss of this state. The decoherence process is, as stated before, due to the not

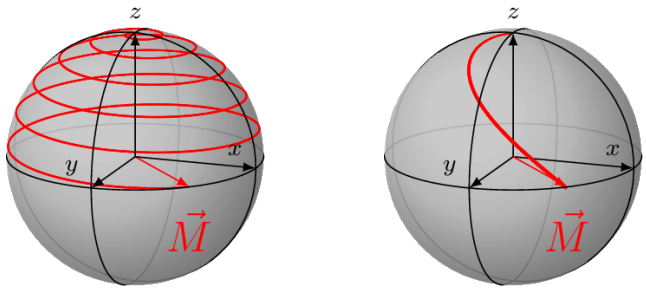

(**a**) (**b**)

Figure 1.6: Motion of macroscopic magnetization $\vec{\mathbf{M}}$ on the Bloch sphere. The measured motion is the result of composition of T_1 and T_2 effects. T_2 is constant in (**a**) and (**b**), T_1 is long in (**a**) and short in (**b**)

perfect insulation of the quantum system from its environment, this result in the dynamics of the surrounding apparatus also being relevant to the quantum system, and its effect will be to make the evolution *nonunitary*.

Entanglement is probably the most peculiar feature of quantum-mechanical systems; besides, it represents a fundamental resource in quantum information processing. Two spins S_1 and S_2 are entangled if the two-spin states $|\psi\rangle$ can be, by no means, written as a product of single-spin states: $|\psi\rangle \neq |\phi_1\rangle \otimes |\phi_2\rangle$, for any $|\phi_1\rangle$ and $|\phi_2\rangle$. For mixed states (Fig. 1.3 **a**), the above criterion translates into the impossibility of decomposing the density matrix in terms of separable states:

$$\rho \neq \sum_i \rho_i^1 \otimes \rho_i^2 \tag{1.4}$$

Such definitions are easily generalized to multi-spin states.

In other words, the state of each subsystem cannot be described independently of the state of the other one.

The major problem outlined above, typically referred to as decoherence [94, 95], resulting from elastic interactions between the quantum system that we want to use as qubit (principal system) and the quantum system that constitutes the remaining environment (ancillary system). Dephasing consists of the loss of phase coherence between the components of a linear superposition, and implies the evolution of a pure state into a statistical mixture (Fig. 1.3 **a**):

$$|\psi\rangle = \sum_i c_i |\phi_i\rangle \rightarrow \rho = \sum_i |c|^2 |\phi_i\rangle \langle\phi_i| \tag{1.5}$$

If the system–environment interaction has a Markovian character [41], both excitation/relaxation and dephasing display an exponential dependence on time.

Providing a mechanistic description of spin dynamics is a necessarily complex task since a comprehensive picture must consider electronic and vibrational aspects of the molecular system and its interaction with surrounding nuclear and electronic spins [96, 97]. In this sense, the study of spin dynamics in molecular systems is a multidisciplinary field involving resonance spectroscopies, molecular magnetism and theoretical chemistry.

2

METHODS

2.1 EPR AND SPIN-HAMILTONIAN THEORY

Spin has implications of two kinds: those which merely arise from the need to recognize it in classifying states through Pauli's exclusion principle, providing the basis for the periodic table, and those which depend on small interactions involving the associated magnetic dipole, that are nowadays investigated by means of the various magnetic resonance techniques [98].

A special power of magnetic resonance is its focus on magnetic dipoles in the system, and hence the ability to obtain microscopic structural information in their environments. The first magnetic resonance experiment was carried out by Zavoisky at Kazan State University in the URSS in 1944 [99]. Nowadays the field is amazingly more complex, not to say labyrinthine [100–105]. Magnetic resonance is now considered to be a "mature" scientific field and, while still evolving with much work to be done [106, 107], the fundamentals are in place [108–112]. Coherence times, for example, can be experimentally detected through nutation experiment [113], employing a pulse sequence called Hahn echo [114]. The resulting signal detected are the so called Rabi oscillations, an example is shown in Fig. 3.11.

Examination of the extensive EPR literature shows a pattern of increasing complexity in the systems studied and in the experimental equipment used. The spectrometers today in use operate not only in the classical continuous-wave mode but also in a pulsed mode [49].

The small interactions observed in EPR spectra (0.1-1 cm^{-1}) have been theoretically understood since the early days of quantum mechanics, long before the invention of the EPR technique itself. In 1921 Stern and Gerlach (four years before Schrodinger and Heisenberg theories) set out the famous experiment to measure the magnetic moments of atoms, of which EPR can be considered a fascinating extension. It provided an experimental basis for the concept of spin. This was a hunch so far; but later it was found that S_z does possess all the properties of angular

momentum, behaving just like L_z, the angular momentum due to orbital motion of particle. A further cornerstone in the theory of atomic spectra was the Pauli theory of spin (1924), which provides an adequate framework for all present day applications in molecular theory, replacing the *ad-hoc* postulates used in the Bohr-Sommerfeld model by an all-embracing *antisymmetry principle*. This theory was still purely phenomenological. Later, an equation for the electron which satisfied simultaneously the requirements of special relativity theory and quantum mechanics was set up by P. A. M. Dirac. The existence of the spin and the magnetic moment are a consequence of this equation.

With the emergence of EPR experiments in 1945, anyway, it quickly became evident that the route from the fundamental theory to the actual data was too long, especially if complicated open shell metal ions in low symmetry environments were studied. A simpler, less fundamental but phenomenologically correct description of the EPR experiment was therefore urgently needed in order to reduce the complexity of the data analysis. The emergence of such a method, the effective Spin-Hamiltonian (SH), in the early 1950s [115–119] must be considered a major intellectual achievement with far reaching consequences for the development of EPR and NMR spectroscopies [120]. The principal idea of the SH is to write down an effective Hamiltonian that only contains spin degrees of freedom together with a few well defined numerical parameters (SH parameters) that are obtained fitting the experimental data. Since the spin only Schrödinger equation is easily solved exactly (or at least numerically with a computer) the experimentalists could now focus their efforts on designing new experiments and plan, describe and analyze them in the framework of the effective SH.

At a basic algebraic level all angular momenta, even of different origins such as orbital angular momentum (L) and spin angular momentum (S), can be summed to form an angular momentum acting in the appropriate tensor product. They can be summed and the energy eigenstates will also be eigenstates of operators in the sum of angular momenta. Each angular momentum lives on a different vector space, but the sum can be represented in the tensor product of the vector spaces. When dealing with systems with many spins (e.g. polynuclear clusters of interacting paramagnetic ions) only the first few eigenvalues and eigenstates are usually needed, the mathematical treatment of this class of spin systems exploits the so called Giant Spin Approximation (GSA), giving rise to the “effective” two-level systems. This approximation can be introduced when the difference in energy between different multiplets (eigenvectors with the same S^2 expectation value) is much higher than the energy splitting of levels inside each multiplet. Thus, it is not even necessary that the spin entering the SH is the “true” spin of the system.

The Spin-Hamiltonian is a rank-0 tensor, i. e. a scalar, but it is composed by products involving rank-2 tensors, this indicates that interactions depend on orientation in space. It is composed by spin operators that follows the angular momenta algebra [121]. Spin operators are usually represented in terms of their Hermitian Cartesian component operators. It is convenient to form algebraic combinations of a rank-2 Cartesian tensor elements to give spherical tensors. Spherical tensors are a class of *irreducible tensors*, they constitute the basis set of the rotations in the 3D Euclidean space. Nonetheless, the theory of angular momentum assigns to each complete set of eigenstates of total angular momentum j a complete set of $(2 \cdot j + 1)^2$ spherical tensor operators.

$$\begin{aligned} \mathbf{A}_0 &= \frac{1}{3} Tr\{A_{ij}\} = \frac{1}{3} \sum_i A_{ii} \\ \mathbf{A}_1 &= A'_{ij} = \frac{1}{2} (A_{ij} - A_{ji}) \\ \mathbf{A}_2 &= A'_{ij} = \frac{1}{2} (A_{ij} + A_{ji}) - \frac{1}{2} Tr\{A_{ij}\} \end{aligned} \tag{2.1}$$

$\mathbf{A}$ is a generic tensor where its nine Cartesian components A_{ij} can be defined in as: $\mathbf{A}_0$, a zero-rank tensor (1 component, scalar), $\mathbf{A}_1$, an antisymmetric first-rank tensor (3 components), $\mathbf{A}_2$, a symmetric second-rank tensor (5 components, traceless) [122, 123]. The advantages of the use of these combination is that the three subspaces do not admix under rotations, and, further, transform as the spherical harmonic functions Y_{00}, Y_{1q}, Y_{2q}. Each physical system can have interactions described by one or more terms of Eq. 2.1, depending on their electronic configuration or on they aggregation state. Liquid solution spectra, for instance, will be characterized only by the isotropic term ($\mathbf{A}_0$), while solid state spectra will be described by all the spherical terms, increasing the complexity of the eigenvalue ladder generated.

As rotations, another symmetry operation that leaves invariant the Hamiltonian of magnetic systems is defined by the time-reversal operator T. Going beyond purely spatial operations, also operations involving the reversal of direction of motion (time) commute with the Hamiltonian in some systems; as a result, the energy levels of a system with an odd total number of fermions (half-integer total spin) remain at least doubly degenerate in the presence of purely electric fields. This is the Kramers theorem [120].

$$|\Psi\rangle = T\,|\Phi\rangle \tag{2.2}$$

The degeneracy of the Kramers doublet (Ψ, Φ) can only be lifted by a magnetic field, which may be either an applied external field.

The main terms of the SH will be now presented. Griffith in 1960 [124] already depicted all the terms that are considered essential for the parametrization of EPR experiments today [125]:

1. The g-matrix which parametrizes the Zeeman splittings providing the linear response of the total electronic magnetic dipole moment to a magnetic field (0-10 cm^{-1}).

$$\mathscr{H}_{Electron\ Zeeman} = \mu_B \mathbf{B}^T \mathbf{g} \hat{\mathbf{S}} \tag{2.3}$$

where T stands for transposed. It is worth highlighting the sharp distinction concerning the g values of organic radicals from transition metal complexes which carry much more angular momentum in their electronic ground states. The dimensionless constant g is very close to 2 for the free electron (~ 2.002318) and the same holds for organic free radical, while, because of the more relevant role played by spin-orbit coupling (SOC) in heavier elements, the g value depends on the orientation of the molecule relative to the magnetic field. The various components of g can be determined from measurement on crystals, while in fluid solution EPR spectra (where the molecules tumble fast enough compared to EPR timescale) only the isotropic average of g is observed (i.e. the Hamiltonian describing the dissolved system is invariant under arbitrary rotations of the total spin). Historically, the division between the organic and inorganic fields became so strong in the 1970s that many workers [118] distinguished "electron spin resonance" (ESR) as a magnetic resonance technique applied to organic radicals with little angular momentum contributions while "electron paramagnetic resonance" (EPR) was used in conjunction with the same technique applied to transition metal complexes with significant angular momentum.

2. The hyperfine tensor is the sum of three contributions, namely the contact, the dipolar and the pseudocontact term. The contact term is given by the electron spin density on the magnetic nucleus, the dipolar term is given by the magnetic dipolar interaction between the electron spin and the nuclear spin, and the pseudocontact term is given by the magnetic dipolar interaction between the orbital moment of the electron and the nuclear spin [4, 126].

$$\mathscr{H}_{Hyperfine} = \hat{\mathbf{S}}^T \mathbf{A} \hat{\mathbf{I}} \tag{2.4}$$

This interaction (10^{-1}-10^{-4} cm^{-1}) causes a mixing in the composition of eigenvectors when the system is placed in low external magnetic fields, raising the field the eigenvector becomes a pure state with well defined S and I quantum numbers [71]

3. The zero-field splitting which parametrizes the interactions that lift the degeneracy of the $2S+1$ components of a spin multiplet with spin S (0-25 cm^{-1}). This

term, that gives rise to the wide thread of anisotropy studies [127], is not discussed further in this work as we deal only with $S = 1/2$ spin systems.

$$\mathscr{H}_{ZFS} = \hat{\mathbf{S}}^T \mathbf{D} \hat{\mathbf{S}} \tag{2.5}$$

4. The quadrupole interaction which parametrizes the interaction of the nuclear quadrupole moment (with spin $I > 1/2$) with the total electric field gradient at the nucleus (< 0.01 cm^{-1}).

$$\mathscr{H}_{Quadrupolar} = \hat{\mathbf{I}}^T \mathbf{Q} \hat{\mathbf{I}} \tag{2.6}$$

5. The nuclear Zeeman interaction which describes the Zeeman splitting due to the nuclear magnetic dipoles interacting with an external magnetic field ($< 10^{-3}$ cm^{-1}).

$$\mathscr{H}_{Nuclear\,Zeeman} = -\mu_n g_n \mathbf{B}^T \mathbf{g} \hat{\mathbf{S}} \tag{2.7}$$

6. Slightly later the SH was supplemented by appropriate terms to describe exchange and dipolar interactions between interacting spin systems, as defined by the Heisenberg Hamiltonian for ferromagnetic systems [128], a very detailed presentation is due to Alessandro Bencini and Dante Gatteschi [129]

$$\mathscr{H}_{Exchange} = \hat{\mathbf{S}}_1^T \mathbf{J} \hat{\mathbf{S}}_2 \tag{2.8}$$

2.2 SIMULATION OF MAGNETIC PROPERTIES

In approaching the subject of the SH, one aspect might require some careful preliminary thought. As outlined in previous section, the SH is a concise summary of the experimental data. Two treatments can be sought involving the SH formalism. One consists of regarding the SH parameters simply as fit parameters [125]. This fitting approach does not require the molecular geometry, the definition of a set of parameters allows to fit data and to characterize the structural symmetry properties of the paramagnetic system. The second point of view is to derive all terms that occur in the SH from first-principles models [130, 131], the only required parameters in this case are the bare atomic coordinates and fundamental physical constants. Hence, the main goal of quantum chemistry is to restore the path that leads from the exact, relativistic many-particle Schrödinger equation to the SH that is used for the analysis of the experiment.

Large-scale computer-based first-principles calculations have now become routine [111, 132]. The field of theoretical calculations [133] was developed in close correspondence with the progress in the experimental techniques.

Quantum chemistry deals with the simulation of quantum states of atomic systems and calculation of their energy [134]. The Linear Variational Method [135] is the starting point for the study of molecules and assumes the wavefunction as a linear combination of N linearly independent functions (often atomic orbitals)

$$|\psi\rangle = \sum_{j=1}^{N} a_j |\psi_j\rangle \tag{2.9}$$

this expression enters the equation to calculate the variational energy

$$E = \frac{\langle\psi|\mathscr{H}|\psi\rangle}{\langle\psi|\psi\rangle} = \frac{\sum_{i,j}^{N,N} a_i^* a_j H_{ij}}{\sum_{i,j}^{N,N} a_i^* a_j S_{ij}} \tag{2.10}$$

where S_{ij} are overlap integrals. The minimization of the total energy with respect to the linear coefficients $\{a_i\}$ is accomplished with differentiation of eq. 2.10 and imposing the condition of minimum $\frac{\partial E}{\partial a_i} = 0$, to form N Secular Equations. These equations can also be written in matrix notation, the Slater determinant of the secular matrix must be equal to zero.

$$|\mathscr{H}_{ik} - E S_{ik}| = 0 \tag{2.11}$$

A secular determinant has got a one-to-one correspondence with the wavevector (eq. 2.9), it represents one possible electronic configuration of the system.

Two approaches are currently used and can be divided in two kinds [136]. In the first category, one *single determinant* is enough to describe the wavefunction, a system well described by a single determinant can be seen as a weakly correlated system, where the electronic correlation arises from non-valence or *external* orbitals, and is usually defined *dynamic correlation*. Usually *mean field* or one-electron theories like Density Functional Theory (DFT) [137–139] or Møller-Plesset method (MP2) [140], are satisfactorily taking into account these effects. Conversely, *multideterminantal* treatments (Complete Active Space SCF, Coupled Cluster, full Configuration Interaction) are more eligible for strongly correlated system, i. e., where electrons feel the presence of other electrons individually and electron correlation, defined as *static correlation*, must be considered more explicitly. Static correlation is the correlation arising from near degeneracies in the valence or active orbitals and associated with the multireference nature of the system. In this thesis, we describe several studies that take advantage of dynamic correlation procedures in single reference systems by DFT or of static correlation procedures in multireference systems by CASSCF, an evaluation of the benefits from each method on the molecules subject of study are shown in Sec. 3.3. In general, only states that are conceptually well described by a single determinant, such as $S = 1/2$ systems, are expected to be well treated by DFT. However, it should also be realized that the systems studied by EPR spectroscopy often have extremely complicated electronic structures and a single Hartree–Fock determinant is almost never a good starting point [141].

In need of a multi-configurational description of the system[142], a further set of variational coefficients is introduced composing a Configuration State Function (CFS), expressed as a combination of determinants:

$$|\Phi_0\rangle = c_0|\Psi_0\rangle + \sum_{ar} c_a^r|\Psi_a^r\rangle + \sum_{\substack{a<b\\r<s}} c_{ab}^{rs}|\Psi_{ab}^{rs}\rangle + \sum_{\substack{a<b<c\\r<s<t}} c_{abc}^{rst}|\Psi_{abc}^{rst}\rangle + \sum_{\substack{a<b<c<d\\r<s<t<u}} c_{abcd}^{rstu}|\Psi_{abcd}^{rstu}\rangle + \cdots \tag{2.12}$$

where the superscript and subscript stands for having the atomic spin orbital χ_a, that is filled in the ground state, replaced by χ_r, that is virtual, e.g. empty [142].

In the most complete multi-determinant theory, such as Full Configuration Interaction method, all possible electronic configurations obtained by filling the different molecular orbitals with the electrons of the quantum system are considered, however this is not a feasible route because also for small molecules the number of excited determinants is very large. Instead, the idea of the CASSCF is to reduce the

number of electronic configurations by dividing the molecular orbitals into different category with a dedicated treatment. The multideterminantal method of CASSCF foresees the division of orbitals in (a) the internal orbitals, doubly occupied; (b) active orbitals, that can be occupied by 0, 1 or 2 electrons, and (c) virtual (external) orbitals that remain unoccupied. A full CI of N-electrons in a subset of M active orbitals set is then defining a CASSCF(N,M) wavefunction. All spin-eigenfunctions for N-electrons in M orbitals are included in the configuration interaction step. Hence in the CAS approach the number of determinats are reduced allowing its application even to larger molecules.

The choice of the active space becomes of paramount importance, since it should account for the static correlation energy to catch the correct electronic and magnetic properties. The active space should at least involve the molecular orbitals where the unpaired electrons is located, usually the orbitals involved can be the seven 4f orbitals, the five 3d orbitals, the π antibonding orbitals of organic radicals [143]. The effect of the extension of the active space to some virtual orbitals, or towards the internal doubly occupied one has not been tested in detail [144]. In the majority of the cases the active space employed has been the less extended one. However, such a restrictive approach seems to provide quite confident results. Several kinds of active spaces were tested for a molecular system focused in Fig. 3.12. Another advantage of this method is that the computed states for the several spin-multiplicities are now eigenfunctions of the total spin operator S^2, due to their multideterminantal nature. This is not true for DFT methods.

Spin–orbit coupling (SOC) plays a fundamental role in molecules behavior. It describes a process in which an electron changes simultaneously its spin and angular momentum or, in general, moves from one orbital wave function to another [145]. The mixing of the spin and the orbital motion is a relativistic effect, which can be derived from Dirac's model of the electron. The mixing is large in heavy ions, where the average velocity of the electrons is higher. Carbon is a light atom, and the spin orbit interaction is expected to be weak. In the simulation of transition metal atoms accomplished in this thesis, the SOC is treated at the second order perturbation theory level, the subtle admixing of ground state wavefunction due to this interaction plays a fundamental role and determines the different performances of magnetic molecules as qubits (see Sec. 3.2).

2.3 SIMULATION OF LATTICE DYNAMICS

Vibrational analysis based on periodic Density Functional Theory (p-DFT) calculations have been performed on the molecular systems presented in this thesis. Vibrational properties are accessible by optimizing the crystal structure to approach the minimum of the potential energy surface (PES). At the minimized energy state all Hellmann-Feynman forces, obtained as the analytic gradient of the PES (eq. 2.13) with respect to ionic position, Φ_i, should vanish.

$$V = \Phi_0 + \Phi_i \cdot U_i + \frac{1}{2!}\Phi_{i,j} \cdot U_i^2 + \frac{1}{3!}\Phi_{i,j,k} \cdot U_i^3 + \cdots \tag{2.13}$$

$$\Phi_0 = V_0 \qquad \text{Total DFT Energy} \tag{2.14}$$

$$\Phi_i = \sum_i \left(\frac{\partial V}{\partial U_i}\right)_0 \qquad \text{Forces} \tag{2.15}$$

$$\Phi_{i,j} = \sum_{ij} \left(\frac{\partial^2 V}{\partial U_i \partial U_j}\right)_0 \qquad \text{Force Constants} \tag{2.16}$$

$$\Phi_{i,j,k} = \sum_{ijk} \left(\frac{\partial^3 V}{\partial U_i \partial U_j \partial U_k}\right)_0 \qquad \text{Anharmonic Constants} \tag{2.17}$$

A tight DFT energy minimization of structures is mandatory for the vibrational analysis to avoid imaginary eigenvalues from diagonalization of Hessian matrix. Every atom in the unit cell is displaced by small amounts and the forces on all other atoms are recorded to calculate the second derivative of PES through numerical differentiation.

Any atomic displacement $\mathbf{U}(\mathbf{m},\mu) = \sum_i X_i(\mathbf{m},\mu) - \bar{X}_i(\mathbf{m},\mu)$, where $\bar{X}_i(\mathbf{m},\mu)$ is the equilibrium position, generates forces on all other atoms of the determined cell according to the relationship

$$F_i(\mathbf{n},\nu) = \sum_{\mathbf{m},\mu,j} \Phi_{i,j}(\mathbf{n},\nu,\mathbf{m},\mu) U_j(\mathbf{m},\mu) \tag{2.18}$$

where n and m are the primitive unit cell indices, ν and μ are the atomic indices. This relates the *forces* generated to the *force constants*, or Hessian, matrix $\Phi(\mathbf{n},\nu,\mathbf{m},\mu)$ and atomic displacements $\mathbf{U}(\mathbf{m},\mu)$. We imposed a set of constraint equations on the force constant matrix known as the *acoustic sum rule* to ensure that the crystal energy

is invariant under global translation of the whole crystal, i. e., that $\omega_{acoustic} = 0$ at the Γ-point.

$$\forall\ i,\mathbf{n},\nu: \quad \sum_{\mathbf{m},\mu,j} \Phi_{i,j}(\mathbf{n},\nu,\mathbf{m},\mu) = 0 \tag{2.19}$$

The equation of motion for the atoms is then expressed as:

$$M_\mu \ddot{U}_j(\mathbf{m},\mu) = -F_i(\mathbf{n},\nu) + eZ_i(\mathbf{n},\nu)\cdot\mathbf{E} \tag{2.20}$$

M_ν is the mass of atoms. The first term on the right side accounts for the analytic force due to the short-range interatomic interaction, where **U** represents the whole set of atomic displacements; the second term, with $-e$ the electron charge, accounts for the nonanalytic force due to the long-range coulombic interactions shown as the dot product between the Born effective charge 2-rank tensor Z and the averaged electric field (**E**) induced by the atomic vibration.

After the construction of Hessian matrix it is possible to express the equation of motion in the reciprocal space, that reads in the compact matrix form:

$$\omega^2(\mathbf{k},j)\mathbf{e}(\mathbf{k},j) = \mathbf{D}(\mathbf{k})\mathbf{e}(\mathbf{k},j) \tag{2.21}$$

Where **k** is the reciprocal space wave vector. The dynamical matrix is defined as the mass-weighted Fourier transform of Hessian matrix [146–148]

$$D_{\alpha,\beta}(\mathbf{k};\mathbf{n},\nu,\mathbf{m},\mu,i,j) = \sum_{\mathbf{n}} \left[D^A_{\alpha,\beta}(\mathbf{k};\mathbf{n},\nu,\mathbf{m},\mu,i,j) + D^N_{\alpha,\beta}(\mathbf{k};\mathbf{n},\nu,\mathbf{m},\mu,i,j) \right] e^{i\mathbf{k}\cdot\mathbf{R_n}} \tag{2.22}$$

where $D^A_{\alpha,\beta}$ and $D^N_{\alpha,\beta}$ are, in resemblance to the terms in Eq. 2.20, the analytic contribution under zero-averaged electric field and the effects of the vibration-induced macroscopic field, respectively [148].

The force constants calculation and diagonalization are implemented within a in-house software written by Alessandro Lunghi, the solution of the eigenproblem (eq. 2.21) gives eigenvalues $\omega^2(\mathbf{k},j)$ and eigenvectors $\mathbf{e}(\mathbf{k},j)$ of $3N$ orthogonal normal modes of vibrations.

At date, only the first term, $D^A_{\alpha,\beta}$, is implemented in the software:

$$D^A_{\alpha,\beta}(\mathbf{k};\mu,\nu) = \frac{1}{\sqrt{M_\mu M_\nu}} \sum_{\mathbf{m}} \Phi(0,\nu,\mathbf{m},\mu) exp\{-2\pi i\mathbf{k}\cdot[\mathbf{X}(0,\nu) - \mathbf{X}(\mathbf{m},\mu)]\} \tag{2.23}$$

Here, M_μ and M_ν are masses of atoms, and $\mathbf{k}$ is the wave vector.

From a computational perspective, a shortening of cpu-time required for vibrational analysis is possible exploiting the crystal symmetry and calculating the displacements on the only asymmetric unit of the crystal. For some of the molecules investigated in this thesis (see Sec. 3.2), I exploited the symmetry elements in the unit cell for the SCF calculation so that second derivative calculations were only performed on irreducible atoms. The full Hessian matrix was then generated by applying the point group symmetry to the irreducible part, and the corresponding mass-weighted matrix was diagonalized to obtain eigenvalues, which were transformed into frequencies (cm^{-1}). The resulting eigenvectors were converted into normal modes.

The calculation of the periodic crystal phase is usually restricted to one primitive cell finite differentiation of forces, giving access only to zone-center phonons ($k = 0$ or "Γ-point"). A macroscopic crystal containing N atoms has a practically infinite number, $3N$, of displacement degrees of freedom and, consequently, of vibrational modes. The use of space group symmetry and the introduction of the reciprocal lattice allows a fundamental rationalization of this huge number of states. At the centre of the Brillouin zone (BZ), the degrees of freedom are reduced to $3N$, N being the number of atoms in the crystal unit cell, so that the vibrational modes are $3N - 3$ (3 are the rigid displacements of the unit cell, corresponding to zero frequency). Only the $k = 0$ vibrations can be measured with optical techniques such as IR spectroscopies; the remaining vibrational modes are classified, throughout the entire BZ, in $3N$ dispersion bands and are optically inaccessible. The Γ-point approximation in theoretical calculations, though, comes with no loss of information. The box used for simulation in this case is the unit cell of the crystal, allowing to calculate $3N - 3$ optical normal modes energies at the Γ point.

A peculiar feature of most molecular crystals is that intramolecular forces are much stronger than intermolecular ones, so that, the intramolecular vibrations arising chiefly from the oscillation of atoms within a molecule in the crystal are almost unchanged from those of the isolated molecule. If the crystal unit cell contains n molecules, there are then $6n - 3$ intermolecular phonons at $k = 0$, corresponding to *rigid* translations and rotations of the molecules [149]. These "external" phonons have frequencies much lower (typically, less than 200 cm^{-1}) than the intramolecular vibrations (Fig. 2.1). However, in some cases, where molecular vibrations of unusually low frequency are present, the separation of "internal" and "external" phonons is impossible and low frequency phonon modes have mixed character (see ref. [150] fig. 4; [151].

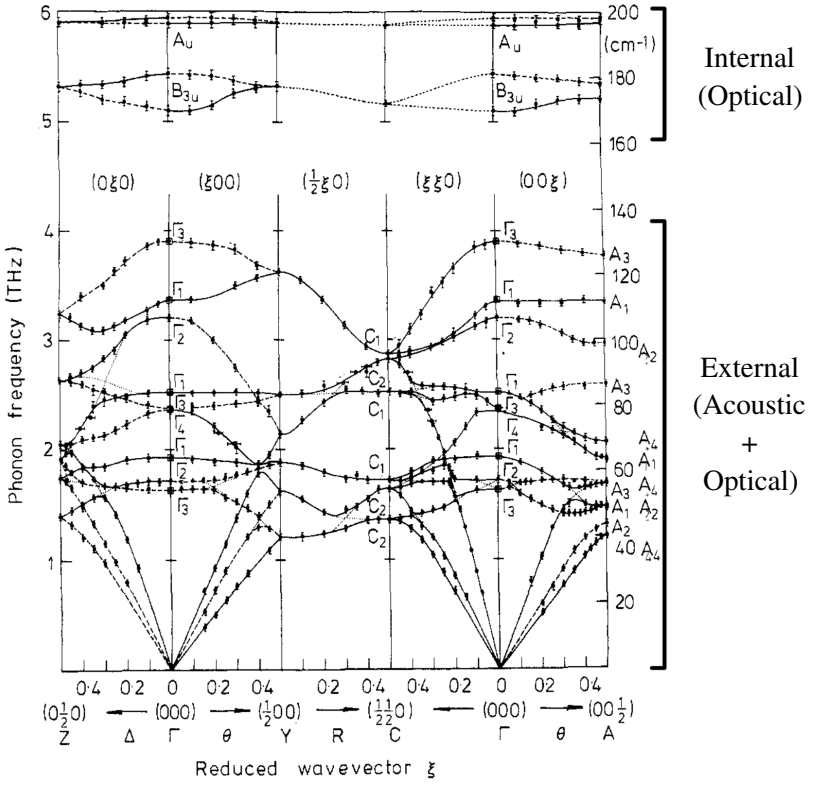

Figure 2.1: Experimental phonon dispersion curves for d_8-naphthalene at T = 6 K. The full and broken lines denote symmetric and antisymmetric phonon branches with respect to the twofold screw axis in [O, ξ, 0] direction and to the glide plane in [ξ, 0, 0] and [0, 0, ξ] directions. The crossings of eigenvectors (anticrossing of branches) are indicated by dotted lines. The image was taken from ref. [152]

The extension to the whole Brillouin zone to calculate the entire **k** vs. ω dispersion relation of phonons has been attempted by means of the *frozen-phonon* or *supercell* approach [153–156].

The periodic ionic displacements entering a frozen-phonon calculation are constructed with cells larger than the primitive cell, or supercells (Fig. 2.2). The calculation of lattice vibrations at a generic **k** vector requires a supercell having **k** as a reciprocal-lattice vector and whose linear dimensions must be therefore at least of the order of $2\pi/|\mathbf{k}|$. The monochromatic perturbation **u** to atomic positions **X** are applied on the atoms of the unit cell,

$$X[u_i(k)] = R_l + \tau_i + u_i e^{i\mathbf{k}\cdot R_l} \tag{2.24}$$

where X_l is the lattice vector, τ_i is the equilibrium position of the i-th atom in the unit cell. Fourier transform of force constants (Eq. 2.3) at $\mathbf{k}$ are calculated from finite differences of forces induced on all the atoms of the supercell. The main advantage of the frozen-phonon approach is that it does not require any specialized computer code, as Density Functional Perturbation Theory (DFPT) does. This technique can in fact be straightforwardly implemented using any standard total energy and forces from available packages, and only moderate care is needed in the evaluation of numerical derivatives.

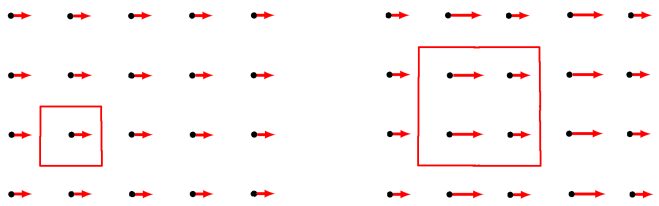

Figure 2.2: Square 2-dimensional Bravais lattice showing the unit cell (**a**) and a supercell with doubled dimensions, the periodic boundary conditions are applied at the border of the red square. Phonons with different phase from one lattice point to another ($\mathbf{k} \neq 0$) can be captured.

A problem closely related to these considerations is that of the calculation of phonon dispersion is systems where the inversion center symmetry is disrupted by the vibrations and hence possibly developing a net electric dipole moment. In centrosymmetric systems, phonons can break the inversion center and determine an electric polarization. In the expansion of calculation of phonons to the entire Brillouin zone (see Sec. 3.5 [VO(tpp)]) we faced the occurrence of a wrong behaviour for acoustic phonons, even increasing the accuracy of calculations, triggering us to dig deeper in the reasons of this behaviuor. An aspect, to better take into account the polarization effects, is to insert in the dynamical matrix $\mathbf{D}$ the macroscopic electric field induced by phonons at the borders of the unit cell [148]. The lone first term in Eq. 2.22 is still enough for reproducing phonons of crystals in which electric field is compensated by symmetry, or when we attempt to calculate gas-phase systems that experience no electric field with their translational replica (see Sec. 3.3).

The full inclusion of the Brillouin zone integration, important to quantitatively estimate the phonon bands, is a task already accomplished for the [$VO(acac)_2$] case of study [90, 157] but deserves further investigation from solid-state physics perspective, such as macroscopic electric field establishing at cell borders of unit cell, to be a robust generally applicable method in modern quantum chemistry.

2.4 COMPUTATIONAL PROCEDURES

We now pass through the detailed definition of techniques employed for the magnetic and vibrational analysis.

Calculations of the spin Hamiltonian parameters were carried out with the ORCA package [158]. The level of theory used was DFT, with the PBE0 hybrid functional and all-electron basis sets: def2-TZVP basis set for the metal and first coordination shell atoms and def2-SVP for the C and H atoms in the ancillary part of molecules, for the Landè factor, while hyperfine values were calculated by adopting a specialized basis set for accurate hyperfine coupling constants (aug-cc-pVTZ-J). The molecular geometry used for these simulations was obtained by the periodic DFT calculations for the optimized molecular structure in CP2K. The hybrid functional PBE0 contains an exact-exchange contribution that is missed in GGA functionals. Thus, the significant potentials imposed by these functionals is different [159]. Hartree-Fock/DFT hybrid functionals admix a certain amount of Fock exact exchange (E_x) to the exchange part (E_x^{PBE}) and correlation part (E_c^{PBE}) of the PBE GGA density functional:

$$E_{xc}^{PBE0} = \frac{1}{4}e_x + \frac{3}{4}E_x^{PBE} + E_c^{PBE} \tag{2.25}$$

This kind of functional turns out to be more accurate than common local or semilocal DFT functionals for calculation of static magnetic properties, i. e., EPR parameters.

For the calculation of phononic structures of potential molecular qubits, and spin densities and exchange coupling constants of functionalized graphene in Ch. 4, periodic DFT calculations were performed by the the Quickstep module [160] present in CP2K atomistic simulation package [161, 162]. GTH pseudopotentials [163–165] for the core electrons and valence pseudo-wavefunctions are expanded in Gaussian-type orbitals and the density is represented in a plane wave auxiliary basis set. In particular, DZVP-MOLOPT-SR-GTH basis set were used [160]. The use of a plane wave basis to represent the Kohn–Sham orbitals allows the efficient calculation of the energy using fast Fourier transforms and the inclusion of the translational symmetry through Born–von Kármán periodic conditions. The Perdew-Burke-Ernzerhof (PBE) parametrization [166] was choosen for the calculation. A pairwise dispersion correction proposed by Grimme [167–170] was included in the DFT calculations. The Broyden–Fletcher–Goldfarb–Shanno (BFGS) [171, 172] or, alternatively, the Conjugate Gradient (CG) algorythms [173] were employed as minimizer to carry out the unit cell optimization. Basis set size, furthermore, depends on volume of computational box and on cut-off of plane waves energy included. The basis set functions are discretised on numerical grids in the real space; adding high

frequency plane waves will therefore require increasingly finer grid points to be described, quickly increasing the computational cost. The convergence of the plane waves basis cut-off was tested for one molecule (see Sec. 3.4 [$VO(acac)_2$]) and reached the value of 10000 *Ry* with a convergence threshold of $1.0 \cdot 10^{-9}$ *a.u.* for the energy self-consistency and $5.0 \cdot 10^{-8}$ *a.u.*/Å for the forces. A cut-off of 10000 *Ry* is cumbersome and the best compromise between accuracy and cpu-time consumption was chosen to be from 1000 *Ry* (Sec. 3.3) to 5000 *Ry* (Sec. 3.4 and Sec. 3.5). Such a choice was taken also on the basis of the convergence of vibrational energies in the low energy range (0-100 cm^{-1}). Indeed, the error between the frequency values computed for 10000 *Ry* and 5000 *Ry* is just few decimal digits of wavenumber. Substantially more loose convergence threshold of $1.0 \cdot 10^{-7}$ or $1.0 \cdot 10^{-7}$ *a.u.*/Å for the forces in larger systems, as reported for [VO(tpp)] supercells in Sec. 3.5. All graphene based systems were simulated with an electron density grid cutoff of 500 Ry and a convergence threshold for the forces of $4.5 \cdot 10^{-4}$, as this study is not focused on vibrational analysis, but only on structural and magnetic analysis, less restrictive potential energy surfaces minimization is enough to reach the required accuracy.

3

V(IV) AND CU(II) SPIN QUBITS DYNAMICS

3.1 THE SPIN-PHONON COUPLING INTERACTION

As introduced in Sec. 1.3, the longitudinal (T_1) and transverse (T_2) spin-relaxation times characterize how rapidly a non-equilibrium spin states decays to equilibrium configuration and, therefore, whether a material is suitable for quantum technology purposes.

The recent trends in transition metal ion based qubits foresees several synthetic strategies to minimize the *spin-spin interactions*, such as the use of nuclear spin free ligands [22] to cancel out the deleterious effects of hyperfine or dipolar coupling on the coherence lifetime. For this reason, some of the ligands presented in next sections [71, 174] are composed of carbon with either oxygen or sulfur atoms which are almost entirely composed of $I = 0$ isotopes, switching off sources of intramolecular magnetic dipolar disturbance affecting the bonded metal ion. The dipolar coupling between electron and nuclear spins depends on the mutual distance of each pair of magnetic moments and can be possibly reduced maximing these distances. Magnetic noise is, indeed, usually further minimized through the use of magnetically diluted solid samples obtained by co-crystallization of the complex of interest with a diamagnetic and isostructural analogue [19, 71, 175]. The crystalline dispersion, with a content of magnetic compound varying from 10 to 0.1%, dramatically changes the EPR spectrum. With metal-phtalocyaninates, for instance, at very low concentrations, $\sim 0.1\%$, the superhyperfine spectral features due to the further coupling with the neighboring nuclear spins of the chelating ^{14}N nuclei ($I = 1$) become visible [176].

The hyperfine interaction with the metal ion magnetic moment, on the other hand, represents an unavoidable interaction. It was thought to represent the fundamental limitating interaction of the electron-spin coherence [70]. Recently, anyway, it was demonstrated that in peculiar cases [177], in which these electron-nuclear levels can be singularly addressed, electron-nuclear interaction can constitute a boost for the

employability of such molecules enlarging the controllable set of quantum levels available.

The contribution of *spin-lattice interactions* to the decoherence is more difficult to control since it involves the coupling of the spins with the vibrations. Electron spin–lattice relaxation, as depicted in Sec. 1.3 is a recovery of a spin system to equilibrium after excitation. In the crystalline solid phase, thermodynamic spin relaxation transfers energy to lattice phonons. At high temperatures, this relaxation process causes T_m to become T_1-limited, defining the spin-phonon regime of decoherence, that this the focus of subsequent work.

The general way we understand spin-relaxation is that the relaxation time (either T_1 ot T_2) is measured as a function of some external parameter, usually temperature or external magnetic field, and that we fit the results with different phenomenological models. Even it is not always straightforward one then tries to understand the relevant factors affecting the relaxation by the parameters of the fit. The phenomenological models commonly used to reproduce Temperature (T) or Field (B) dependence of the spin-lattice relaxation are based on the seminal work of Orbach [178]. It predicts, for $S = 1/2$ systems for example, functional forms describing the temperature dependence of T_1 resulting in $1/T_1 \propto B^4T$ for the direct process and $1/T_1 \propto T^9$ or B^2T^7 for the Raman process [25]. Often, different dependences are found for Raman process as $1/T_1 \propto T^n$ [157, 179–181]; n appears to be system-dependent and may vary between 2 and 9. In $S > 1/2$ system, the Orbach relaxation process is active and its functional form is $Ae^{\left(\frac{-\Delta E}{kT}\right)}$, where A is a prefactor in the fit and ΔE is the energy difference between ground state and first excited spin state.

The phonon contribution to the relaxation is based on the Debye model. In the Debye model, the dispersion relation is linear, $\omega = c|k|$, and the density of states is quadratic as it is in the long wavelength limit.

$$D(\omega) = \frac{3\omega^2}{2\pi^2 c^3} \quad \left[s\,rad^{-1}\,m^{-3}\right] \tag{3.1}$$

Here c is the speed of sound. This holds up to a maximum frequency called the Debye frequency ω_D. In three dimensions there are 3 degrees of freedom per atom so the total number of phonon modes is $3n$.

$$3n = \int_0^{\omega_D} D(\omega)d\omega \tag{3.2}$$

n is the atomic density. There are no phonon modes with a frequency above the Debye frequency. The Debye frequency is $\omega_D^3 = 6\pi^2 nc^3$. Optical phonons, which

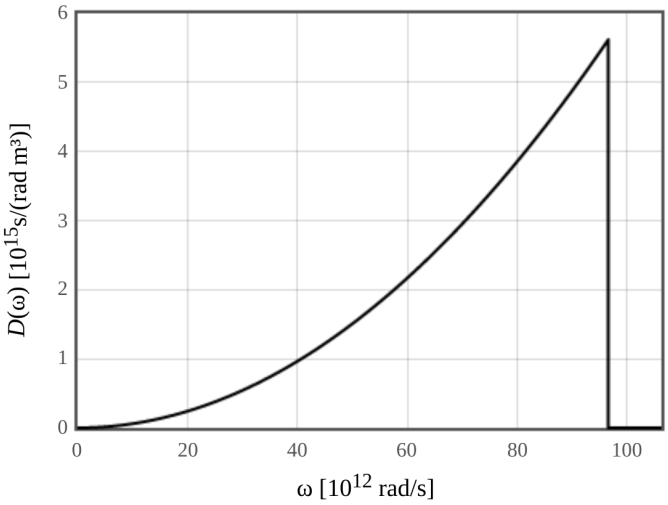

Figure 3.1: The Debye density of states is reported. The abscissa reports the angular frequency ω in rad/s and the second column is the density of states $D(\omega)$ in units of $s/(radm^3)$. Here $c = 6320\ m/s$ and the atomic density $n = 6.03 \cdot 10^{28}$. The resulting Debye frequency is $9.66 \cdot 10^{13}$.

include the intramolecular vibrations commonly analyzed in molecular vibrational spectroscopy, are not considered in the Debye model.

This model is not able to describe accurately the experimental temperature dependence of the relaxation rate $1/T_1$ in the whole temperature range. The assumptions of this model have indeed two key consequences for a spin–phonon coupling description: (1) relaxation takes place exclusively through scattering of acoustic phonons rather than optical phonons, and (2) the spin-phonon coupling constants for each phonon mode are equal or follow some predictable functional form, as no provision can be made for unique spin–phonon coupling for distinct intramolecular vibrations.

Before focusing on the specific systems investigated in the thesis, a sketch of the theory used to analyze them will be provided. The total Hamiltonian of the system [76] and environment is:

$$\mathscr{H} = \mathscr{H}_s + \mathscr{H}_{Ph} + \mathscr{H}_{Sp-Ph} \tag{3.3}$$

where $\mathscr{H}_s = \mathscr{H}_{BO} + \mathscr{H}_{SO} + \mathscr{V}_0$ describes the electronic structure, it is composed of $\mathscr{H}_{BO}$, the non-relativistic Born-Oppenheimer Hamiltonian for the free ion, $\mathscr{H}_{SO}$, where all the spin–orbit interaction are included, $\mathscr{V}_0$, the potential energy of the ion due to the crystalline electric field; $\mathscr{H}_{Ph}$ and $\mathscr{H}_{Sp-Ph}$ the phonons Hamiltonian and the spin-phonon coupling Hamiltonian, respectively.

What we intend to calculate is the probability of particular spectroscopic transition between spin states to take place. The transition amplitude associated with a physical process will be the evolution-operator matrix element between the initial and final states of the process under study. The calculation of these amplitudes frequently uses perturbation theory and is based on the splitting of the total Hamiltonian $\hat{\mathscr{H}}$ into an unperturbed part $\hat{\mathscr{H}}_0$ and a coupling $\hat{V} = \hat{\mathscr{H}}_{Sp-Ph}$ [182]. In the present analysis, this term is composed of SH derivatives with respect to the phonons. Any kind of atomic displacement that is going to modify the parameters inside SH is an atomic motion that couples spin and lattice and produces spin relaxation. Lattice vibrations (phonons) modulate distance between unpaired electrons and surrounding ligand atoms, i.e. they modulate a local crystal field contributing to the orbital magnetic moment of the unpaired electron. This contribution is due to the spin–orbit interaction which, however, is not explicitly included in the existing relaxation theories [183].

For each molecule, $(\hat{\mathscr{H}}_s)$ is a SH that contains all the terms mandatory to describe its EPR spectrum, and $\hat{\mathscr{H}}_{ph} = \sum_{\alpha\mathbf{q}} \hbar\omega_{\alpha\mathbf{q}}(\hat{n}_{\alpha\mathbf{q}} + \frac{1}{2})$ correspond to a term to describe the lattice, usually in the harmonic approximation.

The fundamental ingredient is the coupling between these terms:

$$\hat{\mathscr{H}}_{Sp-Ph} = \sum_{\alpha\mathbf{q}} \left(\frac{\partial \hat{\mathscr{H}}_s}{\partial Q_{\alpha\mathbf{q}}}\right) \hat{Q}_{\alpha\mathbf{q}} + \sum_{\alpha\mathbf{q},\beta\mathbf{q}'} \left(\frac{\partial^2 \hat{\mathscr{H}}_s}{\partial Q_{\alpha\mathbf{q}} \partial Q_{\beta\mathbf{q}'}}\right) \hat{Q}_{\alpha\mathbf{q}} \hat{Q}_{\beta\mathbf{q}'} + \cdots \tag{3.4}$$

The dynamics of the spin and bath systems can be described by means of Liouville equation

$$i\hbar \frac{\partial \rho(t)_I}{\partial t} = [V_I, \rho(t)_I] = [\mathscr{H}_{Sp-Ph}, \rho(t)_I], \tag{3.5}$$

$\mathscr{H}_{Sp-Ph}$ operator is here intended in the *interaction picture*. The *interaction configuration* is usually adopted when treating a time dependent perturbation Hamiltonian $V(t)$ that is little compared to the other terms in $\mathscr{H}$. We can, in this case, describe the transitions induced by the perturbation $V(t)$ as acting on the unperturbed Hamiltonian $\mathscr{H}_0$ states, writing the matrix element of the V_I operator as:

$$\begin{aligned} (V_I)_{kl} &= \langle k|V_I|l\rangle = \langle k|U_0^{\dagger}(t,t_0)V(t)U_0(t,t_0)|l\rangle \\ &= \langle k|e^{\frac{\mathscr{H}_0}{\hbar}(t-t_0)}V(t)e^{-\frac{\mathscr{H}_0}{\hbar}(t-t_0)}|l\rangle \\ &= e^{-\frac{(E_l-E_k)}{\hbar}(t-t_0)}V_{kl} \end{aligned} \tag{3.6}$$

As the interest is on dynamics of only spin degrees of freedom [184] it is convenient to define a reduced density operator with a formal integration over bath degrees of freedom, $\rho_s(t) = \mathrm{Tr}_B(\rho(t))$, where Tr_B indicates that we took the trace on the bath only. In order to remove the bath dependence, it is useful to make the Born approximation: $\rho(t) = \rho_s(t) \otimes \rho_{eq}^B$. In virtue of the supposed weak coupling between bath and spin degrees of freedom the Born approximation assumes the bath to relax much faster than the spin system, and hence it always lays in thermal equilibrium. Before to explicitly write $\mathscr{H}$ also the Markov approximation should be done, in order to let ρ_s to be a dynamical semi-group [41]:

$$i\hbar^2 \frac{\partial \rho_s(t)}{\partial t} = \int_0^\infty dt' Tr_B \left[H(t), [\mathscr{H}(t-t'), \rho_s(t) \otimes \rho_B]\right]. \tag{3.7}$$

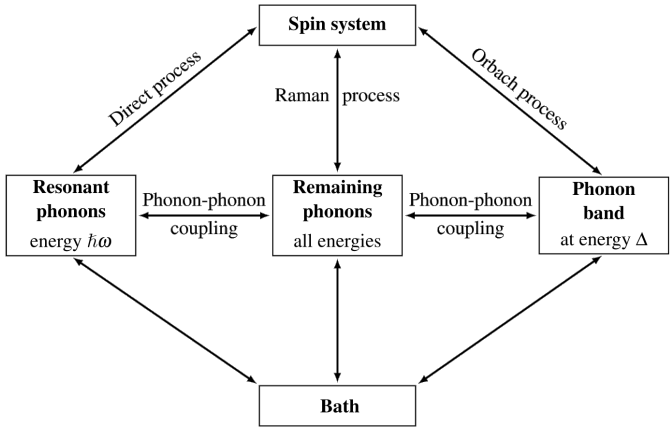

Figure 3.2: Schematic representation of the various paths for spin-phonon relaxation, phonon-phonon coupling and phonon-bath relaxation. The double sided arrows indicate that the energy flow can assume both directions toward the spin system or toward the bath, from the "hot" one to the "cold" one. Image adapted from ref. [120]

In the following we will show that, by exploiting an appropriate master equation we can today rationalize spin relaxation in Kramers system by using ab initio calculation. Generally, we restrict ourselves to two different level of theory: first

order time dependent perturbation theory (TDPT) (Eq. 3.8), and second order one (Eq. 3.9).

$$\frac{d\hat{\rho}^s(t)}{dt} = -\frac{1}{\hbar^2}\int_0^t ds\, Tr_B\left[\hat{\mathscr{H}}_{Sp-Ph}(t), \left[\hat{\mathscr{H}}_{Sp-Ph}(s), \hat{\rho}(s)\right]\right] \tag{3.8}$$

$$\frac{d\hat{\rho}^s(t)}{dt} = -\frac{1}{\hbar^4}\int_0^t ds \int_0^s ds' \int_0^{s'} ds'' \\ Tr_B\left[\hat{\mathscr{H}}_{Sp-Ph}(t), \left[\hat{\mathscr{H}}_{Sp-Ph}(s), \left[\hat{\mathscr{H}}_{Sp-Ph}(s'), \left[\hat{\mathscr{H}}_{Sp-Ph}(s''), \hat{\rho}(s'')\right]\right]\right]\right] \tag{3.9}$$

The spin–phonon coupling has been included in description of relaxation processes since long time[185], but a quantitative description has been hindered in the past due to the lack of computational resources and methods to approach the study at the required level of subtlety. The main goal of the research on theoretical description of spin relaxation is integrating spin–phonon interactions into the current computational methodologies of spin relaxation. A less complex electronic structure need to be taken into account to model magnetic relaxation of $S = 1/2$ spin qubits. Spin-orbit coupling, derived from second order perturbation theory procedures [158], plays for our systems a fundamental role. Furthermore, vibrations that couple to spin states is currently recognised to be the key factor in these systems. In the following treatment, we focus on master equation for $S = 1/2$ systems, the $\mathscr{H}_s$ will therefore contain only the Zeeman term $\mathscr{H}_s = -\mathbf{g}\mu_B \cdot \mathbf{S} \cdot \mathbf{B}$. The hyperfine interaction, that is in principle present as mentioned in Sec. 1.2, can be at first stage neglected considering a sufficient high external magnetic field that foster the hyperfine coupling relaxation. The following treatment can be straightforwardly extended to more complex SH with no loss of generality.

Sp-Ph-mediated relaxation processes showed in Fig. 3.2 can occur if some conditions are met:

1) energy conservation must be satisfied, implying that only lattice processes matching the spin-flip energy can occur.

2) there must be a nonzero transition probability for the energy to transfer from the spin to the lattice phonon, a criterion known as *spin-phonon coupling*, hereafter called Sp-Ph for brevity.

The energy conservation can be satisfied through:

i) single phonon processes (direct mechanism Fig. 3.3 (**a**) and (**b**)),

$$\frac{d\rho^s_{aa}(t)}{dt} = \sum_b W_{ab}\rho^s_{bb}(t)$$

$$W_{ab} = \frac{2\pi}{\hbar^2}\sum_{\alpha\mathbf{q}}\left|\sum_{ij}\mu_b\left(\frac{\partial g_{ij}}{\partial Q_{\alpha\mathbf{q}}}\right)B_j\langle a|S_i|b\rangle\right|^2 G^{1-ph}(\omega_{ab},\omega_{\alpha\mathbf{q}})$$

$$G^{1-ph}(\omega_{ab},\omega_{\alpha\mathbf{q}}) = \delta(\omega_{ab}-\omega_{\alpha\mathbf{q}})\bar{n}_{\alpha\mathbf{q}} + \delta(\omega_{ab}+\omega_{\alpha\mathbf{q}})(\bar{n}_{\alpha\mathbf{q}}+1) \quad (3.10)$$

where $\left(\frac{\partial g_{ij}}{\partial Q_{\alpha\mathbf{q}}}\right)$ is the first order spin-phonon coupling, and $G^{1-ph}(\omega_{ab},\omega_{\alpha\mathbf{q}})$ phonon's correlation function,

ii) inelastic scattering of two phonons processes with the correct energy difference *via* a virtual state (Raman mechanism Fig. 3.3 (**c**) and (**d**)),

$$\frac{d\rho^s_{aa}(t)}{dt} = \sum_b W_{ab}\rho^s_{bb}(t)$$

$$W_{ab} = \frac{2\pi}{\hbar^2}\sum_{\alpha\mathbf{q}}\sum_{\beta\mathbf{q}'}\left|\sum_{ij}\mu_b\left(\frac{\partial^2 g_{ij}}{\partial Q_{\alpha\mathbf{q}}\partial Q_{\beta\mathbf{q}'}}\right)B_j\langle a|S_i|b\rangle\right|^2 G^{2-ph}(\omega_{ab},\omega_{\alpha\mathbf{q}},\omega_{\beta\mathbf{q}'})$$

$$G^{2-ph}(\omega_{ab},\omega_{\alpha\mathbf{q}},\omega_{\beta\mathbf{q}'}) =$$
$$\delta(\omega_{ab}+\omega_{\alpha\mathbf{q}}-\omega_{\beta\mathbf{q}'})\bar{n}_{\beta\mathbf{q}'} + \delta(\omega_{ab}-\omega_{\alpha\mathbf{q}}+\omega_{\beta\mathbf{q}'})\bar{n}_{\alpha\mathbf{q}}(\bar{n}_{\beta\mathbf{q}'}+1) \quad (3.11)$$

where $\left(\frac{\partial^2 g_{ij}}{\partial Q_{\alpha\mathbf{q}}\partial Q_{\beta\mathbf{q}'}}\right)$ is the second order Sp-Ph coupling coefficient,

iii) two phonon processes through a real electronic excited state (Orbach mechanism). In dilute monometallic $S = 1/2$ qubits, contributions from the Orbach mechanism are often negligible owing to the lack of thermally accessible electronic excited states, contrarily to high spin SMMs, where a bunch of accessible magnetic states can be populated by thermal energy or radiation. The tools to describe the Orbach relaxation mechanism in large ZFS molecules need a slightly modified treatment with first order Sp-Ph and second order perturbation theory, and are not reporteed here [186].

The detailed description of Sp-Ph coupling can then be applied for every kind of spin system [157, 187, 188] that accounts for the relaxation properties of magnetisation at higher temperatures, too.

We ascertained in this work that the spin-phonon coupling terms in molecular solids may vary by orders of magnitude depending on the phonon mode under consideration [174]. These effects are not captured in the Debye model temperature

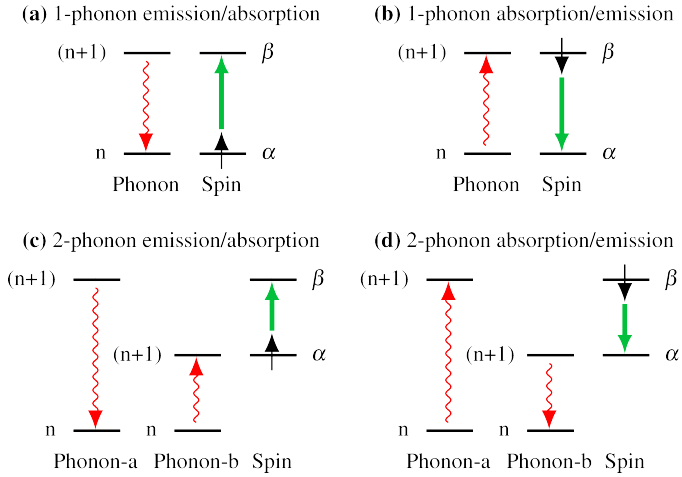

Figure 3.3: Schematic illustration of the direct process (**a**), (**b**) and the Raman process (**c**), (**d**) in spin-lattice relaxation. (**a**) a phonon of frequency equal to the magnetic resonance frequency is absorbed by a spin which makes a transition to the upper state. (**b**) a spin makes a transition to the lower state, emitting a phonon at the resonant frequency. (**c**) a phonon of frequency ω_a is scattered as a phonon of frequency ω_b, accompanied by an "up" transition of the spin. (**d**) a phonon of frequency ω_b is scattered as a phonon of frequency ω_a, accompanied by a "down" transition of the spin.

scaling predictions. More insightfull microscopic models [189–191] of spin-lattice relaxation are thus required to understand the spin-phonon regime and pinpoint the specific vibrational modes that contribute to decoherence.

As spin-phonon coupling depends on the fine details of each particular lattice, to capture the wide casuistic of molecular crystals any theoretical model should be plastic enough to incorporate all system subtleties. This means distinguishing and studying the effect of each individual vibrational mode, and this is the starting idea which current models rely on [27].

A critical approximation at this step arises when periodic boundary conditions are not incorporated into these point calculations, so they are performed on a single isolated molecule. This may impose a severe limitation on the calculation quality, as long-range effects derived from the presence of charged species in the crystal are being completely removed [27].

The common strategy is to determine the vibrational modes and corresponding energies with DFT calculations, using periodic or discrete models for the molecules. Once the vibrational modes are determined, the second step is to calculate the spin-phonon coupling for each vibrational mode using a multiconfiguration (CASSCF)

or single determinant method (DFT). Thus, it is possible to determine which are the most relevant vibrational modes affecting spin relaxation. Normally, this information is fed into a master matrix the eigenvalues of which are the characteristic rates of the system [97].

It is clear that fundamental theoretical challenges in the study of spin relaxation in molecular systems still remain unsolved. Current efforts point to several directions: (i) direct and accurate calculation of the relaxation times T_1 and T_2 for molecular qubits; (ii) a better description of the Raman process with, a clear account of the states involved on such a relaxation process.

3.2 LIGAND FIELD EFFECTS – $VO(cat)_2$ AND $VO(dmit)_2$

Published paper: [174]

Albino, A.; Benci, S.; Tesi, L.; Atzori, M.; Torre, R.; Sanvito, S.; Sessoli, R. & Lunghi, A. "First-Principles Investigation of Spin–Phonon Coupling in Vanadium-Based Molecular Spin Quantum Bits" *Inorg. Chem.*, **2019**, 58(15), 10260–10268.

The present work reports a comparative theoretical investigation of the spin-lattice relaxation in four vanadium-(IV) molecular complexes. In particular, we have focused on pentacoordinated vanadyl (VO^{2+}) and hexacoordinated vanadium(IV) molecules, where the coordination is obtained by catecholate [192] and dithiolate [71] ligands, namely, $[PPh_4]_2[VO(cat)_2]$ (**1**), $[PPh_4]_2[V(cat)_2]$ (**2**), $[PPh_4]_2[VO(dmit)_3]$ (**3**), and $[PPh_4]_2[V(dmit)_3]$ (**4**), where cat = catecholate, dmit = 1,3-dithiole-2-thione-4,5-dithiolate, and PPh_4 = tetraphenylphosphonium (Fig. 3.4).

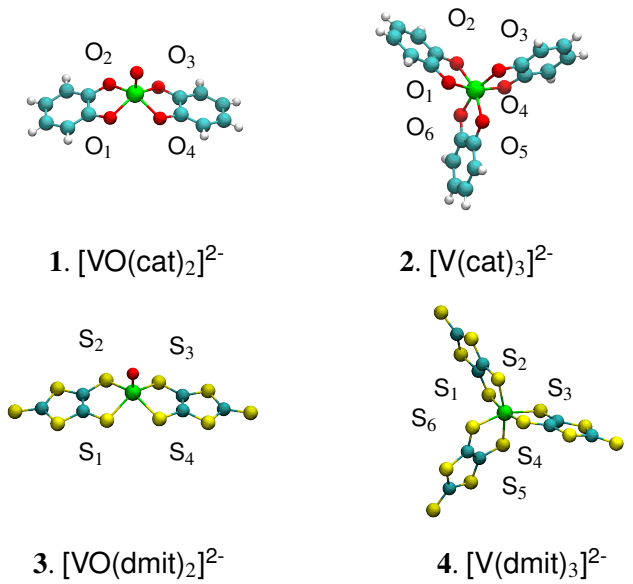

Figure 3.4: Molecular structures of the dianionic complexes **1**-**4** with the first coordination sphere atom labelling scheme.

These complexes have already experimentally shown to possess long coherence times and remarkable differences in the temperature dependence of the spin-lattice relaxation time [71, 192].

Our approach consists of modeling their magnetic properties by first principles, when perturbing the molecular structures along the normal modes of vibration, following a strategy adopted in previous works [193]. DFT vibrational analysis is performed in the crystal phase.

The quality of our computed vibrational properties is ascertained by IR vibrational spectroscopy in the terahertz range. When displacing the atoms we have taken into account the crystal's symmetries and only inequivalent displacements have been considered (Fig. A.1). The exploitation of symmetry allows us to reduce the computational overheads by a factor of four for all the systems considered.

The analysis also focuses on restoring the molecular features from the extended crystal lattice dynamics, directing the attention on the motion of the single molecule when the crystal vibrates at finite temperature. Normal modes of vibration could lead to different kinds of motion of the molecular building blocks, initially divided into rigid and nonrigid. The rigid motions are described as translations [1] and rotations of the molecules, and nonrigid motions are defined as intramolecular or internal and are connected to bond angle and bond length variations. The efficiency of each normal mode can be ascertained considering the fraction of rigid motions with respect to the fraction of nonrigid motions transferred to the molecule. The geometrical displacement that strongly determines spin-state perturbation is the intramolecular one, which twists molecules affecting the first coordination shell. The information extracted from the DFT and post-HF methods together provides a fingerprint description of the interaction between vibrations and magnetism and directly correlates to the structure of each compound. The correlation found between the spin-phonon interaction amplitudes and experimental spin-lattice relaxation times for the four compounds is then discussed.

This approach requires a number of $\mathbf{g}$-derivatives equal to $3M = 78$, instead of $3N = 1392$ for $[VO(cat)_2]^{2-}$, and $3M = 111$ instead of $3N = 1524$ for $[V(cat)_3]^{2-}$ (see Tab. 3.1). The $\mathbf{g}$ tensor is therefore calculated for six displaced geometries (± 0.0050Å, ± 0.0075Å, ± 0.0150Å) around the equilibrium configuration for each of the M atoms. The $\mathbf{g}$-versus-displacement curves are then fitted to a second order polynomial expression (see Fig. A.2).

The Cartesian derivatives of the $\mathbf{g}$ tensor are used to compute two important parameters: the cumulative molecular spin-phonon coupling, $|\partial \mathbf{g}|$, and the phonon-

1 The computation has been performed at the Γ point of the Brillouin zone, that is, with conservation of the center of mass of the crystallographic cell and no relative translation between cells. However, because of the presence of more than one molecule in the crystallographic cell, rigid translations of a molecules inside the cell, the so called external modes shown in Fig. 2.1, exist already at this point.

Table 3.1: Collection of structural data obtained from single crystal X-ray diffraction[71, 192] and from theoretical calculations.

	1		**2**		**3**		**4**	
MOLECULE	$[VO(cat)_2]^{2-}$		$[V(cat)_3]^{2-}$		$[VO(dmit)_2]^{2-}$		$[V(dmit)_3]^{2-}$	
Counter-ion	$2\times[PPh_4]^+$		$2\times[PPh_4]^+$		$2\times[PPh_4]^+$		$2\times[PPh_4]^+$	
Molecule Atoms (M)	26		37		18		25	
Unit Cell Atoms (N)	464		508		432		460	
Crystal System	monoclinic		monoclinic		monoclinic		monoclinic	
Spatial Group	$P2_1/c$		C2/c		C2/c		$P2_1/c$	
Site symmetry (Z)	4		4		4		4	
	exp.	sim.	exp.	sim.	exp.	sim.	exp.	sim.
Cell Volume, Å^3	4734.95	4477.07	5015.83	4758.34	5346.43	4941.81	5744.23	5428.57
a, Å	13.25	12.95	15.31	14.99	20.47	19.62	24.57	24.10
b, Å	12.25	11.95	13.23	13.16	12.73	12.29	13.81	13.69
c, Å	29.19	28.96	25.32	24.55	20.60	20.53	18.13	17.56
β, deg.	92.80	92.58	102.02	100.87	95.29	93.33	111.01	110.39
V–L, Å (av.)	1.973	1.974	1.946	1.959	2.387	2.382	2.386	2.373
V=O, Å (av.)	1.614	1.640	-	-	1.594	1.621	-	-

projected spin-phonon coupling coefficients, $(\partial\mathbf{g}/\partial q_\alpha)_0$. The former is defined as:

$$|\partial\mathbf{g}| = \sum_{lv}^{M,3}\sum_{jr}^{3}\left|\left(\frac{\partial g_{jr}}{\partial X_{lv}}\right)_0\right|, \tag{3.12}$$

where the index l runs over the number of atoms in the molecule and v runs over the cartesian coordinates. The phonons projected spin-phonon coupling coefficients are defined as:

$$\left(\frac{\partial\mathbf{g}}{\partial q_\alpha}\right)_0 = \sum_{i}^{3M}\sqrt{\frac{\hbar}{\omega_\alpha m_i}}L_{i\alpha}\left(\frac{\partial\mathbf{g}}{\partial X_i}\right)_0, \tag{3.13}$$

where the index α runs over the normal modes, the index i over the $3M$ molecular cartesian coordinates, $L_{i\alpha}$ is the Hessian's eigenvectors matrix, m_i is the atomic mass, ω_α is the normal mode frequency. The subscript 0 indicates that derivatives have been calculated in the DFT-optimized equilibrium configuration. The calculation of first order Sp-Ph coupling coefficients (Eq. 3.4) followed the procedure outlined in [90] and was applied to $[PPh_4]_2[VO(cat)_2]$ (**1**), $[PPh_4]_2[V(cat)_2]$ (**2**), $[PPh_4]_2[VO(dmit)_3]$ (**3**), and $[PPh_4]_2[V(dmit)_3]$ (**4**) crystal structures, whose

details are summarized in Tab. 3.1 and Fig. A.3. The coordination geometries around the metal centers are square-pyramidal for the pentacoordinated compounds ($[PPh_4]_2[VO(cat)_2]$ (**1**), $[PPh_4]_2[VO(dmit)_3]$ (**3**)), and trigonally distorted octahedral for the hexacoordinated ones ($[PPh_4]_2[V(cat)_2]$ (**2**), $[PPh_4]_2[V(dmit)_3]$ (**4**)).

It is worth noting that the metal-ligand (V-L) distances in S-containing ligands are longer than those of the O-containing ones (Tab. 3.1), consistent with the difference in the atomic radii between the O and S atoms. The starting point for understanding the effects of the first coordination shell on the spin-relaxation properties is the analysis of the crystal vibrations. Our study is limited to the Γ-point, where the three acoustic modes all have $\omega_\alpha = 0$. Experimental far-IR terahertz spectroscopy as a function of temperature with a spectral window between 15 and 120 $cm^{-1}$is employed here to support the quality of our simulations for complexes **1-4** (Fig. 3.5). The lowest temperature spectrum (10 K) shows an overall good agreement with our simulated spectra. A temperature increase causes a red shift of some vibrational modes because of the presence of anharmonic interactions, together with a softening of the crystal lattice. Simulations corresponding to 0 K, indeed, show a blue shift with respect to the experimental lowest temperature spectra, this aspect will be clarified in Sec. 3.4.

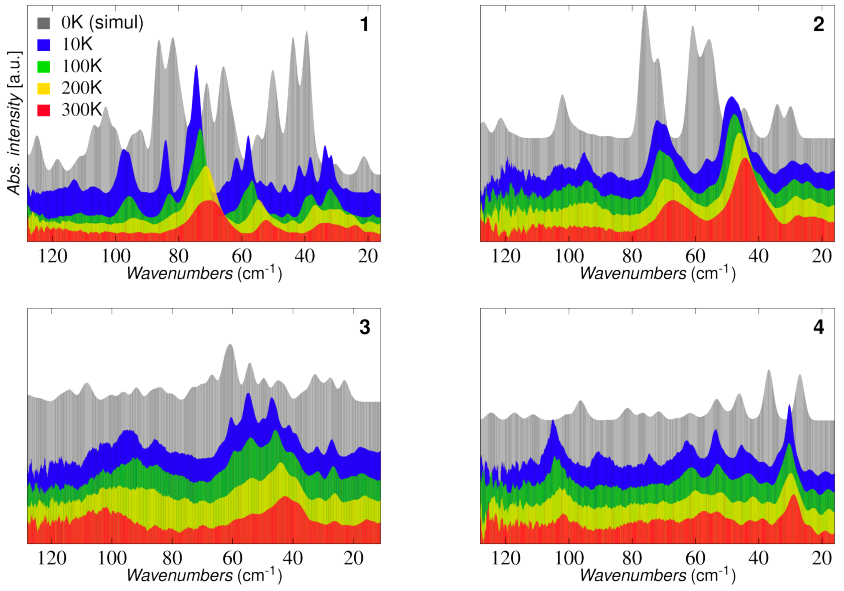

Figure 3.5: Experimental (10-300 K) and simulated (0 K) THz spectra for compounds **1-4**. The baselines for the different temperatures have been displaced for clarity.

The lowest calculated vibrations occur at 13.3 cm^{-1} for **4** and 18.5 cm for **3** and also at 27.6 cm for **2** and 20.7 cm for **1**. Dithiolate compounds show vibrations at lower frequencies with respect to the catecholate ones, probably because of the larger radius of the first coordination sphere and the higher atomic weight of S. Accordingly, longer bond lengths are generally associated with softer bonding atoms and, therefore, with lower vibrational frequencies. A deconvolution of translations, rotations, and intramolecular motions of the single molecule has been carried out from the normal modes of the whole crystalline structure, following the method outlined in previous works, [147, 194] (Fig. 3.6). The low-energy modes are dominated, as expected for all compounds, by rigid translations and rotations of the molecule in the crystal, but intramolecular contributions, i.e., where bond lengths and angles get distorted, are also present and become the dominant ones in increasing the energy modes. The calculated decomposition shows, for hexacoordinated compounds, a higher average internal contribution. Among the hexacoordinated ones, the catecholate compound shows a reduced rotational contribution (see the blue lines in Fig. 3.6).

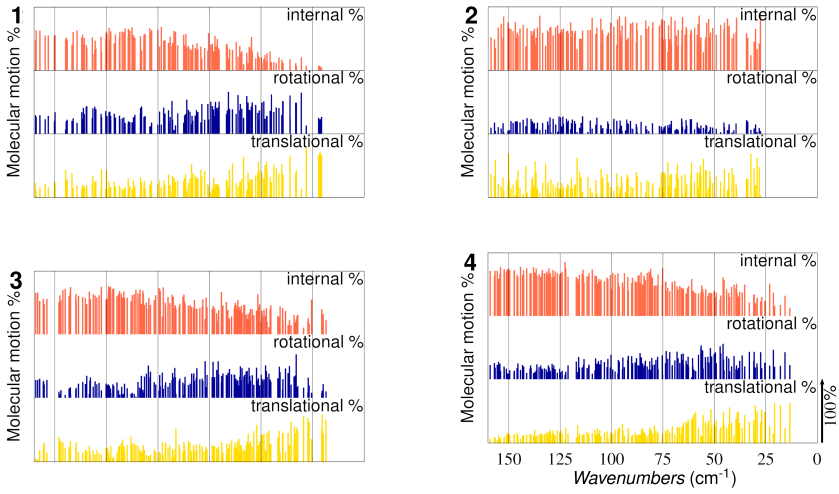

Figure 3.6: The total molecular motion associated to normal modes with frequency in the range 0–150 cm^{-1} is decomposed in intra-molecular percentage (red), rotational percentage (blue) and translational percentage (yellow). In the supporting material four gif files are available showing the first vibrational modes for each metal complex.

3.2.1 *Spin-phonon coupling analysis*

Tab. 3.2 shows the calculated and experimental **g**-values. The deviation of **g** from the free electron value of 2.0023 is caused by the presence of spin-orbit coupling.

Table 3.2: Best fit parameters extracted from simulation of the experimental CW-EPR X-band (ca. 9.5 GHz) spectra and CASSCF simulation results from optimized equilibrium geometry of **1**-**4**.[71, 192]

	1	**2**	**3**	**4**
	$[VO(cat)_2]^{2-}$	$[V(cat)_3]^{2-}$	$[VO(dmit)_2]^{2-}$	$[V(dmit)_3]^{2-}$
	Experimental Parameters (room T)			
g_x	1.980(1)	1.945(1)	1.986(1)	1.961(1)
g_y	1.988(1)	1.945(1)	1.988(1)	1.971(1)
g_z	1.956(1)	1.989(2)	1.970(1)	1.985(1)
	Simulated Parameters (0K)			
g_x	1.978(1)	1.906(1)	1.987(1)	1.943(1)
g_y	1.984(1)	1.914(1)	1.988(1)	1.956(1)
g_z	1.935(1)	1.997(1)	1.953(1)	1.997(1)
	Cumulative Spin-Phonon Coupling			
$\lvert\partial\mathbf{g}\rvert$ (Å^{-1})	1.5456	6.1460	0.3838	2.5774

In general, a good agreement between experiment and theory is observed and the trend in magnitude among the different molecules is correctly reproduced. Tab. 3.2 also reports the averaged molecular spin-phonon coupling coefficients, as defined in Eq. 3.12. These parameters represent the sum of every atomic contribution to the spin-phonon coupling and allow us to define dynamical magneto-structural correlations. It should be noted that the differences in the average spin-phonon coupling across the series can be due to both the chemical nature of the ligand and the coordinating geometry around the metal centre. For complexes with the same ligand, the **g** tensor elements are less perturbed in the pyramidal coordination with respect to the octahedral one. When comparing complexes with the same coordination geometry but different ligands, it appears that a stronger effect on the spin-phonon coupling is observed, with the catecholate being more prone to **g** tensor perturbations than the dithiolate ones. In order to explain these features it is important to correlate the **g**-tensor anisotropy and how this is modified by atomic displacements, i.e. **g** and $|\partial\mathbf{g}|$. These two quantities show the same trend across the series of molecules investigated as a consequence of a common microscopic origin, namely the magnitude of orbital angular momentum in the ground state [195]. This

quantity, accessible from our *ab initio* calculations, can be conveniently estimated from the magnitude of the 3d orbital energy splitting [195], shown in Fig. 3.7 for compounds **1**-**4**. The splitting of the d-orbitals is a proxy for angular momentum of ground state wavefunction. Its width correlates, indeed, with the mixing of orbital basis set function in the ground state, the lower is the energy splitting the higher is the mixing and the higher is the degeration restored in the ground state, i. e., the angular momentum associated to that state. The splitting is dominated by the oxido vs. non-oxido coordination mode. For the same coordination mode, cathecolate ligands induce smaller splitting than dithiolate ones. The transition energy to the first excited-state (marked with an arrow Fig. 3.7), calculated by CASSCF+NEVPT2, shows a good correlation with both the **g** factors (Tab. 3.2) and their derivatives, where larger **g**-shifts and **g** derivatives correspond to smaller ΔE. Interestingly, oxygen ligands yield a smaller splitting of the electronic states with respect to the sulphur ones. Although useful to understand general trends, the average spin-phonon coupling coefficients $|\partial \mathbf{g}|$ do not provide any information concerning the temperature at which specific atoms will start vibrating.

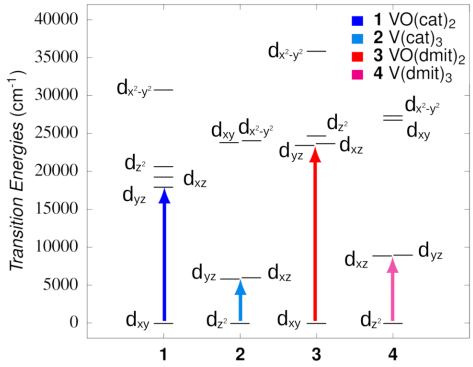

Figure 3.7: CASSCF + NEVPT2 calculated energy ladder of the 3*d* valence shell of the four compounds analysed. The arrows represent the lowest energy electronic transition in each complex.

This information can be obtained from the study of the spin-phonon coupling coefficients projected on the normal modes, as displayed in Figure 3.8(**a**) and 3.8(**b**) as a function of the phonons' vibrational frequency. The overall behavior of the spin-phonon coupling follows the one observed for $|\partial \mathbf{g}|$, that is the strength of the coupling and ranks the molecules in the following order [$VO(dmit)_3$] (**3**) < [$VO(cat)_2$] (**1**) < [$V(dmit)_3$] (**4**) < [$V(cat)_2$] (**2**). Thus, the spin-phonon coupling in vanadyl compounds is weaker than that in hexa-coordinated molecules. Furthermore, catecholate ligands offer a stronger coupling than dithiolates. The presence

of different donor atoms has different effects on the low and high energy ranges of the vibrational spectrum. Indeed, dithiolate ligands, which exhibit a more diffuse coordination sphere due to the softer nature of S, show *i*) the presence of several normal vibrations at lower frequencies, *ii*) a weaker perturbation of the spin states by vibrational modes, as shown by the lower calculated spin-phonon coupling amplitudes. The second effect is particularly remarkable in the higher energy vibrations, suggesting that the spin lattice relaxation time of dithiolate should exhibit a weaker temperature dependence.

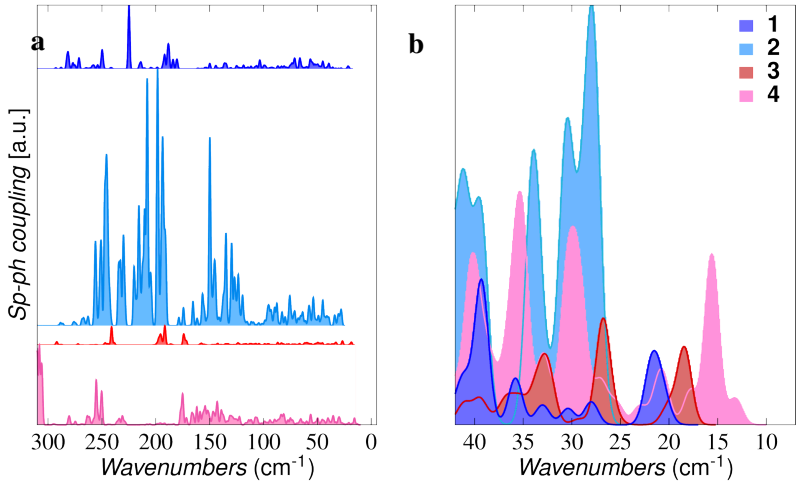

Figure 3.8: Left panel: spin-phonon coupling coefficients in the 0-300 cm^{-1} range for the four analysed compounds. A Gaussian line shape was applied to each harmonic normal mode, considering a width parameter equal to 2 cm^{-1}. Right panel: zoom of the low frequency modes with superimposed coupling coefficients pattern. The scale is kept fixed for the four molecules to allow comparison of relative intensities.

3.3 VIBRATIONAL SIMMETRIES – Cu(ttdpz) AND Cu(pc)

Published paper: [196]

Santanni, F.; Albino, A.; Atzori, M.; Ranieri, D.; Salvadori E.; Chiesa, M.; Sorace, L.; Totti F.; Bencini, A. & Sessoli, R.

"Probing Vibrational Symmetry Effects and Nuclear Spin Economy Principles in Molecular Spin Qubits" *Inorg. Chem.*, **2021**, 60(1) 140-151

This study focuses on two compounds: (**1**) Copper(II) tetrakis(thiadiazole)-tetraazaporphyrinate and (**2**) Copper(II) tetrabenzo-tetraaza-porphyrinate (or tetrabenzo-phtalocyaninate). Systematic calculations of molecular vibrations exemplify the effect of normal modes on the spin-lattice relaxation process, unveiling a different contribution to T_1 depending on the symmetry of normal modes. We describe and employ a model to fit the measured relaxation data that relies on a more physical description of the relaxation process [197], with respect to the phenomenological approach showed in Sec. 3.1. Furthemore, we observed that removing active nuclei from peripheral positions of (**1**) entails a moderate but appreciable coherence gain with respect to compound (**2**) due to the absence of H atoms aside from the spin diffusion barrier (purple in Fig. 3.9), when the electronic spin dilution reduces the electron spin-spin contribution. We notice that T_m values significantly longer than

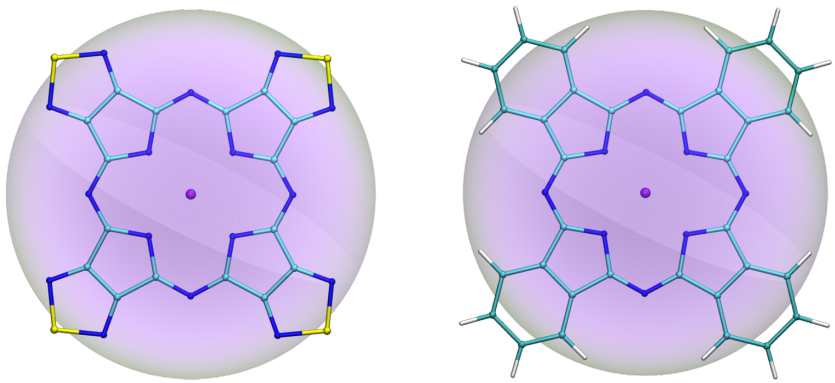

Figure 3.9: Molecular structures of [Cu(tpp)](left) [198] and [Cu(pc)](right) [199]. The violet spheres behind structures highlight the spin diffusion barrier of 6 Å. Color code: cyan, C; blue, N; yellow, S; purple, Cu.

those measured here were reported for thin films [20] of (**2**) and for frozen solution in D_2SO_4 [21]. My colleague Fabio Santanni, therefore, tried to further validate such

a nuclear spin economy strategy by comparing the behaviour of the two complexes in diluted solutions of D_2SO_4, but the porphyrazine complex turned out to show significantly modified EDFS spectra under these conditions.

Pulsed EPR spectroscopy was used to investigate the coherence time of the system (T_m) and its spin-lattice relaxation time (T_1), as it directly guarantees access to the spin dynamics of the system. T_m as a function of temperature was measured for ($\mathbf{1}_{0.1\%}$) and ($\mathbf{2}_{0.1\%}$) poly-crystalline powder samples in the 4.3-150 K range at the Q-band frequency ($\sim$ 33 GHz) and at a magnetic field corresponding to the maximum echo intensity (i.e., probing molecules with their unique axis perpendicular to the magnetic field).

The echo decay traces were fitted using both a stretched-exponential and a biexponential equation

$$I = I_0 + k_m e^{-\left(\frac{2\tau_p}{T_m}\right)^{\beta_m}} \tag{3.14}$$

$$I = I_0 + k_1 e^{-\left(\frac{2\tau_p}{T_m}\right)} + k_2 e^{-\left(\frac{2\tau_p}{T_m}\right)} \tag{3.15}$$

as usually done for transition metal systems [112], where I indicates the echo intensity, $2\tau_p$ is the delay between the initial pulse and the echo detection, and β_m is the stretch factor, giving qualitatively similar results (see Fig. A.4). The thermal variation of T_m (Fig. 3.10) shows an almost temperature-independent behavior in the 4.3-50 K range, with values on the order of 1 μs, falling to about 0.5 μs at 150 K.

Furthermore, the T_m value of ($\mathbf{1}_{0.1\%}$) is about 1 μs longer than that of ($\mathbf{2}_{0.1\%}$) at all the investigated temperatures. Both ($\mathbf{1}_{0.1\%}$) and ($\mathbf{2}_{0.1\%}$) present a peculiar behavior at low T, where T_m has a maximum between 15 and 20 K. The observed downturn of T_m at $T < 20$ K has been already observed in other systems [200], and it has been attributed to a switch of the dynamic regime, i.e. from a T_1-limited regime to one affected by the rotation of methyl groups. The proposed explanation does not seem to be applicable here because *i*) there is a lack of methyl groups or other substituents with rotational degrees of freedom and *ii*) the T_1-limited regime becomes more relevant at temperatures higher than those involved here. A direct comparison between the T_m values observed for ($\mathbf{1}_{0.1\%}$) and ($\mathbf{1}_{2\%}$) (see Fig. A.5) shows that stronger spin-spin interactions lead to a noticeable loss of coherence, confirming previous reports on [Cu(Pc)] [20]. Moreover, the observation of Rabi oscillations in ($\mathbf{1}_{0.1\%}$) up to 50 K (Fig. 3.11) guarantees control of coherent spin manipulation on this system.

Inversion recovery experiments were performed to investigate the temperature dependence of T_1. The experimental traces were fit with a stretched-exponential function, and the corresponding T_1 values are plotted in Fig. 3.10. The full set of T_1

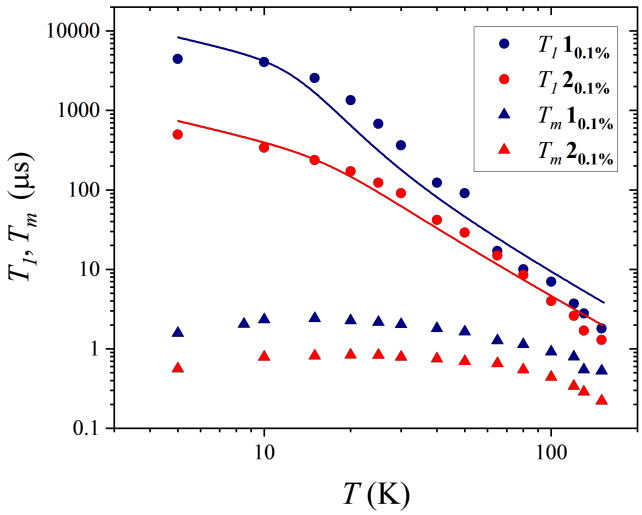

Figure 3.10: Comparison between T_1 and T_m values extracted from experimental measurements conducted on $\mathbf{1}_{0.1\%}$ and $\mathbf{2}_{0.1\%}$. Both T_1 and T_m values were obtained by a stretched-exponential fit of the experimental traces. Solid lines represent the best fit obtained by using Eq. 3.17.

and T_m values as a function of T are reported in **??**. The fit of T_1 as a function of temperature is commonly performed using the phenomenological Eq. 3.16 [112]

$$T_1^{-1} = a_{dir}T^x + a_{Ram}T^n \tag{3.16}$$

where a_{dir} and a_{Ram} are two weight constants that define the relative contributions of direct and Raman processes to the relaxation, x is usually equal to 1, and n can vary in the range 2-9 depending on the system, as mentioned above. As discussed above, such a model has been often employed in previous studies [19, 71, 175, 201], but it does not give physical insights into the microscopic features of the system.

We first note that Raman relaxation due to lattice vibrations, namely acoustic phonons, and local-mode relaxation, generally associated with the activity of optical phonons, are both due to a two-phonon spin relaxation mechanism. The usual distinction between the two mechanisms is only practical, and it is made to account for the different T dependences of the relaxation rate [112]. In the case of acoustic modes following a Debye model, Raman relaxation rate is predicted to vary as T^9, in clear disagreement with experimental findings for $S = 1/2$ magnetic molecules [71]. Instead, as it has been recently shown by Lunghi [197], the use of optical

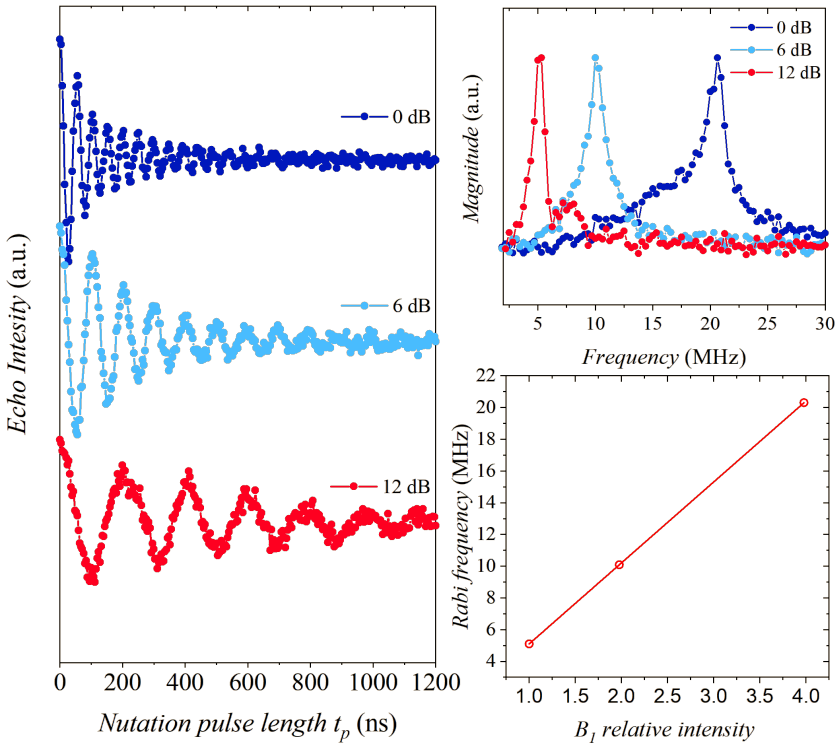

Figure 3.11: Rabi oscillations observed for $\mathbf{1}_{0.1\%}$ at 50 K for three different attenuation values of 0, 6, and 12 dB. On the right side are reported the Fourier transform of the echo intensities (top) and the linear dependence of the Rabi frequencies with respect to the B_1 relative strength.

phonons as a source of Raman relaxation leads to a relaxation rate proportional to T^2 , in much closer agreement with experimental findings. The latter mechanism is equivalent to a local-mode relaxation mechanism, and we adopted it to model the experimental data in this work with Eq. 3.17.

$$T_1^{-1} = \tilde{a}_{dir}\frac{exp(\hbar\omega_1/k_BT)}{exp(\hbar\omega_1/k_BT)-1}+ \\ \tilde{a}_{Ram}\sum_i V_i^{Sp-Ph}\frac{exp(\hbar\omega_i^{sp-ph}/k_BT)}{(exp(\hbar\omega_i^{sp-ph}/k_BT)-1)^2} \tag{3.17}$$

This includes the contribution of the molecular vibrational properties and considers both the energy of vibrational modes and the associated Sp-Ph couplings. The model was then rearranged on the basis of several assumptions reported in Supplemental

Material Appendix, Eq. A.1. The first term resembles the direct contribution to the relaxation in which $\tilde{a}_{dir}$ is a pre-exponential parameter, and ω_1 represents the Zeeman splitting under the operational conditions, which was fixed to the Q-band characteristic energy of about 1.17 cm^{-1} . The second term is a sum over all of the possible contributions arising from the whole set of normal modes, and it is representative of the Raman contribution to the relaxation. Here, ω^{Sp-Ph} represents the energy of the ith optical mode and V_i^{Sp-Ph} is the Sp-Ph coupling of the employed mode. Furthermore, $\tilde{a}_{Ram}$ is a parameter which rescales the Sp-Ph contribution to the relaxation process. *Ab initio* calculations of normal-mode frequencies and their corresponding Sp-Ph properties were performed for compounds (**1**) and (**2**) to minimize the number of fitting parameters.

3.3.1 *Ab initio Sp-Ph calculation*

The low-energy spectrum of the $S = 1/2$ systems analyzed here is composed by a Kramers doublet of spin levels, whose degeneracy is removed by the external magnetic field. A first qualitative fingerprint of this mechanism, shedding light on the interaction between magnetism and vibrations in each molecule, requires the calculation of the phonon spectrum and the amplitude of Sp-Ph coupling for all possible modes:

$$V_\alpha^{Sp-Ph} = \left(\frac{\partial \hat{\mathcal{H}}_{spin}}{\partial q_\alpha} \right) \tag{3.18}$$

The SH is here composed only by the Zeeman term and hence the only parameter we obtain from *ab initio* methods is the g matrix. A careful evaluation of the best method for static magnetic properties such as g matrix was accomplished before starting the perturbation along each normal mode. The methods employed belong to different levels of theory, as distinguished in Sec. 2.2, say, DFT and CASSCF. Several kinds of active space were choosen, as shown in Fig. 3.12. The minimum CAS in our system is [9,5], constituted by 9 electrons distributed in the five d shells. The def2-TZVP basis set as implemented in ORCA were used. The overestimation of g_z is substantial at this level, therefore an extension of the active space must be evaluated to reach the minimum set of orbitals describing the wavefunction with significant multireference character. The first choice falls on the non-bonding unoccupied d shell orbitals, included in the external orbital set in the previous CAS calculation. This step leads to a [9,10] CAS, none of the two averaged states, i.e., over 6 and 10 roots, gave a correct set of g values. A further step is attempted trying to include some covalency in the wavefunction, and, therefore, the highest

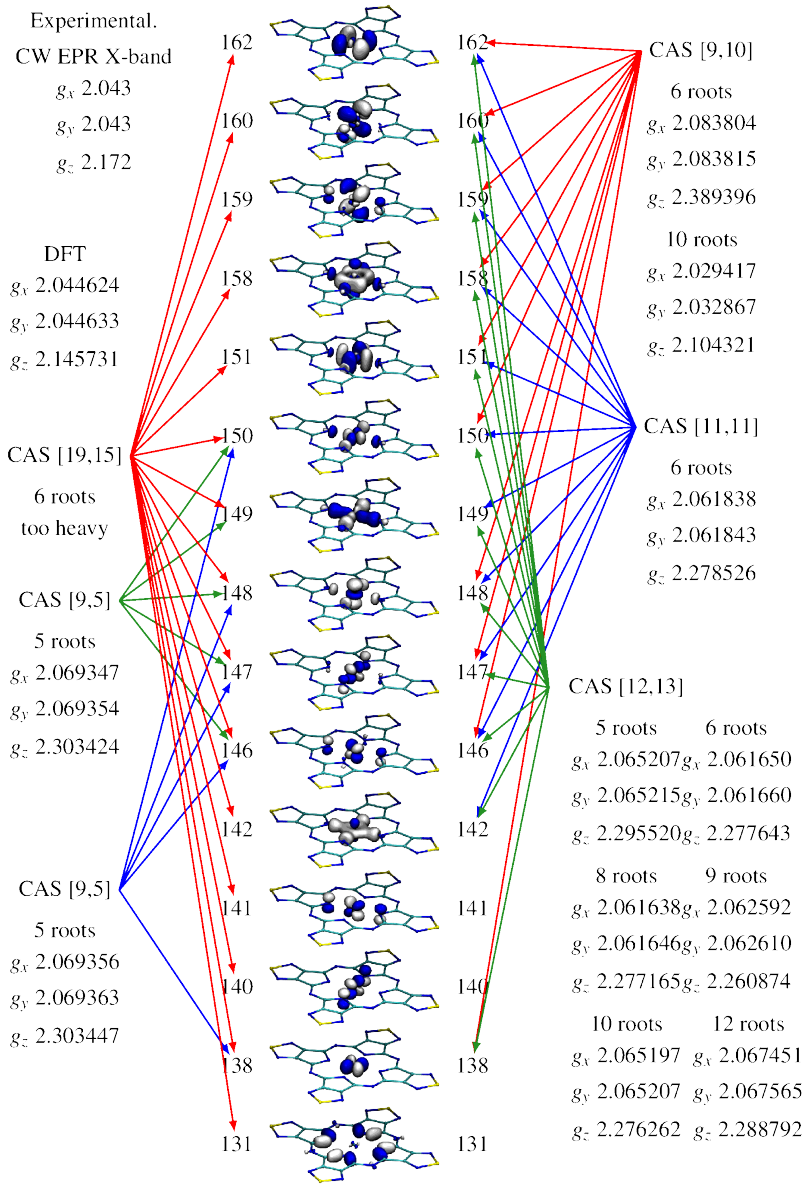

Figure 3.12: DFT calculated Unresticted Natural Orbital (UNO) set used as starting point for several CASSCF calculation, as showed by colored arrows. The SOMO orbital is the $d_{x^2-y^2}$, no. 150.

doubly occupied orbital is added to the active space (CAS [11,11]). It is a bonding orbital, belonging to an occupied metal-ligands orbital. The obtained g values were improved with respect to the ones computed from calculation with the same averaged state from CAS [9,10], but they were still not satisfying. An even more computational demanding attempt was made with a CAS [13,12] where a further bonding orbital from an occupied metal-ligands based orbital with strong character of the latters. The results are not close to experimental values and enlarging to further active spaces (CAS [19,15]) was not a viable route in our in-house HPC facility.

The further switch to Hybrid Functional DFT with PBE0 parametrization led, on the contrary, to fair results in comparison with experimental. This case of study shows the potential of DFT approach for $S = 1/2$ systems, for which static correlation contributions are not too relevant.

3.3.2 *Normal modes symmetry*

Unrestricted open shell density functional theory based calculations have been performed for the magnetic complexes mentioned in Fig. 3.13. Strict convergence parameters for DFT structural optimizations are required to improve the agreement between experimental and calculated vibrational spectra.

The search of a local minimum of the energy, corresponding to the equilibrium geometry of the N atom system, requires a strict minimization procedure to ensure the average total forces are around $1 \cdot 10^{-8}$ au. The second derivatives of the energy are calculated numerically by finite differences perturbing the equilibrium geometry along the 3N coordinates. The DFT scheme adopted, as implemented in the Quickstep module, uses pseudopotentials (GTH-PBE) in order to integrate out the core electrons from the problem. The valence pseudowave functions are expanded in Gaussian-type orbitals (DZVP-MOLOPTSR- GTH), and the density is represented in a plane wave auxiliary basis. It was ascertained that a cutoff of at least 1000 Ry was necessary to achieve a good quality of vibrational spectra in the low-energy range (0-100 cm^{-1}). The symmetry properties of a normal mode with wave vector $\mathbf{k}$ can be determined by studying the transformation properties of the creation and annihilation operators $a^{\dagger}$ and a under the operation of the point group of the molecule and assigning them to the appropriate representation.

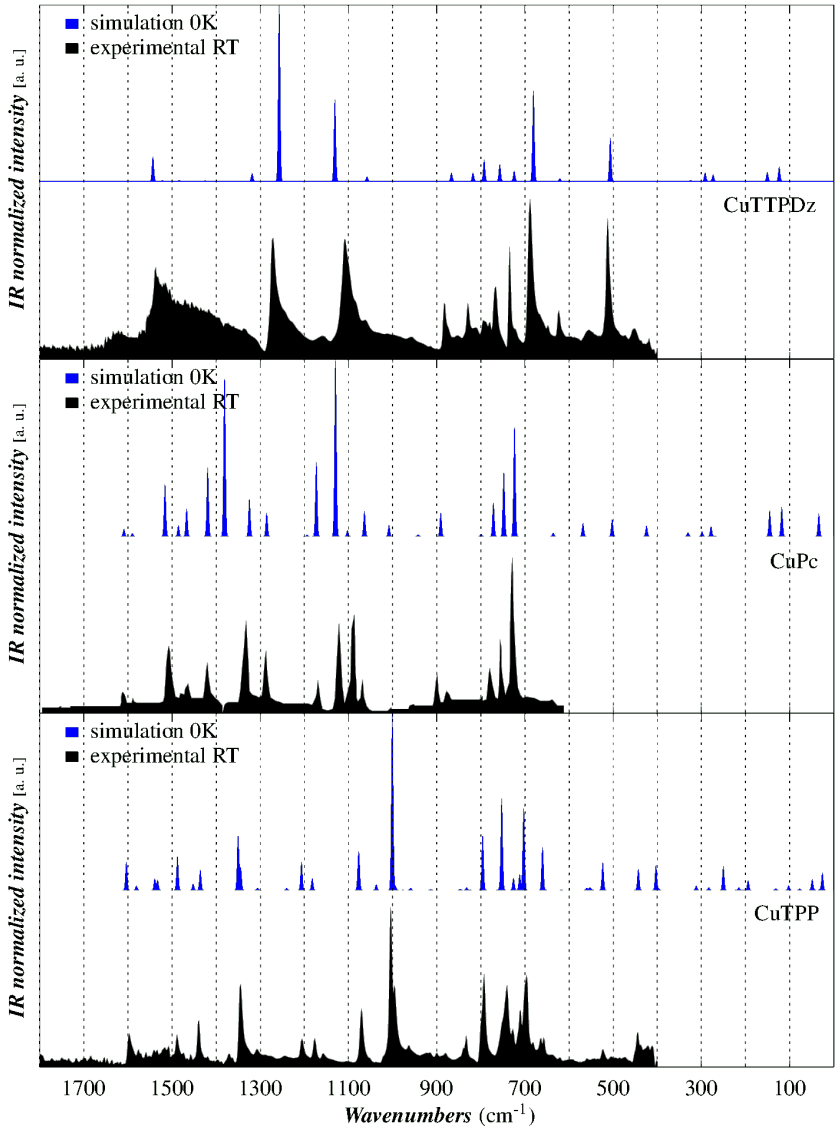

Figure 3.13: Experimental FT-IR spectra (black) of [Cu(tpp)], [Cu(pc)] and [Cu(tpp)]are reported together with the calculated ones resulting from *ab initio* calculations (blue) as function of wavenumbers (cm^{-1}). The third Cu-based molecule, [Cu(tpp)] is discussed in Sec. 3.5.4.

3.3.3 *Discussion*

At first glance, a qualitative analysis of chemical differences between (**1**) and (**2**) helps rationalize the results of the calculations. Compound (**1**) shows eight nitrogen atoms bonding with the eight β-carbon atoms of pyrrole and bridging four sulfur atoms. Hence, the four β substituents form a five-membered ring that does not increase the strain by acting on the peripheral carbon atoms of this tetrakis(thiadiazole)-tetraazaporphyrin. The same feature is present in (**2**), and it is strengthened by the phenyl substituents, establishing a higher conjugation along the four isoindole groups of this tetrabenzotetraazaporphyrin. Such outlined features modulate the structural rigidity of (**2**), which cannot be considered as flexible as (**1**), considering the first normal mode of vibration occurring at 11.21 cm^{-1} for (**1**) and 17.38 cm^{-1} for (**2**) (see Fig. A.3 and Fig. A.4). The difference is not so particularly relevant if one considers the coupling of the spin system and the vibrational modes. The two compounds (**1**) and (**2**) belong to the idealized D_{4h} point group, whose group order is 16 with 10 representations (hereafter "reps" for brevity): A_{1g}, A_{2g}, B_{1g}, B_{2g}, E_g, A_{1u}, A_{2u}, B_{1u}, B_{2u}, and E_u [202]. The inversion center allows us to discriminate Raman-active modes (gerade) from IR-active modes (ungerade). One sample normal mode is shown for each symmetry in Fig. 3.14 for molecule (**1**). The most effective normal modes, i.e., those bearing the highest couplings with the spin systems, are found to show the same reps of d orbitals. The active modes showing the highest Sp-ph constants over an arbitrary threshold of 10^{-7} and for $\omega < 500$ cm^{-1} are reported for compounds (**1**) and (**2**) in Fig. 3.3.

The active vibrations displace the donor atoms out of the plane of the porphyrazine core, as visible in E_g modes 10 and 11 of (**1**) (Fig. 3.14) and E_g modes 10 and 11 of (**2**) (in ref. [196]), or in-plane, back and forth along with the Cu–N directions (A_{1g}, B_{1g}, and B_{2g} modes 23, 20, and 21 of (**1**) and 26, 20, and 23 of (**2**) (Fig. 3.14). The ungerade modes that cause out-of-plane displacements (A_{1u}, A_{2u}, B_{1u}, and B_{2u} modes 39, 19, 22, and 18) (Tables S3 and S4 in ref. [196]) have low couplings since they leave the four donor atoms still or displace them rigidly. A rigid shift of the metal atom and its first coordination sphere is also given by the in-plane modes corresponding to rotations (A_{2g} mode 22 of (**1**) and 21 of (**2**)) and translations (E_u modes 13 and 14 of (**1**) and 16 and 17 of (**2**)) (see Fig. A.3 and Fig. A.4), and therefore, they show small Sp-Ph coupling. In summary, the first coordination sphere is strongly perturbed only by gerade modes, as was recently restated by Hadt and his collaborators [203].

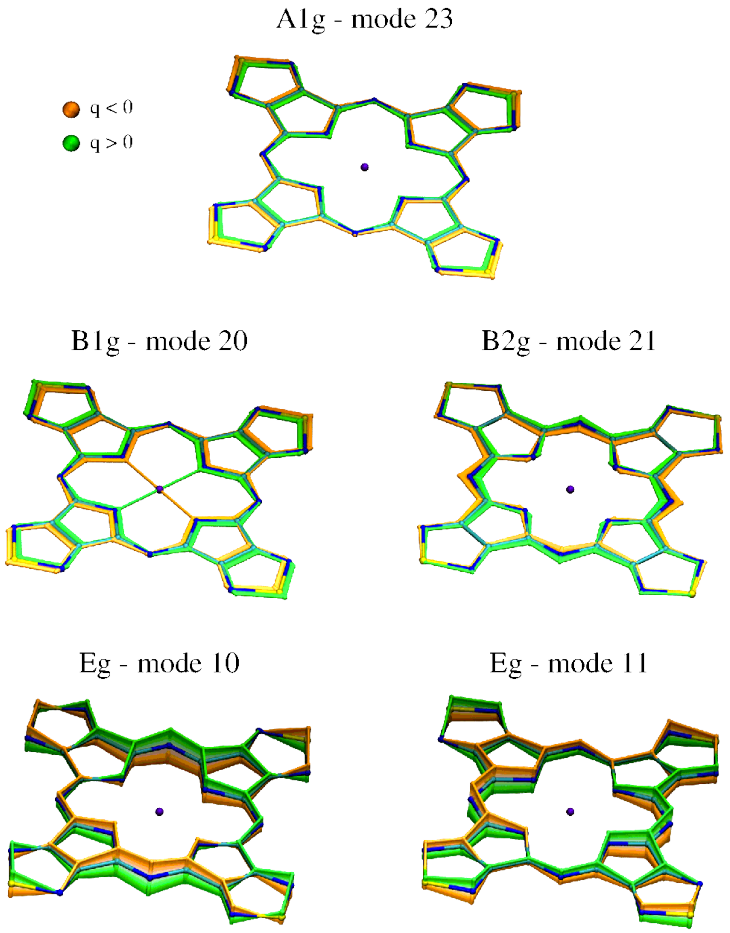

Figure 3.14: Pictorial representation of exemplar normal modes of **1**. The orange and green structures represent the evolution in negative and positive directions of normal coordinate, respectively. An irreducible representation of point group D_{4h} can be assigned to each mode [202].

In the analysis of T_1, the information gained through the ab initio investigation of the spin and vibrational properties of (**1**) and (**2**) allows us to rationalize the spin dynamics of the two molecules. In the model described by Eq. 3.17, the whole set of vibrational energies and spin-phonon coupling coefficients resulting from ab initio calculations are adopted to define ω_{Sp-Ph} and V_{Sp-Ph}, respectively. It follows that only two parameters of the model are left free to vary. The first is $\tilde{a}_{dir}$: its independent computation will require the computation of acoustic phonons out of the Γ-point of the Brillouin space where energy matching with Zeeman splitting

Table 3.3: Calculated values of ω (cm^{-1}) and Sp-Ph coefficients (au) for (**1**) [Cu(tpp)] and (**2**) [Cu(pc)]at $\omega < 500$ $cm^{-1}$and Sp-Ph $> 10^{-7}$ reported with their respective representations expressed in Mulliken notations

[Cu(TTDPz)]			
α	ω	Sp-Ph	Mulliken
NO.	cm^{-1}	a.u.	Symbol
10	58.161	1.77E-005	E_g
11	58.471	1.61E-005	E_g
16	131.03	5.82E-006	E_g
17	131.27	5.85E-006	E_g
20	154.79	3.48E-006	B_{1g}
21	223.79	4.30E-008	B_{2g}
23	244.19	2.55E-005	A_{1g}
24	257.81	1.87E-005	E_g
25	257.92	1.77E-005	E_g
29	277.85	1.63E-007	B_{2g}
33	293.09	4.08E-006	E_g
34	293.21	4.26E-006	E_g
37	499.08	2.18E-007	E_g
38	499.20	1.85E-007	E_g
44	577.04	2.48E-007	E_g
45	577.18	2.74E-007	E_g
46	588.84	1.29E-005	A_{1g}
47	590.81	1.36E-006	B_{1g}

[Cu(Pc)]			
α	ω	Sp-Ph	Mulliken
NO.	cm^{-1}	a.u.	Symbol
10	57.782	1.48E-005	E_g
11	58.048	1.45E-005	E_g
12	109.55	5.03E-009	B_{2g}
14	117.59	6.41E-006	E_g
15	117.77	6.32E-006	E_g
20	167.31	2.79E-006	B_{1g}
23	228.23	1.39E-008	B_{2g}
24	234.47	1.32E-005	E_g
25	234.55	1.32E-005	E_g
26	253.06	2.33E-005	A_{1g}
28	270.02	8.06E-006	E_g
29	270.09	8.02E-006	E_g
36	411.51	6.91E-007	E_g
37	411.59	6.96E-007	E_g
41	479.23	5.66E-010	B_{2g}
42	485.09	6.98E-008	E_g
43	485.14	7.43E-008	E_g
47	552.00	8.67E-007	B_{1g}

Table 3.4: Best-Fit Parameters Obtained Using the Model (Eq. 3.17) to Reproduce the Temperature Dependence of T_1 Shown in Fig. 3.10

	$\tilde{a}_{dir}$ (ms^{-1})	$\tilde{a}_{Ram}$ (ms^{-1})
($\mathbf{1}_{0.1\%}$)	$(3.32 \pm 1.47) \times 10^{-2}$	$(1.99 \pm 0.41) \times 10^{6}$
($\mathbf{2}_{0.1\%}$)	$(3.87 \pm 0.64) \times 10^{-1}$	$(4.20 \pm 0.55) \times 10^{6}$

is observed. This goes far beyond the scope of our isolated molecule calculation. Additionally, the unique scale factor $\tilde{a}_{Ram}$ connecting the Sp-Ph to the relaxation rate is introduced for the whole set of vibrational modes to preserve the relative weight of each mode in the relaxation process. Best-fit parameters are given in Table 3. An extensive comparison between the spin-lattice relaxation processes of the two systems is provided by the multitechnique approach employed. As shown in Fig. 3.10, the T_1 trends of ($\mathbf{1}_{0.1\%}$) and ($\mathbf{2}_{0.1\%}$) above 40 K are similar, and they are comparable with AC susceptibility data of ($\mathbf{1}_{20\%}$) and ($\mathbf{2}_{20\%}$) (Fig. 3.15).

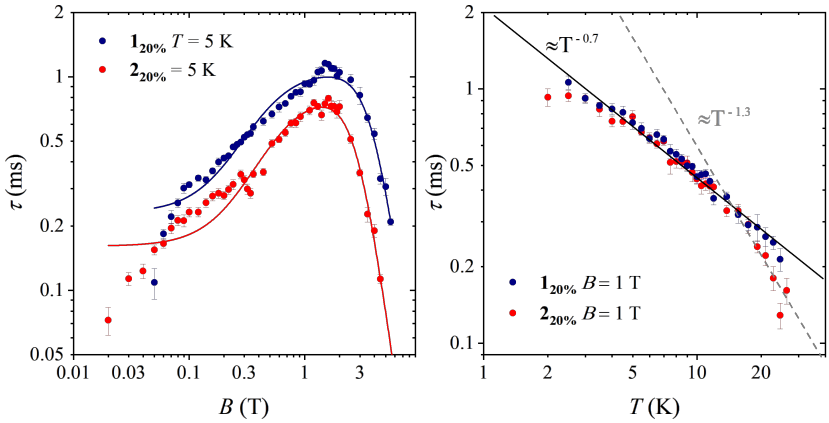

Figure 3.15: Comparison between the experimental τ (ms) values obtained for $\mathbf{1}_{20\%}$ and $\mathbf{2}_{20\%}$. The relaxation times are reported in a log-log scale as a function of B(T) at T = 5 K on the left side and as a function of T(K) at B = 1 T on the right side. Solid lines represent the best fits obtained by using models reported in the main text. The broken line represents the power law that best reproduces the high temperature data of **2**.

This is also highlighted by the results of the fits reported in Tab. 3.4.

Indeed, a similar weight of Raman contribution emerged from the fit performed with the alternative employed model (Eq. 3.17). The further analysis of the single-mode contribution to the relaxation rate indicated that the most effective modes are

those with Sp-Ph coefficients higher than 10^{-7} and energies lower than 500 cm^{-1}. Among them, the first two gerade optical modes placed at 58.16 and 58.47 cm^{-1} ($\mathbf{1}_{0.1\%}$) and 57.78 and 58.05 cm^{-1} ($\mathbf{2}_{0.1\%}$) have the largest influence on the relaxation (Fig. 3.16).

Higher energy optical modes or modes with lower Sp-Ph couplings introduce a small contribution to the relaxation of the two compounds. In order to understand why relatively high energy phonons, such as the first optical phonons, can contribute to spin relaxation, it must be stressed that the thermal population is not the only ingredient determining the spin relaxation rate. Indeed, the vibrational density of states and the magnitude of Sp-Ph couplings (Fig. 3.17) are two additional quantities that need to be carefully considered.

Both of these quantities are much larger for optical phonons than for acoustic phonons and largely compensate for the difference in the thermal population. The striking dependence of the Sp-Ph on the symmetry of the involved vibrational modes is remarkable. Strong Sp-Ph coupling characterizes gerade modes, of which A_{1g} modes present the most intense coupling constant in both compounds (Fig. 3.3). This can be explained by considering that, in copper(II) systems, the orbital contribution to the **g** tensor comes from the admixing of the ground state with excited states through spin-orbit coupling. For the analyzed systems, the unpaired electron occupies the $d_{x^2-y^2}$ orbital, which points toward the Cu–N bonds. The distortion carried out by symmetric vibrations modifies the overlap between metal and ligand orbitals, significantly affecting the energy difference between the ground and excited states. Consequently, this modifies the weight of the spin-orbit-induced perturbation. In contrast, asymmetric vibrations present an almost null net variation of the overlap (see Fig. 3.18).

Disentangling the role of different types of vibrations is mandatory for a rational design of molecules exhibiting long coherence times over a wide temperature range. On the other hand, below 40 K T_1 trends are divergent for the two compounds, and this is reflected in the different values of the fitting parameter $\tilde{a}_{dir}$. By relation of this evidence with what has been extracted from AC susceptibility measurements, it emerges that, at high concentration, the direct mechanism of relaxation is affected by spin-spin interactions, which are similar for the two compounds having comparable Cu–Cu distances. When the spin concentration is lowered to 0.1%, it appears that the spin-lattice relaxation is less efficient for the porphyrazine complex than for the phthalocyanine complex. We hypothesize that this might be related to the role of the highly polarizable sulfur atoms, which can be relevant for van der Waals interactions affecting the acoustic phonon dispersion, but further calculations are necessary to confirm this hypothesis.

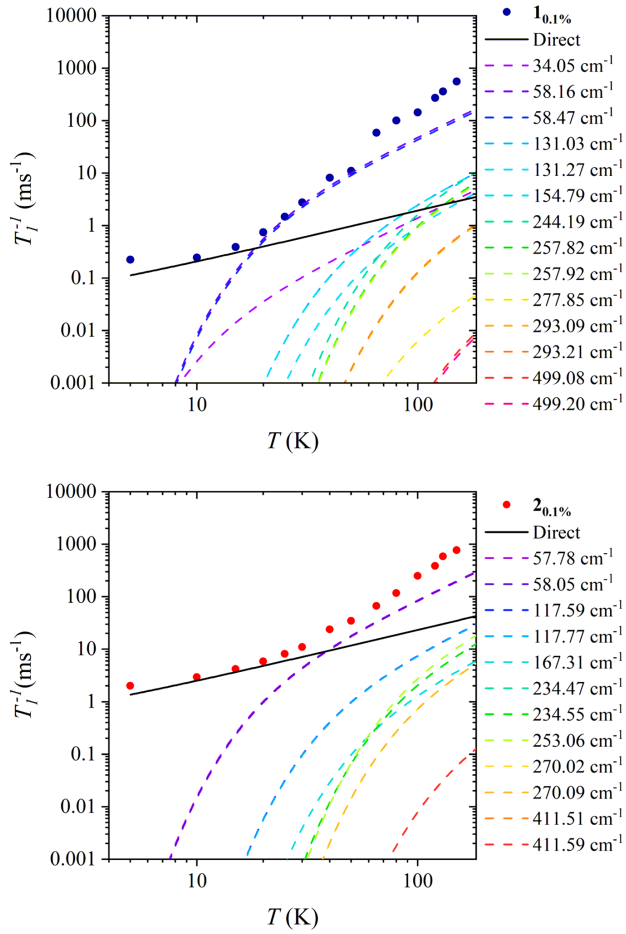

Figure 3.16: Plots of experimental T_1^{-1} data of $\mathbf{1}_{0.1\%}$ (top, blue circles) and $\mathbf{2}_{0.1\%}$ (bottom, red circles) reported together the simulated curves of direct (solid lines) and Raman (dashed lines) contributions to the spin-lattice relaxation. The curves are obtained by considering the $\tilde{a}_{dir}$ and $\tilde{a}_{Ram}$ values extracted from fits and reported in Table 3 of the main text. Each Raman contribution is simulated by employing the energy of one of the most active modes which are reported in legends. Note that the normal modes with lower energy contibute to the relaxation more than high energy ones.

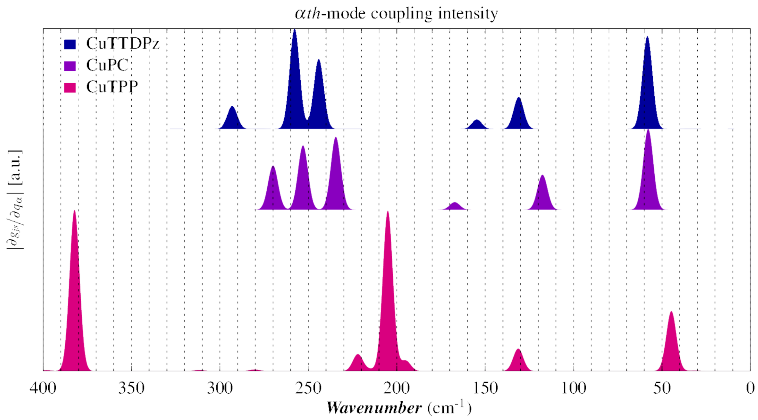

Figure 3.17: Plot of Sp-Ph coupling intensities (in au) as a function of normal mode energy extracted from calculations conducted on [Cu(tpp)], [Cu(pc)], and [Cu(tpp)] by adopting the model reported in the main text.

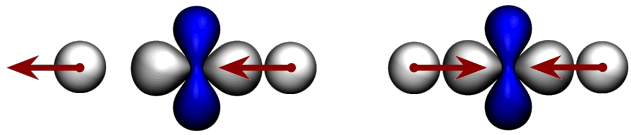

Figure 3.18: Schematic representation of the overlap variation between the two nitrogen σ orbitals interacting with the copper $d_{x^2-y^2}$ orbital in response to asymmetric (left) and symmetric (right) displacements in molecular vibrations.

3.4 A CLOSER GLIMPSE OF PHONONS – $VO(acac)_2$

Published paper: [204]

Albino, A.; Benci, S.; Atzori, M.; Chelazzi, L.; Ciattini, S.; Taschin, A.; Bartolini, P.; Lunghi, A.; Righini, R.; Torre, R.; Totti, F. & Sessoli, R.

"The Temperature Dependence of Spin-Phonon Coupling in $[VO(acac)_2]$: a Computational and Spectroscopic Study" *J. Phys. Chem. C*, **2021**, 125(40) 22100–22110

The aim of this work is an in-depth study of the spin-phonon (hereafter Sp-Ph for brevity) coupling in vanadyl acetylacetonate, $[VO(acac)_2]$, both from spectroscopic and theoretical point of view. Thanks to its simplicity (only 60 atoms in the unit cell), $[VO(acac)_2]$ has the physique du rôle as a perfect training ground for extensive DFT investigation of its rich vibrational properties [197]. $[VO(acac)_2]$, already studied by inelastic neutron scattering [205], is here investigated in crystalline powder by means of an in-house built setup performing THz time-domain spectroscopy (THz-TDS)[206–208].

The harmonic approximation of molecular vibrations is highly valuable for interpretation of the main features of the vibrational spectra but it cannot explain all their temperature-dependent fine structure. At finite temperatures, anharmonic motions of the molecules must be considered since they allow for the possibility of interactions among the harmonic phonons, resulting in slight changes in the energy and composition of characteristic vibrations. The most straightforward parameters to be considered as modified by anharmonicity are the cell parameters. The crystal structures obtained from X-ray diffraction collected at cryogenic and room temperatures allowed us to calculate the observed THz anharmonic frequency shift with high accuracy.

The overall differences in the spin-coupling magnitudes as a function of the temperature are highlighted in this study. It turned out that Sp-Ph coupling can decrease or increase its magnitude on raising the temperature. Such trends have to be ascribed to variations of primitive vectors and unit cell angles observed for the two considered temperatures. Indeed, the cell volume tunes the normal modes by modifying the perturbation to the first coordination sphere of the vanadium ion. The overall results presented have also a general relevance allowing the quantification of the errors introduced by neglecting the temperature effects on the cell parameters. The cell parameters obtained by full optimization at 0 K does not follow the trends outlined by 100 K and 300 K experimental structures, suggesting the possibility that a constrained optimization employing the experimental cells could yield more accurate results.

The results of this study represent further pieces of the puzzle of the role played by vibrations in determining the relaxation properties of potential molecular Qubits at the quantitative level.

3.4.1 *Crystal Structure*

$[VO(acac)_2]$ metal center is constituted by a vanadyl ionic moiety, VO^{2+}, coordinated by two chelating bidentate β-diketonate ligands (Fig. 3.19). The coordination geometry around the penta-coordinated V^{IV} metal centre is a distorted square pyramid [157]. This molecule crystalizes in a P-1 space group (n° 2), for which the only point symmetry element is the inversion. The asymmetric unit contains one molecule and the unit cell contains two molecules, for a total of 60 atoms (see Tab. 3.6).

The crystallographic structure has been already solved using high-resolution data in 1995 [209] at 294 K. Here we present new data collected at 300 K, $\mathbf{1_{300K}}$, and 100 K, $\mathbf{1_{100K}}$, on the same single crystal (Tab. 3.5). A good agreement between 300 K and 294 K datasets is found, while a shrinking of the cell parameters is observed at 100 K (see Tab. 3.6).

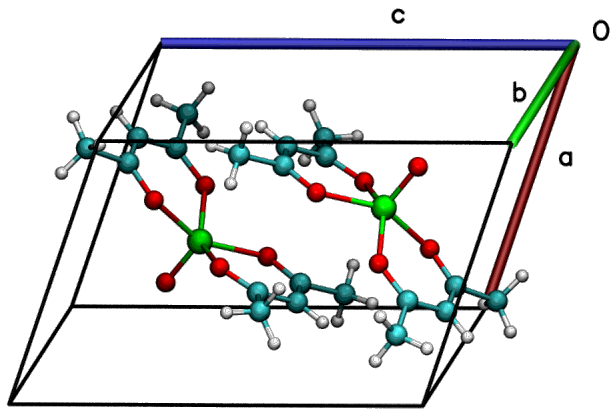

Figure 3.19: Unit cell content of $[VO(acac)_2]$, crystallizing in triclinic P-1 space group. Color code: Vanadium = green; Oxygen = red; Carbon = cyan; Hydrogen = white.

Table 3.5: Summary of X-ray Crystallographic Data for $[VO(acac)_2]$ at 100 K and 300 K

Property	$\mathbf{1}_{100K}$	$\mathbf{1}_{300K}$
empirical formula	$C_{10}H_{14}O_5V$	$C_{10}H_{14}O_5V$
formula weight	265.15	265.15
crystal system	triclinic	triclinic
space group	P-1	P-1
a, Å	7.3005(12)	7.5132(5)
b, Å	8.1172(13)	8.2015(6)
c, Å	11.1782(18)	11.2206(8)
α, deg	72.901(7)	73.174(4)
β, deg	72.282(7)	71.476(4)
γ, deg	67.064(6)	66.718(4)
volume, $Å^3$	569.37(16)	591.45(8)
Z	2	2
T, K	100(2)	300(2)
ρ (calc), Mg/m^3	1.547	1.489
μ, mm^{-1}	7.351	7.077
θ range, deg	4.24–68.42	4.24–68.32
goodness of fit, Goof	1.191	1.139
R1[a]	0.0563	0.0707
wR2[b]	0.1685	0.1990

[a] $R1 = \Sigma||F_o|-|F_c||/\Sigma|F_o|$,

[b] $wR2 = \left[\Sigma\left[w\left(F_o^2-F_c^2\right)^2\right]/\left[\Sigma w\left(F_o^2\right)^2\right]^{1/2}\right]$,
where $w = 1/\left[\sigma^2\left(F_o^2\right)+(aP)^2+bP\right]$,
and $P = \left[\max\left(F_o^2,0\right)+2F_c^2\right]/3$.

3.4.2 *Powder Samples THz Spectra*

In order to check that the applied pressure, essential to make the pellet, does not induce any phase transition or changes in the crystal structure samples were prepared by my colleague dr. Stefano Benci according to two different procedures, and are hereafter labeled as $\mathbf{1_a}$ and $\mathbf{1_b}$. THz spectra of the ($\mathbf{1_a}$) and ($\mathbf{1_b}$) are shown in Fig. 3.20.

The spectra of the two samples are identical, except for the intensity that is related to the different concentration of vanadyl-acetylacetonate in the samples. No evident effects of the applied pressure occur; the same result is observed by PXRD investigation on ($\mathbf{1_b}$) compared with vanadyl-acetylacetonate powder and pure HDPE. Therefore, from here on, the discussion will focus on ($\mathbf{1_a}$).

Fig. 3.21 shows the THz spectra measured in the temperature range 10 – 300 K. At the lowest temperature, five peaks ($\mathbf{p1-5}$) are detected. As sample temperature

Table 3.6: The three cell parameter sets studied in this work. Note that the cell parameters of $\mathbf{1_{100K}}$ and $\mathbf{1_{300K}}$ are the experimental ones while $\mathbf{1_{0K,cell-opt}}$ are optimized by DFT. Lattice parameters are reported in Å and deg. The volume is in Å^3

	a	b	c	α	β	γ	Vol.
$\mathbf{1_{300K}}$	7.513	8.201	11.221	73.174	71.476	66.718	591.445
$\mathbf{1_{100K}}$	7.300	8.117	11.178	72.901	72.282	67.064	569.372
$\mathbf{1_{0K,cell-opt}}$	7.662	7.802	11.056	70.869	71.162	64.315	549.943

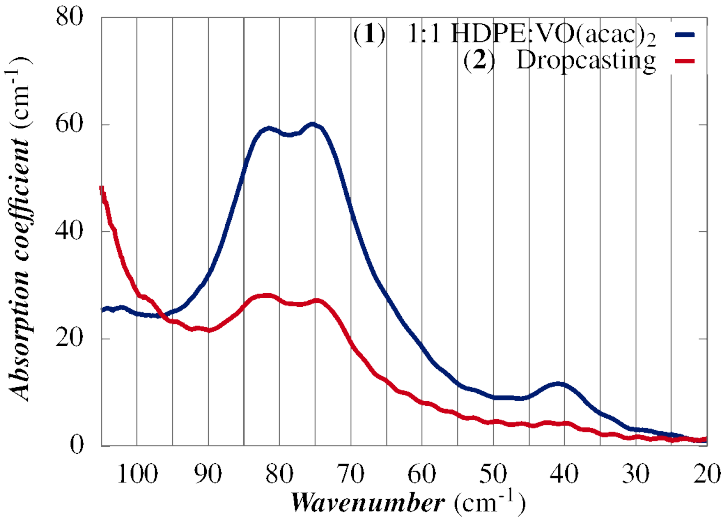

Figure 3.20: Comparison of ($\mathbf{1_a}$) and ($\mathbf{1_b}$). No significant effects are originated by the preparation method of each sample, confirming that the applied pressure, necessary to make the pellet, does not change the structure of $[VO(acac)_2]$

is raised, all of them become broader and most of them shift to lower energy. It is worth noting that the lowest phonon detected falls at 43.9 cm^{-1} (**p1**), that is exactly the value predicted by the Brons-van Vleck model applied to the spin–lattice relaxation rate in our previous work [192].

The extraction of the peaks' parameters, i.e., central frequency and linewidth (Γ), has been performed by fitting each of them with a pseudo-Voigt function. Moreover, the base-line correction has been taken into account. Fig. 3.22 summarizes the temperature dependence of the five bands. The error analysis on the five peaks' position led to an average standard deviation less than 1%. The weak peak at ca. 71 cm^{-1} (**p2**) is not detectable above 120 K, as it becomes too broad and the strong peaks at higher frequency get closer and broader. The general trend is a decrease of

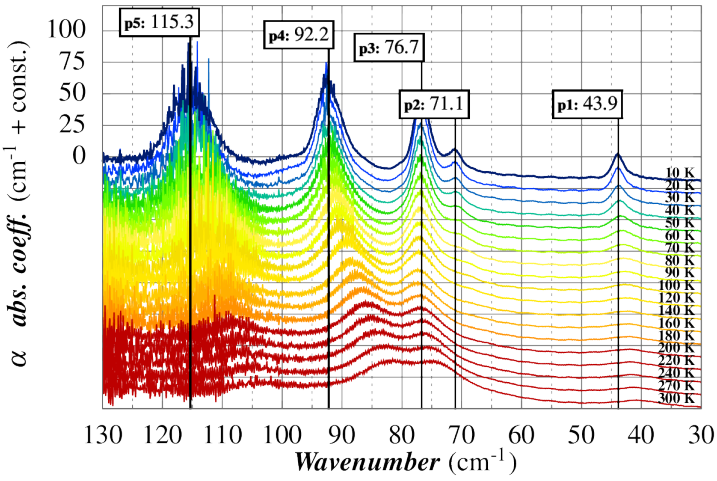

Figure 3.21: The THz spectra of ($\mathbf{1_a}$) as a function of temperature.

frequency when temperature increases and it is ascribed primarily to the effect of the thermal expansion of the lattice, which results in the softening of the intermolecular forces [147].

The peak at ca. 77 cm^{-1} (**p3**) is the only one that deviates from the general trend: its temperature dependence is very weak and not monotonous.

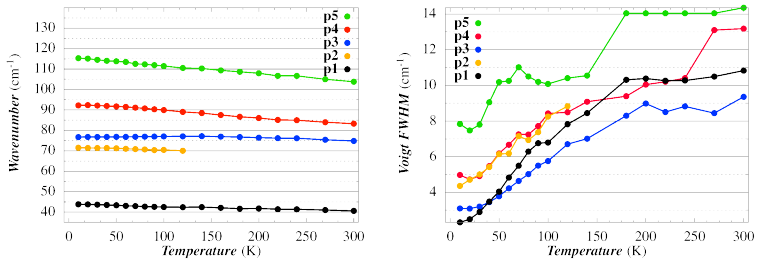

Figure 3.22: Left: The temperature dependence of the peaks' frequency. Right: Temperature dependence of linewidths obtained using a Voigt fit function for each peak and a baseline correction.

Fig. 3.22 shows how the linewidth of each peak, in terms of pseudo-Voigt, varies by increasing temperature from 10 K to 300 K. A deconvolution process was carried out to separate the Lorentzian contribution (Γ_L) and the Gaussian one (Γ_G). The first contribution takes into account the homogeneous broadening, connected to the phonon-phonon and phonon-lattice interactions through the anharmonic terms of the crystal potential expansion, whereas the second one takes into account the

inhomogeneous broadening, that is predominantly attributed to the variation of frequency with the phonons wave vector (**k**) direction of the phonons active in IR. Indeed, in common spectroscopic techniques, e. g. IR and Raman, the conservation of the moment is fullfilled in a small surrounding of the Γ-point ($\mathbf{k} \simeq 0$), making the phonons' frequency dependent on **k** direction.

The results collected in Fig. 3.23 show that, for the temperature range 10–100 K, the homogeneous broadening of peaks **p1**, **p3**, and **p4** increases almost linearly with temperature, while the inhomogeneous width is practically constant. The relative standard deviation is of the order of 10-20% since Γ_G and Γ_L are particularly sensitive to the irregularity of the peak tails. In addition, the loss of a well defined shape of **p2** above 70 K and the high noise that affects **p5** do not allow to deduce for these peaks a clear temperature trend.

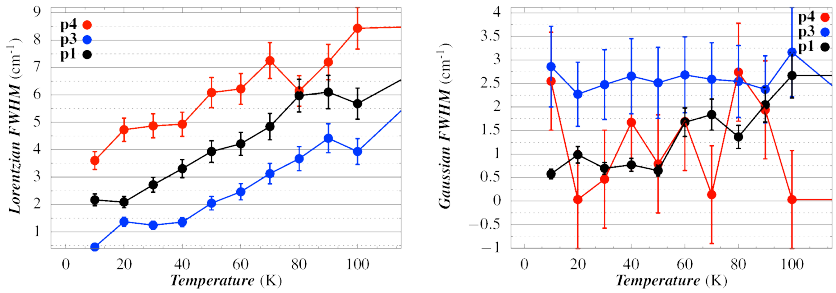

Figure 3.23: Lorentzian component (left panel) and Gaussian component (right panel) of the Voigt profile of each peak.

3.4.3 *Single Crystal Spectroscopic Characterization*

$[VO(acac)_2]$ (**1**) has been placed with the [0 -1 -1] crystal face perpendicular to the THz beam and it has been rotated to collect THz spectra along the entire goniometric angle. In Fig. 3.24, a sketch of the geometry of the experiment is reported, the rotation angle is the one between the black dashed line in the red plane, parallel to the vanadyl groups, and the vertical polarization of the THz beam (black arrow).

Since the sample is rather thick and cannot be sufficiently thinned without damaging it, saturation phenomena occur above 85 cm^{-1} [210]. Consequently, the available THz frequency range is narrower than those reported above for powder samples. Nevertheless, four peaks are clearly distinguishable and their shape, as well as their position, dramatically change as a function of the rotation angle. To extrapolate the peaks features, a fit procedure has been applied. The fit function contains four

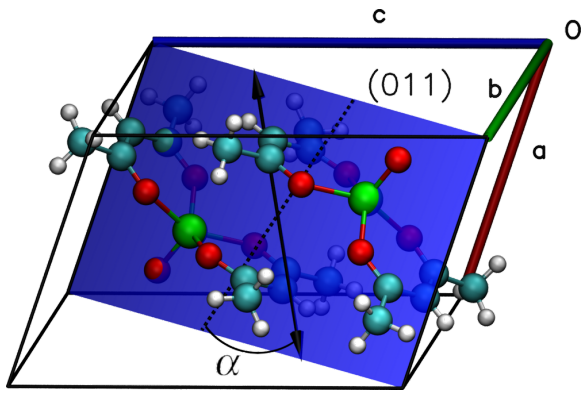

Figure 3.24: The angle α between the dashed line, parallel to the vanadyl groups, and the black doublesided arrow (THz beam polarization), represents the rotation angle. The THz beam is perpendicular to (011) crystal face.

Gaussian contributions and a linear base-line correction, as shown in the following equation.

$$f(\omega) = \sum_{i=1}^{4} A_i e^{\frac{-(\omega-\omega_i)^2}{\sigma_i^2}} + a\omega + b \tag{3.19}$$

The angle dependence of the position of each peak is displayed in Fig. 3.25 The first two bands are strongly influenced by the orientation of the crystal, while those at higher energy are less affected by it. When the angle ranges from 120° to 190° and from 320° to 360°, the signal saturates and, thus, it is absent in Fig. 3.25.

A comparison of single crystal and powder measurements evidences that the available spectral window is wider for the latter sample because of the impossibility to make the crystal thin enough, as already mentioned above. For this reason, the absorption saturates for **p4** in the 120°–180° angular portion. If one focuses on the room temperature spectra in the common frequency region it is further evident that powder spectrum contains on peak less than the single crystal one. Indeed, powder sample (blue line in Fig. 3.26) seems to have no peak between 45 and 60 cm^{-1}, while single crystal (red line in Fig. 3.26) clearly shows a peak in that frequency range, even if only at some orientation.

As Fig. 3.26 shows, no evident peak in the above mentioned frequency region is visible because it is related only to few orientations. If all the possible orientations of the crystallites in space are taken into account, the relative weight of the orientations that definitely show that peak could be assumed to be much lower than in the angular average. Looking at the position of the other peaks and comparing them in the two samples, as reported in Tab. 3.7, it is evident that a good agreement is present.

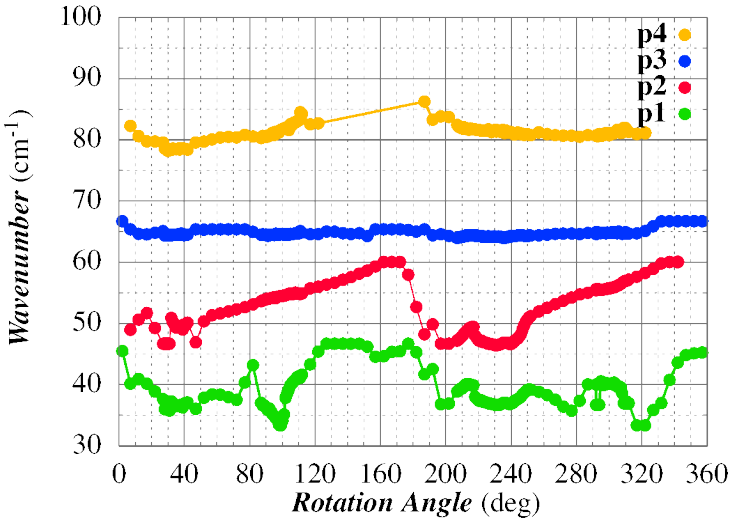

Figure 3.25: The Angle dependence of the peaks' frequency of the five observed bands. The two lowest in frequency are remarkably affected by the orientation of the crystal with respect to THz propagation.

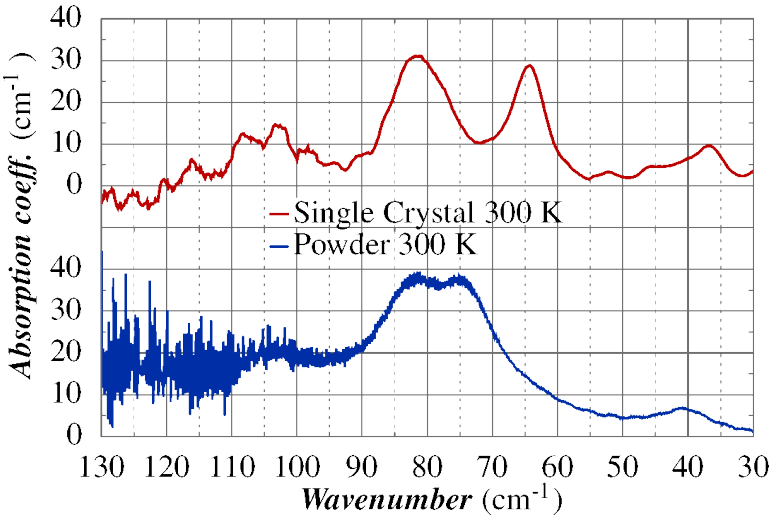

Figure 3.26: Comparison of powder THz IR spectrum and averaged THz IR spectrum of single crystal sample in [0 1 1] plane

The unusual frequency behaviour of the observed phonons reported in Fig. 3.25 is ascribed to their nature of oblique phonons. This is a peculiar class of polar

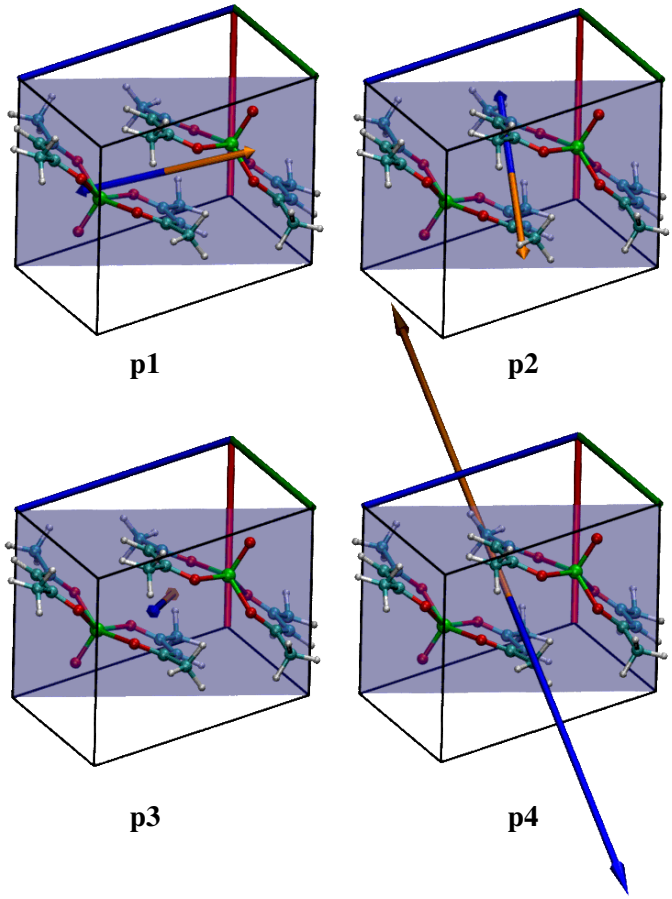

Figure 3.27: Electric dipole moment generated when the system is distorted of one unit of normal mode (blue for the positive direction along coordinate and orange for the negative), along four different normal modes. The perspective is perpendicular to the [0 1 1] plane, hence highlighting the electric dipole moment component lying in the plane where the radiation polarization is rotated during angular resolved measurements.

phonons, which develop a strong dipole moment. A polar phonon can be defined transverse optical (TO) or longitudinal optical (LO) whether its dipole moment develops perpendicular or parallel to the propagation direction (defined by the wave vector **k**) [147]. Generally, in crystals having high-symmetry unit cell, the phonon modes are classified according to their irreducible representations and their dipole moments develop along the symmetry elements of the cell. In such a case, LO-TO splitting often occurs removing the degeneracy of the TO and LO phonons

Table 3.7: Comparison between the phonons' frequency of **1** averaged on the rotation angle and of powder sample **2**.

	Averaged single crystal (**1**)	Frequency (**1**)
peak	ω (cm^{-1})	ω (cm^{-1})
p1	38.9	40.6
p2	52.1	-
p3	64.7	74.8
p4	81.1	83.3
p5	-	103.8

at $\mathbf{k} = 0$. It is caused by the long-ranged nature of the Coulomb interaction. Since the $[VO(acac)_2]$ crystallizes in the low-symmetry triclinic P-1 space group, each polar phonon has a mixed LO-TO character, i.e. oblique phonon. Their frequency varies from that of the pure LO to that of the pure TO according to the propagation direction of the radiation. This means that by changing the direction of the THz field with respect to the crystal system, phonons continuously shift their frequency passing from that of pure LO to TO and vice versa [147]. An explanation for the measured angular dependence of phonons' frequency can be found calculating the electric dipole moment of the $[VO(acac)_2]$ crystal unit cell, when the atomic position are subject to the action of the creation and annihilation operators a and $a^{\dagger}$, distorting the structure along one normal mode coordinate. The same level of theory of vibrational analysis is here employed. The resulting dipoles are shown in Fig. 3.27, where the unit cell is oriented with the [0-1-1] plane parallel to the paper. Each of the four modes shows a correlation between the frequency variation and the component of electric dipole moment contained in the plane where the light polarization is rotated. Normal mode **p4** is characterized by the strongest dipole and the corresponding measured frequency (in yellow in Fig. 3.25) is saturating in the region $120 < \theta < 180$, also the three modes reported **p2** and **p1** show a component of their electric dipole in the plane, justifying the frequency shift measured of about 10 cm^{-1}. **p3** bears the lowest dipole component in plane from calculation and can be correlated to the almost flat angular dependence of its frequency.

3.4.3.1 *Phonon decay mechanisms from linewidth analysis*

A further investigation focused on the homogeneous linewidth as function of temperature. It allows the rationalization of *i*) the decay mechanism of the phonons and *ii*) the estimation of the third-order anharmonic coefficients. Indeed, in the limit

$kT > h\nu$ (where ν is the frequency of the phonon), a linear trend of the Lorentzian linewidth on temperature indicates that a three-phonon decay process is the main source of relaxation. The frequency of the effective phonons involved in the decay was possible to be estimated, too.

The decay pathway identified for **p1**, **p3** and **p4** corresponds to the down-conversion process, consisting in the creation of two phonons whose total energy summation corresponds to the optically excited one[211]. The simplest process fulfilling the conservation of energy and momenta requires that the energy of generated phonons is the half of the starting one, $2\hbar\omega = \hbar\omega_0$. Its contribution to the homogeneous linewidth reads [211, 212]

$$\Gamma = \Gamma_0 + Bn\,\delta(\omega_0 - 2\omega) \tag{3.20}$$

where Γ_0 is the residual linewidth at zero temperature, $n = [exp(h\nu/kT) - 1]^{-1}$ is the occupation number of the phonon involved in the decay at temperature T, and B is the third-order anharmonic coefficient. The Kronecker δ functions ensure the energy conservation.

In principle, all the possible triples of phonons which satisfy the conservation law of energy and momentum can interact with each other.

The numerical analysis requires the introduction of all vibrational frequencies. Since the only experimental available spectra are the Γ-point IR, it will be presented in the next section.

3.4.4 *Calculated vibrational spectra*

For the Density Functional Theory based calculations we used the $[VO(acac)_2]$ crystallographic unit cell coordinates. The temperature effects on the crystal structure were tested exploiting the X-ray data collected at cryogenic and room temperature (100 and 300 K). The availability of these data allowed to minimize the DFT energy with respect to the molecular coordinates, keeping fixed the experimental cell parameters [213], prompting the estimation of the errors introduced in the vibrational analysis when the temperature effects on the structure are neglected, i. e., when cell parameters are free parameters in the energy minimization procedure. The simulation of cell parameters at finite temperature can be accomplished only *via* dynamical DFT methods (*ab initio* molecular dynamics). Vibrational properties at 0 K were also computed by fully relaxing the electronic degrees of freedom, lattice constants, and atomic positions, the resulting crystal structure is hereafter referred as $\mathbf{1}_{\mathbf{0K,cell-opt}}$. The full inclusion of the Brillouin zone integration, important to

quantitatively estimate the optical phonon bands, is not part of the main focus of the present work [90]. A more than fair approximation in the analysis of phonons' decay mechanisms is achieved limiting the calculation to the DFT Γ-point optical modes, along with the acoustic phonons in the whole Brilloiun zone. The latters were already computed by some of us at the Force Field (FF) level[157], at DFT level with the finite displacement method at the Γ-point [90] and in the Brillouin zone [205].

We denote $\mathbf{1_{0K,cell-opt}}$, $\mathbf{1_{100K,opt}}$ and $\mathbf{1_{300K,opt}}$ as the DFT optimized structures; in $\mathbf{1_{0K,cell-opt}}$ both cell parameters and atomic coordinates are optimized while in $\mathbf{1_{100K,opt}}$ and $\mathbf{1_{300K,opt}}$ only atomic coordinates were left to relax keeping fixed the cell parameters to experimental values. Lowering the temperature from 300 K to 0 K, a contraction occurred along the **b** and **c** axes, while a non-monotonous expansion along the **a** axis was observed. The overall variation of the cell parameters led to a unit cell volume contraction. $\mathbf{1_{0K,cell-opt}}$ was found to be more stable than $\mathbf{1_{100K,opt}}$ of 2.80 kcal/mol, while $\mathbf{1_{100K,opt}}$ more stable than $\mathbf{1_{300K,opt}}$ of 0.92 kcal/mol, as expected for the most enthalpic favoured structure. The full relaxation of $\mathbf{1_{0K,cell-opt}}$ led to optimized cell parameters that show the maximum deviation with respect to the $\mathbf{1_{100K}}$ of 4.8% and 2.8% for lattice constants lengths and angles, respectively. The volume underwent a shrinking of ca. 5%. Even more, it is worth to highlight that **a**, β and γ parameter computed for $\mathbf{1_{0K,cell-opt}}$ do not completely follow the expected trend indicated by the experimental parameters obtained for $\mathbf{1_{100K}}$ and $\mathbf{1_{300K}}$ unit cells. These results have also a general relevance, as they show that neglecting the temperature effects on cells, i. e. using static DFT cell parameters optimized at 0 K, a poorer agreement in reproducing the vibrational spectra at finite temperatures can be attained. See, for instance, the computed $\mathbf{p1_C}$ which is shifted of almost 20 cm^{-1} from 0 K to 300 K calculated phonons.

The computed IR spectra for the three cells are reported in Fig. 3.28. The frequencies of the lowest 20 Raman active (9) and IR active (11) modes are reported in Tab. Tab. 3.8 with the trends for the first IR modes gathered in Fig. 3.29.

The computed red shifts of peaks in the range 30-130 cm^{-1} are in an overall good agreement with those observed for the THz spectra measured at 10 K, 100 K, and 300 K. A correspondence one-to-one with the experimental peaks is valid for $\mathbf{p1-4}$; the comparison is impossible for **p5**, as this band results, according to our calculation, as the superposition of four peaks ($\mathbf{p5_C-8_C}$). The calculated relative intensities are also in a nice agreement with the experimental ones with the only exception for **p2** and **p3**, for which an inversion of their intensities can be claimed. This interpretation is more plausible than an energy swap of the two modes because $\mathbf{p3_C}$ shows a larger shift as a function of the temperature than $\mathbf{p2_C}$ as, indeed, experimentally observed. The comparison of the calculated linewidths at

Table 3.8: The frequencies of the lowest 20 Raman and IR active modes are here reported. α is the normal mode index, ν_α the frequency, int. the IR intensity and Sp-Ph the magnitude of spin-phonon coupling coefficient.

IR normal modes											
$\mathbf{1}_{\mathbf{0K,cell-opt}}$				$\mathbf{1}_{\mathbf{100K,opt}}$				$\mathbf{1}_{\mathbf{300K,opt}}$			
α	ν_α	int.	Sp-Ph	α	ν_α	int.	Sp-Ph	α	ν_α	int.	Sp-Ph
n°	cm^{-1}	a. u.	a. u.	n°	cm^{-1}	a. u.	a. u.	n°	cm^{-1}	a. u.	a. u.
6	55.323	0.311	2.331E-7	4	42.411	0.303	3.905E-7	4	38.137	0.335	3.787E-7
8	73.267	0.509	4.399E-7	9	69.518	0.383	8.549E-7	9	64.171	0.430	8.199E-7
11	83.461	0.220	2.453E-7	10	76.013	0.140	4.069E-7	10	69.467	0.072	2.448E-7
13	99.240	0.446	3.330E-7	12	94.864	0.862	6.695E-7	12	86.907	1.0	6.289E-7
15	112.346	0.395	5.968E-7	15	108.685	0.0769	3.620E-7	15	102.072	0.109	2.255E-7
17	116.558	0.274	2.171E-7	17	116.262	0.339	4.334E-7	17	106.960	0.272	4.870E-7
18	125.108	0.0947	2.842E-7	18	120.492	0.328	1.231E-7	18	113.787	0.283	6.313E-8
20	145.745	0.234	8.805E-8	20	125.933	0.087	2.795E-7	19	115.077	0.149	4.863E-7
Raman normal modes											
$\mathbf{1}_{\mathbf{0K,cell-opt}}$				$\mathbf{1}_{\mathbf{100K,opt}}$				$\mathbf{1}_{\mathbf{300K,opt}}$			
α	ν_α		Sp-Ph	α	ν_α		Sp-Ph	α	ν_α		Sp-Ph
n°	cm^{-1}		a. u.	n°	cm^{-1}		a. u.	n°	cm^{-1}		a. u.
4	43.313		1.130E-7	5	46.320		1.430E-7	5	40.497		2.427E-8
5	50.872		1.648E-7	6	48.492		3.037E-7	6	43.222		3.545E-7
7	63.349		6.260E-7	7	57.788		7.608E-7	7	53.353		5.580E-7
9	75.290		2.357E-7	8	66.991		3.717E-7	8	61.592		3.906E-7
10	81.218		3.927E-7	11	79.998		9.584E-8	11	73.577		1.711E-7
12	98.285		4.581E-7	13	100.610		9.038E-7	13	89.691		6.472E-7
14	111.392		2.764E-7	14	104.128		4.613E-7	14	96.560		4.950E-7
16	114.618		2.050E-7	16	110.094		1.703E-7	16	102.096		3.003E-7
19	135.847		2.568E-7	19	124.879		8.979E-8	20	115.669		6.292E-8

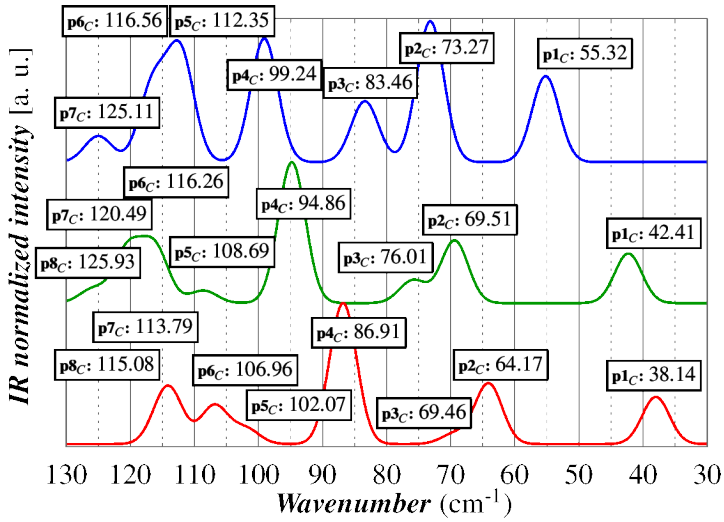

Figure 3.28: DFT vibrational analysis of $\mathbf{1}_{\mathbf{0K,cell-opt}}$ (blue) $\mathbf{1}_{\mathbf{100K,opt}}$ (green) and $\mathbf{1}_{\mathbf{300K,opt}}$ (red).

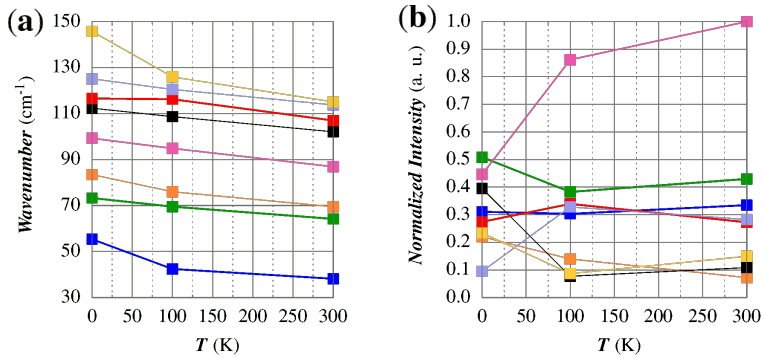

Figure 3.29: The calculated frequencies (**a**) and intensities (**b**) of the lowest 8 IR active modes are here depicted.

different temperatures is impracticable, as in our approach the effects of temperature are taken into account only by using different cell parameters.

In Fig. 3.30 we report the decomposition procedure outlined by Neto *et al.* [194] and developed by Lunghi *et al.* [151] to compute the amplitude of local translation, local rotation and internal vibrations of a single $[VO(acac)_2]$ molecule inside its crystal. The nature of the lowest eight peaks shows that the reticular contributions decrease as the energy of modes increases, as expected. Such a contribution is still

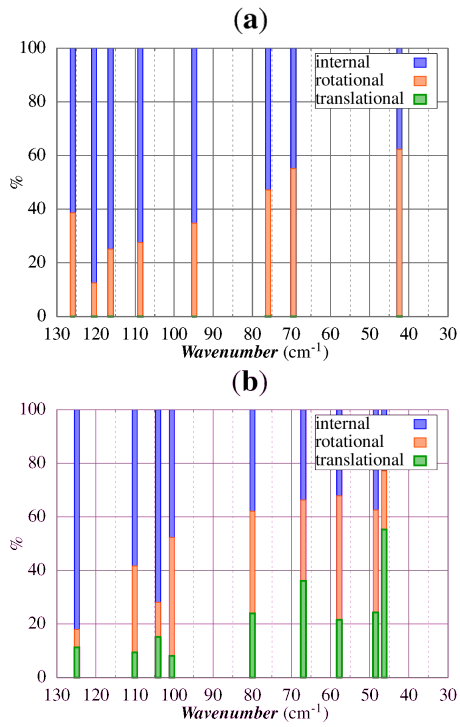

Figure 3.30: Total molecular motion associated with: (**a**) IR and (**b**) Raman normal modes from $\mathbf{1}_{\mathbf{100K,opt}}$ set in the low wavenumbers range (30–130 cm^{-1}) decomposed in intramolecular percentage (blue), rotational percentage (orange), and translational percentage (green). In (Fig. S10) we show the plots of the first vibrational modes composition for each temperature.

detectable up to the 20th mode with a 20-30% of external character. The modes can be sketched as the following:

1) in $\mathbf{p1_C}$ two [$VO(acac)_2$] molecules rigidly tilt one with respect to the other (Fig. A.6)

2) $\mathbf{p2_C} - \mathbf{3_C}$ can be considered quasi-degenerate modes where the two acac ligands of a [$VO(acac)_2$] molecule tilt out-of-phase ($\mathbf{p2_C}$) or in-phase ($\mathbf{p3_C}$) with respect to one acac belonging to a neighbouring [$VO(acac)_2$] molecule: in $\mathbf{p2_C}$ the neighbouring molecule is inside the unit cell; in $\mathbf{p3_C}$ in an adjacent one (Fig. A.6 and Fig. A.7)

3) in $\mathbf{p4_C} - \mathbf{8_C}$ the vanadyl group bending and acac oxygen wagging contributions became significant (Fig. A.7, Fig. A.8 and Fig. A.9)

Applying the model of phonon relaxation by down-conversion (*vide supra*) to the phonons $\mathbf{p1_C}$, $\mathbf{p3_C}$, and $\mathbf{p4_C}$, a clear matching of the energy and momenta conservation law can be determined (see Fig. 3.31).

In the case of down-conversion a mode separates into two modes, whose sum in energy must match the energy of the original one.

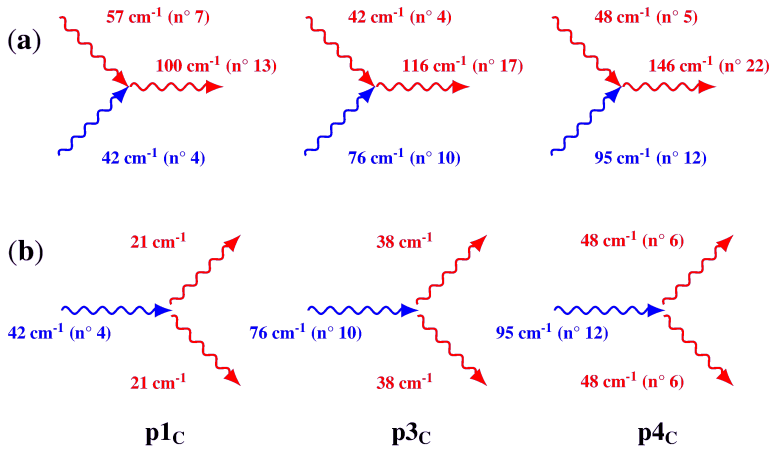

Figure 3.31: Two-phonon up- (**a**) and down-conversion (**b**) processes. The optical phonons' frequencies are chosen among the $\mathbf{1_{100K,opt}}$ set. The blue phonons refer to the ones appearing in THz spectrum, the red ones are those IR or Raman modes participating to the multi-phonon relaxation processes.

In our framework, $\mathbf{p1_C}$ is the first optical mode, therefore its decay pathway must involve the acoustic branches at $\mathbf{k} \neq 0$. Indeed, the acoustic modes play an important role in the relaxation of low-energy phonons, being the only ones sufficiently populated to provide an effective relaxation channel. As previously reported [157], the acoustic modes extend up to ca. 40 cm^{-1} at the border of the Brillouin zone. We therefore assume that down-conversion process might be allowed generating two acoustic phonons at frequency 21 cm^{-1}. Also $\mathbf{p3_C}$ undergoes down-conversion generating two acoustic phonons at frequency 38 cm^{-1}.

Phonon $\mathbf{p4_C}$ can decay through down-conversion process generating two optical phonons at frequency 48 cm^{-1} (mode 6).

Therefore, the resulting third-order anharmonic coefficients are comparable and of ca. 2 cm^{-1} for $\mathbf{p1_C}$ and $\mathbf{p3_C}$, while its value is twice (ca. 4 cm^{-1}) for $\mathbf{p4_C}$.

3.4.5 *Spin-phonon coupling analysis*

A first qualitative fingerprint of interaction between magnetism and vibrations in each molecule requires the calculation of the phonon spectrum and the amplitude of Sp-Ph coupling for all possible modes, $V_{\alpha}^{Sp-Ph} = \left(\frac{\partial \mathscr{H}_0}{\partial q_\alpha}\right)$, as depicted in previous section. The computed Sp-Ph couplings for all the energy range (0-1200 cm^{-1}) for both Raman and IR modes are reported in Fig. 3.32 for all the three considered cells. Unfortunately, the lack of the inversion center in the molecule did not allow to fully exploit symmetry considerations in the rationalization of the normal modes, as evidenced in previous works[196].

As stated in previous section, some cell parameters computed for $\mathbf{1_{0K,cell-opt}}$ do not completely follow the expected trend indicated by the experimental parameters obtained for $\mathbf{1_{100K}}$ and $\mathbf{1_{300K}}$ unit cells. The different cell parameters led to an alteration of the compositions of the normal modes and, therefore, to their Sp-Ph couplings. A closer similarity of $\mathbf{1_{100K}}$ vs. $\mathbf{1_{300K}}$ Sp-Ph coefficients is indeed found, in contrast to $\mathbf{1_{100K}}$ vs. $\mathbf{1_{0K,cell-opt}}$ and $\mathbf{1_{300K}}$ vs. $\mathbf{1_{0K,cell-opt}}$.

The spectrum can be divided in two regions. Above 300 cm^{-1}, the coupled modes are dispersely grouped for all the frequencies range with very similar distributions among the three different cells. The group of vibrations located at 1000 cm^{-1} showed the strongest Sp-Ph coefficients. Indeed, the involved normal modes are characterized by a relevant contribution of characteristic $V{=}O_{vanadyl}$ stretching. Strong couplings are also observed for groups centered at 470 cm^{-1} (O_{acac}–V–O_{acac} simmetric stretching) and 365 cm^{-1} (O_{acac}–V–O_{acac} simmetric stretching). No temperature effects on the Sp-Ph coupling magnitudes are evident in this frequency range. Below 300 cm^{-1} a denser distribution of coupled modes was computed. The most coupled modes are in the 200-300 cm^{-1} energy window, and a variation of the magnitude as a function of the temperature is now observed. The largest dependence (a factor 5 or higher between 0 and 300 K) was computed for the Raman mode 5 (46.32 cm^{-1} at 100 K, symmetric translation of molecules) and IR modes 18 (120.49 cm^{-1} at 100 K, V–O_{acac} bendings), 45 (260.53 cm^{-1} at 100 K, O_{acac}–$V{=}O_{vanadyl}$ wagging and twisting) and 47 (264.08 cm^{-1} at 100 K, O_{acac}–V–O_{acac} wagging). For the first three modes, raising the temperature, a decrease of Sp-Ph magnitude was observed. An opposite behaviour was observed for the fourth, instead. Several other modes are decreasing or increasing their Sp-Ph coupling though, even if the variation in temperature is not so pronounced. This differences can be ascribed to the modified perturbation of the first coordination sphere caused by the variation of the primitive cell parameters observed for the three considered temperatures (see Tab. 3.6).

The nonmonotonous (**a**, β, γ) and monotonous (**b**,**c**,α) trends of the cell parameters can differently alter the composition of the normal modes and modify their Sp-Ph coupling efficiency.

Even though the computed Sp-Ph coupling variations are small, the overall computed variation becomes mandatory when a high level of accuracy to reproduce T_1 values in the whole temperatures range is required.

Focusing our attention on the IR modes in the experimental THz range (30-130 cm^{-1}), the differences between the computed Sp-Ph dispersions of $\mathbf{1_{0K,cell-opt}}$and $\mathbf{1_{100K}/1_{300K}}$ are more evident.

The computed Sp-Ph coefficients are reported in Fig. 3.32. Only $\mathbf{1_{100K,opt}}$ and $\mathbf{1_{300K,opt}}$ will be discussed for homogeneity.

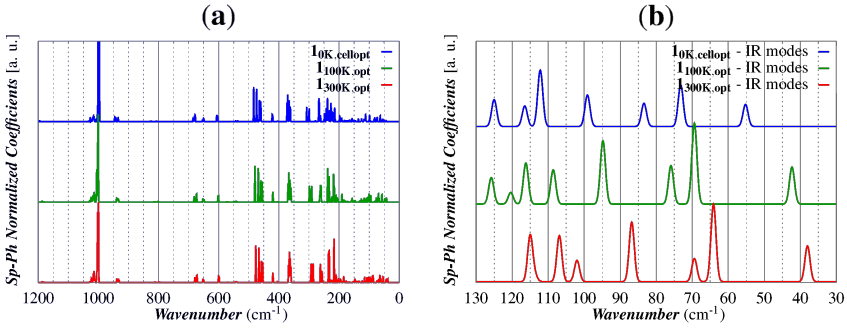

Figure 3.32: The comparison between coupled modes at different temperature is here depicted. (a) DFT Sp-Ph coupling interaction in the 0-1200 cm^{-1} spectral range. (b) zoom on the 30-130 cm^{-1} spectral range.

The Sp-Ph coupling can decrease its magnitude or remain unaffected with the raise of the temperature; its variation is not constant for each peak going from a slight variation of the Sp-Ph coupling for $\mathbf{p1_C}$ (rigid tilting of molecules) to a significative one for $\mathbf{p3_C}$ and $\mathbf{p5_C}$ (first coordination sphere distortion).

In a recent paper, it has been shown for $[Dy(acac)_3(H_2O)_2]$ [141] complex that a large Sp-Ph coupling is found for those normal modes which can induce large polarizations on the atoms of the first coordination sphere. Even in the case of $[VO(acac)_2]$ such a statement is confirmed. In details, the normal modes 45, 62, and 91 (depicted in Fig. A.10) which involve the largest charges variation, show the largest Sp-Ph coupling (see Fig. 3.33).

The indications from the computed results are dual. From a strictly computational point of view, this analysis shows that the use of static approaches for the description of the phonons distribution should be performed when the temperature effects can be indirectly accounted through the use of crystallographic cells collected at

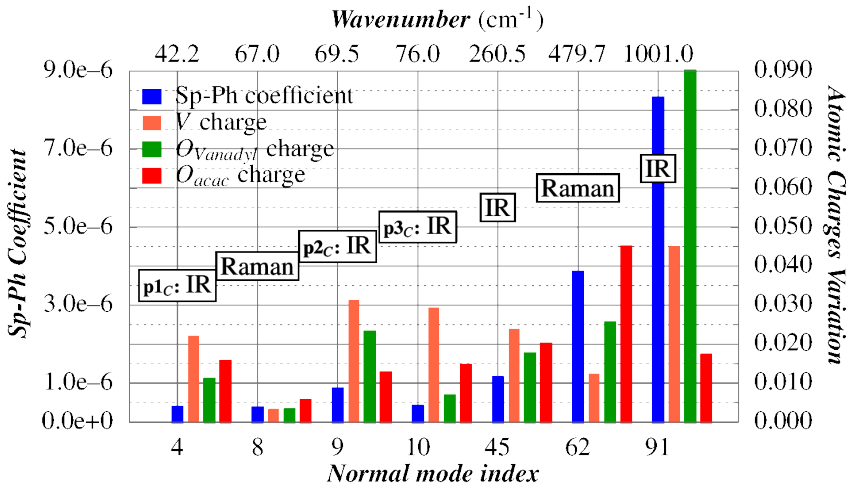

Figure 3.33: Charge variation of one molecule of $[VO(acac)_2]$ crystal is analysed along several normal modes from $\mathbf{1}_{\mathbf{100K,opt}}$ structure. The metal center and first coordination sphere atomic charges are reported. The data are reported in Tab. S5, while the phonons' composition is depicted in Fig. S10.

different temperatures. In such a framework a quantitative agreement with the THz experiment was obtained, while the ordinary approach of optimizing the geometries along with or without the crystallographic cell parameters can lead only to qualitative results for the vibrational spectrum and for the Sp-Ph coupling. From a structural point of view, it is possible to explicitly show how the Sp-Ph coupling associated to a single normal mode can vary as a function of the temperature as a direct consequence of the variation with the temperature of the crystal cell parameters. It is also evident that the Sp-Ph relaxation mechanism can give rise to a more complex behaviour than the polinomial or exponential functions usually considered in literature [25, 214] for the T_1 temperature dependence.

3.5 A COMPREHENSIVE MODEL OF RELAXATION – VOtpp

Manuscript in preparation:
Unveiling relaxation dynamics in a prototype molecular qubit by phonon mapping, *ab initio* simulation and Inelastic X-ray Scattering measurement.
Elena Garlatti, Alessandro Chiesa, Simone Chicco, Luigi Paolasini, Roberto Caciuffo, Claudio Mazzoli, Stefano Carretta, Fabio Santanni, Andrea Albino, Alessandro Lunghi, Federico Totti, Roberta Sessoli

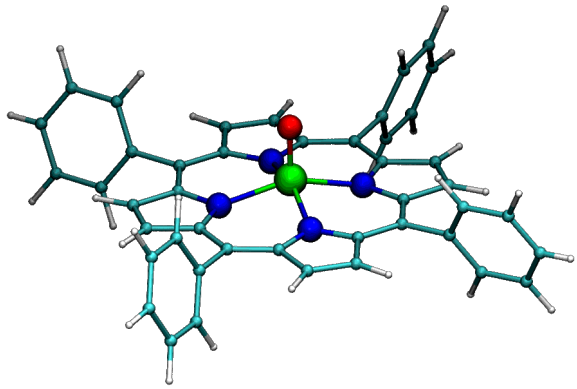

Figure 3.34: Molecular structure of [VO(tpp)] compound with coordination geometry of the metal ions highlighted with spheres. Color codes: green: vanadium, red: oxygen, dark blue: nitrogen, cyan: carbon, white: hydrogen.

We here focus on the vanadyl complex [VO(tpp)] (VO = vanadyl, tpp = tetraphenylporphyrinate) [175] (Fig. 3.34), since, as discussed in the previous paragraphs, vanadyl molecules are currently emerging as archetypes of a new generation of molecular qubits with long coherence times even at high temperatures. [VO(tpp)] shows remarkably long spin-lattice and phase memory times [175], allowing to perform coherent manipulations of the spin state in a wide range of temperatures. This molecule was selected because it exhibits the expected electronic and structural features to behave as a molecular spin qubit combined with other technologically relevant physical properties, such as extrinsic semiconductivity and the ability of being deposited on different surfaces in oriented dispositions, fundamental requisites for a suitable processability and incorporation of these materials in real devices. [VO(tpp)] can also be integrated in a 2D-3D covalent lattice and thus its environment and phonons can be further engineered [175]. Moreover, it is one of the most radiation-robust compounds of the family.

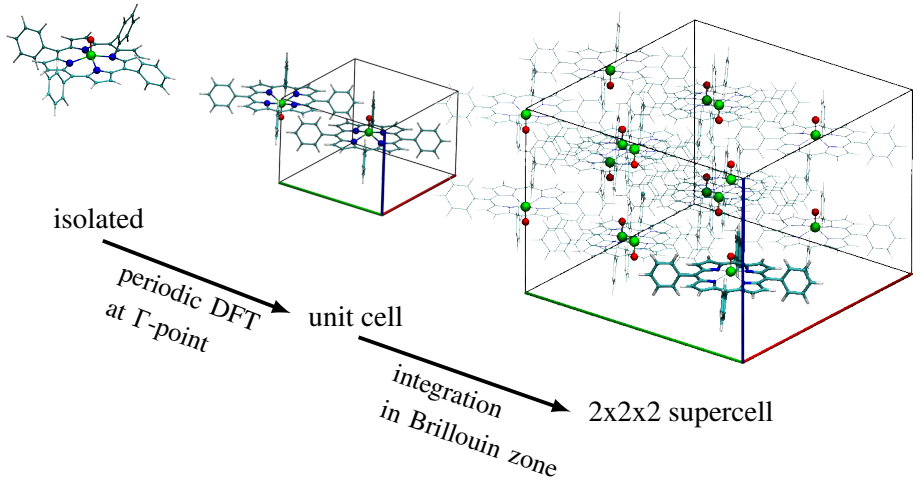

Figure 3.35: Pictorial representation of the increasing complexity of the system used for vibrational analysis.

The main goal of this investigation is to construct a reliable model of phonon-induced relaxation dynamics in MNMs, having access to phonon dispersions and eigenvectors is a necessary step for a quantitative evaluation of spin-phonon coupling coefficients.

Here we report the first step of the experiment that foresees to use for the first time the inelastic X-ray scattering (IXS) technique, at the ESRF facility [215], to measure phonon dispersions in a MNM. This characterisation will be crucial for validating *ab initio* calculations and for developing a sound model of the spin-phonon interactions and the resulting relaxation dynamics in this prototype molecular qubit. Since both phonon energies and polarisation vectors are necessary for the modelling, we need an experimental technique like IXS directly addressing both quantities. In this sense, the use of beamline ID-28 [216] can be instrumental in paving the way for the use of this technique in molecular magnetism and it will have a wide impact on the scientific community. The experimental measurements of phonon dispersion will be compared with the results obtained with state-of-the-art DFT calculations, allowing us to benchmark theoretical models and to investigate the vibrational properties at very low energies and the physics behind relaxation mechanisms in molecular qubits due to these vibrations. Some of the authors working on this experiment investigated the phonon modes in the parent compound [$VO(acac)_2$] with DFT [157] and, for the first time in a MNM, with 4-dimensional inelastic neutron scattering

(INS) [205, 217, 218]. Its acoustic branches extend up to 5 meV ($\sim$ 40 cm^{-1}) and display anticrossings with low-lying optical branches. The INS technique allowed them to measure acoustic modes dispersions, but it didn't enable to well-resolve optical modes, especially at energies above 11 meV, because energy resolution was not sufficient [205].

The main advantages of X-ray scattering with respect to neutron scattering are: *i)* the energy-independent resolution, which will allow us to investigte optical modes with increased sensitivity, *ii)* the possibility to use very small samples, compared to the large amount of single crystal MNMs, often difficult to grow, needed for INS, and *iii)* unlike neutron scattering, the measurements are not dominated by the hydrogen signal as the signal is proportional to the atoms' mass, like other X-ray based techniques. The incident energy at ID-28 is 23.725 keV. The experiments used the Si(12, 12, 12) monochromator reflection to get a mind-blowing resolution of 1.3 meV in determining the phonon energies and linewidths.

A single crystal of [VO(tpp)], synthesized and indexed by my colleague PhD student Fabio Santanni, was glued with vacuum grease on the standard beamline holder and it was cooled down to cryogenic temperatures (5 K). My colleagues from the University of Parma, ITU and ESRF designed and performed the experimental measurements and fully exploited the standard data reduction software available at the ESRF facility, they analysed the obtained dispersion curves and cuts with standard software. Constant-**k** scans were performed for several **k** values along high-symmetry directions, namely along [1 0 0], [0 1 0], and [0 0 1]. Brillouin zone of [VO(tpp)] crystal system is given in Fig. 3.36, where the elements which transform a point **k** of the zone into itself or into some equivalent **k** vector are shown. These elements form a subgroup that is the symmetry group of **k**. The energy resolution of $\sim$1.5 meV is sufficient to resolve both acoustic and optical modes [220]. Several points in q are needed in order to accurately map the phonon dispersions, and achieve the scientific target of the experiment. It is worth to note that no magnetic transitions are expected below 10 cm^{-1} ($\sim$1 eV) for V(IV).

Ab-initio calculations can, in the data analysis process, assist the fits of experimental phonon dispersions and intensities, and are the starting point to simulate the cross-section, allowing to fine-tune the experimental setup, too. Both the measured and calculated phonon dispersions (Fig. 3.37) confirm the presence phonons of unusually low energy ($\sim$10 cm^{-1}) even lower than the [VO(acac)$_2$] archetype [157]. The structural origin of these very low optics external modes (see Fig. 2.1), deserve a special attention, especially in the perspective of understanding their role in the relaxation dynamics.

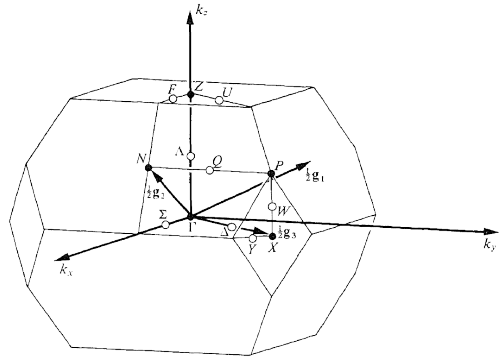

(b)

The Brillouin zone for Γ_q^v. (a) $a > c$, $\Gamma = (000)$; $N = (0\frac{1}{2}0)$; $X = (00\frac{1}{2})$; $Z = (\bar{\frac{1}{2}}\frac{1}{2}\frac{1}{2})$; $P = (\frac{1}{4}\frac{1}{4}\frac{1}{4})$; (b) $c > a$, $\Gamma = (000)$; $N = (0\frac{1}{2}0)$; $X = (00\frac{1}{2})$; $Z = (\frac{1}{2}\frac{1}{2}\bar{\frac{1}{2}})$; $P = (\frac{1}{4}\frac{1}{4}\frac{1}{4})$.

Tetragonal, I, Γ_q^v (Fig. 3.10)	Γ	(000)	$4/mmm\ (D_{4h})$	$E, C_{4z}^{\pm}, C_{2z}, C_{2x}, C_{2y}, C_{2a}, C_{2b}, I, S_{4z}^{\mp}, \sigma_z, \sigma_x, \sigma_y, \sigma_{da}, \sigma_{db}$
	N	$(0\frac{1}{2}0)$	$2/m\ (C_{2h})$	E, C_{2y}, I, σ_y
	X	$(00\frac{1}{2})$	$mmm\ (D_{2h})$	$E, C_{2z}, C_{2a}, C_{2b}, I, \sigma_z, \sigma_{da}, \sigma_{db}$
(a) (b)	Z	$(\bar{\frac{1}{2}}\frac{1}{2}\frac{1}{2})$ $(\frac{1}{2}\frac{1}{2}\bar{\frac{1}{2}})$	$4/mmm\ (D_{4h})$	$E, C_{4z}^{\pm}, C_{2z}, C_{2x}, C_{2y}, C_{2a}, C_{2b}, I, S_{4z}^{\mp}, \sigma_z, \sigma_x, \sigma_y, \sigma_{da}, \sigma_{db}$
	P	$(\frac{1}{4}\frac{1}{4}\frac{1}{4})$	$\bar{4}2m\ (D_{2d})$	$E, C_{2x}, C_{2y}, C_{2z}, \sigma_{da}, \sigma_{db}, S_{4z}^{\mp}$
(a) (b)	$\Lambda(\Gamma\Lambda)$ $\Lambda(\Gamma Z)$	$(\alpha\alpha\bar{\alpha})$	$4mm\ (C_{4v})$	$E, C_{4z}^{\pm}, C_{2z}, \sigma_x, \sigma_y, \sigma_{da}, \sigma_{db}$
(a)	$V(ZV)$	$(-\frac{1}{2}+\alpha, \frac{1}{2}+\alpha, \frac{1}{2}-\alpha)$	$4mm\ (C_{4v})$	$E, C_{4z}^{\pm}, C_{2z}, \sigma_x, \sigma_y, \sigma_{da}, \sigma_{db}$
	$W(XP)$	$(\alpha, \alpha, \frac{1}{2}-\alpha)$	$mm2\ (C_{2v})$	$E, C_{2z}, \sigma_{da}, \sigma_{db}$
(a) (b)	$\Sigma(\Gamma Z)$ $\Sigma(\Gamma\Sigma)$	$(\bar{\alpha}\alpha\alpha)$	$mm2\ (C_{2v})$	$E, C_{2x}, \sigma_y, \sigma_z$
(b)	$F(ZF)$	$(\frac{1}{2}-\alpha, \frac{1}{2}+\alpha, -\frac{1}{2}+\alpha)$	$mm2\ (C_{2v})$	$E, C_{2x}, \sigma_y, \sigma_z$
	$Q(NP)$	$(\alpha, \frac{1}{2}-\alpha, \alpha)$	$2\ (C_2)$	E, C_{2y}
	$\Delta(\Gamma X)$	(00α)	$mm2\ (C_{2v})$	$E, C_{2a}, \sigma_z, \sigma_{db}$
(b)	$U(ZU)$	$(\frac{1}{2}, \frac{1}{2}, -\frac{1}{2}+\alpha)$	$mm2\ (C_{2v})$	$E, C_{2a}, \sigma_z, \sigma_{db}$
(a) (b)	$Y(XZ)$ $Y(XY)$	$(\bar{\alpha}, \alpha, \frac{1}{2})$	$mm2\ (C_{2v})$	$E, C_{2b}, \sigma_z, \sigma_{da}$

Figure 3.36: Top: the various points and lines of symmetry for the Brillouin zones of tetragonal Bravais lattices are shown on the drawings (pag. 105 from [219]). Bottom: The group P(**k**), the symmetry group of **k**, for each point and line of symmetry in the basic domain of [VO(tpp)] Brillouin zones is given (pag. 113 from [219])

3.5.1 *Simulated Phonon Dispersion*

The PBE-DFT + DFT-D3 vdW corrections [170] calculation were performed with the frozen-phonon, or supercell, approach (see Sec. 2.3). The unit cell was employed, as in the previous studies, for the Γ-point vibrational analysis. Subsequently, the 2x2x2 (1248 atoms) and 3x3x3 (4212 atoms) supercells were used for the vibrational analysis in the whole Brillouin zone. The comparison of vibrational frequencies of

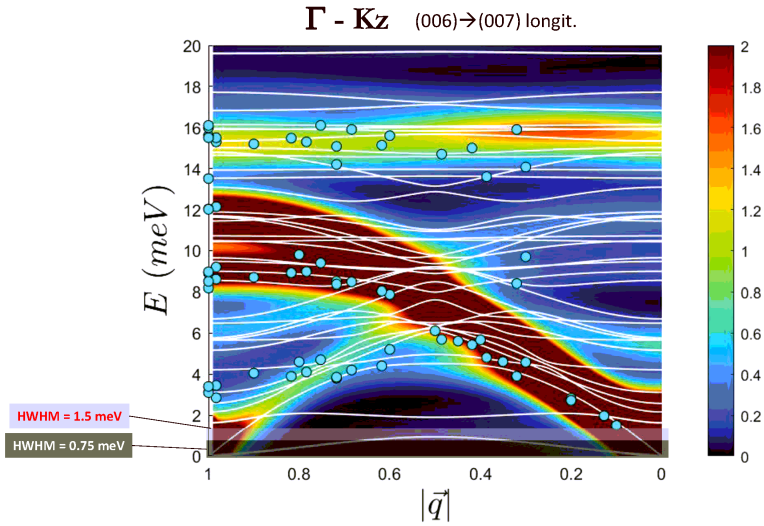

Figure 3.37: White lines: DFT-calculated phonons' dispersions. Color map: inelastic cross section simulated by my colleague PhD student Simone Chicco using DFT-calculated phononic eigenstates. Cyan scatters: energies of phonons excitations extracted from the fits in the [006] → [007]. The two Half Width Half Maximum values delimit the blind zones due to the width of the elastic peaks in low resolution (pale gray) and high resolution mode (dark gray). The zones in which the cross section amplitude differs significantly from zero are in good accordance with the measured points.

isolated molecule, unit cell, and 3x3x3 supercell is shown in Fig. 3.38. The periodic (red and green) low energy spectrum between 0 and 200 cm^{-1} show several features in common, that cannot be noticed in the isolated phase calculation. An example is the phonon at 160 cm^{-1} that is not present among the molecular vibration in the isolated phase (see Fig. 3.50 where IR intensities are included). On passing from the unit cell to the 3x3x3 supercell, a slight red shift of the low energy normal modes is calculated. A non-perfect convergence of the energy minimum is noticeable in the isolated phase spectrum as a very low-energy molecular vibration ($\sim$8cm^{-1}) arises and it is not found in the unit cell calculations. Also in this case low energy normal modes around 10 cm^{-1} are calculated in the supercell. They are assigned in this case to lattice vibrations.

Two kinds of supercells were generated because wrong dispersions were obtained from the first one generated, the 2x2x2 (Fig. 3.39). Two sets of phonons were calculated for this supercell, the first one (top row in Fig. 3.39) was optimized with relatively loose convergence threshold of $1.0 \cdot 10^{-6}$ *a.u.*/Å for the forces due to

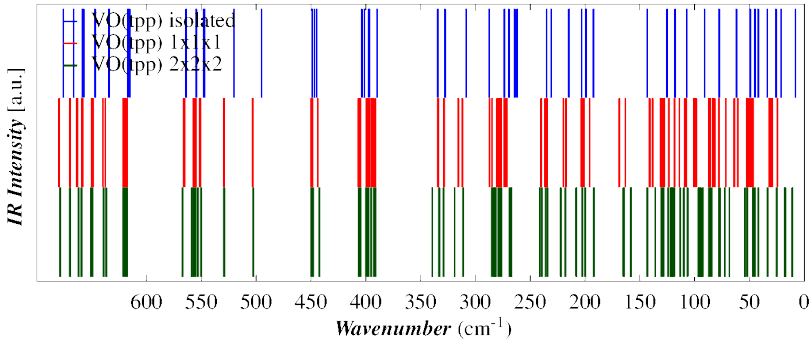

Figure 3.38: Comparison of vibrational frequencies (no intensity is included here) of [VO(tpp)] as resulted from the gas phase (blue), unit cell (red) and supercell (grenn) calculations.

the large number of atoms in the computational box. The plane wave cutoff was fixed at 3500 Ry. The acoustic phonons, in red in the graph, have negative values confirming the necessity to push beyond the refinement of simulation with a more tight geometry optimization. It was accomplished with a convergence threshold of $1.0 \cdot 10^{-7}$ *a.u.*/Å for the forces. Furthermore, the cutoff parameter of D3 vdW corrections by Grimme [170] were enlarged to test whether long range effects could affect the quality of calculated phonons. The results are shown in the bottom row of plots in Fig. 3.39. It is clear that even if the dispersion show a more realistic behaviour, we still face some problems in the long range contributions that show their effects mainly in the lattice motions.

The simulation of a larger supercell, 3x3x3, was then attempted. Following the computational procedure adopted for the 2x2x2, two optimization level were performed. The top row of Fig. 3.40 show the phonon dispersion from a relatively loose optimization, with convergence threshold of $1.0 \cdot 10^{-6}$ *a.u.*/Å and 650 Ry for plane wave cutoff. The bottom row dispersion were obtained with convergence threshold of $1.0 \cdot 10^{-7}$ *a.u.*/Å for the forces and 950 Ry for plane wave cutoff.

Althought a better result for acoustic phonons dispersions is obtained in tight optimization of both 2x2x2 and 3x3x3 supercells, and the phononic structure above 100 $cm^{-1}$is practically unchanged, this calculation cannot be safely employed to calculate the Sp-Ph coupling coefficients at the level of subtlety required due to the uncorrect dispersion relation of first phonons. As showed in Sec. 2.3, a further term in the dynamical matrix is needed, that takes into account the effects of macroscopic electric field due to the atomic motions. These effects can be taken into account through the Born effective charges [221], and will be part of the next

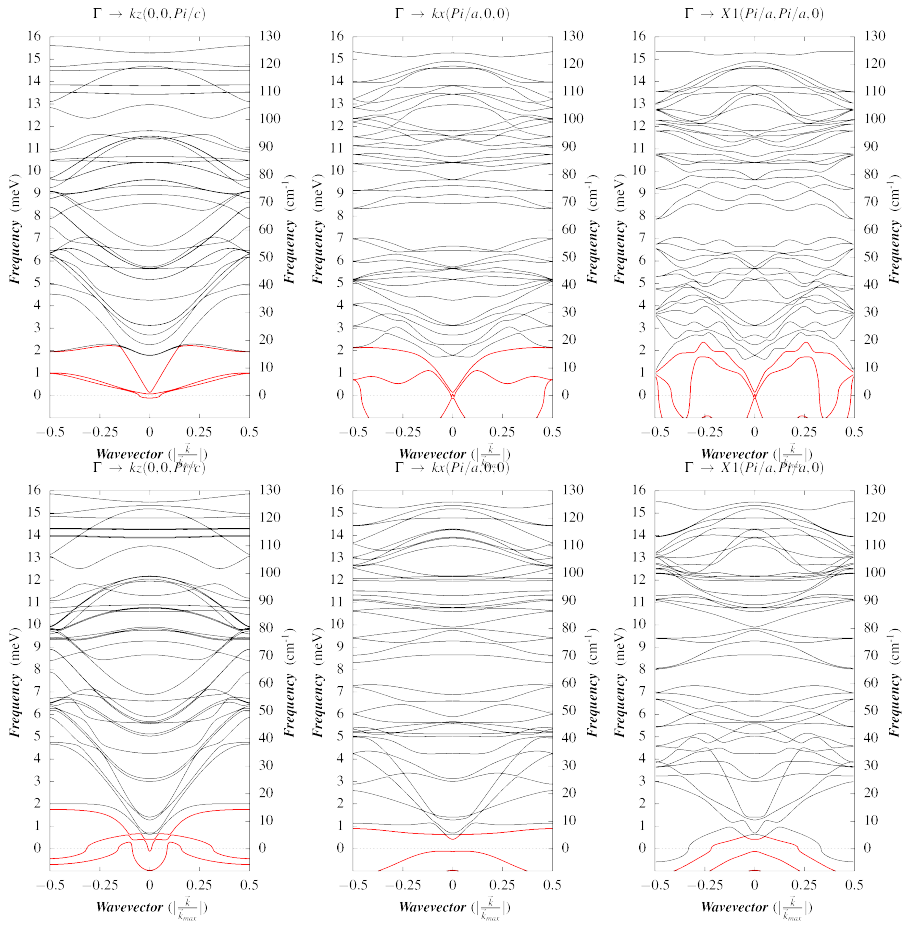

Figure 3.39: 2x2x2 supercell dispersions. Acoustic (red) and optical (black) phonons dispersions along three special directions (from left to right): $\Gamma \rightarrow k_z$, $\Gamma \rightarrow k_x$, $\Gamma \rightarrow X1$. Top row: phonons from loosely optimized structure. Bottom row: phonons from tightly optimized structure.

step in this study. At last, the present study represents an important test for vdW-corrected DFT in describing phonon dispersions. We showed that while qualitative features of experimental results are reproduced, a full quantitative reproduction of both eigenvalues and eigenvectors will require further improvements of DFT to treat vdW interactions. The comparison with IXS measured phonon dispersion will be pursued with a new set of calculated phonons. The direct comparison with experimental estimation is known to represent a challenge, due to the presence of multiple effects contributing to the measured values (e.g., finite-temperature and

zero-point-energy effects). We can, anyway, already state that uncommon low energy phonons were found in [VO(tpp)] crystal. We have a direct comparison between the practically zero-temperature experimental data and the calculated phonon energies, dispersions and polarization vectors. This comparison for molecular crystals of such a complexity is almost unique and it could represent also a new standard in the benchmarking of vdW correction schemes.

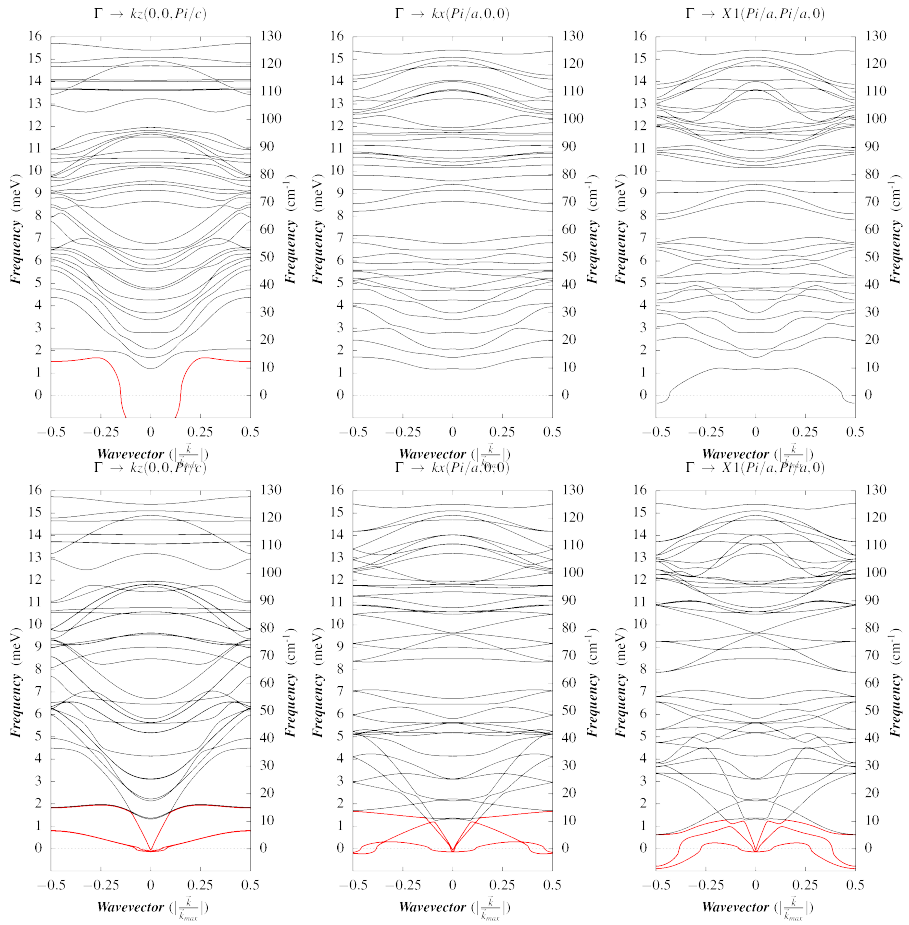

Figure 3.40: 3x3x3 supercell dispersions. Acoustic (red) and optical (black) phonons dispersions along three special directions (from left to right): $\Gamma \rightarrow k_z$, $\Gamma \rightarrow k_x$, $\Gamma \rightarrow X1$. Top row: phonons from loosely optimized structure. Bottom row: phonons from tightly optimized structure.

3.5.2 *Dynamics under THz radiation – VO*tpp

Manuscript in preparation:
Spin dynamics in [VO(tpp)] under high-power THz radiation: insights into spin-phonon coupling.
Anatoly R. Melnikov, Yaroslav V. Getmanov, Oleg A. Shevchenko, Stefano Benci, Fabio Santanni, Andrea Albino, Renato Torre, Lorenzo Sorace, Federico Totti, Alessandro Lunghi, Roberta Sessoli, Matvey V. Fedin, Sergey L. Veber

The study discussed in this chapter aims at obtaining some insights into the spin relaxation mechanisms when the $S = 1/2$ system is irradiated by high power THz pulses.

Great attention is dedicated in literature to the reversal of the magnetization by short laser pulses in anisotropic metal ions in exchange coupled systems [222–225] or quantum dots [226], but no study is today present on potential $S = 1/2$ electron-spin qubits. The final goal is to investigate through EPR measurements the possibility of polarizing the spin state trough THz irradiation of a specific phonon that "talks" with the spin thanks to the spin-phonon coupling.

It is known in laser physics that a population inversion cannot be achieved through incoherent excitation of a two-level atom. At best, a laser pulse with duration much longer than the coherence time of the two-level system T_2 can only drive the system to the transparency point where the populations of the upper and lower levels are equal. However, if the two-level atom is coupled to a vibrational continuum, it has been predicted that inversion can be possible even in the incoherent regime through the interaction of the dressed states with the Boson bath [226]. The rationalization of this mechanism could lead to the development of novel types of multifrequency approaches to initialize the state of the qubit.

We present the first attempt to directly measure a change in the spin dynamics of vanadyl tetraphenylporphyrinate, [VO(tpp)], when a specific phonon is excited by a high power THz radiation. The [VO(tpp)] shows remarkably long spin-lattice and phase memory times [175], that allows to perform EPR measurements in a wide range of temperatures, the EPR signal is detected in [VO(tpp)] samples including 0.5%, 2%, 100% magnetic dilutions of [VO(tpp)] in diamagnetic isostructural analog [TiO(tpp)]. Isostructural magnetically diluted cocrystals of [VO(tpp)] in [TiO(tpp)] diamagnetic matrix were prepared by my colleague Fabio Santanni, paying particular attention to possible contaminants in the synthesis, such as other metal ions coordinated to tpp ligand that can act as fast-relaxing species, covering the effect investigated on [VO(tpp)] species. Moreover, the [VO(tpp)] compound vibrational properties in the THz range were analysed in previous works [175], it

exhibits a single IR-active phonon below 100 cm^{-1} (2.14 THz - 71 cm^{-1} at 300 K), as shown in Fig. 3.41. In this framework, a system having a well-isolated and separated phonon is a suitable test bench for studying the effect of laser pulses on spin dynamics of $S = 1/2$ electron spin. It is possible, indeed, to test the system response either on resonance with the phonon band or not, on the band central frequency as well as on its edge, being sure not to irradiate any other vibrational modes.

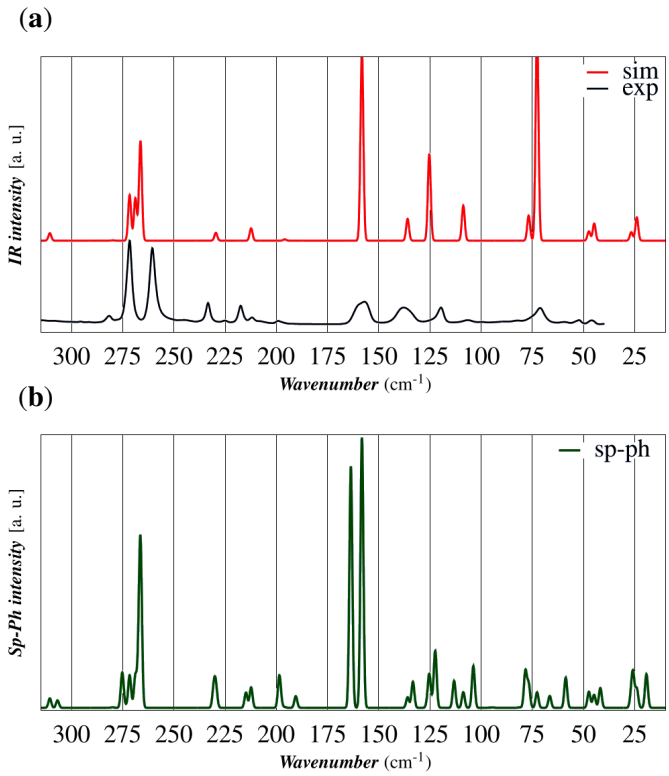

Figure 3.41: (**a**) experimental (black) and calculated (red) THz-IR spectrum of [VO(tpp)]. The simulation is pursued on the crystal unit cell. The calculated spectrum is shifted of -5cm^{-1} to obtain the superimposed 71cm^{-1} experimental and simulated peaks. (**b**) simulated Sp-Ph coupling pattern comprising both IR and Raman modes coefficients.

The experiment was performed at the FEL-Magnetic resonance joint facility (NovoFEL [227, 228]) by Prof. Matvey Fedin, Dr. Sergey Veber and Dr. Anatoly Melnikov, from the International Tomography Center (ITC SB RAS) in Novosibirsk. The Free Electron Laser facility is a source of high power THz radiation, that is

characterized by extreme monochromaticity and high tunability in a wide frequency range spanning the THz wavelengths (0.1–10 THz). This is the range of energies resonant with the low energy phonons (0–200 cm^{-1}) of molecular crystals under investigation. The laboratory is equipped with Free Electron Laser able to produce high-power radiation in THz regime (Fig. 3.42) coupled to an X-band (∼9 GHz) EPR spectrometer [228, 229].

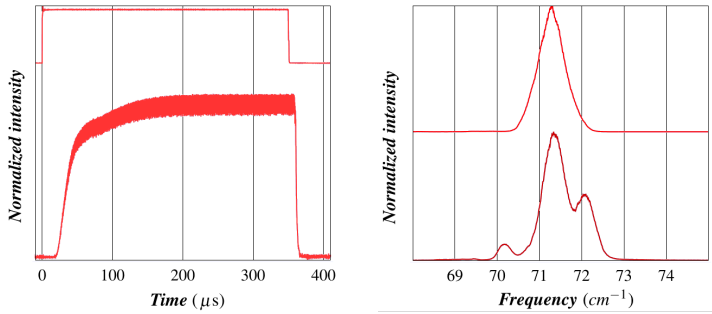

Figure 3.42: The THz pulse generated at the NOVOfel. (**a**) time duration. (**b**) spectral width.

The spin state of the complex was probed by EPR spectroscopy, the EPR spectra before and after IR excitation being compared. Pulse, CW-, and time resolved THZ EPR experiments were performed as function of of MW power, temperature, frequency and power of the THz radiation by the russian coworkers in Novosibirsk. They also carried on simulations of the experimental data by a simple model based on a modified version of Bloch equations. An example of a time resolved measurement as a function of magnetic field is reported in Fig. 3.43; each slice at constant time is constituted by an EPR spectra, the CW X-band microwave (MW) is, therefore, acting as a probe and it is recorded as a function of the delay time from the THz pulse to map the dynamics of EPR absorption. Such experiments can be called “THz-pump – EPR-probe” [228].

The set of measurements as a function of EPR MW power is employed in this section for comparison with results obtained with a model based on the Liouville equation developed by me and Alessandro Lunghi (Fig. 3.49). More details on the experimental measurements can be found in PhD thesis of Stefano Benci [230]. The [VO(tpp)] molecule showed a very peculiar behaviour under specific interplay of external perturbations:

- when the MW is resonant with an EPR transition
- when the MW power is tuned to saturate the EPR signal
- when a bright THz pulse resonant with a phonon is shined on the sample

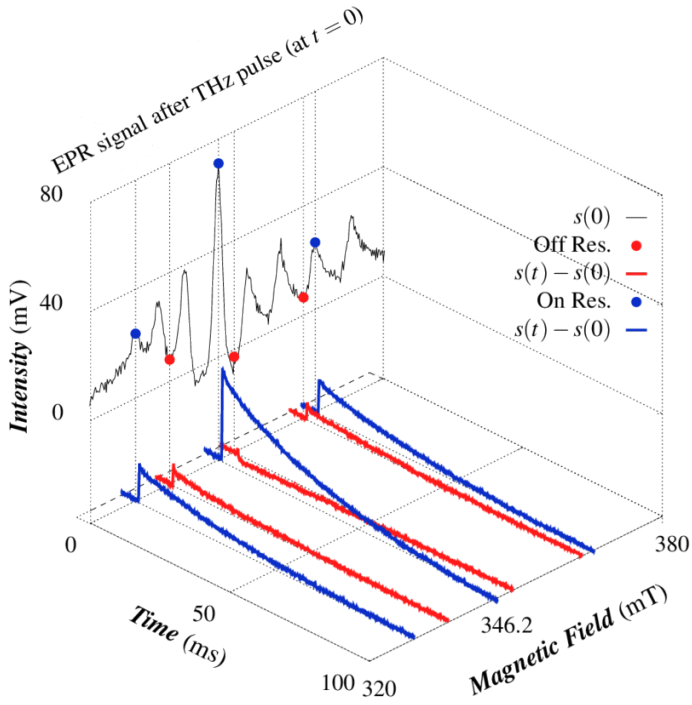

Figure 3.43: THz-pump EPR-probe experiment on [VO(tpp)]at 20 K. The 3D plot reports the difference of equilibrium EPR spectrum $s(0)$ and the THz-perturbed one $s(t)$. Blue and red dots represent the THz-induced signal when tuned on-resonance with EPR transitions or off-resonance, respectively.

When all these three conditions are met, the TR-THz-EPR signal, i. e., the difference of CW EPR spectra when the THz radiation is hitting the sample, $s(t)$, or not, $s(0)$, (for $t > 0$ in Fig. 3.43), changes from negative (red TR spectra) to positive (blue TR spectra). The acceleration of the spin relaxation process is determining a positive signal $s(t) - s(0)$, overcoming the usual decrease of signal due to the lowering of spin population difference, expected when a sample is irradiated with light and the transferred energy raises the temperature.

Such an effect can be caused by two phenomena:

i) The temperature dependence of T_1: during the THz irradiation, the sample is heated and its temperature rapidly jumps of several Kelvins. Since the T_1 of [VO(tpp)] drops on increasing temperature, a signal increase is observed.

ii) The THz-induced spin relaxation: this phonon-mediated process induces a further relaxation pathway of the spin state when the phonon is perturbed by

the THz radiation. The magnitude of this effect is smaller compared to that of the change in T_1, but it is clearly visible at 20 K (see Fig. 3.43).

While the former is a well-known effect, the latter is, for the best of our knowledge, unprecedented. The indispensable requirement of the resonance condition of the THz radiation with the phonon, as well as the linear behavior of the TR-THz-EPR signal intensity by varying the THz power, corroborate the hypothesis of a process mediated by the spin-phonon coupling.

At the state-of-the-art, this additional relaxation phenomenon is treated phenomenologically by introducing a relaxation term in the z-component of the magnetization of the Bloch equation.

Moreover, to confirm the phonon-mediated nature of such effect, other TR-THz-EPR experiments irradiating a different phonon with a different spin-phonon coupling as well as performed on other suitable compounds, are in progress to further elucidate the origin of the phenomenon. The choice of the next phonons to analise was aided by the simulated vibrational spectra and spin-phonon coupling patterns with the procedure outlined in Sec. 3.1, highlighting a second relevant feature of THz-IR spectrum of [VO(tpp)] at $\sim$160 cm^{-1} (Fig. 3.41).

The goal of my contribution to this study is to supply microscopic information through a simple *ab initio* model of the spin dynamics of Vanadium(IV)-based porphyrinic complexes, when a far infra red (Far-IR) source is irradiating the sample. A modelization of photon-phonon-spin interaction will permit to provide a theoretical support to the correlations between spin-relaxation and phonons evinced experimentally. This is expected to lead to a significant increase of our knowledge on the processes occurring in the solid state at the molecular scale, with potential consequences regarding the possibility to achieve new, better performing, molecular qubits, by structural and chemical modifications.

3.5.3 *Ab initio modelization*

The quantum dynamics (QD) of a spin system under THz radiation can be treated as a four-level system composed of two couples of states: a crystal ground state with up or down spin, $|0,\uparrow\rangle$, $|0,\downarrow\rangle$, and a neutral exciton with two spin states as well, $|1,\uparrow\rangle$, $|1,\uparrow\rangle$ (Fig. 3.44), assuming a direct coupling between the spin and the vibrational states.

The state of the spin system can be described in term of the spin density matrix, ρ, whose dynamics is regulated by the Liouville equation. The equation assumes the form $\dot{\rho} = -i[\mathscr{H}, \rho] \equiv \mathscr{L}\rho$ in the familiar Hamiltonian formalism, while it reads $d/dt\rho = \tilde{L}|\rho\rangle\rangle$ in the Fock Liouville space (FLS) [231, 232]. FLS is a linear space

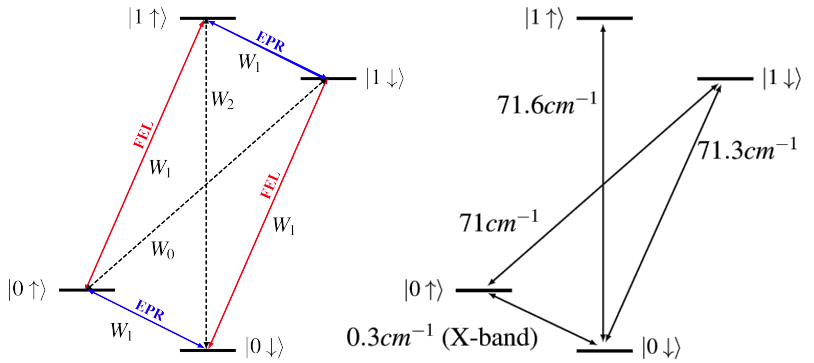

Figure 3.44: Schematic representation of the simple four level model adopted to reproduce the THz-induced signal measured.

of matrices, converting the matrices effectively into vectors ($\rho \rightarrow |\rho\rangle\rangle$), justifying the analogous form of Liouville equation in the FLS and Schrödinger equation in the wave function Hilbert space, $d/dt\,|\Psi(t)\rangle = -i\hbar\,|\Psi(t)\rangle$. More precisely, FLS is itself a Hilbert space of density matrices, i. e., the Liouvillian superoperator maps the element of density operator on a operator space, in analogy to Hamiltonian mapping the element of the wave function in a wave function space. The Liouville operator can be expressed in both wave function and density operator formalism thanks to the isomorphism of tetradics algebra to matrices algebra.

The FLS is the only one permitting a consistent treatment of the transition from a pure state into a mixture [233]. A further utility of the FLS is the extra compactness of the matrix representation of the evolution operator, offering a simple way to combine effects of relaxation and coherent evolution during the course of a single pulse or multipluse experiment.

The following approach consists in working on a truncated Liouvillian space, where the states considered are chosen among the ones deemed relevant (only four in the present case). The spin-phonon coupling model here accounts for one intervening vibration resonant with FEL radiation coupling to the $m_S = \pm 1/2$, sublevels of $S = 1/2$ spin. The Hamiltonian of the spin-phonon coupled system of a spin (S) with one vibration is composed of three terms representing the spin, $\mathscr{H}_S$, the phonons, $\mathscr{H}_{Ph}$, and the spin phonon coupling, $\mathscr{H}_{Sp-Ph}$ (Eq. 3.21).

$$\mathscr{H} = \mathscr{H}_{Ph} + \mathscr{H}_Z + \mathscr{H}_{Sp-Ph} = \tag{3.21}$$
$$= \sum_\alpha \hbar\omega_\alpha(n_\alpha + \frac{1}{2}) + \mu_B \mathbf{g}\cdot S_z \cdot B_z + \mu_B \left(\frac{\partial \mathbf{g}}{\partial q}\right) q \cdot \mathbf{S} \cdot B_z$$

The spin–phonon wavefunction can be expanded into a series of products as spin-sublevels and the vibrational function:

$$\Psi = |M_S\rangle \chi(q_\alpha) \tag{3.22}$$

Pure initial density operators may be constructed from their corresponding wavefunction. Thermal initial states can be constructed by a Boltzmann weighting of energy eigenstates. The Liouville operator is constituted by two perturbations, i. e., the continuous microwave field resonant with spin transition $\mathscr{H}_{MW-spin}$ and the pulsed THz field resonant with a vibrational transition $\mathscr{H}_{THz-phonon}$.

The $\mathscr{H}_{MW-spin}$ expression is the following:

$$\mathscr{H}_{MW-spin} = -\hat{\mathbf{m}}\cdot\hat{\mathbf{B}} = \tag{3.23}$$
$$= -\mu_B \cdot \mathbf{S}\cdot\mathbf{g}\cdot B_1 = -9.274\cdot 10^{-24}\frac{[J]}{[T]}\cdot 2\cdot\frac{1}{2}\cdot B_1[T]$$
$$\text{where } B_1[G] = C\frac{[G]}{[\sqrt{W}]}\cdot\sqrt{P[W]} \tag{3.24}$$

Where B_1 is the magnetic field component of MW in the cavity, $C = 4.2G/\sqrt{W}$ is the conversion factor specific for the cavity used in this experiment expressed in Gauss over square root of Watt, P is the power of MW. A conversion of $\mathscr{H}_{MW-spin}$ from Joule to cm^{-1} is reported in the chart of Fig. 3.49.

The $\mathscr{H}_{THz-ph}$ reads [182, 234]:

$$\mathscr{H}_{THz-ph} = \hbar g_{EM} \quad \text{with} \quad g_{EM} = \sqrt{\frac{\hbar\omega_{EM}}{2\varepsilon_0 V}}\frac{\vec{d}\cdot\vec{\varepsilon}_{EM}}{\hbar} = |\vec{E}_{EM}|\frac{\vec{d}\cdot\vec{\varepsilon}_{EM}}{\hbar} \tag{3.25}$$

where $|\vec{E}_{EM}|$ is the laser electric field amplitude. A rough estimation of this interaction was made of $\sim 10^{-2}$-10^{-3} cm^{-1}.

The laser electric field amplitude is calculated from instrumental parameters in the following way:

$$I = \frac{E_{EM}B_{EM}}{2\mu_0} \quad \text{with } c\cdot B_{EM} = E_{EM} \Rightarrow |E_{EM}| = \sqrt{\frac{2I}{c\varepsilon_0}} \tag{3.26}$$

where I is the intensity of the radiation, E_{EM} and B_{EM} are the electric and magnetic components of the radiation, c is the speed of light, μ_0 the magnetic permeability. To calculate the intensity I, the energy per pulse (E_p) is needed, obtained from the average power of each pulse ($P_{av} = 100W$) and the time rate of pulses ($R_{rate} = 1.8Hz$), and the peak power (P_{peak}), calculated from energy per pulse (E_p) and pulse duration (t_{pulse}):

$$E_p = \frac{P_{av}}{R_{rate}} = \frac{100[W]}{1.8[Hz]} = 55.56[J] \tag{3.27}$$

$$P_{peak} = \frac{E_p}{t_{pulse}} = \frac{55.56[J]}{3.5 \cdot 10^{-4}[s]} = 1.587 \cdot 10^5[W] \tag{3.28}$$

$$I = \frac{P_{peak}}{A} = \frac{1.587 \cdot 10^5}{0.000016} = 9.921 \frac{[GW]}{[m]^2} \tag{3.29}$$

$$|\vec{E}_{EM}| = \sqrt{\frac{2I}{c\varepsilon_0}} = \sqrt{\frac{2 \cdot 9.921 \cdot 10^9 \frac{[W]}{[m]^2}}{3 \cdot 10^8 \frac{m}{s} \cdot 8.85 \cdot 10^{-12} \frac{[C]^2}{[N][m]^2}}} =$$

$$= 1.933 \cdot 10^6 \frac{N}{C} \left(or \frac{[V]}{[m]} \right) \tag{3.30}$$

The electric dipole moment, $\vec{d} = \frac{\partial \vec{d}}{\partial q} q = 0.134822 \frac{[D]}{[m]}[m]$, is obtained in Debye/meter for the normal mode no. 23 with ω= 77.82 cm^{-1} from *ab initio* calculations. These parameters allow to compose the interaction as:

$$\mathscr{H}_{THz-ph} = |\vec{E}_{EM}| \cdot \vec{d} \cdot \vec{\varepsilon}_{EM} \tag{3.31}$$

$$= 1.933 \cdot 10^6 \cdot 3.336 \cdot 10^{-30} \cdot 0.1348 = 8.694 \cdot 10^{-25}[J] \tag{3.32}$$

$$= 4.47 \cdot 10^{-2}[\text{cm}^{-1}] \tag{3.33}$$

where $3.336 \cdot 10^{-30}$ is the conversion factor from $[D]$ to $[C] \cdot [m]$.

The time propagation consists of two main parts [95], namely the accumulation equation and the recursion relation. The former consists in the construction of the total Hamiltonian matrix and its diagonalization, giving an initial density matrix; the latter is the propagation of the generated matrix according to the scheme:

$$\rho(0) \xrightarrow{U_{MW}(\tau_1)} \rho(\tau_1) \xrightarrow{U_{MW+THz}} \rho(\tau_2) \xrightarrow{U_{MW}} \rho(\tau_3) \tag{3.34}$$

where $U_{MW}(t - t_0) = e^{\mathscr{H}_{MW}(t-t_0)}$ and $U_{THz}(t - t_0) = e^{\mathscr{H}_{THz-ph}(t-t_0)}$. This procedure is repeated for all time steps until the total propagation time is reached. In this simulation the MW field resonant with spin transition is always active, the THz pulse

is active in the timestep $\tau_1 < t < \tau_2$. For each physical system a characteristic time scale exists, of the order of ps for phonons and μs for spins. The total propagation time is estimated with regard to this time scale. As the density operator contains all dynamical information on the system, the time dependence of any observable of interest may be followed. The expectation value of the dynamical observable constituted by population difference between α and β spin states is accumulated, it is proportional to the experimental time resolved signal. The model is still in its infancy as several assumptions were made:

- Phenomenological values of T_1(T) were used both for phonons and spin to consider the relaxation of excited spin states. The phonon T_1(T) is fixed at 1 ps, while the electron spin T_1 included is a function that fits the T_1 values measured by pulsed EPR in Novosibirsk. At this stage of the modelization, a fitting expression with no physical insights would be enough to fit the measured T_1(T) values and include the temperature dependence in the simulation, as for instance $T_1^{-1}(T) = f + (g + h*T + i*T^2*)exp(-T/l)$ (Fig. 3.45). Nonetheless, an attempt to verify the models to fit T_1(T) introduced in Sec. 3.3

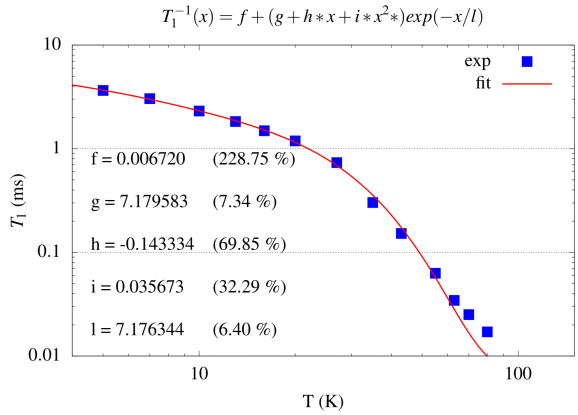

Figure 3.45: T_1 values from inversion recovery experiments (blue dots), and fit (red) with phenomenological function showed above the graph.

was made, giving promising results. As showed in Fig. 3.46 and Fig. 3.47, several fitting expressions were used:

$$T_1^{-1}(T) = a\frac{exp(b/k_BT)}{exp(b/k_BT)-1} + c\frac{exp(d/k_BT)}{(exp(d/k_BT)-1)^2} \tag{3.35}$$

$$T_1^{-1}(T) = a*T + c\frac{exp(d/k_BT)}{(exp(d/k_BT)-1)^2} \tag{3.36}$$

$$T_1^{-1}(T) = a\frac{exp(\hbar\omega_{X-band}/k_BT)}{exp(\hbar\omega_{X-band}/k_BT)-1} + c*V^{Sp-Ph}\frac{exp(\hbar\omega_\alpha/k_BT)}{(exp(\hbar\omega_\alpha/k_BT)-1)^2} \tag{3.37}$$

The first term of T_1 accounts for the direct one-phonon process, it is chosen as a local mode term [112] with an exponential function (Eq. 3.35 and Eq. 3.37) or with a linear temperature dependence (Eq. 3.36), as usually described [112]. The a parameter is a constant to rescale the interaction. The value of b parameter in Eq. 3.35 represents the EPR transition energy in X-band spectrometer, it is indeed fixed in Eq. 3.37 at $\hbar\omega_{X-band} = \sim 0.3\text{cm}^{-1}$. The second term accounts for two-phonons processes. The d parameter corresponds to the energy of the αth vibrational transition, $\Delta E = \hbar\omega_\alpha$; if it is a free parameter of the fit (Fig. 3.46(**b**,**d**)), it converges to the value of a normal mode of the [VO(tpp)] vibrational spectrum at $\sim$160cm^{-1} it is indeed fixed in (Fig. 3.46(**a**,**c**)) giving good fits. Furthermore, it is fixed in Eq. 3.37 to four transition energies of [VO(tpp)] vibrational spectrum (Fig. 3.47), to check whether other transitions could have a weight in the relaxation process. The best fits assign to this relaxation term a frequency near to the calculated phonon at 160 cm^{-1}. The c parameter, called in Sec. 3.3 a_{Ram} [196], is a magneto-elastic constant that rescales the summation over the normal modes. Here, only one phonon was included in the fit, bearing the highest calculated Sp-Ph coupling coefficient. As a future step, the simulated T_1(T) will be calculated from Sp-Ph coefficients by Alessandro Lunghi and inserted in the model.

- A phenomenological lowering of 10% of T_1(T) was imposed, when the THz pulse is active ($\tau_1 < t < \tau_2$).
- Phenomenological exponential dampings with characteristic times T_1^{Spin} and T_1^{Phonon} of states populations was included.
- So far the fields are considers as semi-classical i.e. no spontaneous emission is included.

- A temperature profile was imposed during the simulation. A linear raise and an exponential decay of temperature was set during and after the THz pulse, respectively. The raise of T due to THz pulse is estimated from saturation experiments (Fig. 3.48) as 14K. Intense THz radiation substantially heats the sample and increases the real temperature of the sample. The aim of experiments shown below was to compare the saturation curve under THz radiation and without it in order to estimate the real temperature of the sample. Other temperature dependence of signal decay were tested, the exponential dependence gave the best accordance with measured data. A more physical meaningful simulation can be performed using the specific heat, that is easy calculated parameter from the phononic structure of a crystal [235].

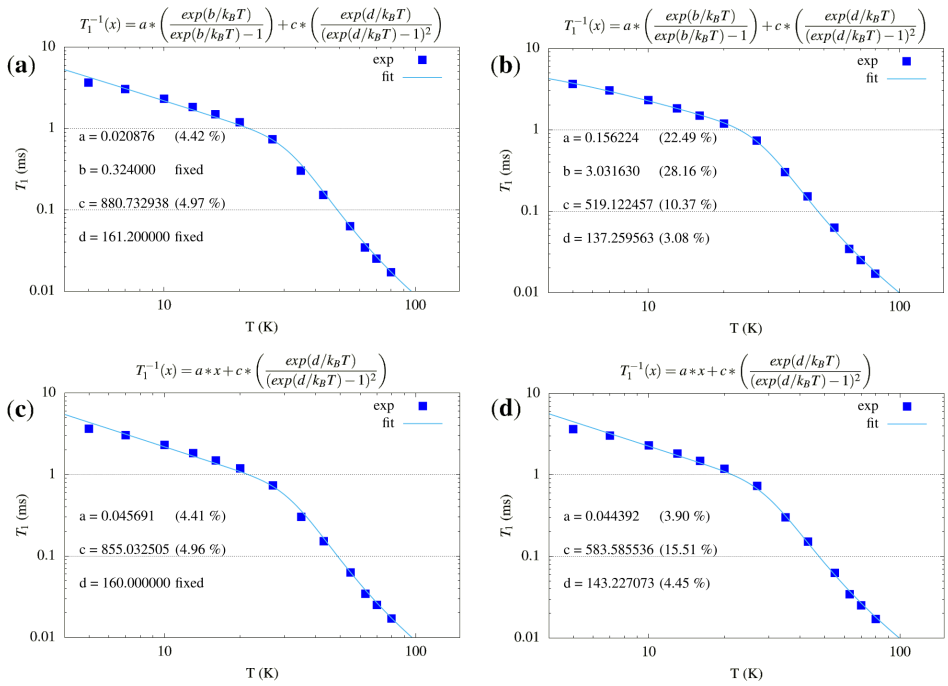

Figure 3.46: T_1 values from inversion recovery experiments (blue dots), and fit (cyan) with expression taking into account *direct* and *Raman* relaxation mechanisms (see Eq. 3.17). (**a**) Local-mode + Raman with fixed X-band and phonon energy (b and d parameters). (**b**) Local-mode + Raman with free fit parameters. (**c**) Linear + Raman with fixed phonon energy (d parameter). (**d**) Linear + Raman with free fit parameters. Each direct and Raman term is multiplied by a magneto-elastic scaling factor composed by a free fit parameter.

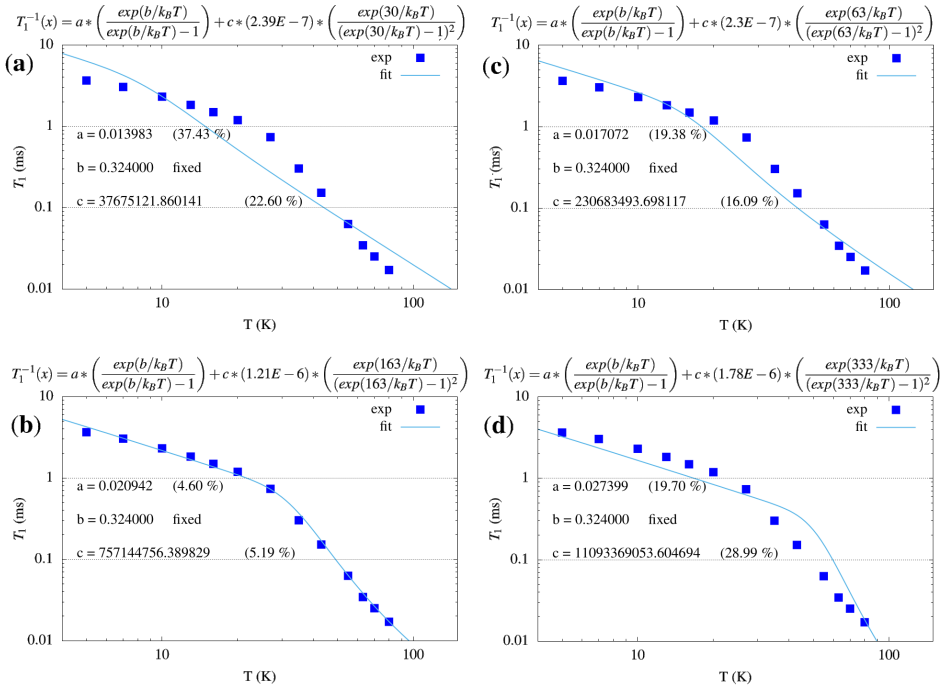

Figure 3.47: T_1 values from inversion recovery experiments (blue dots), and fit (cyan) with expression taking into account *direct* and *Raman* relaxation mechanisms (see Eq. 3.17). (**a**)-(**d**) Local-mode + Raman with fixed X-band energy (b parameter) and variable phonon energies. (**a**): 30 cm^{-1}. (**b**): 163 cm^{-1}. (**c**): 63 cm^{-1}. (**d**): 333 cm^{-1}. Each Raman term is multiplied by a magneto-elastic scaling factor composed by a free parameter and Sp-Ph coupling coefficient corresponding to each normal mode.

The first results, accomplished with our model show the dependence of spin dynamics on the MW-spin interaction Hamiltonian, $\mathscr{H}_{MW-spin} = -\hat{\mathbf{m}} \cdot \hat{\mathbf{B}}$, as a function of the MW power (Fig. 3.49(**a**)), and the comparison with experimental measurements (Fig. 3.49 (**b**)). The simple four-level model correctly reproduced the spin dynamics when MW power is raised, switching from a negative signal after THz pulse to a positive one, the extra signal measured experimentally when the specimen is irradiated with THz light was taken into account with a THz-dependent decrease of T_1.

The positive and negative kinetics, experimentally measured and simulated within the model presented, can be explained taking into account the combined effects of MW radiation and increase of temperature due to the THz pulse. Indeed, the temper-

ature increase determines two main effects: it modifies the Boltzmann populations and it changes the $T_1(T)$ relexation time. When the MW is not intense enough to saturate the EPR transition and, hence, a population difference between α and β states is still present, the temperature raise has, in this case, the predominant effect of redistributing particles according to Boltzmann distribution, lowering population difference. Contrarily, when the MW power is enough to equalize the populations, a temperature raise is not showing its effects on Boltzmann distribution of populations, but it is changing the T_1 that now promotes a more prominent relaxation from the excited state that turns out to increase population difference and, hence, the measured signal.

The great capabilities of such approach must be further developed, and, overcoming the phenomenological patches included at the moment, it will offer the possibility to investigate in a full *ab initio* framework such kind of experiment with the fine tuning of involved parameters. The inclusion of $T_1(T)$ dependence from *ab initio* spin dynamics is the next step, allowing to quantitatively estimate the relaxation effects of non-equilibrium phonon populations induced by THz pulses, and to take into account in parameter-free model the THz-dependent relaxation pathway. The calculated values, dependent on the specific Sp-Ph coupled normal mode irradiated, will be included in the four level model.

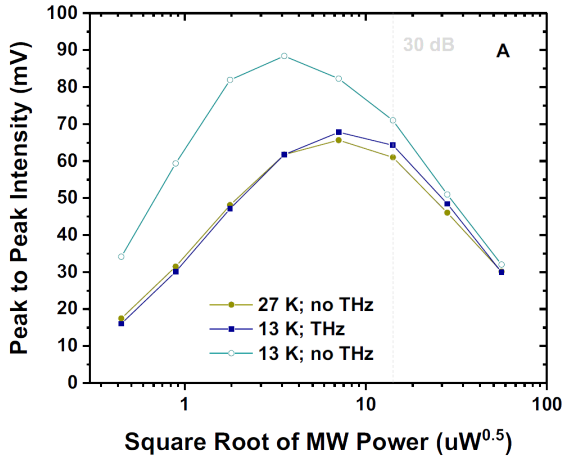

Figure 3.48: Comparison of saturation curves of [VO(tpp)]with (dark blue) and without (dark green - 27K, dark gray - 13 K) THz radiation. Cryostat temperature is 13 K, real sample temperature under THz radiation is 27 K (estimated at 60 dB).

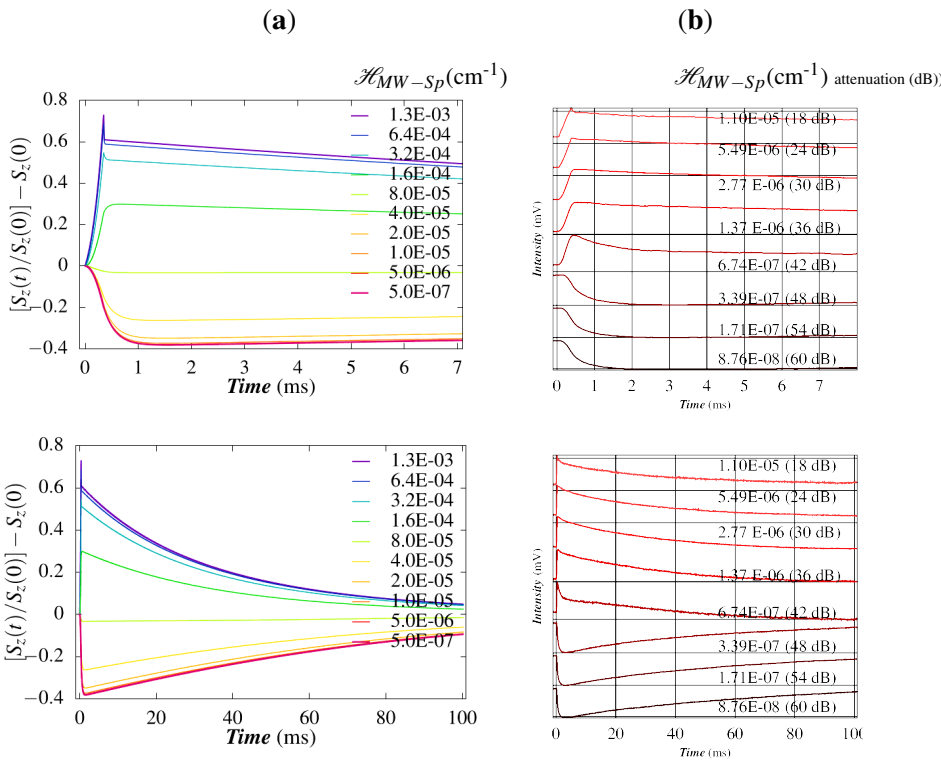

Figure 3.49: (**a**) Simulations using the model described above at different MW-spin interaction strength, fixed in the model to values between 1.3E-03 and 5.0E-07 cm^{-1}. (**b**) Experimental data at different MW power; the estimated value of $\mathscr{H}_{MW-Sp}$ is calculated by Eq. 3.23 reported in the chart, using different power attenuations, showed in dB in parentheses. MW power was changed from ∼3170 μW (18 dB) to ∼0.2 μW (60 dB) with the step of 6 dB, a decrease of 6dB attenuates the power to 1/4 of its value. Each subsequent spectrum is horizontally shifted. Top and bottom graphs show the same data at different time scales.

3.5.4 *Comparison of [VO(*tpp*)] and [Cu(*tpp*)] molecules*

The results obtained under THz irradiation of [VO(tpp)] were quite interesting, but they needed further investigations. The choice of a new system to pursue the same measurements would aid to dig into the chemical nature of spin relaxation, being the rationalization process corroborated by the simulated vibrational spectra and spin-phonon coupling patterns. The strategy adopted to choose a new system foresees the variation of only one feature of [VO(tpp)] to obtain a new chemical

species where the different behaviour can be mostly inherited to the modified feature. The VO^{2+} moiety coordinated to the tetrabenzotetraazaporphyrin macrocycle (tpp) was substituted with a Cu^{2+} ion. The following section collects some consideration about the metal center's role in affecting the relaxation properties, developed in parallel with the synthesis and characterization of other Cu-based systems presented in Sec. 3.3.

The vanadyl [175] or copper(II) [196] metal centers, coordinated to the tpp ligand, give rise respectively to C_{4v} and D_{4h} point group symmetry coordination compounds. The spin dynamics model assumed to define the Sp-Ph coupling coefficients is the aforementioned based on Redfield theory [151, 236]. We are, therefore, proceeding to investigation of their phononic structure and, subsequently, comparison of their Sp-Ph coupling coefficients.

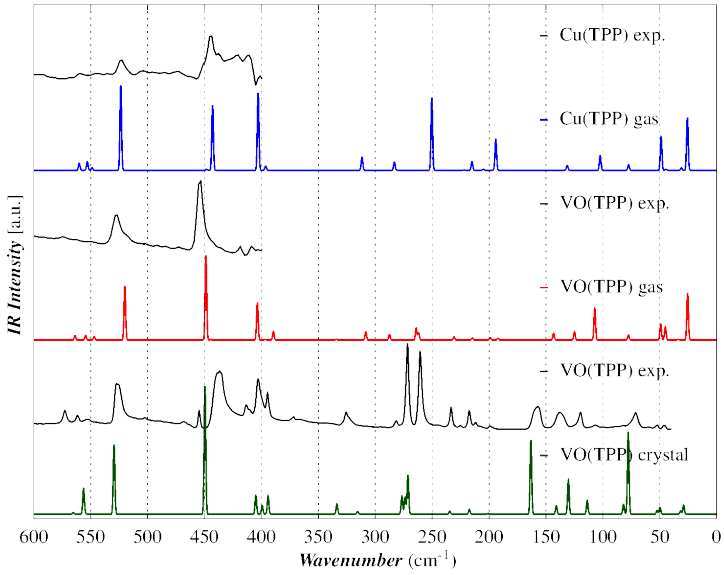

Figure 3.50: Top and mid panel: experimental FT-IR spectra (black) of [Cu(tpp)], [VO(tpp)] are reported together with the calculated ones resulting from gas phase *ab initio* calculations (blue and red) as function of wavenumbers (cm^{-1}). Bottom panel: experimental THz spectrum (black) of [VO(tpp)] together with the calculated one from unit cell *ab initio* calculations (green).

As depicted in Fig. 3.50, small differences can be noticed in the gas-phase calculated IR spectra of [VO(tpp)] (red) and [Cu(tpp)] (blue) molecules. The experimental FT-IR spectra (4000-400 cm^{-1}) are shown in comparison with the gas-phase calculations. The crystal calculation are made on a 1x1x1 unit cell containing two

molecules (Fig. 3.35). They are compared with THz spectra on the [VO(tpp)] crystal recorded by Sergey Veber and its collaborators at NovoFEL, as mentioned in Sec. 3.5.2.

We recall that the point-group is centrosymmetric for [Cu(tpp)] and non-centrosymmetric for [VO(tpp)]. For this reason in [Cu(tpp)] we have IR and Raman active modes as distinguished sets, while in [VO(tpp)] the parity selection rule is relaxed an the modes can be active in both Raman and IR.

An effect arising from crystalline environment is the shifts at higher energies of the localized vibrations that are still active in the gas-phase calculated spectra.

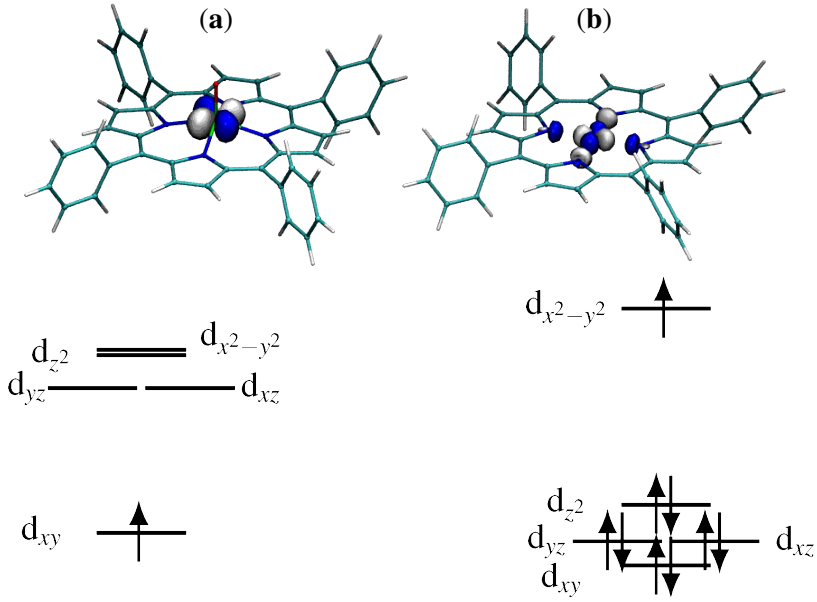

Figure 3.51: (**a**) [VO(tpp)] and (**b**) [Cu(tpp)] SOMO orbitals from DFT calculated UNO set, and ground state electronic configuration of d-shell orbitals.

The comparison of Sp-Ph patterns plot (Fig. 3.52) shows that [Cu(tpp)] has less normal modes coupled with the spin, due to the inversion center that forbids ungerade mode to couple.

In spite of fewer modes being coupled in [Cu(tpp)] than in [VO(tpp)], they bear a coupling one order of magnitude stronger. The normal modes showing the same irreducible representation of *d* orbitals are coupled with spin. *d* orbital reps. in D_{4h} are: A_{1g}, B_{1g}, B_{2g}, E_g. Ungerade mode have low couplings. *d* orbitals reps. in C_{4v} are: A_1, B_1, B_2, E. The selection rules on *g* and *u* are relaxed and all the E modes couple with spin. The coupling of E vibrations in C_{4v} is weaker than E_g vibrations in D_{4h}. Moving to the [VO(tpp)] gas and crystal phase comparison,

the coupling of a mode in the gas phase is spread onto several crystal modes. The irreducible representations of space groups are more complex to analyse, contrary to simple point-group representations for isolated molecules. Usually, looking at local atomic motions in Sp-Ph coupled crystal-phase modes, the same symmetries of first coordination shell perturbation of gas-phase Sp-Ph coupled modes is noticeable. In summary, the first coordination sphere is strongly perturbed only by gerade modes, as was recently pointed out [203]. The results (Fig. 3.52) show that the vibrational modes are coupled to spin depending on several features, connected to the metal substitution.

i) The spin-orbit coupling, peculiar of each element

ii) The coordination geometry of metal atom

iii) The symmetry group of the molecule and the space group of crystal

We want here to investigate if the difference of Sp-Ph coupling calculated can be ascribed to different overlap with ligand atoms (nitrogen) orbitals Fig. 3.51 with d_{xy} SOMO orbital of [VO(tpp)] and $d_{x^2-y^2}$ SOMO orbital of [Cu(tpp)].

Especially, in [Cu(tpp)] molecule, σ-type overlap is established between copper(II) and nitrogen. This is not true for [VO(tpp)], that has a π bonding with ligands. Hence, while distorting geometry, a larger overlap change is expected for [Cu(tpp)] with respect to [VO(tpp)], leading to a larger perturbation of the *g* tensor during normal vibration. Basis set and overlap matrices between *atomic* orbitals were printed with ORCA package. The basis set chosen for V, N and O atoms is polarized valence triple-zeta basis set, def2-TZVP, while polarized valence double-zeta basis set, def2-SVP, for C and H. Type V atoms have 17s11p7d1f orbital shells, contracted to 6s4p4d1f, while type N have 11s6p2d1f orbital shells contracted to 5s3p2d1f.

All the relevant overlaps involved in bonding between ground state SOMO and nitrogen orbitals are reported in Tab. 3.9 and Tab. 3.10. [VO(tpp)] orbitals are N**5s**, N**1p**$_x$, N**1p**$_y$, N**2p**$_x$, N**3p**$_x$, V**1d**$_{xy}$, V**2d**$_{xy}$, V**3d**$_{xy}$, V**4d**$_{xy}$, while [Cu(tpp)] orbitals are N**5s**, N**1p**$_x$, N**1p**$_y$, N**2p**$_y$, N**3p**$_y$, Cu**1d**$_{x^2-y^2}$, Cu**2d**$_{x^2-y^2}$, Cu**3d**$_{x^2-y^2}$, Cu**4d**$_{x^2-y^2}$.

Equilibrium geometry orbitals and orbitals from distorted geometry along one normal coordinate *q* (corresponding to the green geometry in Fig. 3.53) are reported. No SCF step was performed because only the atomic orbital overlap is here required. The distorted geometry was generated from the normal modes eigenvectors calculated on the isolated molecule in CP2K. A slightly the larger change of overlap in [Cu(tpp)] molecule can be noticed. The difference of overlap cannot be a standalone correlation to difference of Sp-Ph coupling.

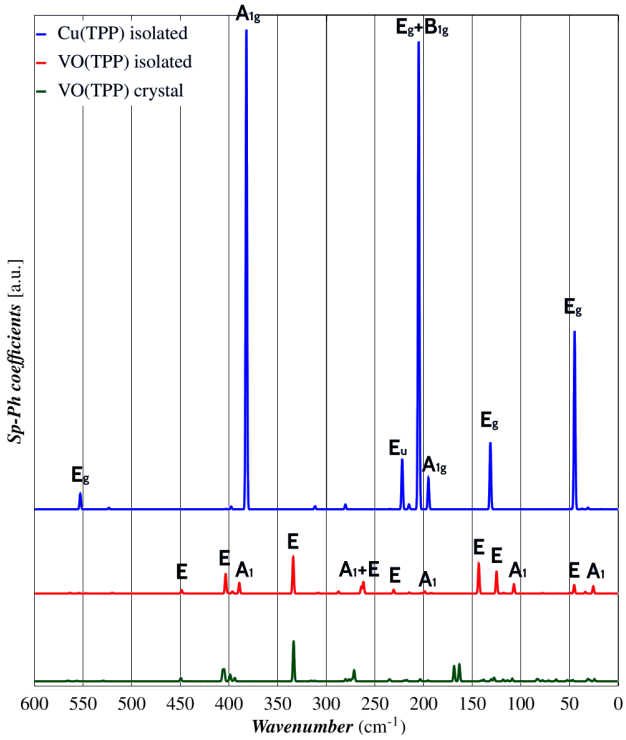

Figure 3.52: Comparison of Sp-Ph coupling coefficients of [Cu(tpp)] from gas phase calculations (blue), [VO(tpp)] from gas phase calculations (red), and [VO(tpp)] from unit cell calculations (green).

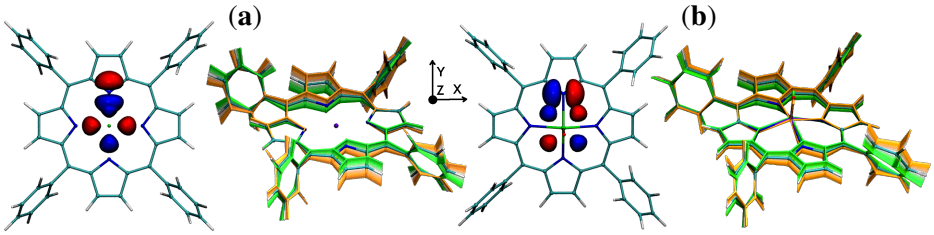

Figure 3.53: (**a**) π-type overlap of N_{2p_x} and $V_{3d_{xy}}$ atomic orbitals of [VO(tpp)](̇**b**) σ-type overlap of N_{2p_y} and $Cu_{3d_{x^2-y^2}}$ atomic orbitals of [Cu(tpp)]. The atomic orbitals are plotted with a 0.1 isovalue. The right panels show the geometric perturbations (green) used to calculate overlap differences.

Table 3.9: Overlap integrals of [VO(tpp)] isolated molecule.

			Equilibrium geometry					Distorted geometry				
			Nitrogen					Nitrogen				
	no.		49	51	52	54	57	49	51	52	54	57
		orb.	**5s**	**1p$_x$**	**1p$_y$**	**2p$_x$**	**3p$_x$**	**5s**	**1p$_x$**	**1p$_y$**	**2p$_x$**	**3p$_x$**
Vanadium	19	**1d$_{xy}$**	0	0.000500	0	0.005002	0.017000	-0.000406	-0.000240	0.013922	0.004324	0.016247
	24	**2d$_{xy}$**	0	0.005929	0	0.054683	0.111013	-0.002633	0.004987	0.000976	0.049165	0.105553
	29	**3d$_{xy}$**	0	0.073300	0	0.252219	0.396223	-0.009566	0.068061	0.004999	0.237935	0.382057
	37	**4d$_{xy}$**	0	0.078715	0	0.280234	0.571517	-0.014267	0.076580	0.001214	0.273299	0.560178

Difference of Equilibrium and Distorted geometries

			Nitrogen				
	no.		49	51	52	54	57
		orb.	**5s**	**1p$_x$**	**1p$_y$**	**2p$_x$**	**3p$_x$**
Vanadium	19	**1d$_{xy}$**	0.000406	0.000740	-0.013922	0.000678	0.000753
	24	**2d$_{xy}$**	0.002633	0.000942	-0.000976	0.005518	0.00546
	29	**3d$_{xy}$**	0.009566	0.005239	-0.004999	0.014284	0.014166
	37	**3d$_{xy}$**	0.014267	0.002135	-0.001214	0.006935	0.011339

Table 3.10: Overlap integrals of [Cu(tpp)] isolated molecule.

			Equilibrium geometry					Distorted geometry				
			Nitrogen					Nitrogen				
	no.		49	51	52	55	58	49	51	52	55	58
		orb.	**5s**	**1p$_x$**	**1p$_y$**	**2p$_y$**	**3p$_y$**	**5s**	**1p$_x$**	**1p$_y$**	**2p$_y$**	**3p$_y$**
Vanadium	18	**1d$_{x^2-y^2}$**	-0.005184	0	-0.000090	0.009393	0.007321	-0.004817	0	0.000057	0.007666	0.006762
	23	**2d$_{x^2-y^2}$**	-0.041132	0	-0.009144	0.086483	0.047785	-0.038456	0.000021	0.006812	0.073538	0.044412
	28	**3d$_{x^2-y^2}$**	-0.205954	0	0.124628	0.288104	0.113570	-0.195439	0.000468	0.109285	0.261554	0.106966
	36	**4d$_{x^2-y^2}$**	-0.420759	0	0.015489	0.009778	-0.131494	-0.408077	0.000456	0.014608	0.008720	-0.128454

Difference of Equilibrium and Distorted geometries

			Nitrogen				
	no.		49	51	52	55	58
		orb.	**5s**	**1p$_x$**	**1p$_y$**	**2p$_x$**	**3p$_x$**
Copper	18	**1d$_{x^2-y^2}$**	-0.000367	0	-0.000147	0.001727	0.000559
	23	**2d$_{x^2-y^2}$**	-0.002676	-0.000021	0.015956	0.012945	0.003373
	28	**3d$_{x^2-y^2}$**	-0.010515	0.000468	0.015343	0.026550	0.006604
	36	**4d$_{x^2-y^2}$**	0.012682	0.000456	0.000881	0.001058	0.003040

3.6 CONCLUSIONS

This studies meant to give a rationalization of the origin of the relaxation processes that act at microscopic level on the spin states of molecular systems. Vandium(IV)- and Copper(II)-based mononuclear molecules have been at the center of the investigation due to the wide interest they have recently captured. One of the possible sources of relaxation, represented by interaction of the spin with the lattice environment, has been here addressed by means of DFT and postHF calculations. A practical way to calculate the vibrational spectra in the condensed phase at the DFT level has been set up, evaluating the best strategy in the description of the complex molecular crystals under analysis. Such kind of crystals require a close estimate of the long range inductive and dispersive interactions, their effects must be described through a fine tuning of van-der-Waals correction. The aim is the correct framing for the study of low temperature regime dynamics, driven by the first vibrational modes, primarly determined by the intermolecular interaction. The proposed case studies make possible to push beyond the investigation on the correlation between electronic structure and relaxation rates inside a S=1/2 family of molecules, lacking of stronger sources of relaxation, usually predominant in other paramagnetic complexes.

The analysis of vibrational properties was approached with the aim of disentangling the lattice dynamics from the molecular dynamics. This treatment is supposed to highlight how the molecule changes its own behaviour when the effect of environment is taken into account. Hence, separate contributions to spin-phonon coupling coefficients, arising from separate degrees of freedom, can also be computed by simply adopting the projection on specific displacements $\mathbf{q}$. This last step can be taken as many times as one wants as there are no additional computational costs beyond the already done calculations of phonons and spin-phonon coupling coefficients. Analysis of the derivatives of the g tensors highlights the importance of several factors, both intrinsic and extrinsic. Intrinsic effects are due to the chemical nature of the first coordination shell, and extrinsic effects are related to the lattice environment and how it affects the fine structure of the first coordination shell and the vibrational properties. These extrinsic factors can be tuned following two possible strategies: by stiffening the metal-ligand bonds and by tailoring supramolecular structures to modify vibrational energies and shift the phonon spectrum at higher frequencies.

The spin-phonon coupling depends dramatically on intrinsic molecular features, such as the coordination geometry and ligand-field strength. The sensitivity of the spin-phonon coupling on such structural features makes the design of new ligands able to stabilize specific electronic ground states. However, the average magnitude of the spin-phonon coupling has been found to correlate with spectroscopically accessible physical quantities such as the static g shift (from EPR) and the energy of

the first excited electronic state (from electronic absorption). This suggests a "rule of thumb" to experimentally assess the potential of a magnetic molecule to function as a qubit.

A deeper undestanding of the role that the symmetry plays in spin-phonon coupling was then accomplished to figure out the active mechanisms at the microscopic level. This was highlighted by *ab initio* calculations, confirming the pivotal role played by the low-energy vibrational modes at around 57 cm^{-1} for Cu based compounds. Furthermore, vibrational modes with gerade symmetry are the most coupled modes, describing the crucial role played by the symmetry of vibrations. In such cases, Raman spectroscopy in the terahertz regime, more demanding than absorption measurements, appears to be necessary for a complete experimental characterization of the vibrational properties of relevance for the spin dynamics of centrosymmetric 3d-metal complexes.

In this framework, the harmonic approximation of molecular vibrations is highly valuable for interpretation of the main features of the vibrational spectra but it cannot explain all their fine structures, which depend on the temperature. At finite temperatures, anharmonic motions of the molecules must be considered since they allow for the possibility of interactions among the harmonic phonons, resulting in slight changes in the energy and composition of characteristic vibrations. The most straightforward parameters to be considered as modified by anharmonicity turned to be the crystal cell parameters. The presented results can have a general relevance regarding the calculation of the T_1 values. Indeed, even if significant results have been recently achieved in its computation at the *ab initio* level, the T_1 temperature dependence has been until now only explicit in the phonon thermal distribution, keeping the Sp-Ph coupling as temperature-independent. However, our calculations suggest that even though the computed Sp-Ph coupling variations are small, the overall calculated variation becomes mandatory for a more rigorous reproduction of T_1 along a wide temperature range.

The results of these studies represent further pieces of the puzzle of the role played by vibrations in determining the relaxation properties of potential molecular qubits at the quantitative level. In particular, the deeper knowledge of the Sp-Ph coupling might allow one to exploit phonons for the accurate control, e.g., initialization and readout of the qubits. This can, for instance, be performed by using THz pulses by means of time resolved ultrafast spectroscopy.

4

CHEMISTRY AND MAGNETISM OF GRAPHENE DERIVATIVES

Manuscript in preparation:

Are stable magnetic graphene derivatives attainable?

Andrea Albino, Francesco Buonocore, Massimo Celino, Roberta Sessoli, Federico Totti

4.1 SPINTRONICS

Spintronics, or spin electronics, involves the study of active control and manipulation of spin degrees of freedom in solid-state systems [237–239].

The primary focus in this field is the study of basic physical principles underlying the generation of spin-polarized currents in semiconductors and metals. Generation of spin polarization, that is, nonequilibrium spin population, can be achieved by electrical spin injection or by optical techniques in which circularly polarized photons transfer their angular momenta to electrons. In electrical spin injection, more desiderable for device implementation, a magnetic electrode is connected to the sample. When the current drives spin-polarized electrons from the electrode to the sample, nonequilibrium spin accumulates there. The rate of spin accumulation depends on spin relaxation, i. e., the non-reversible process of bringing the accumulated spin population back to equilibrium. The goal of spintronics is to understand the interaction between the particle's spin and its solid-state environments and to make useful devices.

Spintronic devices are playing an important role for various applications including magnetic field sensors and memory devices [240]. The prototypical kind of device is the spin valve, the term coined in 1991 by Dieny [241]. Its spintronics effect arises due to the parallel or antiparallel alignment of magnetizations of the ferromagnetic (FM) electrodes separated with an interposed spacing layer [242]. The purpose

of interlayer is to decouple the two FM layers and it could be any non-magnetic semiconductor material. Both inorganic and organic semiconductor (OSC) materials were studied as spacer layer [243, 244]. The current across the device is measured as a function of a magnetic field and changes as the mutual orientation of the electrodes' magnetizations is reversed. The materials' interfaces play a crucial role in efficiency of spin injection and the research is directed towards the engineering the properties and performance of spin-devices also at the molecular level [245]. For such a reason, the changes of physical properties of both the metal and organic molecule at the interface have attracted great scientific interests, in particular towards the study of hybrid interfacial states ("spinterface science") [246]. Indeed, spin-filtered currents in spin valves are caused by the spin-dependent hybridization of the organic and metallic orbitals, leading to different interfacial broadening (and hence transmissivity) of the localized organic states for the two spin channels.

4.2 ENGINEERING PROPERTIES OF GRAPHENE

Graphene, hereafter called G-ene for brevity, is an ideal candidate material for spintronics due to its layer structure, weak spin–orbit coupling that facilitates spin transport and modulation of electrical properties. For this reasons, a wide variety of novel devices were set up, whose principal component is a graphene-based heterostructure [245, 247–251]. G-ene is a two-dimensional (2D) allotrope of carbon isolated for the first time in 2004 by mechanical exfoliation of pyrolytic graphite [252]. Chemical vapor deposition (CVD) technique is today the most widely used because it allows to achieve large scale production [253].

One of the most interesting aspects of the G-ene system is that its low-energy excitations are massless, chiral, Dirac fermions [145, 249]. Dirac fermions behave in unusual ways when compared to ordinary electrons if subjected to magnetic fields, leading to new physical phenomena such as the anomalous integer quantum Hall effect (IQHE) which was measured experimentally [254, 255].

G-ene should also present unusual mesoscopic effects [256]. These effects have their origin in the boundary conditions required for the wave functions in mesoscopic samples with various types of edges G-ene can have. The most studied edges, zigzag and armchair, have drastically different electronic properties. Zigzag edges can sustain edge (surface) states and resonances that are not present in the armchair case.

The use of G-ene for applications in electronics suffers from a major drawback: graphene is, in its pristine state, a zero-band-gap semiconductor [254], as pointed out in 1947 by Wallace [257]. To use G-ene in possible applications such as pho-

todetector, photovoltaics, sensors, organic light-emitting diodes, organic thinfilm transistors, supercapacitor, and catalytic applications, it is essential to precisely modulate its electronic properties. The defining concept for semiconductor materials for such applications is indeed the presence of a band gap for the essential controlling of the conductivity by electronic means.

Several ways have been explored to induce a finite band gap in G-ene. It was found experimentally that a band gap can be opened by confinement effects of electrons in graphene nanoribbons [258], or by applying a potential difference over a graphene bilayer [259].

A different route is by modifying the pristine G-ene at the chemical level, opening a challenging playground for chemists [260–262]. The resilient C–C bonds allow chemical modification of G-ene without breaking the structure, offering the possibility to synthesize different substrates from the same starting material. Functionalization can be categorized into two types, non-covalent (dominated by van der Waals forces) and covalent.

From a fundamental scientific and technological standpoint, also the idea of making G-ene magnetic has attracted interest [263]. Indeed, making G-ene magnetic could lead to high-Curie-temperature diluted magnetism and, ultimately, thin, two-dimensional (2D) magnetic materials, which could match the demands of ever increasing magnetic information storage density. However, in the absence of d or f electrons, the production of magnetic moments is not trivial. Basically, magnetism in G-ene can be introduced by using zigzag nanoribbons (ZGNR) or by including efficient spin injection into G-ene or defects. In the latter case magnetic moments can be induced by chemical modifications using adatoms or vacancy defects. Nonetheless, there is still much work to be done to develop more efficient synthesis schemes oriented to the growth of chemical modified graphene (CMG). The goal is obtaining perfect control of the geometrical features and of the selectivity of functional groups [264].

With the aid of combined atomic and magnetic force microscopy, it could be proven that the attached moieties are located in randomly dispersed regions. This lack of a periodic functionalization pattern of the G-ene sheet prevents the achievement of long range ferromagnetic order, thus limiting the use of such samples in spintronic devices [265].

Hydrogenation of G-ene is an attractive solution and it is foreseen to open a band gap [266] and to produce a magnetic behavior [267].

The question of inducing magnetic ordering, or just magnetic moments as a first step, is of vital importance. The hope is to develop new physical properties by introducing exchange fields and spin–orbit coupling in G-ene by adatom doping and/or overlayer growth, to achieve tunable magnetism that could be changed by gating,

doping or functionalization [268]. Notably, the above-mentioned properties are highly dependent on the hydrogenation degree, while hydrogenation is a reversible process. In this light, hydrogenated G-ene will undoubtedly become a prominent two-dimensional nanomaterial with finely controlled properties [269, 270]

The full-hydrogenated derivative $(C_1H_1)_n$, or graphane (G-ane) can be difficult to achieve at the experimental level while partially hydrogenated scenarios can be much easier obtained. Experimental and theoretical characterizations show that in G-ane covalent bonds with hydrogen atoms above and beneath the carbon plane are formed. G-ane was experimentally ascertained [271–274] and theoretically predicted [275, 276]. It shows covalent bonds with hydrogen atoms above and beneath the carbon plane. though most of the studies just led to partially hydrogenation. To date, various isomers have been reported for graphane structures, such as boat and chair [269, 277, 278], with the latter as the most energetically favorable one. Though different isomers of G-ane possess different atomic structures, some common characteristics can still be observed (Tab. 4.1). However, no magnetic properties have been observed for fully hydrogenated G-ane as confirmed at the computational level, too.

Conversely, partial hydrogenation, occurred as a misstep of full-hydrogenation process [278], or obtained by electron-beam lithography techniques [272], showed several theoretical [279, 280] and experimental [267, 281] evidences that, along with the opening of a band gap, as in G-ane, a magnetic moment can be induced for low hydrogenation incidence. Partial hydrogenation of G-ene can likely lead to the formation of islands of G-ane diluted in a G-ene matrix. In this case some magnetic impurities were observed. However, the amount of magnetic moment introduced is limited to fractions of μ_B per single unprotonated sp^2 C atom [267, 281–283].

Potentially attractive turns out to be the particular case of the half-hydrogenated G-ene (empirical formula, C_2H), discussed hereafter, called graphone (G-one) (Fig. 4.1 (**d-e**)). Its attractiveness is due to the fact that one isomer of it can potentially show an ordered magnetic behavior. Indeed, a comprehensive investigation of G-one isomers showed that only the chair one (Fig. 4.1 (**d**)) is found to be ferromagnetic [284] with ca 1 μ_B per sp^2 C atom. Unfortunately, the chair conformation is not the most stable. The boat one (Fig. 4.1 (**e**)), showing diamagnetic behaviour, is indeed several atomic units energetically more stable. The stabilization of the chair vs. boat configuration by G-ene fluorination was studied both at the experimental [285] and theoretical level [286]. The literature on G-ene derivatives is usually restricted to one single structure or to the G-one conformational space, or G-ane's [287, 288], separately. The lack of a transversal analysis between G-one and G-ane structures, both as infinite periodic systems or as a local environment at interfaces, motivates us to enlarge the energy stability and magnetic analysis to a wider range of G-ene derivatives. More experimentally affordable non-periodic structures are evaluated

to engineer the material for maximization of spin density per unit area. In such a framework, this computational study aims at examining structural and magnetic properties of CMG graphene across its conformational space when covalently functionalized by hydrogenation or fluorination at different stoichiometry, C_nH and C_nF, respectively. In particular, a comprehensive conformational analysis filling the gaps present in the literature will be performed. Different hydrogenation (fluorination) percentages were also considered to verify their influence on the number of magnetic moments introduced and to monitor the relative energy variation between the different conformations. Stacking effects on a layer of G-ene and covalent ones on a surface of unreconstructed Au(111) substrate were also investigated as possible driving forces towards the stable ferromagnetic state of G-ene derivatives. An alternative creation and stabilization route for magnetic moments in G-ane/G-one derivatives in a G-ene matrix will be extensively investigated, too. In this regard, size and shape of in silico designed G-ane islands and ribbons embedded in G-ene matrix will be considered.

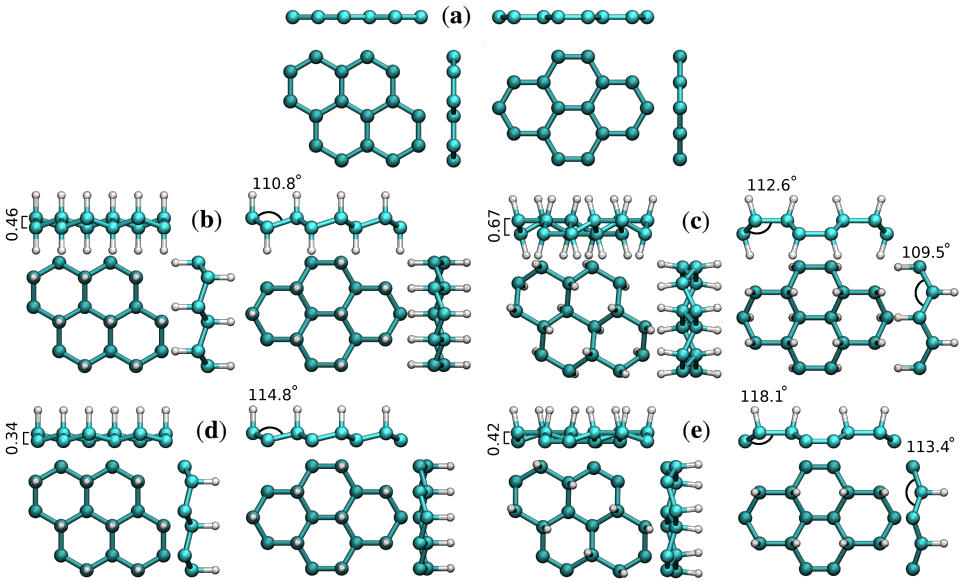

Figure 4.1: Side and top views of G-ene, G-ane and G-one structures in the isolated phase. (**a**) pristine G-ene. (**b**) chair G-ane. (**c**) boat G-ane. (**d**) chair G-one. (**e**) boat G-one.

4.3 METHODS

Modeling large systems in a more realistic environment in an ab initio computational framework has become possible only in the past few years thanks to overall progress of both computational resources and theoretical approaches, enabling extensive work on more and more complex systems comprising hundreds of atoms in one unit cell [289]. The modeling of surfaces through slabs within PBC showed to be mandatory to have a reliable picture of the substrate@adsorbate scenarios [290]. The packages of software CP2K were used for the periodic DFT calculations [161]. Calculation of energy and forces were performed by direct diagonalization using the Quickstep module [160, 162]. GTH pseudopotentials [163–165] for the core electrons and valence pseudo-wavefunctions are expanded in Gaussian-type orbitals and the density is represented in a plane wave auxiliary basis set (GPW) to achieve the efficient calculations of very large condensed systems. In particular, for Au, C and H elements DZVP-MOLOPT-SR-GTH basis sets were used. The revised Perdew-Burke-Ernzerhof (revPBE) functional [166, 291] was chosen for the calculation. The rVV10 non-local dispersion corrections [292] were also included. The Conjugate Gradient [173] minimizing procedure was employed to carry out the structure optimization. The convergence of the plane waves basis cut-off was reached for 500 Ry with a convergence threshold of $1 \cdot 10^{-7}$ a.u. for the SCF energy and $4.5 \cdot 10^{-4}$ a.u./Å for the forces. The uncommon high plane-waves cut-off was chosen for these systems to gain a level of precision mandatory for the study of magnetic properties [293].

4.3.1 *Supercell Choice*

Only Γ-point calculations were carried out [294, 295]. The correct accounting of the symmetry and number of k-point were assured by the choice of an adequate number of G-ene unit cells to build up the supercell by using comparing the computed electronic structure with the ones reported in literature (see Results section) [156]. In this regard, supercells were generated by constructing a $n \times n$ array of copies of the two-atoms non primitive hexagonal unit cell of the G-ene structure, with $n = 12, 14, 16$. The correct Electronic Density of States was achieved for $n = 16$.

However, being the study of hydrogenated and fluorinated G-ene derivatives the aim of the paper, and in particular, their applicative usage (i.e, their adsorption on a surface), the dimensions of the G-ene supercells used throughout this paper must also consider the presence of the Au(111) surface. In this regard, the number of 16 non-primitive hexagonal unit cells was also found to have the best matching between the

gold and G-ene supercells dimensions (vide infra). A "perfect" match is mandatory to avoid biased interaction with substrate and consequently significant artificial stretching or compression of the two lattices. Therefore, an Au(111) slab of four layers containing 768 gold atoms (each slab contains 192 atoms) was fully optimized (atomic positions and cell parameters). The optimized Au cell parameter measures 2.498 Å. Therefore, the G-ene, the 50% G-one, and 100% hydrogenated derivative cells measure $39.962 \times 39.962 \times 70.000$ Å. The structural and cell parameters are reported in Tab. 4.1. A further important issue is the avoiding of the replica interactions along the z direction: to minimize this spurious contribution to the energy, the finite vacuum layer thickness was here set to 70 Å.

All the G-ene, G-ane, and G-one supercells were also relaxed to check the error introduced by constraining their cells to the gold parameter for the subsequent simulations. Computed lattice parameters *a* and *b* are 2.470/2.470 Å for G-ene vs an experimental value of 2.46 Å [257]); 2.537/2.537 Å for chair G-one; 2.542/2.542 Å for chair G-ane; 2.568/2.589 Å for boat G-one, 2.585/2.496 Å for boat G-ane. Therefore, the above-mentioned constraining introduced an error of $\sim$1% for chair structures and $\sim$4% for boat structures. However, being the latter diamagnetic, only chair structures will be of interest for this study making the error more than tolerable.

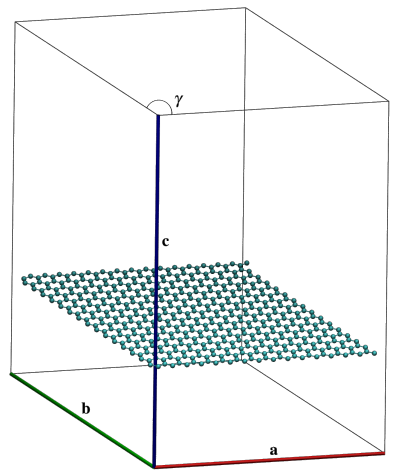

Figure 4.2: Graphene supercell containing 512 C atoms built for simulation of hydrogentation and adsorption on Au(111). **a** = 39.962 Å, **b** = 39.962 Å, **c**= 70.000 Å.

4.3.2 *Broken-Simmetry state calculations for exchange coupling estimation*

In the broken-symmetry, BS, formalism [296], which is commonly utilized for quantitative estimates of exchange-coupling constants in polynuclear transition metal complexes, a one-to-one correspondence is established between the energy of a Slater determinant built up with orbitals localized on different centers and bearing electrons with opposite spin computed and the energy of a microstate with $m_S = 0$ computed using the effective Heisenberg-Dirac-Vleck spin Hamiltonian.

$$\mathscr{H}_{HDvV} = J\mathbf{S}_1 \cdot \mathbf{S}_2 \tag{4.1}$$

where J is related to the multiplet energy splitting according to

$$J = \frac{E(S) - E(S-1)}{S} \tag{4.2}$$

In Eq. 4.2, $E(S)$ represents the energy of a state with total spin S. J is the magnetic exchange-coupling constant, and Eq. 4.1 is often used to reproduce experimental data. In the case of negative J, the antiferromagnetic (AF) state is the ground state; in the case of positive J, the ferromagnetic (FM) state is the fundamental one. The energy of the BS state for a binuclear system with spin $S_1 = S_2$ is a weighted average of the energies of pure-spin multiplets, and J may be calculated using the equation:

$$J = \frac{E(S_1 + S_2) - E(BS)}{2S_1S_2} \tag{4.3}$$

where $E(BS)$ is the energy of the broken-symmetry determinant [297, 298]. The term BS state means that a localized solution of the spin states is usually obtained by using an electronic symmetry lower than the actual geometric symmetry. In the present work, the G-one system contains 256 unsaturated radical carbon atoms and hence the high spin (HS) solution with total energy $E(S_{max})$ was calculated from a ferromagnetically coupled system with $S_{max} = 128$ and multiplicity $(2S+1) = 257$, while the BS solution, with total energy $E(BS)$, was calculated from the singlet state with $m_S = 0$. The generalization for arbitrarily large clusters is given by the formula [299]:

$$\Delta E(S_{max} - S) = \sum_{i<j} J_{ij}(2|s_i s_j| + s_j)\lambda_{ij} \quad (s_i \geq s_j) \tag{4.4}$$

where $\lambda_{ij} = 0$ if s_i and s_j have the same sign in $|s\rangle$ and 1 otherwise. The J_{ij} matrix has, in G-one system, equal values for all the possible pairs of spins, and hence it can be taken out the summation as a scalar constant. Due to the high symmetry of this system, the calculation of only two determinants' energies is required. The left hand side of Eq. 4.4 is the energy differences between the HS and the BS states, with the appropriate values of s and λ it yields all the equations needed to compute the J values.

4.4 RESULTS AND DISCUSSIONS

4.4.1 *Tuning Method*

4.4.1.1 *Graphene*

The reliability of a proposed computational protocol is based on the accurate reproduction of the available observables. In consideration of the fact that most of the systems considered in this work do not have or have a limited number of experimental data to be compared to, it is of basic importance to test our computational protocol on similar systems where there is an abundance of them. For such a reason, our reference calculations were performed on one layer of pristine G-ene through a Γ-point supercell approach. It is worth mentioning that the supercell dimensions have been chosen as the ones obtained by a supercell optimization of a four layers slab of Au(111) for a total of 768 Au atoms (see Methods). Notwithstanding the expected mismatch between the two lattices, an error of only 1.5% with respect to the experimental values was computed both for the G-ene lattice parameter and C–C distance (Tab. 4.1). Our GPW protocol has also shown to be consistent with different methods ranging from pure plane waves (PW) to pure Gaussian (G) basis sets. The correct degree of sp^2 hybridization is confirmed.

The correct description of the electronic structure, i.e., the semiconductor character with the presence of the Dirac's cone at the Fermi energy, was reached varying the supercell dimension up to 16×16 (see the Methods section), confirming the correct accounting for the needed **k** points to obtain the correct dispersion of G-ene electronic wavefunctions. The calculated Density of States of the different cells, and the DOS from tight binding approximation [303], are presented in Fig. 4.3: the 12×12 presents a maximum at the Fermi energy and so it not is reproducing the Dirac cones; the 14×14 and 16×16 have instead quite similar features, with a minima at 0 eV and two specular maxima. For the 14×14, however, the DOS shows only two maximum. Clearly, among the proposed cells, the 16×16 supercell presents features more similar to the expected ones and it can be considered the best

Table 4.1: Comparison of G-ene, G-one, and G-ane calculated structural parameters with previous calculation avaliable in literature, experimental data are reported for G-ene. The shaded rows indicate the calculation obtained in this work.

System	Package	Functional	vdW	Basis set	Lattice par. a	C–C (Å)	Δz (Å)	C–H (Å)	Refs.
G-ene	exp.	-	-	-	2.46	1.42	0	-	[257]
G-ene	TAPP	PW91	off	PW	2.44	1.41	0	-	
G-ene	CP2K	revPBE	rVV10	GPW	2.497	1.442	0	-	this work
G-one Chair	VASP	PBE	off	PW	-	1.495	0.322	1.157	[284]
G-one Chair	CASTEP	PBE	off	PW	-	1.495	-	1.140	[280]
G-one Chair	SIESTA	PBE	off	G	2.46	1.495	0.322	1.157	[300]
G-one Chair	Q-ESPRESSO	PBE	Dft-D	PW	2.516	1.49	0.33	1.16	[279]
G-one Chair	Q-ESPRESSO	PBE	off	PW	-	1.45	-	1.17	[301]
G-one Chair	CP2K	revPBE	rVV10	GPW	2.497	1.483	0.268-0.374	1.145	this work
G-one Boat	CASTEP	PBE	off	PW	2.319-2.030- 2.524	-	0.39	1.133	[280]
G-one Boat	CP2K	revPBE	rVV10	GPW	2.498-2.444- 2.622	1.563-1.494-1.354	0.419	1.124	this work
G-ane Chair	TAPP	PW91	off	PW	2.51	1.52	0.45	1.12	[302]
G-ane Chair	CASTEP	PBE	off	PW	2.516	1.52	-	1.11	[276]
G-ane Chair	CP2K	revPBE	rVV10	GPW	2.497	1.517	0.400-0.521	1.107	this work
G-ane Boat	CASTEP	PBE	off	PW	2.505	1.52-1.56	-	1.10	[276]
G-ane Boat	CP2K	PBE	rVV10	GPW	2.496- 2.585	1.528-1.577	0.657-0.693	1.102	this work

system to model a sheet of G-ene. As underlined also by the differences between 14×14 and 16×16, if an even larger cell was considered, the DOS would converge towards the desired features, but then the supercell would become too expensive in terms of computational resources. Anyhow, the accordance with DOS calculated with other models is satisfactory and we can be confident that electronic structure is correctly reproduced. Such results represent a robust starting point for a detailed study on hydrogenated and fluorinated G-ene derivatives.

4.4.1.2 *Hydrogenation*

The hydrogenation and fluorination of G-ene have been also widely studied in the literature [284, 286, 300, 304, 305] and, therefore, its study in this work must be

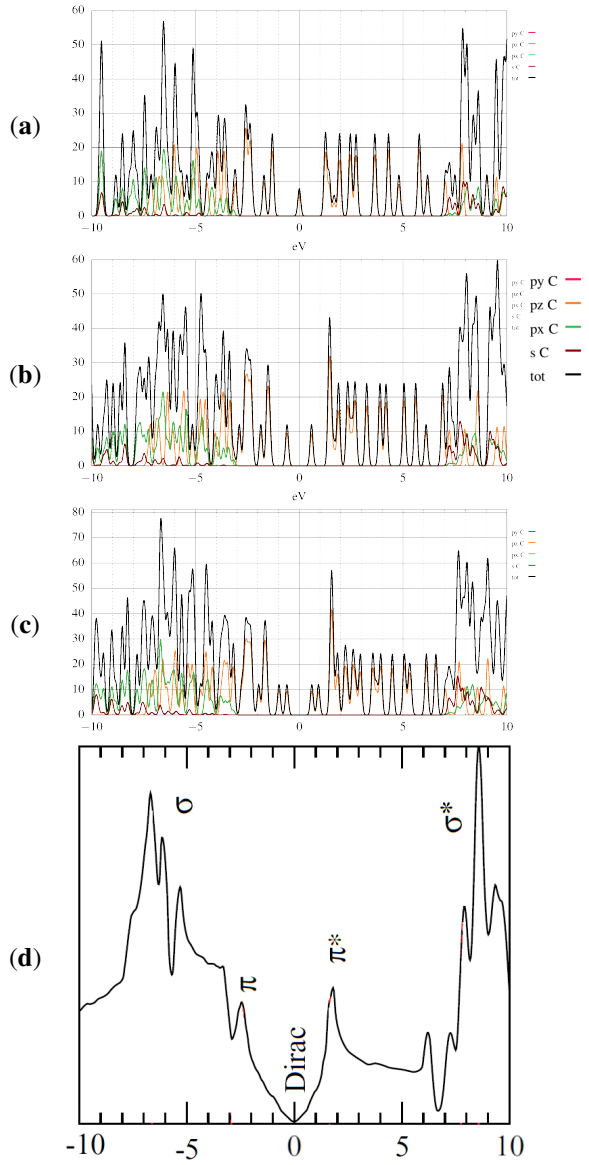

Figure 4.3: G-ene electronic DOS calculated with DFT (**a**,**b**,**c**). (**a**) 12×12, (**b**) 14×14, (**c**) 16×16 G-ene slab. (**d**) shows the electronic DOS calculated by tight binding model in [303].

considered basically as another test for our computational protocol with a few new data added to those already present in literature.

The structural perturbation due to hydrogenation is caused by the formation of covalent bonds between C and H atoms, since this reaction converts the carbon hybridization from sp^2 to sp^3, triggering significant changes in the geometric structure of G-ene. The addition of hydrogen atoms deforms the planar structure; the projection of bond angles in the plane parallel to the surface is still 120°, in resemblance with G-ene structure, but C–C bonds acquire diamond-like structure with bond angles ranging from ∼110.8° to 118.1° (Fig. 4.1). Consequently, their length changes from the calculated value of 1.442 Å (G-ene), to ∼1.380 up to 1.579 Å in G-ane. The length of C–H bonds ranges between 1.106 and 1.145 Å, as in 1D hydrocarbons. Two degrees of G-ene hydrogenation were considered: the 50% and 100% coverage (Tab. 4.1). In the case of homogeneous hydrogenation, the process involves only one C atom of the two in the unit cell or both of them, leading to the formation of the G-one and G-ane derivatives, respectively. On the other hand, the non-homogeneous process, with less than 100% coverage, can lead to the formation of G-ane islands in a G-ene matrix.

The hydrogenation process can lead to different isomers both in G-ane and G-one derivatives. The chair and boat are the ones that have been considered in this work (see Fig. 4.1(**b**-**c**) and Fig. 4.1(**d**-**e**), respectively), being the other possible isomers less stable [287]. In agreement with the literature, the G-ane chair isomer is the most energetically favorable conformation (-4 kcal/mol vs. a previously calculated -7.8 kcal/mol [287] per C_2H unit), while it is not the case in G-one, where the boat conformation (Fig. 4.1(**e**)) is the most stable (-20 kcal/mol per C_2H unit). In Tab. 4.2 is reported the energetics. To the best of our knowledge, no energy comparison between G-one isomers is available in literature and that no experimental value is available in the literature.

As previously reported [306], the hydrogenation process proceeds with the anchoring of the first hydrogen and consequent breaking of the π network that leaves an unpaired electron in the ortho positions with respect to the new formed C–H bond. The further hydrogen bond formation energetically favored are those that minimize sublattice imbalance, i.e., those A_nB_m structures for which $n_I = (n - m)$ is minimum. This principle constitutes the driving force that stabilizes the boat arrangement in G-one, accompanied by the π-bonding resonance stabilization that hinders the formation of unpaired electrons and, consequently, the possibility to induce long-range ordering. Furthermore, for the chair conformation of G-ane, hydrogen atoms from different sides of the plane bond the carbon atoms belonging to different sublattices. With regards to the effect induced by the introduction of hydrogen atoms on the electronic structure, the striking effect is the break of delocalization of the π-bond network leading to the decrease of electron mobility. In the case of 100% hydrogenation, as a consequence, the formation of localized valence

bonds (strong C–H σ-bonds) leads to the formation of a bandgap for both isomers of G-ane (Fig. 4.4): ∼4.65 and ∼4.75 eV for chair and boat, respectively. The band gap values in literature, calculated within the GGA DFT level of theory, are ∼3.5 [276] for chair conformation and ∼3.7 [276] for boat one; higher and more accurate band gap calculations are accomplished within GW approximation [307], for chair G-ane a value of ∼5.4 eV is reported [308].

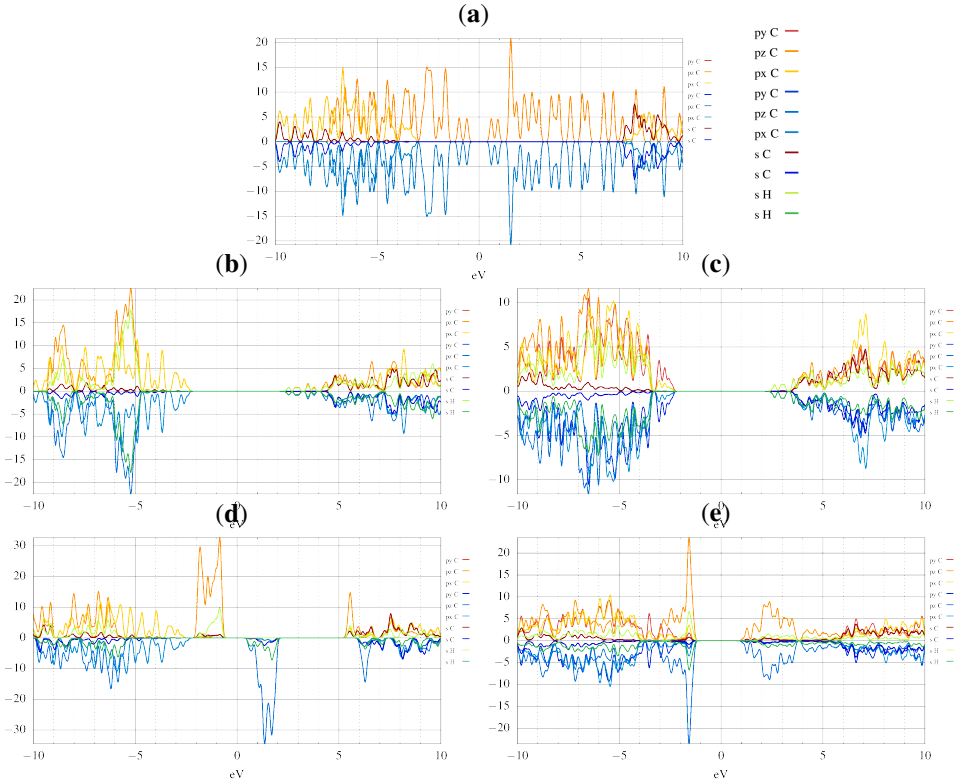

Figure 4.4: Calculated electronic DOS of (**a**) G-ene, (**b**) chair G-ane, (**c**) boat G-ane, (**d**) chair G-one, (**e**) boat G-one.

Therefore, our results are able to recover almost the 90% of the G-ane band gap computed at a higher level of computation supporting the good accuracy of our computational approach as also confirmed below for the other G-ene derivatives. Interestingly, in the case of G-one, two different scenarios were obtained. For the boat isomer, a formation of a bandgap was observed, with its value smaller than the ones observed in the G-ane: ∼2.27 eV (compared to ∼2.45 in [280]). Such a

result comes from the fact that hydrogenation occurs on two vicinal carbon atoms leading to the formation of a local aliphatic character, as in G-ane, able to induce the formation of a bandgap. As for G-ane, the system is diamagnetic. A completely different scenario was observed for the chair isomer of G-one. The calculated band gap is narrower: ∼0.80 eV (compared to ∼0.67 in [280] and ∼0.46 eV in [284]). The homogeneous hydrogenation for the 1,3,5 carbon positions of the aromatic ring leads to the formation of localized magnetic moments on the 2,4,6 positions, where the sp^2 hybridization is maintained. Differently from the scenarios where the gapless semiconductor G-ene [145] (Fig. 4.4(**a**)) turned into insulating and nonmagnetic systems for both chair- and boat-type G-ane (Fig. 4.4(**b-c**)) and boat-type G-one (Fig. 4.4(**d**)), semiconducting and ferromagnetic behavior was observed for the chair-type G-one (Fig. 4.4(**e**)). Such results are all in agreement with the literature [280].

The presence of a ferromagnetic and diamagnetic order for the chair- and boat-type G-one isomers, respectively, was confirmed by calculating the following three magnetic configurations: ferromagnetic (FM) coupling; antiferromagnetic (AF) coupling, and non-magnetic coupling (NM). The two spin states (FM and AF) were obtained by high spin and a Broken Symmetry states, respectively, both for chair (Fig. 4.5(**a**-**b**)) and boat (Fig. 4.5(**c**-**d**)) G-one isomers.

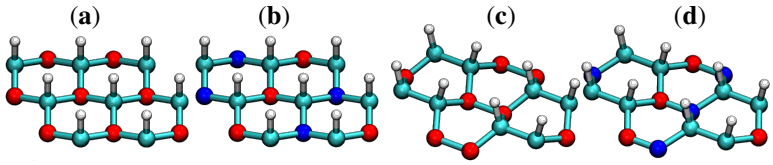

Figure 4.5: Starting Broken Symmetry states prepared for the chair and boat G-one energy minimization. (**a**) FM chair G-one, (**b**) AF chair G-one, (**c**) FM boat G-one, (**d**) AF boat G-one.

The chair-type conformation exhibits a higher symmetry since it does not break the hexagonal symmetry of the pristine G-ene precursor and each unprotonated sp^2 carbon atom has six nearest neighbors; conversely, the boat-type one has only one (Fig. 4.6). Therefore, the different observed magnetic behaviors observed for the two isomers can be explained accordingly to the Lieb's theorem [309]: for the localized spin occupying the same sublattice as in the chair-type G-one isomers, a ferromagnetic ordering of their spins would be energetically favored, while this cannot be the case when the spin are localized on different sublattices (the boat-type isomer) [283, 310]. Indeed, in the last case, we have the formation of a π bond quenching the magnetic moments.

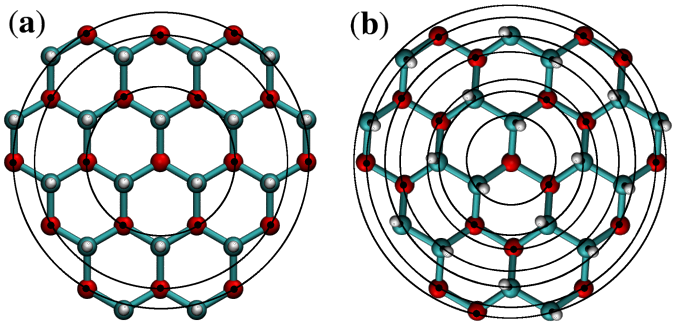

Figure 4.6: Unprotonated C atoms and its first 18 neighboring unprotonated C atoms for chair (**a**) and boat (**b**) G-one.

In the chair-type G-one, the sp^2 carbon atoms have a Mulliken spin population of 0.90 μB, confirming the previous prediction of the remarkable value of almost one localized electron per unprotonated C atom, ranging from $\sim$0.76 μB [301] to $\sim$1 μB [52]. Surprisingly for an organic-based system, a large ferromagnetic exchange coupling constant, J = -50 cm^{-1}, was estimated according to Eq. 4.4 outlined in Methods section [299].

All the energies computed for the different spin states and isomers are reported in Tab. 4.2.

Table 4.2: Comparison of DFT calculated energies of G-one and G-ane isomers.

System	Magnetism	Energy (E_h)
G-one Chair	FM	-3046.569877
G-one Chair	AF	-3046.220109
G-one Boat	NM	-3054.784962
G-ane Chair	NM	-3215.373656
G-ane Boat	NM	-3213.759753

The NM state is found to be the ground state for chair and boat G-ane isomers and boat G-one, no possible convergence on FM or AF states is possible due to the absence of localized moments. Conversely, for the chair-type G-one isomer, the FM state resulted to be more stable than the AF one in agreement with what was reported in the literature. No NM state was possible due to the presence of well isolated localized moments. The indications of the above results are dual. While it is possible to obtain an incredibly large ferromagnetic coupling for G-one structure, the overall more stable structure is the rectangular one, characterized by diamagnetic

character, hence hindering the possibility to obtain, at the isolated phase level, a thermodynamically stable ferromagnetic hydrogenated G-ene.

4.4.1.3 *Fluorination*

Because fluorine is known to replace hydrogen in many hydrocarbons [311], the existence of fluorinated form gives further room to check the stability of the different isomers. Indeed, literature [277, 312] reports that fluorinated G-one isomers have the same stability of hydrogenated ones, but different electronic and magnetic properties, fluorination can, indeed, p-dope G-ene, which is complementary to the n-doping introduced through hydrogenation [313, 314].

The addition of fluorine atoms deforms the planar structure, in resemblance with the hydrogenation process; the projection of bond angles in the plane parallel to the surface is still 120°; C-C bonds again acquire a diamond-like structure with bond angles now ranging from ∼113° to 117.8°. Consequently, the length of C-C bonds changes from the calculated value for G-ene, 1.442 Å, to the calculated for the other structures, from ∼1.358 to 1.580 Å, while the length of C–F bonds is between 1.417 and 1.478 Å, in agreement with the literature (Tab. 4.3).

Table 4.3: Comparison of GF-one, and GF-ane calculated structural parameters with previous calculation avaliable in literature. The shaded rows indicate the calculation obtained in this work.

System	Package	Functional	vdW	Basis set	Lattice par. *a*	C–C (Å)	Δz (Å)	C–H (Å)	Refs.
GF-one Chair	Q-ESPRESSO	PBE	off	PW	-	1.50	-	1.48	[301]
GF-one Chair	TAPP	PW91	off	PW	2.44	1.41	-	-	[312]
GF-ane Chair	CP2K	revPBE	rVV10	GPW	2.494	1.478	0.267-0.413	1.478	this work
GF-ane Boat	CP2K	PBE	rVV10	GPW	2.499- 2.630	1.580-1.497-1.358	0.462-0.468	1.417	this work

The cell parameters are constrained to the Au(111) (see Methods) with an introduced error with respect to the isolated fully relaxed systems of ∼3%. In consideration of our results and indications obtained from the literature our interest in looking for stable magnetic G-ene derivatives lead us to consider only the 50% of fluorination. The chair-type fluoro G-one (GF-one) showed a different behavior of its electronic and magnetic properties; the Mulliken population on the sp^2 C atoms are reduced from ∼0.90 μB of G-one to ∼0.75 μB of chair GF-one (compared to ∼0.59 μB of previous calculations of chair GF-one [301]) it is characterized by an AF ground state with J = 119 cm^{-1}, in good accordance with the previously reported

[301]. The opposite sign in the exchange coupling constant and its magnitude doubled with respect to the hydrogenated counterpart can be explained by the addition of the C_{p_z}-F_{p_z} interaction in the sp^3 carbon atom. Indeed, such an interaction introduces some overlap between the localized C_{p_z} via super-exchange interaction. NM state was observed for the boat-type GF-one as expected (vide supra). The density of states for the chair- and boat-type isomers are reported in Fig. 4.7, and only minor differences are advisable in comparison with the hydrogenated systems (Fig. 4.4). As reported [300], a slight decrease in the bandgap was observed: ∼0.70

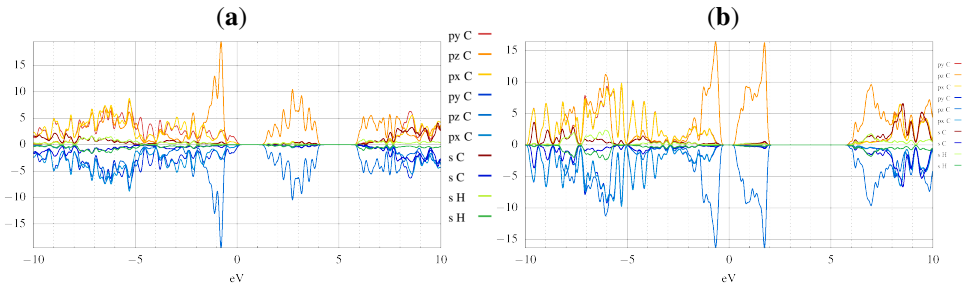

Figure 4.7: Chair (**a**) and boat (**b**) fluorinated graphone (GF-one) DOS, calculated for the isolated systems.

eV for chair GF-one and ∼1.26 eV for boat GF-one. The energies of different isomers are available in Tab. 4.4. Even in the case of the GF-one, the most stable conformation is the boat-type one precluding the hypothetical use of the appealing AF behavior predicted for the chair-type isomer in real applications. However, the introduction of a more electronegative substituent in alternative to the hydrogens lead to the stabilization of the latter of ∼2 E_h, a value not sufficient to make it yet the fundamental one, though $\Delta E_{chair\text{-}boat}$ = ∼6 $_h$.

Table 4.4: Comparison of DFT calculated energies of GF-one boat and chair isomers.

System	Magnetism	Energy (E_h)
GF-one Chair	AF	-9095.396177
GF-one Boat	NM	-9101.222400

4.4.2 *Stabilization of magnetic moments in hydrogenated/fluorinated graphene*

The way to straightforwardly stabilize the magnetic semiconductors above introduced as chair-type isomers is hard to pursue. Indeed, the selectivity for the 1,3,5 G-ene ring positions could be able, in principle, to induce a selective attack with an

inhibited kinetic process to collapse to vicinal substitutions, it has anyway several drawbacks, first of all the inhomogeneity in the addition process and the limited coverage limits [313, 315, 316]. Therefore, the stabilization of the magnetic moments in hydrogenated G-ene turns out to be a subtle goal to accomplish, and several indirect experimental strategies in hydrogenated G-ene were reported in the literature [313]. Among them, the stabilization of the magnetic moments was attempted by hydrogenating G-ene once adsorbed on a substrate [267, 281, 316, 317]; through a patterned hydrogenation by e-beam lithography [314]; by chemical vapor deposition (CVD) [318]; by creation of H-vacancies in G-ane flakes [283]; by stoichiometric fluorination [282]; by substitution fluorine atoms with different functional groups [319], or by adatoms implantation [320]. Following the intensely debated topic of ferromagnetism in G-ene derivatives, magnetic ordering was detected in some of the aforementioned studies, others showing only paramagnetic behavior. In every case, the hypothetically possible magnetism of one moment unit per carbon atom ($\mu_{Carbon} \sim 1\ \mu$B), as calculated for the chair-type G-one isomer, has never experimentally been reported. The defect-induced magnetism experimentally prompted and measured on hydrogenated G-ene derivatives [267, 281] has reached only fractions of μB per carbon atom, due to the interfacial nature of the magnetic moments that can be implanted. It is worth mentioning that in literature it is not always clear what such values refer to the unit cell or to a single carbon atom, for instance. The possibility of having a stable and significant magnet moment in a 2D pure organic system is very appealing but a comprehensive in silico study aimed to rationalize the possible ways to synthesize a stable magnetic phase for hydrogenated G-ene that can show long-range ordering, i. e., FM or AF coupling, is still missing. Hereafter, two main approaches aimed to achieve a stabilization of the magnetic moments for homogenous and non-homogenous hydrogenation will be presented. In the former scenario, it will be exploited the adsorption of both types of G-one isomers on a substrate (Au(111) with the aim to see the effects from the new substrate@surface interactions to stabilize the FM phase vs. the NM one. In the case of non-homogenous hydrogenation, selective patterning of hydrogenation positions to form localized islands characterized by a local G-ane structure will be presented. In this regard, a wide variety of different new hydrogenation patterns will be studied and compared to some already presented in the literature. All of these systems will be studied within the same computational framework, allowing a detailed and reliable comparison of structural, energetic, and magnetic properties.

4.4.2.1 *Adsorption on Au(111)*

Several studies focused on the adsorption of hydrogenated G-ene derivatives on metallic surfaces [279, 317, 321], but for all of them, a mismatch between the lattices was present. This is not the case for the Au(111) surface, where a better matching with the G-ene and its derivatives can be observed [317].

In particular, the chair-type G-one presents all the hydrogenated carbons on the 1,3,5 sublattice while all the saturated carbons on the 2,4,6 sublattice. Being all the hydrogens on the same side of the G-one layer, Au(111) surface could be suited for stabilizing the ferromagnetic chair-type G-one by forming strong σ/π interactions with the gold atoms positioned at the doubled of the G-one lattice parameters. Indeed, the superlattice of the G-one@Au(111) system has a periodicity doubled with respect to the pristine G-ene and for such a reason an even number of G-ene ring rows is necessary to fulfill the periodic boundary conditions (Fig. 4.8.

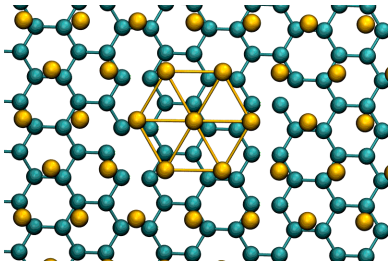

Figure 4.8: G-ene@Au(111) superlattice, it is evident the doubled period of Au hexagon compared to fulfill periodic boundary conditions of the G-ene structure.

Both the chair- and boat-type G-one isomers deposition was simulated to evaluate if a possible stabilization of the former with respect to the latter could happen. The symmetry of the isolated G-one is lowered during adsorption on the gold surface for both structures. In the case of the chair-type one, the unit cell is now composed of 8 atoms and the 1-3 vicinal C–C distances (the cell parameters in G-ene) are a distribution of values between 2.462 and 2.545 Å. Shorter distances correspond to C_{sp^2} atoms. The simple C–C bond distances stretch (1.486-1.517 Å) as a consequence of the increased Δz value of carbon atoms, now ranging between 0.163 and 0.466 Å (such a variation was not observed for pristine G-ene passing from the isolated to the adsorbed scenario, where the C–C bonds maintain both the same lengths of 1.442 Å and Δz of 0.000 Å). The C-H bond is shrunk up to 1.120 Å (see Tab. 4.1 for a comparison with isolated phases). The C–Au distance is in the range 2.211-2.671 Å, compared to 3.487 Å obtained for pristine G-ene

adsorbed on Au(111). Also in this case, shorter distances correspond to C_{sp^2} atoms. The chair-type isomer adsorbed with the hydrogen atoms pointing away from the surface strongly interacts with the surface retaining only 1/4 of the original magnetic moments of the isolated phase. As shown in Fig. 4.9(**b**), the sp^2 carbon atoms that are in a quasi-atop position with respect to the first layer of gold atoms (yellow) lose their magnetic moment: indeed, in such a case a bonding interaction is expected and as a consequence a significant quenching of the magnetic moment.

A different situation is expected for those sp^2 carbon atoms which are atop of those gold atoms that belong to the second layer (brown atoms in Fig. 4.9(**b**)(**d**)). In that case, the Au–C bonding interactions with the atoms of the first layer are reduced and, therefore the quenching of the unpaired electron (carbon atoms drawn in red) is not complete. To confirm this scenario, in the former cases a ∼0.15-20 μB value for the 192 sp^2 carbon atoms was calculated while for the latter more than a doubled value, 0.54 μB, that is roughly one half with respect to the isolated system. Even if a partial quenching of the magnetic moment happened upon adsorption, still a considerable fraction is retained and these results would be worthy in terms of surface spintronic engineering.

The magnetic exchange constant via the Broken Symmetry approach was hence calculated, obtaining a reduction of its magnitude from 50 cm^{-1} to 3 cm^{-1}. Such a reduction can be explained by: i) the doubled distance intercurring between unpaired electrons on sp^2 carbon atoms with respect to the isolated scenario so that the spin-polarized C atoms are now four bonds apart from each other; ii) the interaction between sp^2 carbon atoms with the valence density of states of the fold surface. However, the resilient FM behavior can be ascribed to the maintaining of a certain degree of wavefunction localization for those C atoms that are not on a *quasi-atop* configuration due to not efficient overlap interactions both with Au atoms belonging to the first and the second layers. The established Au–C_{sp^2} interactions become evident from the analysis of the DOS of the carbon atoms (see Fig. 4.9). Clear spin polarization is still evident but the band gap between the two C_{sp^2} spin components computed for the isolated scenario is substituted by the new Au–C_{sp^2} covalent interactions.

For the boat-type G-one isomer, an even lower symmetry with respect to the chair-type one was found. The unit cell is now composed of 16 atoms and the 1,3 vicinal C–C lengths (the a cell parameter in G-ene) vary from 2.462 up to 2.545 Å. The C–C bonds and the Δz values span wider lengths distributions compared to the chair-type G-one, 1.380-1.564 Å and 0.331-0.676 Å, respectively. The C–H bond shrunk up to 1.120 Å. The C–Au distance is in the range 2.214-2.890 Å, compared to 3.487 Å obtained for the pristine G-ene adsorbed on Au(111), the shorter distances are the C_{sp^2}–Au while the longer ones correspond to C_{sp^3}–Au

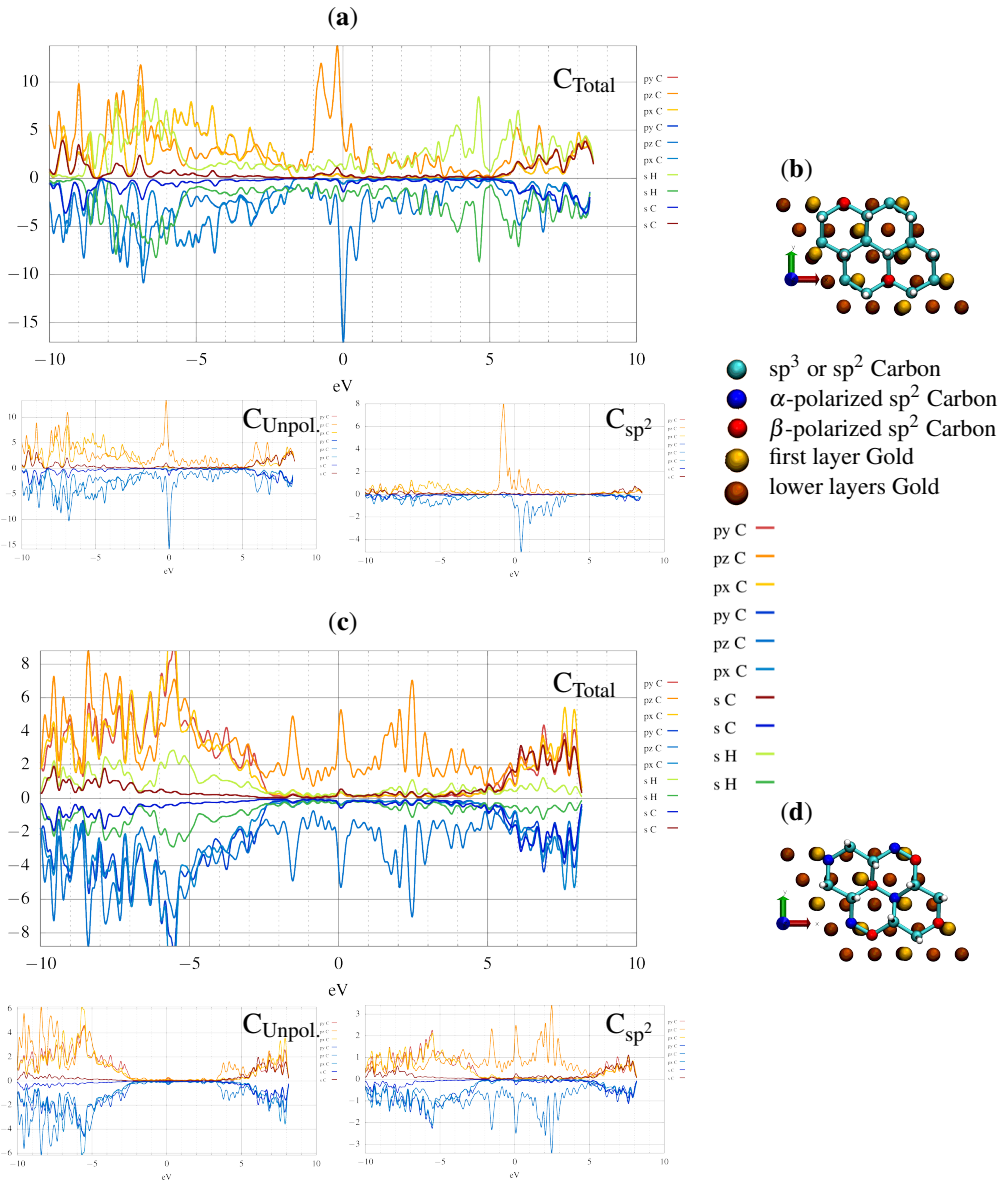

Figure 4.9: Chair G-one on Au(111) C atoms DOS(**a**) and structure (**b**). Boat G-one on Au(111) C atoms DOS (**c**) and structure (**d**). The unpolarized (sp^2+sp^3) C atoms and the polarized (sp^2) C atoms are shown in the small plot beneath the total C atoms DOS.

distances. The outcomes of these calculations indicate that our intuition was partially correct since the magnetic moment (even if partially quenched) can be maintained

also in the adsorbed scenario but the stabilization in energy with respect to the boat-type G-one is still not sufficient to make it the most stable isomer. Indeed, the stabilization of ∼3 E_h energy of the chair-type G-one isomer reduced the energy separation of ∼8 E_h in the isolated scenario (see Tab. 4.1) to ∼5 E_h in the @Au(111) one.

Encouraged by these results, the adsorbed scenario with the hydrogen atoms pointing toward the surface was also attempted. The idea behind this choice was to verify if the magnetic moment could be better protected by the surface due to the presence of the hydrogen atoms (longer distance between Au–C_{sp^2}). Moreover, due to the affinity of the gold atoms toward the hydrogen ones, it could be a way to "freeze" the positions of the latter in the case selective hydrogenation in 1,3,5 positions could be possible. Unfortunately, the Au(111) surface acted as a catalyst since cleavage of the C–H bonds was observed leading to the formation of H_2 species between the gold and the G-ene layer.

In view of the fact that the substitution of the hydrogen atoms with fluorine ones reduced the $\Delta E_{chair\text{-}boat}$ of ∼2 E_h (Tab. 4.5), a further step of the investigation led us to adsorption of the GF-one on the same substrate to verify if a synergic stabilization energy effect could take place. However, the polarization of the C–F bond has a detrimental effect on the carbon magnetic moment leading to a stronger interaction with the substrate (Au–C = 2.172-2.621 Å). Consequently, a non-magnetic phase was found for the chair GF-one, as well as for the boat GF-one, as expected from the isolated phase calculation. As the final step in these attempts of stabilizing the

Table 4.5: Comparison of DFT calculated energies of G-one boat and chair isomers adsorbed on Au(111).

System	Magnetism	Energy (E_h)
G-one Chair@Au	FM	-28577.889420
G-one Chair@Au	AF	-28577.887105
G-one Boat@Au	NM	-28582.711844

magnetic moment in hydrogenated and fluorinated G-ene derivatives by surface interactions was the application of the intercalation of a new pristine G-ene layer between Au(111) and G-one. We here evaluate the effects of a graphene "buffer" layer. Usually, the stacking of two G-ene layers show two kind of symmetries: AA or AB [322].

Neither of the two is obtained for the G-ene@G-one system; a middle configuration is nonetheless found (Fig. 4.10(**b**)). The structure of Au(111)@G-ene@G-one preserves the C–C bond lengths (1.483 Å) and lattice parameters (2.498 Å) of the isolated phase. The G-ene/G-one distances are in the range 3.261-3.609 Å,

the shorter distance being the G-ene$_{sp^2}$/G-one$_{sp^2}$ carbon atoms, the longer is the G-ene$_{sp^2}$/G-one$_{sp^3}$. The G-ene/Au distance in Au(111)@G-ene@G-one is the same of the Au(111)@G-ene, say, 3.500 Å. Indeed, as for the structural parameters, the electronic DOS of G-one C atoms restores the original shape observed in the isolated system (Fig. 4.10). An intercalated buffer layer is hence decoupling the layers above and below, it can hence be exploited to restore the original properties of the constituents, thanks to the strong π-network that insulate from covalent interactions.

In summary, the exploitation of the stabilization mechanisms underlying the magnetic ordering along with the introduction of the Au substrate showed not to be enough to make stable FM or AF phases of G-one and GF-one, respectively (Tab. 4.3).

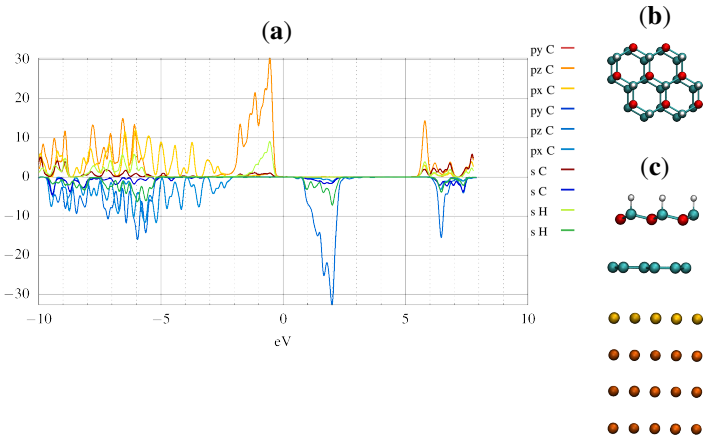

Figure 4.10: (**a**) C atoms DOS of chair G-one FM adsorbed on G-ene@Au(111). Top view (**b**) and side view (**c**) of the adsoprtion configuration.

4.4.2.2 *Islands and Ribbons*

Extended systems showing a finite spin density on sp^2 carbon, such as chair-type G-one, turned out not to be stable with respect to non-magnetic structures, such as boat-type G-one. Our attempts to stabilize the formers through a surface as a die, even if the idea led in the right direction, the overall result was not exciting. To look for another method to implant magnetic moments on graphene, it is, therefore, necessary to investigate more stable arrangements of hydrogens. Some studies pointed out a fundamental query regarding the ferromagnetically ordered localized states (H-vacancies) in G-ane. Increasing the vacancy concentrations, the stability of the spin

alignment is decreased and the total magnetization is suppressed [283, 310]. Both the pristine G-ene and G-ane, as standalone systems, are not favoring the establishment of a magnetic moment as also confirmed by our studies; a possible shortcut is represented by the exploitation of the interphase between these two materials, that is, sp^2 and sp^3 domains [323, 324], to allow the growth and maximization of the spin moment per unit cell. To do so, we must imagine breaking the infinite symmetry of the G-ene layer to give rise to new properties at the nanoscale. The kind of structures widely studied as standalone 1D graphene are the so-called nanoribbons (GNR) [325–327]. They are characterized by having borders of non-three coordinated C atoms which can exhibit edge states and different electronic, chemical and magnetic properties depending on the size and type of border. These edge states are present only for zigzag edges as a flat band around the Fermi level, they extend along the ribbon's edge, leading to a metallic nanoribbon if the width is large enough [328, 329], in Fig. 4.11 two exemplary structures of zigzag (**a**) and armchair (**b**) nanoribbons

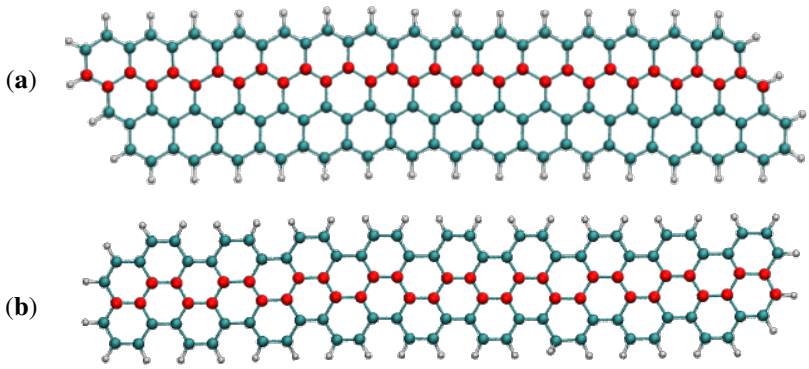

Figure 4.11: (**a**) zigzag and (**b**) armchair edges of G-ene nanoribbons. The atoms highlighted in red represent one row of C atoms.

Some fundamental questions regarding several important aspects of nanoribbon systems remain open. These include the ability to control the electronic structure and the band gap depending on the chirality of their edges [328] or the nature of the edge passivation with H atoms, among other important issues such as the effect of structural defects on the electronic and thermodynamic properties. Recently, there has been an increasing interest in realizing graphene electronic circuits without physical cutting due to the nontrivial experimental challenge in controlling and

manipulating the geometry of nanoribbon. Some evidence, in fact, points out that the zigzag edge is metastable with respect to a magnetic polarization [330], because it shows a planar reconstruction that lowers its energy [331].

An alternative route to obtain the same 1D structure but more stable than for isolated G-ene nanoribbons is the one where the G-ene is embedded in a G-ane matrix. Such a scenario can be obtained saturating with hydrogen specific carbon atoms rows in G-ene, or, complementary, creating vacancies in a stoichiometric G-ane structure [332]. Moreover, contrarily to the extended systems, as G-one, where the activation barrier for H migration is very low [333] the direct and inverse H migration are limited once G-ane islands are formed [334].

Indeed, at G-ene/G-ane interfaces, i.e., sp^2/sp^3 a spin polarization mechanism can be induced on the zigzag edge states [323], and contrary to G-ene nanoribbons, a stable injection of the magnetic moment is possible. The stability of such interfaces has been recently asserted [335]. Furthermore, during the hydrogenation process there is a significant probability for the formation of different domains of sp^3 carbon atoms showing H frustration [336], i.e., the ideal sequence of alternating up and down H atoms is broken (frustrated) across multiple sp^3 domains, leading to the impossibility to achieve complete hydrogenation, and consequently, to the presence of some sp^2 carbon atoms domain interposed to different sp^3 domains. This aspect makes the strategy of building small domains of fully hydrogenated G-ene appealing because it shows few constraints in the construction of multiple adjacent domains and a potential way to implant magnetic moments in G-ene with the perspective of a controlled patterning and scaling-up on the G-ene backbone [314, 337]. As mentioned above, the portion of this composite material where spin-polarized states localize is the G-ene nanoribbon domain, adjacent to G-ane domain, its electronic properties are similar to a free standing nanoribbon [338]. The spin-polarization is not confined to the edge but also to 1-3 vicinal spin-polarized sp^2 carbon atoms [338, 339].

The rows of C sp^2 atoms at the interfaces are composed of ferromagnetically coupled spins; when the geometric pattern of the hydrogenation allows for the formation of non-communicating rows (like two opposite sides of a ribbon or the borders of an island whose continuity is disrupted by the lack of vicinal 1-3 sp^2 C atoms), each row polarizes antiferromagnetically to the others. The ground state of such systems is overall antiferromagnetic. The study of these systems shows that the spin population on each edge reaches a plateau value of 0.25 μB per unit cell when they are at least 12 C_{sp^2} rows far apart. Such a result indicates that a significant magnetic moment can be instilled but, at the same time, that a high density of nanoribbons, i.e., 1-2 C_{sp^2} rows apart, cannot be reached due to the quenching of the momentum. To overcome such a limitation and to verify if there is an alternative

way to improve the magnitude of magnetic moment per unit cell, we investigated the possibility of spin moment implantation when the 1D dimensionality of the ribbon structure is further lowered to 0D islands, allowing a more complex design of interfaces. We then attempt a rationalization of the implanted magnetic moment as a function of the ribbon or of the island dimensions, shape, structure, and termination. To keep the consistency of our results, the number of atoms in the system is kept fixed for several systems to allow a direct comparison of G-one, and G-ane/G-ene systems' energies towards a stability analysis. All the ribbons and islands structures present an even number of H atoms because an odd number would imply the existence of an unpaired electron in the carbon backbone, that is a metastable state from which reaction with further hydrogen is very likely [306].

We will investigate the possibility to implant magnetic moments in hydrogenated G-ene starting from the most stable structure that is ought to form in large abundance and to be stable in thermodynamically driven reactions, for example undergoing an annealing step after hydrogenation [275]. Several other structures were considered among stoichiometric G-ane compounds $(C_1H_1)_n$, but the chair-type G-ane (Fig. 4.1(**a**)) [288, 340] is the most stable structure, as confirmed in literature [276]. Therefore, it is likely to expect that, during the hydrogenation process, islands of the most stable isomer can form, and gradually grow at the expense of other structures [275].

The structures simulated hereafter are non-homogeneous coverages, i. e., islands, with isolated spot or continuous ribbon shapes with different hydrogenation content, ranging from 2 to 50%. The rationalization of different magnetic properties was possible from the analysis of prototypical systems.

THE STABILITY AS A FUNCTION OF THE sp^2/sp^3 INTERFACE

The investigated interfaces have two possible shapes, the so-called armchair (boat-like) and zigzag (chair-like) edges [331]. An island of G-ane with armchair edges has only a single way to be built up, as shown in Fig. 4.12(**a-b**). It ensures a strong bonding of adjacent 1-2 vicinal sp^2 C atoms and hence a truly diamagnetic state (NM). A zigzag-edges island, instead, may be terminated in two ways, say α and β [323], depending on how many C atoms are hydrogenated in the sp^2/sp^3 interface ring (Fig. 4.12(**c-f**)): three and five for α and β, respectively. These edges are formed by C atoms belonging to the same G-ene sublattice because they are related by (1-3) meta vicinality, allowing, for the Lieb theorem, to bear magnetic moments that order ferromagnetically. A collection of different island structures of the chair-type isomer (Fig. 4.1(**b**)) with armchair or zigzag-α and -β edges was considered, keeping fixed the number of atoms in the system to allow for a direct

comparison of stability with the G-one system (Tab. 4.6), all the islands are far more stable than boat-type G-one (Fig. 4.1(**e**)) of about 8 E_h (see Tab. 4.2).

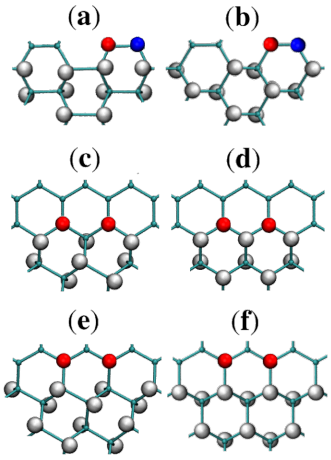

Figure 4.12: Armchair (**a**-**b**), zigzag-α (**c**-**d**), and zigzag-β (**e**-**f**) termination of chair (**a**-**c**-**e**) and boat (**b**-**d**-**e**) G-ane in G-ene/G-ane interface. Two carbon atoms belonging to the nearest neighbor row are shown: the red C atom is part of sublattice A, the blue of the sublattice B. For the definition of row, check Fig. 4.11.

Table 4.6: Comparison of DFT calculated energies of G-ane boat and chair isomers island embedded in G-ene with all possible termination edges: armchair, zigzag-α, zigzag-β.

System	Edge	Energy (E_h)
G-ane Chair	Armchair	-3062.971277
G-ane Chair	Zigzag-β	-3062,217402
G-ane Chair	Zigzag-α	-3062,673169
G-ane Boat	Armchair	-3063.710216
G-ane Boat	Zigzag-β	-3062,999279
G-ane Boat	Zigzag-α	-3063,709245

The NM armchair and the FM zigzag-α edges are the ones with the lowest energies which differ only by 0.06 kcal/mol (0.026 eV) in favor of the former. This means that both edges are equally thermodynamically stable (Tab. 4.6) and, most importantly, that zigzag-α edges can be, therefore, experimentally obtained. The

formation energy of zigzag and armchair G-ene/G-ane nanoribbons are equally favorable at room temperature in a G-ane matrix [287, 335, 338, 341], contrary to the case of freestanding nanoribbons, where it was found that the zigzag edge is metastable and a planar reconstruction occurs leading to lower energy [331]. The spin density is distributed along the zigzag-α edges and it is larger at the center of the row, decreasing towards the ends. From here on, only zigzag-α edges will be considered for subsequent systems. Furthermore, when dealing with 0D structures, several kinds of edges can coexist due to the closed borders of the interface. The edges reported in Fig. 4.12 are, hence, studied for a series of G-ane islands made of 256 H atoms. For each of them a more prevalent edge type has been shaped at their borders (see Fig. 4.13 for complete island structure).

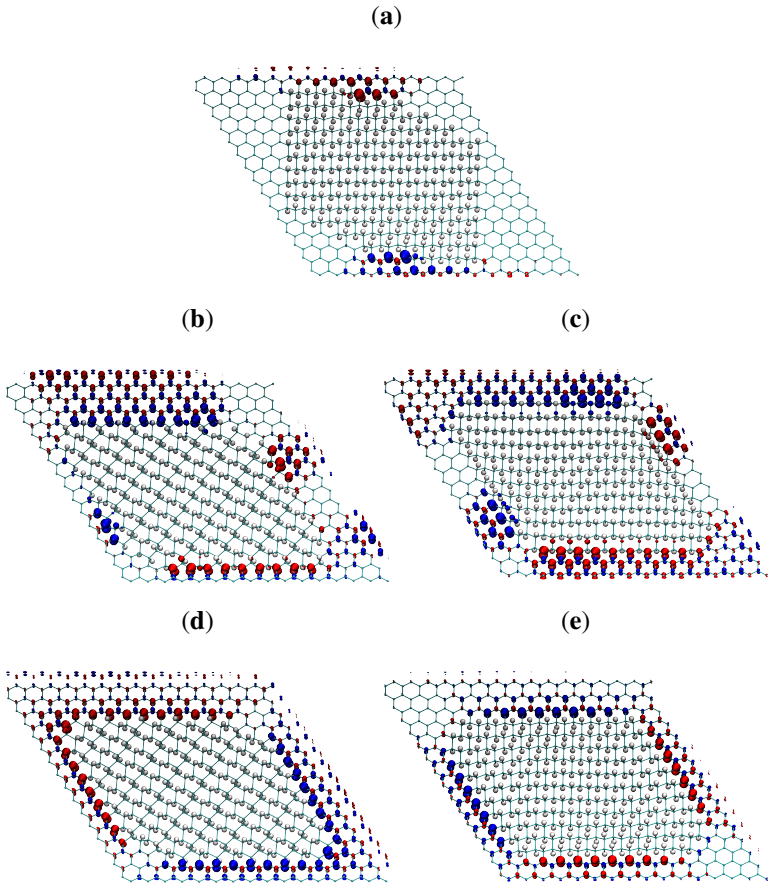

Figure 4.13: Armchair (**a**), zigzag-α (**b**-**c**), and zigzag-β (**d**-**e**) termination of chair (**a**-**c**-**e**) and boat (**b**-**d**) G-ane in G-ene/G-ane interface. The isosurfaces represent the positive (blue) and negative (red) spin density.

and bound by different types of junctions. In such a framework, it is also interesting to notice that different island corners can be obtained. They are characterized by the 1,3 or the 1,4 patterning which have different effects on the propagation of the spin polarization present on the island sides. Such a behavior will be considered in detail in the next paragraph.

THE EFFECT OF THE JUNCTION BETWEEN FERROMAGNETIC ROWS

To rationalize the origin of the magnetic moment, several clusters of G-ene of different sizes were considered. Terminal carbon atoms were saturated by hydrogen atoms. Different G-ene/G-ane interfaces of different shapes and extensions were then created by adding H atoms (Fig. 4.14) in the middle of the cluster to obtain both completely separated or communicating sides. In the former case, the direct interaction between the interface states across the G-ane region is negligible, and symmetric localized degenerate states are expected for the two sides for the AF state. If the two interfaces are put in communication through a G-ene corner with a 1,4 patterning (Fig. 4.14(**b**)), the wavefunction loses its symmetry leading to a delocalized magnetic orbitals, strongly quenching the residual magnetic moment. This is principally due to the disruption of the 1,3 (meta) arrangement of polarized sp^2 carbon atoms at the interphase that allow for a ferromagnetic polarization.

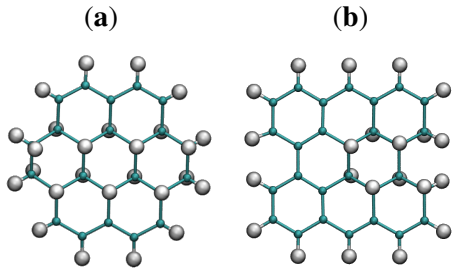

Figure 4.14: Small cluster structures simulated to rationalize the effects of the junction of two zigzag interfaces. (**a**) isolated interfaces, (**b**) interfaces put in connection extending the G-ene portion.

Indeed, it was found that a continuity in the 1,3 patterned C atoms across a sharp corner (Fig. 4.15(**a**)), led to retention of the spin polarization. To confirm such an outcome, several other junction types were considered. For instance, an obtuse angle junction between zigzag edges (Fig. 4.15(**b**)) leads again to 1,4 pattern of the C atoms at the sp^2/sp^3 interface, hence forbidding a FM spin polarization. In such a case, this type of junction becomes a point where the FM spin rows

invert their polarity. Armchair edges may be formed by the junction of zigzag rows (Fig. 4.15(**c**)). They have the same feature of triggering the spin polarity inversion, but they are less efficient than the previous ones because they lead to quenching of spin moment across them, lowering the total density of spin population per unit area.

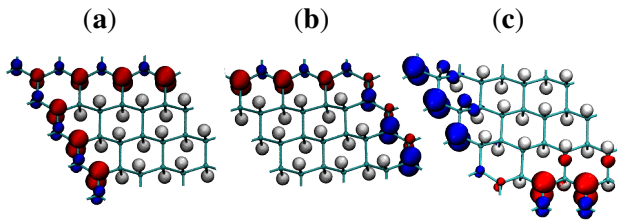

Figure 4.15: Types of corner that can exist in a 0D G-ane/G-ene system. The isosurfaces represent the positive (blue) and negative (red) spin density. (**a**) zigzag sharp angle corner, (**b**) zigzag obtuse angle corner, (**c**) armchair corner.

MINIMUM ISLAND EXTENSION TO GENERATE SPIN DENSITY AND TOTAL SPIN POPULATION IMPLANTED IN A ROW

Verified the effect of quenching of the spin polarization mechanism made by 1,4 type junctions, we investigated how and if such an effect could be detrimental for total magnetic moments for a single side. Therefore, a series of islands were built to investigate such an aspect. In particular, a nanoribbon of G-ane made from 2 to 13 sp^3 C rings (see in Fig. 4.16 the structures) is created in a layer of G-ene with the Au(111)-defined 16x16 cell dimensions used so far. The stacking of rings is increased up to the reaching of boundaries, where the 0D structure becomes a 1D structure. Interestingly, a dependence of the average moment of sp^2 C atoms at the zigzag sp^2/sp^3 interface as a function of the G-ane nanoribbon length up to the fully periodic limit (Fig. 4.17 and Tab. 4.7) was observed. In our case, the latter corresponds to 16 C rings for which a maximum value of 0.29 μ_B was computed. Such a value is in perfect agreement with what was reported in the literature for simulated fully periodic nanoribbons [339] and those experimentally measured even if on SiC (0.1 μ_B [267] and 0.45 μ_B [281]). On the contrary, for very short nanoribbon lengths, i.e, up to 3 C rings atoms, no magnetic moments are instilled. From 4 up to 13 C rings an essentially monotone increase of the magnetic moment tending to 0.3 μ_B was computed.

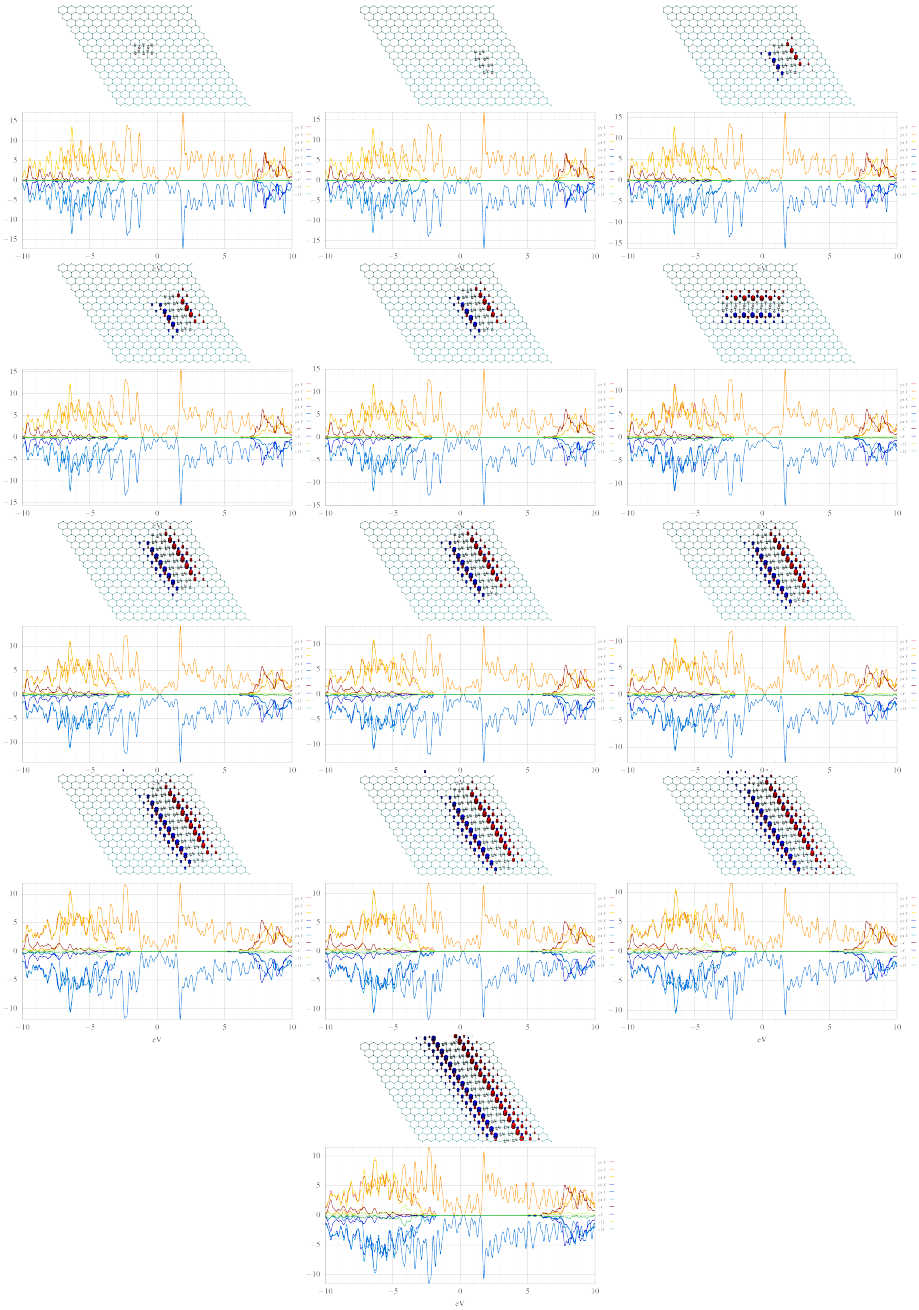

Figure 4.16: DOS and structure of the series from 2 to 16 sp^3 condensed rings embedded in G-ene. The isosurfaces depicted on each structure represent the positive (blue) and negative (red) spin density.

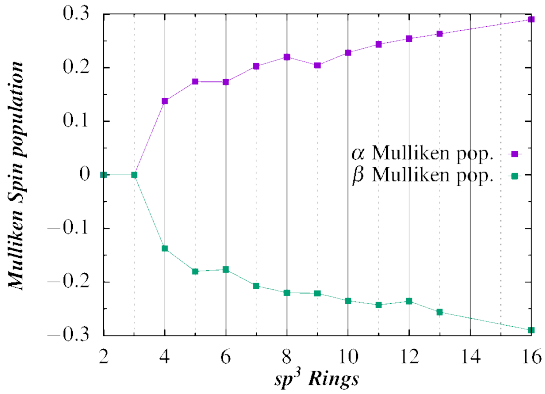

Figure 4.17: Comparison of total α and β Mulliken population of two rows wide islands (from 2 to 13 condensed rings) and 1D nanoribbon (16 condensed rings). Structure are showed in Fig. 4.16

Table 4.7: Comparison of total Mulliken population and Mulliken population per polarized C atom of two rows wide islands (from 2 to 13 condensed rings). The 16 condensed rings system reported is a 1D nanoribbon. Structure are showed in Fig. 4.16

		Polarized		Population	Population
System	C	C	H	α (total)	per C_{sp^2}
2	512	2	10	0	0
3	512	3	14	0	0
4	512	4	18	0.55	0.14
5	512	5	22	0.87	0.17
6	512	6	26	1.06	0.17
7	512	7	30	1.42	0.20
8	512	8	34	1.76	0.22
9	512	9	38	1.84	0.20
10	512	10	42	2.35	0.23
11	512	11	46	2.67	0.24
12	512	12	50	3.05	0.25
13	512	13	54	3.42	0.26
16 (ribbon)	512	16	64	4.64	0.29

The observed trend can be explained by the existence of 1,4 armchair junctions-type at the nanoribbons ends, which lead to a decrease of the magnetic moment of the carbons in their proximity up to the quenching of it exactly at the junction. Such results unveiled that the size and, therefore, the sides of a G-ane island need to

obey a compromise for the best combination between the dimension of G-ane/G-ene interface and magnetic moment per sp^2 C atom.

Interestingly, the only structure that did not converge was the 14 C G-ane rings nanoribbon, i.e., the one that has only two G-ene rings separating the G-ane nanoribbon. A spin frustration at the junctions of the two too close nanoribbons could be claimed as the cause for such discontinuity.

The origin of the plateau value reached for n > 7 can be explained by the formation of a valence/conduction band. The C atoms at the edge (zigzag sp^2/sp^3 interface) theoretically possess a total magnetic moment of 1 μ_B, but, due to the periodic ripples induced by the interface, a large part of the energy degeneration in the Fermi region is removed. Such an effect limits the increase of the instilled magnetic moment proportionally to the number of the C_{sp^2} atoms.

With regards to the evolution of the DOS depending on the length of the G-ane nanoribbon, it can be observed that a Dirac cone-like structure is maintained for all the length values but with the difference that the Fermi energy is shifted from the Dirac point towards the occupied states. Such behavior is expected due to the break up of the G-ene π system because of the formation of σ C–H bonds which contribute to increasing the number of bands around Fermi and makes them asymmetrically populated with respect to it.

INFLUENCE OF THE DISTANCE BETWEEN ZIGZAG sp^2/sp^3 INTERFACES

The other parameter to consider in the perspective of instilling the magnetic moment in G-ene by selective hydrogenation is the distance between the formed G-ane islands. Indeed, it was shown in the literature that for two nanoribbons separated by a number of C_{sp^2} rows, n, (see Fig. 4.18), the computed magnetic moment decreases from a plateau value of 0.29 μ_B for $n = 12$ to 0 for $n = 3$ [339]. Therefore, even in our systems, the different densities of the G-ane islands for a unit cell can directly influence n and, consequently, the momentum at the zigzag sp^2/sp^3 interfaces. To confirm the dependence of both the instilled magnetic moment per C atom and unit cell as a function of n, supercells with single ($n = 3$), double ($n = 7$), and four ($n = 15$) two rows wide G-ane nanoribbons were generated (Fig. 4.18) within the same Au(111)-derived supercell. In the case of the computed magnetic moment for single polarized C_{sp^2} atoms, the results are in agreement with the literature [339]: a value of 0.29 μ_B was computed for $n = 15$, while decreasing moments of 0.25 μ_B and 0.13 μ_B were observed for $n = 7$ and $n = 3$, respectively (see Tab. 4.8). However, differently from what was reported in the literature [339], it was also possible to directly access the total magnetic moment instilled as a function of n, being all the three different n cases derived from the same supercell. Interestingly, despite

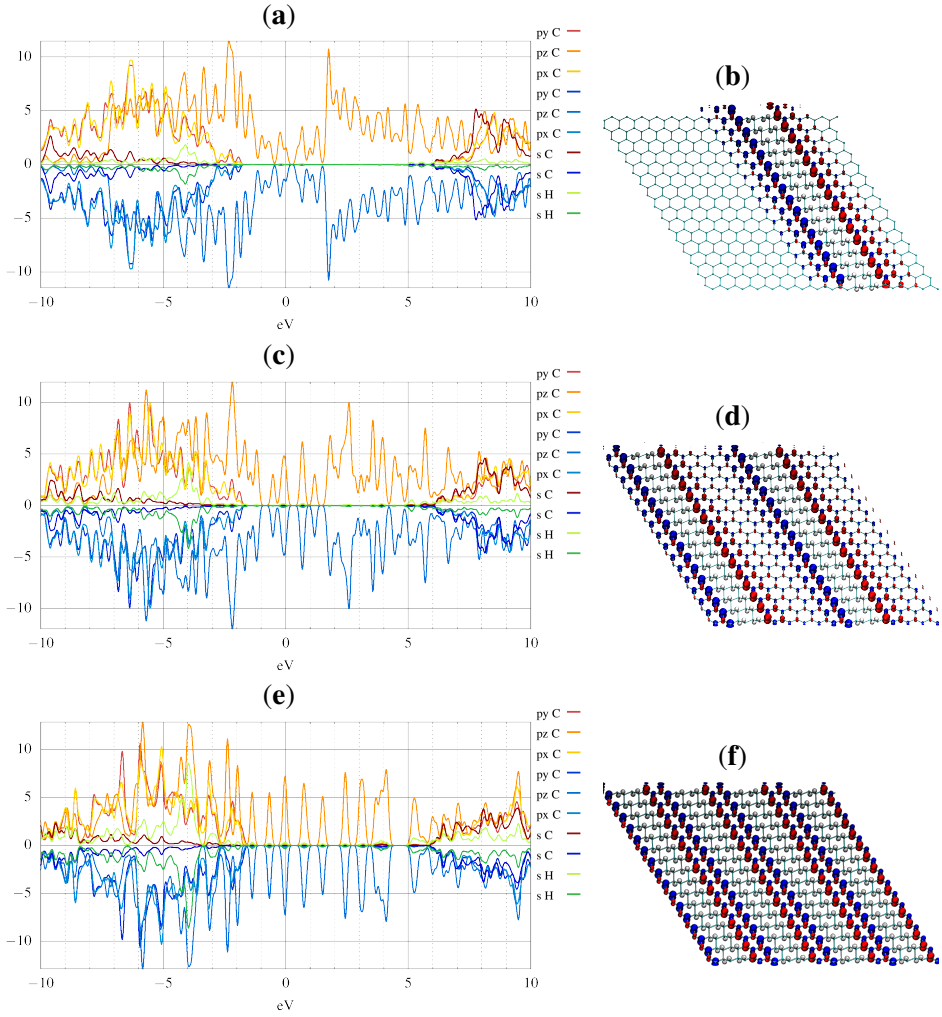

Figure 4.18: Comparison of electronic DOS and structures of several G-ane/G-ene systems with nanoribbon patterns. The isosurfaces represent the positive (blue) and negative (red) spin density.

the quenching of the magnetic moment for small n values, its value per unit cell is almost doubled with respect to the one computed for $n = 15$ (see Tab. 4.8).

Indeed, even if for the $n = 3$ scenario the magnetic moment per C_{sp^2} atoms is quenched by almost three times with respect to the $n = 15$ one, the higher number of polarized atoms makes the former cases, or the one with n up to 7, at least at

Table 4.8: Comparison of magnetic parameters of several G-ane/G-ene systems with nanoribbon patterns.

System	C	Polarized C	H	Population α (total)	Population per C_{sp^2}	Population per cell	Energy (E_h)
1 nanoribbon 64H	512	16	64	4.64	0.29	0.018	-2950,370277
2 nanoribbons 2x64H	512	32	128	2x4.06	0.29	0.018	-2950,370277
4 nanoribbons 4x64H	512	64	256	4x2.02	0.13	0.031	-3062.612797

the theoretical level preferable. Such results pinpoint the general dimension of the islands and reciprocal distances in a G-ene matrix to maximize the magnetic moment per unit area. The reduction of the magnetic moment per C_{sp^2} with the decrease of n can be explained by the reduction of the degenerate states at the interface.

THE PATHWAY TOWARD THE INCREASE OF MAGNETIC MOMENT BY G-ane ISLANDS AND NANORIBBONS

To our knowledge, a comprehensive study on the possible strategies to use to maximize the instilled magnetic moment in the G-ene by selective hydrogenation is not present in the literature. For this reason, the rules that we have derived on the dependence of the instilled magnetic moment by the length of the G-ane nanoribbon, by the distance and the junctions between them need at this stage to be exploited, along with the ones already present in the literature. In this regard, several different structures were generated and compared: ribbons (Fig. 4.18) and islands (Fig. 4.19). Differently from what is reported in the literature, where only ribbons were considered, not only the amount of instilled magnetic moment per C atom will be compared but also the relative thermodynamic stability. In regard to the latter, being the hydrogenation process, in principle, controllable, only those systems with the same number of H atoms will be compared for sake of consistency. The dimensions of the supercell are also consistent for all the considered systems. The studied cases are defined on the basis of the number of hydrogens added to the pristine G-ene layer: 64H, 96H, 200H, and 256H (subscript n and i for nanoribbons and islands, respectively). As mentioned at the beginning of this paragraph, the building up of the islands considered the following insights to achieve the highest instilled magnetic moment in the G-ene layer:

i) Zigzag-α sp^2/sp^3 interface since it is, of course, magnetic and energetically in competition with the non-magnetic armchair as the most stable one.

ii) Consider as many 1,3-type junctions to connect the zigzag-α sp^2/sp^3 interfaces, i.e, now the sides of islands.

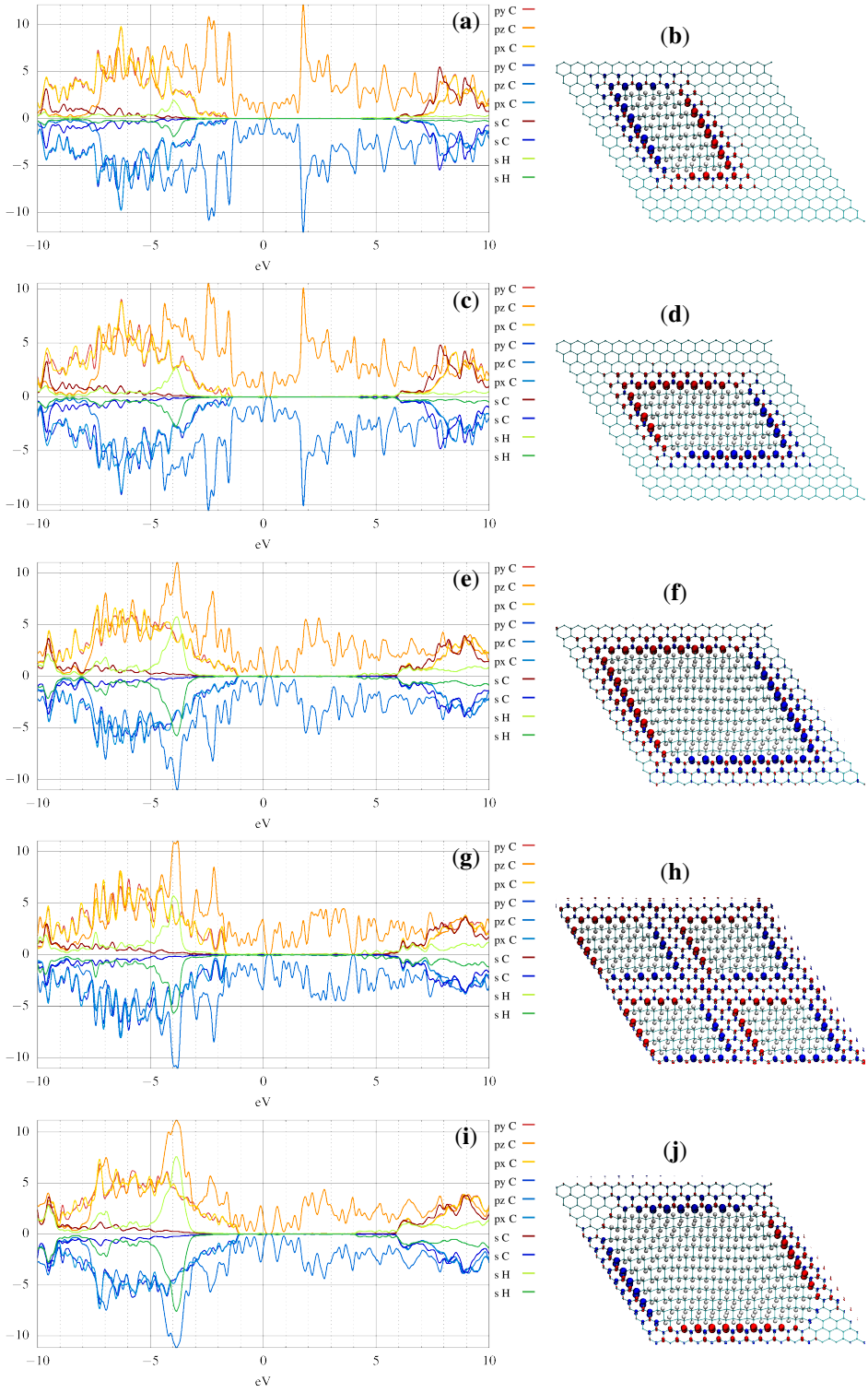

Figure 4.19: Comparison of electronic DOS and structures of several G-ane/G-ene systems with island patterns. The isosurfaces represent the positive (blue) and negative (red) spin density.

iii) Islands with sides neither shorter than 4 nor longer than 14 G-ane rings were considered in consideration of the computed dependence of the magnetic moment with the length of the interface.

iv) The minimum distance between two zigzag-α sp^2/sp^3 interfaces, i. e., n, was set not lower than 3.

64H and 256H (see Fig. 4.19): these two systems were chosen to establish a direct energy comparison between the G-ane nanoribbon and G-ane island patterns in the G-ene matrix as a function of the hydrogenated/not hydrogenated C atoms ratio. The 256H also allows a direct energy comparison with the G-one derivative. In both 64H and 256H cases, the islands showed to be much more stable than the correspondent nanoribbons (78 and 688 kcal/mol, respectively) indicating that islands can effectively represent a stable alternative to them. However, the latter have shown to be able to instill a maximum of 0.29 μ_B per C atom ($64H_n$) and 0.031 μ_B per unit cell ($256H_n$) (see Tab. 4.8). The latter value is lower than expected on the basis of what was obtained for the ($64H_n$) just because the distance between the ribbons was shrunk and this leads to a decrease of magnetic moment at the interfaces (see previous paragraph and [339]). Such values are higher than those achieved in islands, whose maximum values are 0.20 μ_B per C atoms ($64H_i$) and 0.013 μ_B per unit cell ($256H_i$) (see Tab. 4.9). Of course, if these data are compared

Table 4.9: Comparison of magnetic parameters of several G-ane/G-ene systems with island patterns.

System	C	Polarized C	H	Population α (total)	Population per C_{sp^2}	Population per cell	Energy (E_h)
$64H_i$(1)	512	13	64	2.58	0.20	0.010	-2950,494546
$96H_i$(1)	512	15	96	3.12	0.21	0.012	-2969,347745
$200H_i$(4x50H)	512	44	200	4x1.12	0.10	0.018	-3030,072751
$200H_i$(1)	512	21	200	4.63	0.22	0.018	-3030,625088
G-one 256H	512	256	256	255.74	0.99	0.99	-3046.569877
$256H_i$(1)	512	38	256	3.2	0.08	0.013	-3063.709245

with the ones that can be obtained with the homogeneous hydrogenation process of G-ene, i.e., with the G-one, it comes out that only a fraction of the magnetic moment per C atoms and per unit cell can be obtained by the heterogeneous hydrogenation of G-ene. Despite all this, such a fraction of instilled spin, being in the range of 1-3%, can still be detectable for spintronic applications. Being this the case, our results indicate that G-ane islands are by far the most stable systems with respect to both G-one and G-ane nanoribbons. Because of the hydrogenation, a semioccupied

band at the Fermi energy was observed for all the systems with a Dirac cone shifted of ∼0.2 eV at higher energy (Fig. 4.18). Only in the case of the $256H_n$, a larger conduction band was computed in virtue of the larger number of C atoms at the sp^2/sp^3 interfaces.

$64H_i$, $96H_i$, $200H_i$, and $256H_i$ (see Fig. 4.19 and Fig. 4.19): these four systems were considered with the aim to analyze how the magnetic moment could vary in function of the amount of hydrogenation when a single island pattern is chosen. In such systems, however, dual effects are present at the same time: *i)* the number of C atoms at the sp^2/sp^3 interface; *ii)* the different n values. The two effects are, as outlined in the previous paragraph, conflicting with each other. The computed results indicate that these two effects are basically equivalent since the magnetic moments increased by only 0.002 μ_B and 0.003 μ_B for $96H_i$, and $256H_i$ with respect to the value of 0.010 μ_B calculated for $64H_i$, respectively (see Tab. 4.9). Conversely, in the case of $200H_i$, a maximum value of 0.018 μ_B was found, suggesting that a more balanced ratio between the C atoms (21 C) at the sp^2/sp^3 interfaces and the distance between the latters (7 C rings) was reached. It is worth mentioning that another cause of the quenching of the magnetic moment is present in the $256H_i$. Indeed, at the difference of all the other cases where the same junctions-type were used, in such a case for restrictions induced by our supercell dimensions, it was not possible: the two 1,3 sharp corners were "smoothed" by the introduction of a small three-rings-long side connected to the adjacent ones by 1,4 junctions. The latter are known to quench the magnetic moment and, therefore, the obtained value of 0.013 μ_B can be ascribed to that. No significant differences were observed for the DOS but the enlargement of the energy gap (ex G-ene Dirac cone) for the system with the highest hydrogenation coverage (0.06 and 0.11 eV for $200H_i$ and $256H_i$, respectively. See Fig. 4.19).

$200H_i$ single and four islands, $200H_i(1)$ & $200H_i(4)$ (see Fig. 4.19): verified that $200H_i$ shows the best magnetic moment per unit cell, we tried to maximize the number of the C atoms at the sp^2/sp^3 interfaces at the detriment of their distances dividing the single island with four equivalent ones. The number of polarized C atoms is more than doubled (from 21 to 44) and, consequently, the interfaces distances were almost halved (from $n = 6$ to 3). In consideration of their conflicting contributions, the computed value of 0.018 μ_B for the four islands (see Tab. 4.9), i.e., exactly the same computed for the single one, witnesses the proportionality of the two effects. However, in terms of electronic stability, the systems with a single island are far more stable than the one with four islands (346 kcal/mol, 16 eV).

PARTIAL HYDROGENATION ON Au(111) AND Au(111)/G-ene

In order to prove the applicability of the most promising systems in potential devices, the 200H$_i$ system, both in the single and four islands patterns, were adsorbed on different substrates: on a clean unreconstructed Au(111) surface and on a buffer layer of G-ene deposited on the same gold surface. Unlike the Au(111)@G-one scenario, where no hydrogen atoms were present between the gold surface and the G-one carbon skeleton, the two chosen 200H$_i$ systems present half of their H atoms pointing towards the surface beneath. In principle, their presence could prevent an effective overlap between the C_{sp^2} π/π^* system and the gold conduction/valence bands, a scenario that was already found for the G-one@Au(111) and that determined a relevant quenching of the magnetic moment of the adsorbate.

200H$_i$ single and four islands, 200H$_i$(1)@Au(111) & 200H$_i$(4)@Au(111): for the two scenarios, the relaxation of the adsorbate for better interaction with the gold surface was observed. In particular, the evident ripples in the G-ane islands got significantly reduced leading to an overall 200H$_i$ flattened structure. Such a reorganization maximized the adsorbate/substrate interaction which is witnessed by the stretching of the C–H bonds and, to a lesser extent, a shrinking of the C–C ones (see Tab. 4.10 and Fig. 4.20). However, the counterpart of such an effect is

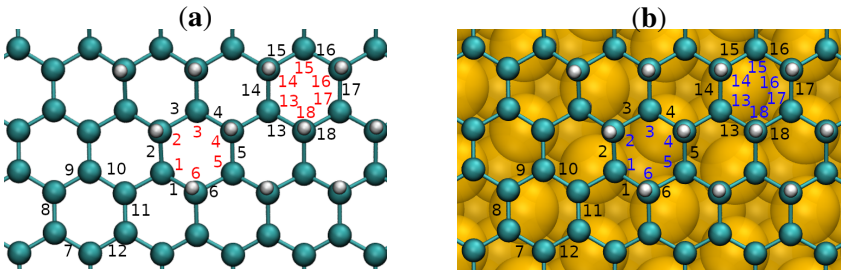

Figure 4.20: C–C and C–H bond lengths of 200H single island system. (**a**) isolated phase. (**b**) Au(111) adsorbed phase. Bond lenghts are reported in Tab. 4.10

that for longer C–H elongations a quenching of the magnetic moment was observed. This can be explained by the partial homolytic cleavage of the C–H bonds with the concurrent formation of the Au–H one, because of the strong affinity of Au atoms towards the H ones. In the 200H$_i$(1)@Au(111) scenario the complete quenching interested not only the C atoms at both 1,3 and 1,4 junctions, where the C–H distances are larger but also two/three more C atoms for single interfaces (island sides): 4/5 C atoms with quenched magnet moment vs. a total of 10 polarized in the isolated scenario (see Fig. 4.19(**f**) and Fig. 4.21). In fact, the magnetic moment

Table 4.10: C–C and C–H bond lengths of 200H$_i$(1) system at the isolated phase and @Au(111).

C–C	Gas	@Au	C–H	Gas	@Au
1	1.542	1.539	1	1.109	1.117
2	1.527	1.526	2	1.105	1.107
3	1.530	1.530	3	1.106	1.111
4	1.532	1.530	4	1.106	1.108
5	1.530	1.530	5	1.105	1.108
6	1.527	1.527	6	1.109	1.111
7	1.444	1.445			
8	1.430	1.430			
9	1.438	1.437			
10	1.445	1.446			
11	1.398	1.400			
12	1.438	1.437			
13	1.529	1.528	13	1.106	1.110
14	1.531	1.531	14	1.106	1.108
15	1.531	1.531	15	1.106	1.110
16	1.528	1.526	16	1.107	1.108
17	1.534	1.533	17	1.106	1.111
18	1.531	1.530	18	1.106	1.108

retained is 2/3 with respect to the latter (see Tab. 4.11) and it has to be compared to 1/4 of the retained magnetic moment for G-one@Au(111). At the first sight, such

Table 4.11: Comparison of magnetic parameters of 200H$_i$ G-ane/G-ene system, when adsorbed directly on Au(111) or on the Au(111)@G-ene system.

System	C	Polarized C	H	Population α (total)	Population per C_{sp^2}	Population per cell
200H$_i$(1)@Au(111)	512	21	200	2.24	0.11	0.009
200H$_i$(1)@Au(111)/G-ene	512	21	200	3.40	0.16	0.013

results indicate that a surface with less affinity towards the hydrogens would be better suited to maintain the magnetic moment in selectively hydrogenated G-ene derivatives and that no spin polarization could be likely obtained when the total number of C atoms for a single sp^2/sp^3 interface is smaller or equal to five. In this regard, the results obtained on the other promising system, 200H$_i$(4)@Au(111), which is formed by four islands with five C_{sp^2} atoms per side and the same number of 1,2 and 1,4 junctions of the 200H$_i$(1), was revealing. Indeed, as expected, a total quenching of the magnetic moment was then observed. Such results gave a mixed picture. They confirmed that it was possible to retain a certain amount of magnetic moment for heterogeneous hydrogenated G-ene derivatives on a metal surface but at

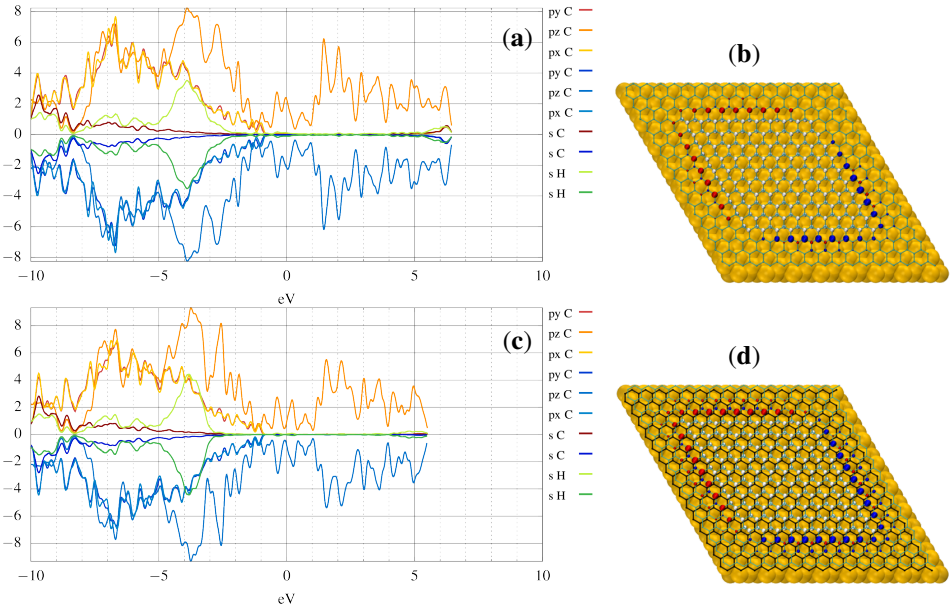

Figure 4.21: Comparison of electronic DOS and structures of 200H single island system. (**a**-**b**) adsorbed on Au. (**c**-**d**) adsorbed on G-ene@Au. The G-ene buffer layer is represented in black in (**d**). See Tab. 4.10 for Mulliken population analysis.

the same time suggested that this is possible if the number of C atoms at the sp^2/sp^3 interfaces are larger than a critical value. The latter consideration derives from the asymmetric Au–H interactions due to the G-ane island ripples.

$200H_i$ single island on G-ene buffer layer, $200H_i(1)$@Au(111)/G-ene: taking advantage of the above results, a buffer layer of G-ene was introduced between the $200H_i$ systems and the Au(111) surface. As in G-one@Au(111)/G-ene where the magnetic moment was almost totally retained, the aim was to decouple the surface from the adsorbate to avoid strong interactions which could lead to a quenching of the magnetic moment. At the structural level, the ripples in the C atoms skeleton are still maintained even if to a lesser extent than the isolated scenario. As a consequence, the C–H bond variations, although present, are less variated than in the $200H_i(1)$@Au(111). Consequently, some quenching of the magnetic moment was found even in this case. Indeed, even if more limited than in the $200H_i(1)$@Au(111) scenario, the original spin polarization of the C atoms at the sp^2/sp^3 interface was significnatly retained. Such a result is very promising since it suggests that the implantation of technologially relevant spin polarization can be achived in such a kind of systems.

4.5 CONCLUSIONS

The quest for magnetic materials for spintronics has been pushed forward, seeking at implantation of stable magnetic moments on covalently hydrogenated graphene. The formation of covalent bonds between carbon atoms and other species (e.g., hydrogen and fluorine) converts the carbon hybridization from sp^2 to sp^3, which has a principal impact on the electronic properties and local structure of the material. The starting point of this analysis is the characterization of homogeneous hydrogenated systems (G-one and G-ane). The G-one, despite bearing a remarkably high degree of spin polarization ($\sim$1 μ_B per unit cell), was revealed to be significantly less stable compared to other diamagnetic isomers; the G-ane is on the other hand a closed-shell system with diamagnetic character and cannot be employed for our purpose. To overcome the magnetic instability which favors the diamagnetic states for hydrogenated G-ene derivatives, two main approaches have been tested: i) the adsorption of hydrogenated G-ene layer on a substrate (gold and pristine G-ene, or the latter used as buffer layer on the former) to check whether the formation of new surface interactions could stabilize the FM phase; ii) the partial patterned hydrogenation of carbon backbone by means of densely hydrogenated C atoms islands, forming locally a G-ane structure, surrounded by G-ene matrix. The first strategy was found to generate a strong surface-adsorbate interaction that basically reduces the magnetic moment of G-one, while the second one consisted in the formation of 0D hydrogenated structures. The latter disclosed new possibilities to obtain stable systems with the formation of a sizable magnetic moment at the sp^2/sp^3 interface portions of the material through the exploitation of several insights on its maximization that were here obtained. The further step was the one where the synergic interplay of the two strategies adsorbing on Au(111) the best prototypes of 0D structures found during this study. The $200H_i$ system was the 0D one chosen for adsorption on Au(111) and on Au(111)/G-ene. In both cases it confirmed its antiferromagnetic character but while for the latter an almost complete retention of the magnetic moment was observed, in the former a reduction of the 50% was instead computed All the results presented are aimed to give a comprehensive and organized study on the G-ene hydrogenated structures like half hydrogenated graphene (G-one) and nanoribbons/islands of G-ane in a G-ene matrix, demonstrating that G-ane islands are the most stable systems for the same number of H atoms and show a stable antiferromagnetic ground state. Our findings thus suggest that this novel and magneto-active G-ene derivative nanostructure could become achievable more easily than extended G-one or nanoribbons.

5

FINAL REMARKS AND PERSPECTIVES

A systematic theoretical and computational approach has been here presented and applied to case studies in the research areas of molecular quantum bits and materials for spintronics.

It has become clear that molecules carrying a paramagnetic center represent resourceful building blocks as they can offer a high structural versatility compared to bulk materials. The combination of low dimensionality and extremely reduced sizes prompt these compounds at the center of a multidisciplinary investigation with roots in material science, physics and, obviously, chemistry. Indeed, molecular qubits give the unique chance to study spin related quantum effects in well-controlled systems, where synthetic chemistry can play a designing role and where the strengths of the various interactions can be monitored and tuned. The detailed analysis on normal modes contribution to the several relaxation pathways helps in the comprehension of this phenomena with consequences also for experimental studies. Solve this question is expected to be a breakthrough in the building of molecular systems having the desired features, in particular long spin relaxation time even at high temperature.

The state-of-art modeling applied to transition metals complexes modeling has been used and pushed forward in order to investigate their properties in isolated environment or embedded in molecular crystals. An accurate computational protocol, able to reproduce magnetic, structural, and vibrational properties of transition metal complexes was set up. A detailed analysis on normal modes contribution to the direct relaxation pathway, and first attempts to include description of Raman relaxation pathway, deepened the comprehension of this phenomena. Some theoretical attempts to analyze in detail the nature of the most relevant vibrational modes giving rise to spin relaxation have been reported, including the investigation of spin–phonon coupling and the identification of the local molecular vibrations that are more detrimental for coherence in each molecular structure. Their disclosure can allow a proper chemical engineering that can lead to their complete suppression.

Besides the results presented and discussed, concerning the development of a rationale for the chemical design of new molecular qubits proceeding through the understanding of the correlations between the spin-phonon dynamics and the chemical identity of the molecular units, the present work is also expected to stimulate further investigations on the presented topics. Indeed, from a perspective point of view, the results on spin relaxation phenomena can represent very promising first steps in this field; further efforts in understanding the symmetry role in the spin relaxation, new synthesis strategies for a better control of T_1 and T_2, and improvements in the description of bright radiation effects on the spin dynamics are expected to push forward the boundaries of the basic knowledge paving the way to new practical applications of these principles. It is important to stress out that the microscopic description of time dependent spin phenomena represents an aspect of paramount importance due to its broad impact in magnetism, as shown in the present thesis work.

We also investigated several avenues to obtain, at the in silico level, a stable magnetic phase for hydrogenated graphene. It is the first time that a comprehensive study on a wide variety of covalently functionalized derivatives with such different magnetic properties is accomplished within the same computational framework, allowing a detailed and reliable comparison of energetics and magnetic properties already studied in literature and new ones. Noting a close resemblance in the magnetic properties to those of graphene nanoribbons, our results show that graphene islands hold the potential for graphene-based spintronics applications. Indeed, graphane islands could be more advantageous than nanoribbon from the standpoint of developing applications because of similar implanted spin density per carbon atom and high thermodynamical stability besides the experimentally less demanding 0D spot shape geometry, compared to 1D nanoribbons, of hydrogenation pattern proposed. Our findings thus suggest that a novel graphene nanostructure such as a dense surface of graphane islands could become achievable with a potential for future spintronics applications with a variable spin-current density.

A

SUPPLEMENTAL MATERIAL

Table A.1: List of T_1 (μs) vs. T (K) extracted from fit with biexponential (T_1^{slow}, T_1^{fast}) or stretched exponential T_1^{str}. A parameters are the relative amplitudes extracted from biexponential fit, β is the stretching exponent.

	1						2				
T	T_1^{slow}	T_1^{fast}	A	T_1^{str}	β	T	T_1^{slow}	T_1^{fast}	A	T_1^{str}	β
K	μs	μs	a.u.	μs	a.u.	K	μs	μs	a.u.	μs	a.u.
5	16.7	1.79	0.467	4.45	0.470	5	1.41	0.231	0.442	0.498	0.620
10	7.33	0.648	0.626	4.07	0.680	10	0.850	0.141	0.474	0.340	0.640
15	13.16	1.89	0.325	2.56	0.700	15	0.592	0.0960	0.482	0.238	0.640
20	2.27	0.313	0.655	1.34	0.690	20	0.426	0.0706	0.470	0.171	0.650
25	1.60	0.401	0.415	0.680	0.710	25	0.285	0.0498	0.488	0.123	0.660
30	0.737	0.222	0.440	0.363	0.770	30	0.149	0.0238	0.660	0.0910	0.750
40	0.156	0.0286	0.809	0.123	0.860	40	0.0725	0.0195	0.563	0.0420	0.780
50	0.108	0.0200	0.835	0.0910	0.790	50	0.0408	0.0110	0.711	0.0290	0.840
65	0.0265	0.00800	0.617	0.0170	0.810	65	0.0204	0.00666	0.694	0.0150	0.870
80	0.0132	0.00300	0.748	0.0100	0.840	80	0.0242	0.00690	0.184	0.00850	0.830
100	0.00980	0.00290	0.706	0.00700	0.850	100	0.00610	0.00220	0.570	0.00400	0.850
120	0.00550	0.00190	0.618	0.00370	0.840	120	0.00470	0.00190	0.355	0.00260	0.880
130	0.00350	0.00090	0.802	0.00280	0.880	130	0.00320	0.00110	0.436	0.00170	0.810
150	0.00230	0.00089	0.728	0.00180	0.890	150	0.00480	0.00110	0.184	0.00130	0.760

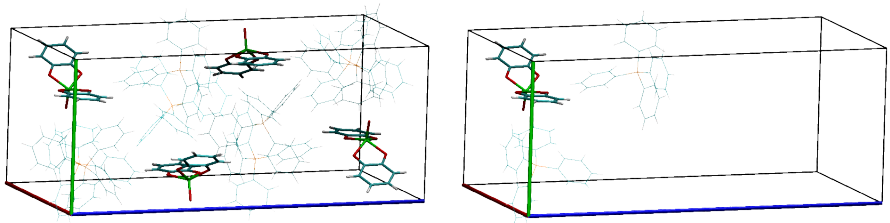

1. $[PPh_4]_2[VO(cat)_2]$

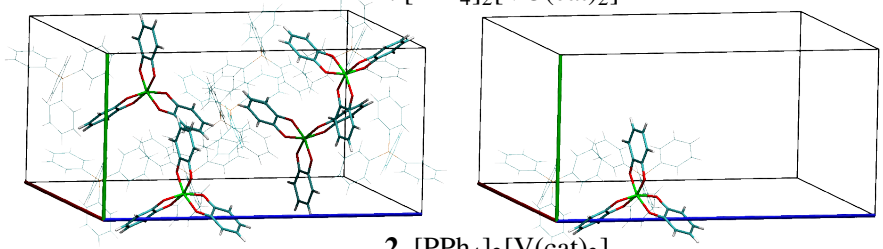

2. $[PPh_4]_2[V(cat)_3]$

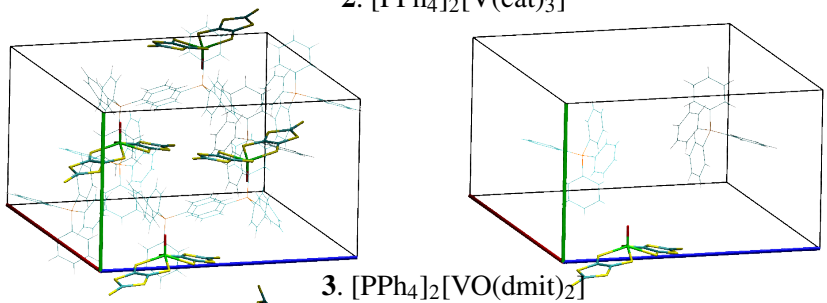

3. $[PPh_4]_2[VO(dmit)_2]$

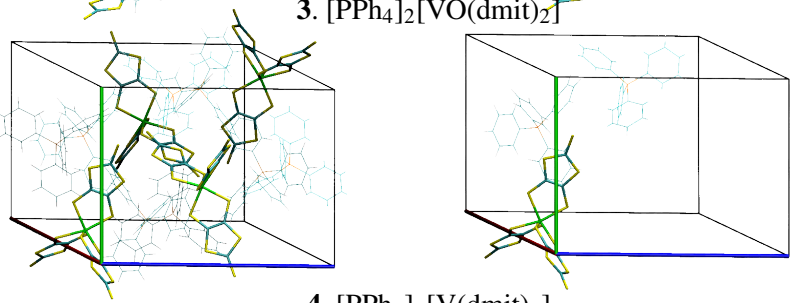

4. $[PPh_4]_2[V(dmit)_3]$

Figure A.1: Left column: orthographic projections of the crystallographic cells. Right column: orthographic projections of general positions of **1** and **4** (asymmetric units) and special positions of **2** and **3** (doubled asymmetric units). Counterions were drawn with thin lines for clarity. The smallest portion containing no fractionary atoms was displayed for each compound.

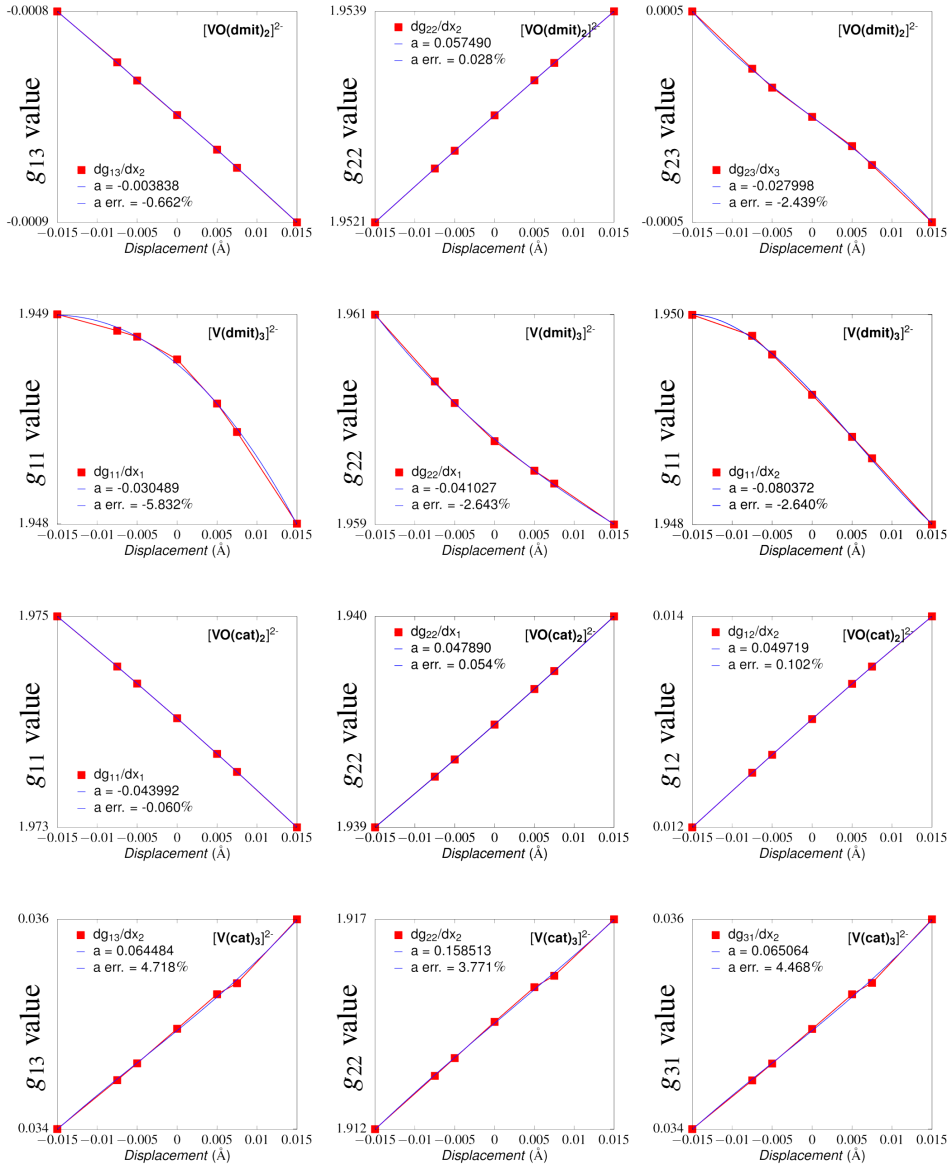

Figure A.2: Spin-phonon coupling coefficients are defined as the first order derivatives of the spin Hamiltonian parameters (in this case the nine components of g tensor) with respect to the normal mode of vibrations $\partial g_{jr}/\partial X_{lv}$. The strategy we employed to compute them starts with the evaluation of the numerical **g** tensor derivatives with respect to the cartesian coordinates of compounds **3**-**4**. The resulting points calculated have then been interpolated with a second order polynomial expression ($bx^2+ax+c=y$) in order to estimate the linear terms, that correspond to the $\partial g_{jr}/\partial X_{lv}$ coefficients. Here we would like to report a few examples to show the details of the method. Graphs reports the scanning of the nine independent g_{jr} elements along the α-th degree of freedom, x.

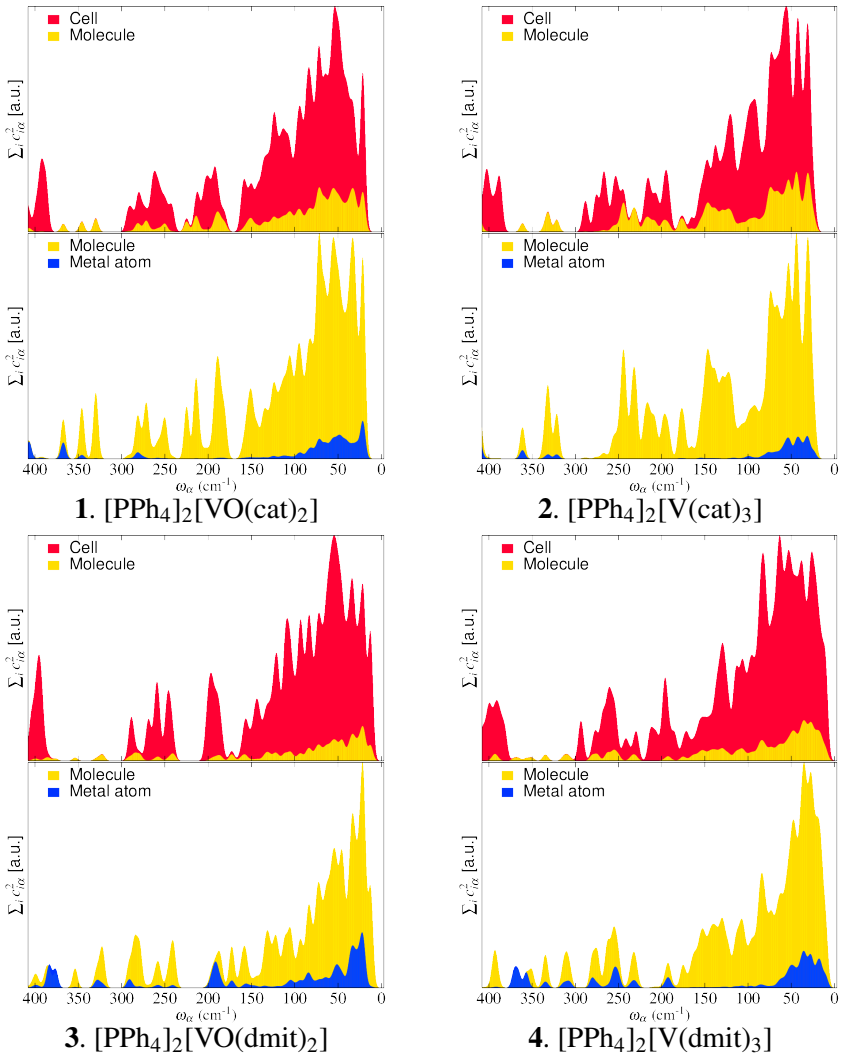

Figure A.3: DFT calculated Density of States (DOS). The red graph shows the sum of squared atomic normal modes coefficients of the whole crystallographic cell. The yellow graph shows the sum of squared atomic normal modes coefficients of the four molecules in the crystallographic cell, neglecting the counterions contribution. The blue graph shows the sum of squared atomic normal modes coefficients of the four vanadium atoms in the crystallographic cell. All the coefficients are referred to a non mass-weighted base set. Normal modes characterized by vanadium atom coefficients are predominantly the low energy ones, as noticeable from the right column.

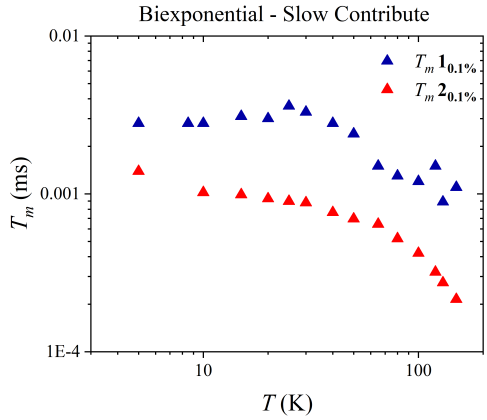

Figure A.4: Log-log plots of T_m (ms) as function of T (K) extracted from fit of Q-band echo decay signals with a biexponential model. Here, slow contribution is reported. The temperature-dependent trends of T_m for $\mathbf{1}_{\mathbf{0.1\%}}$ and $\mathbf{2}_{\mathbf{0.1\%}}$ are comparable with that one extracted by adopting a stretched exponential model (Figure 5 of Main Text). In both cases, compound $\mathbf{1}_{\mathbf{0.1\%}}$ shows higher values of T_m within the probed temperature range.

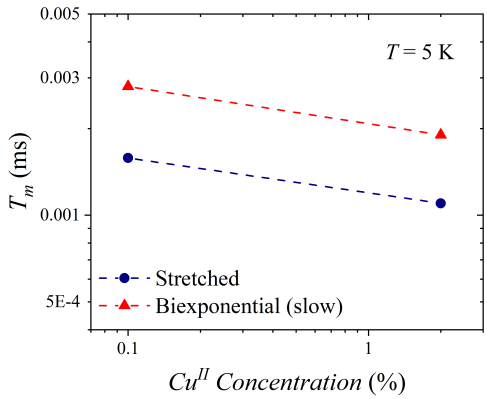

Figure A.5: Plot of T_m (ms) as function of Cu^{II} concentration in the case of [Cu(TTDPz)] an at T = 5 K. The order of magnitude of the lowering in T_m on increasing paramagnetic concentration is in agreement with previous reports on α-[Cu(Pc)] [20].

Table A.2: List of T_m (μs) vs. T (K) extracted from fit with biexponential (T_m^{slow}, T_m^{fast}) or stretched exponential T_m^{str}. A parameters are the relative amplitudes extracted from biexponential fit, β is the stretching exponent.

	1						2				
T	T_m^{slow}	T_m^{fast}	A	T_m^{str}	β	T	T_m^{slow}	T_m^{fast}	A	T_m^{str}	β
K	μs	μs	a.u.	μs	a.u.	K	μs	μs	a.u.	μs	a.u.
5	0.00280	0.000830	0.539	0.00158	0.770	5	0.00139	0.000514	0.101	0.000564	0.940
8.5	0.00280	0.000540	0.758	0.00205	0.790	-	-	-	-	-	-
10	0.00280	0.000480	0.835	0.00234	0.840	10	0.00102	0.000519	0.629	0.000719	0.930
15	0.00310	0.00119	0.815	0.00243	0.890	15	0.000989	0.000455	0.832	0.000817	0.940
20	0.00300	0.00130	0.659	0.00227	0.900	20	0.000933	0.000410	0.866	0.000841	0.00950
25	0.00360	0.00159	0.415	0.00217	0.890	25	0.00089	0.000352	0.914	0.000835	0.960
30	0.00330	0.00140	0.465	0.00204	0.880	30	0.00088	0.000405	0.858	0.000791	0.950
40	0.00280	0.00118	0.519	0.00181	0.870	40	0.000763	0.000155	0.985	0.000753	0.990
50	0.00240	0.000950	0.606	0.00164	0.860	50	0.000695	0.000695	-	0.000697	1.00
65	0.00150	0.00072	0.731	0.00127	0.920	65	0.000643	0.000643	-	0.000658	1.03
80	0.00130	0.000580	0.802	0.00114	0.930	80	0.000521	0.000521	-	0.000549	1.08
100	0.00120	0.000750	0.415	0.000920	0.940	100	0.000420	0.000421	-	0.000444	1.08
120	0.00150	0.000730	0.127	0.000795	0.950	120	0.000320	0.000320	-	0.000341	1.10
130	0.000890	0.000440	0.338	0.000550	0.910	130	0.000274	0.000274	-	0.000288	1.07
150	0.00110	0.000490	0.113	0.000530	0.940	150	0.000215	0.000215	-	0.000221	1.04

Fitting model. Expression (4) of the main text was adopted to fit the temperature dependent behaviour of T_1. The employed expression is reported here for the sake of clarity as (S-4). The latter has been obtained by rearranging the original model reported in [197] in order to introduce our ab initio results. The main assumptions on which our model is based are: i) the trend of second derivatives magnitude involved in the model should be correlated to the first derivatives magnitude for each mode, so that the modulation on $\boldsymbol{g}$ calculated at first order should be similar to the second order modulation; ii) the modulation of A , not included in the model, is correlated to the $\boldsymbol{g}$ modulation as well; iii) the employed model is accounting for the first order $\boldsymbol{g}$ modulation contribution to the spin-phonon coupling interaction. For this reason, a scale factor must be included to encompass both the $\boldsymbol{A}^{Cu}$ tensor modulation and higher order modulations. Additionally, the scale factor is fixed for the whole set of vibrational modes to preserve the relative weight of each mode in the relaxation process.

$$T_1^{-1} = \tilde{a}_{dir}\frac{exp(h\omega_1)/k_BT)}{(exp(h\omega_1)/k_BT)-1)} + \tilde{a}_{Ram}\sum_i \frac{exp(h\omega_i^{s-ph})/k_BT)}{(exp(h\omega_i^{s-ph})/k_BT)-1)^2} \quad \text{(A.1)}$$

Table A.3: List of calculated normal modes (cm^{-1}) with their relative Spin-Phonon coupling (SPC) constants (a.u.) obtained from calculations on **1**. Vibrational modes with higher SPC constants are highlighted in: blue = E_g, orange = B_{2g}, green = B_{1g}, and red = A_{1g}, following associated Mulliken symbols.

α NO.	ω cm^{-1}	Sp-Ph a.u.	Mulliken Symbol
7	11.210	2.15E-008	B2u
8	34.054	1.71E-007	A2u
9	41.048	7.80E-010	B1u
10	58.161	1.77E-005	Eg
11	58.471	1.61E-005	Eg
12	115.09	5.97E-009	B2g
13	123.66	5.54E-009	Eu
14	123.69	1.40E-008	Eu
15	127.08	6.87E-008	B2u
16	131.03	5.82E-006	Eg
17	131.27	5.85E-006	Eg
18	138.66	4.21E-009	
19	150.65	1.00E-008	A2u
20	154.79	3.48E-006	B1g
21	223.79	4.30E-008	B2g
22	230.24	2.80E-008	A2g
23	244.19	2.55E-005	A1g
24	257.81	1.87E-005	Eg
25	257.92	1.77E-005	Eg
26	261.68	2.05E-010	
27	273.43	5.99E-010	
28	273.46	7.34E-009	
29	277.85	1.63E-007	B2g
30	288.41	7.88E-008	A2u
31	291.54	2.84E-008	Eu
32	291.57	6.90E-009	Eu
33	293.09	4.08E-006	Eg
34	293.21	4.26E-006	Eg
35	324.68	4.26E-008	A1u
36	498.14	4.84E-009	B2g
37	499.08	2.18E-007	Eg
38	499.20	1.85E-007	Eg
39	499.48	4.47E-009	
40	506.59	5.65E-010	
41	509.62	3.44E-010	
42	510.34	1.81E-008	Eu
43	510.36	8.86E-010	Eu
44	577.04	2.48E-007	Eg
45	577.18	2.74E-007	Eg
46	588.84	1.29E-005	A1g
47	590.81	1.36E-006	B1g
48	607.65	2.66E-008	A2g
49	620.99	1.09E-008	Eu
50	621.03	1.06E-008	Eu

α NO.	ω cm^{-1}	Sp-Ph a.u.	Mulliken Symbol
51	638.42	1.03E-010	
52	678.40	2.15E-008	A2g
53	680.29	2.97E-008	B2u
54	680.80	6.56E-009	
55	680.88	3.68E-009	
56	701.30	8.71E-006	A1g
57	710.49	1.94E-006	Eg
58	710.57	2.05E-006	Eg
59	720.51	2.67E-007	B1g
60	724.54	2.05E-008	
61	757.17	5.22E-010	
62	757.22	1.04E-009	
63	765.91	7.26E-009	
64	766.57	2.15E-010	
65	771.41	1.36E-007	
66	771.43	1.41E-007	
67	773.85	2.20E-010	
68	787.90	1.72E-008	
69	792.25	7.78E-008	
70	792.55	2.34E-009	
71	792.56	1.24E-010	
72	793.18	2.69E-007	
73	817.89	5.65E-009	
74	817.95	1.86E-008	
75	833.76	8.17E-007	
76	858.29	2.41E-005	
77	866.66	3.48E-009	
78	866.71	3.34E-008	
79	887.98	3.44E-009	
80	1006.2	1.71E-008	
81	1058.3	2.74E-008	
82	1058.3	6.61E-009	
83	1105.7	4.31E-008	
84	1130.9	2.24E-008	
85	1131.0	2.49E-009	
86	1157.7	4.50E-009	
87	1177.8	1.72E-008	
88	1231.1	1.65E-006	
89	1250.7	1.09E-006	
90	1257.2	8.86E-011	
91	1257.2	3.22E-008	
92	1318.6	6.68E-009	
93	1318.7	9.48E-011	
94	1328.4	1.99E-007	
95	1355.2	3.29E-008	
96	1425.1	1.49E-010	

Continued.

α NO.	ω cm^{-1}	Sp-Ph a.u.	Mulliken Symbol
97	1425.2	8.96E-011	
98	1439.5	7.09E-008	
99	1443.3	7.29E-009	
100	1445.3	2.02E-008	
101	1484.1	3.29E-010	
102	1484.2	1.02E-010	
103	1510.8	3.57E-010	
104	1521.9	2.52E-010	
105	1522.1	7.46E-011	
106	1522.2	5.25E-009	
107	1537.8	4.95E-009	
108	1543.4	4.73E-011	
109	1543.5	1.38E-009	
110	1547.8	1.49E-006	
111	1591.5	2.11E-007	

Table A.4: List of calculated normal modes (cm^{-1}) with their relative Spin-Phonon coupling (SPC) constants (a.u.) obtained from calculations on **2**. Vibrational modes with higher SPC constants are highlighted in: blue = E_g, orange = B_{2g}, green = B_{1g}, and red = A_{1g}, following associated Mulliken symbols.

α NO.	ω cm^{-1}	Sp-Ph a.u.	Mulliken Symbol
7	17.383	4.20E-010	B2u
8	33.886	1.17E-009	A2u
9	48.336	2.21E-009	B1u
10	57.782	1.48E-005	Eg
11	58.048	1.45E-005	Eg
12	109.55	5.03E-009	B2g
13	114.77	6.93E-010	A1u
14	117.59	6.41E-006	Eg
15	117.77	6.32E-006	Eg
16	117.85	9.55E-010	Eu
17	117.85	4.32E-009	Eu
18	128.84	3.10E-010	B2u
19	145.28	2.31E-010	A2u
20	167.31	2.79E-006	B1g
21	207.86	7.34E-010	A2g
22	212.97	4.91E-010	B1u
23	228.23	1.39E-008	B2g
24	234.47	1.32E-005	Eg
25	234.55	1.32E-005	Eg
26	253.06	2.33E-005	A1g
27	256.65	1.04E-010	B2u
28	270.02	8.06E-006	Eg
29	270.09	8.02E-006	Eg
30	270.24	6.31E-010	A2u
31	278.25	1.23E-010	Eu
32	278.26	4.73E-011	Eu
33	298.52	7.60E-011	Eu
34	298.53	2.48E-010	Eu
35	330.46	4.92E-010	A2u
36	411.51	6.91E-007	Eg
37	411.59	6.96E-007	Eg
38	411.61	1.14E-009	B2u
39	421.51	1.41E-010	A1u
40	424.53	1.06E-010	A2u
41	479.23	5.66E-010	B2g
42	485.09	6.98E-008	Eg
43	485.14	7.43E-008	Eg
44	502.35	6.05E-010	Eu
45	502.37	4.60E-010	Eu
46	510.38	1.86E-010	B2u
47	552.00	8.67E-007	B1g
48	568.58	1.49E-010	Eu
49	568.60	7.62E-011	Eu
50	573.87	1.31E-009	A2g
51	585.78	1.47E-005	A1g
52	616.47	4.54E-009	A2g
53	616.49	3.20E-011	A1u
54	633.75	1.31E-007	Eg
55	633.77	1.29E-007	Eg
56	636.06	4.68E-011	Eu
57	636.06	2.49E-011	Eu
58	672.79	6.75E-011	B2u
59	673.19	6.53E-007	A1g
60	680.95	5.79E-011	B2u
61	682.06	7.37E-010	B2g
62	711.39	1.23E-006	Eg
63	711.43	1.21E-006	Eg
64	723.84	1.27E-010	A2u
65	743.51	1.69E-007	B1g
66	748.03	3.73E-010	
67	748.07	9.00E-011	
68	766.74	2.13E-010	
69	768.59	2.22E-007	
70	768.74	2.27E-007	
71	771.64	4.29E-011	
72	772.77	1.96E-011	
73	774.24	7.92E-007	
74	774.53	2.06E-011	
75	774.90	1.89E-007	
76	774.95	1.90E-007	
77	799.67	6.47E-011	
78	799.68	6.70E-011	
79	833.16	2.64E-005	A1g
80	848.10	6.82E-009	
81	870.89	3.29E-011	
82	871.08	1.51E-008	
83	871.15	2.83E-011	
84	871.29	1.45E-008	
85	890.96	4.77E-010	
86	890.98	1.35E-010	
87	936.15	7.19E-010	
88	941.44	4.64E-011	
89	941.69	3.53E-009	
90	941.83	3.75E-009	
91	942.11	3.25E-011	
92	971.54	1.19E-010	
93	971.64	1.75E-009	
94	971.80	1.80E-009	
95	971.87	1.20E-010	

Continued.

α NO.	ω cm^{-1}	Sp-Ph a.u.	Mulliken Symbol
96	1008.0	1.02E-008	
97	1008.3	1.72E-011	
98	1008.3	4.69E-011	
99	1008.8	1.24E-007	
100	1034.1	3.84E-009	
101	1063.9	9.04E-011	
102	1063.9	3.83E-011	
103	1091.4	2.43E-010	
104	1102.4	7.48E-011	
105	1102.4	7.78E-012	
106	1106.0	7.20E-009	
107	1122.4	5.57E-009	
108	1125.9	3.43E-006	A1g
109	1129.5	1.50E-011	
110	1129.6	4.39E-011	
111	1143.6	1.67E-007	
112	1170.3	5.07E-007	
113	1173.0	1.78E-011	
114	1173.1	1.01E-010	
115	1185.9	5.45E-007	B1g
116	1189.8	1.71E-010	
117	1194.4	9.17E-012	
118	1194.5	2.53E-011	
119	1203.4	1.51E-008	
120	1285.5	2.35E-011	
121	1285.6	2.72E-011	
122	1286.1	2.85E-010	
123	1293.1	5.46E-009	
124	1305.9	8.41E-007	
125	1324.7	5.83E-011	
126	1324.7	2.53E-011	
127	1357.2	7.66E-007	A1g
128	1381.0	1.84E-011	
129	1381.1	6.16E-012	
130	1389.4	2.16E-008	
131	1407.8	2.64E-009	
132	1419.3	3.33E-011	
133	1419.3	1.81E-011	
134	1427.5	4.93E-008	
135	1442.6	9.12E-010	
136	1449.3	1.31E-008	
137	1467.1	1.52E-011	
138	1467.1	7.00E-011	
139	1468.1	2.15E-010	
140	1475.2	3.33E-010	
141	1485.7	1.52E-011	
142	1485.8	1.33E-011	
143	1495.2	2.36E-009	
144	1516.1	4.01E-011	
145	1516.2	1.10E-011	
146	1525.0	1.34E-006	A1g
147	1562.2	2.29E-007	
148	1590.1	1.72E-011	
149	1590.1	2.18E-011	
150	1591.2	1.86E-009	
151	1591.8	7.35E-010	
152	1607.1	1.14E-010	
153	1609.1	1.59E-012	
154	1609.2	1.20E-011	
155	1610.9	3.90E-010	
156	3177.6	6.18E-011	
157	3177.6	3.77E-011	
158	3177.6	3.78E-011	
159	3177.7	5.53E-010	
160	3182.2	2.19E-010	
161	3182.2	5.22E-012	
162	3182.4	9.14E-012	
163	3182.4	1.26E-010	
164	3186.9	2.72E-011	
165	3187.0	1.70E-011	
166	3187.0	2.40E-011	
167	3187.0	3.97E-010	
168	3191.4	5.77E-010	
169	3191.5	2.27E-011	
170	3191.5	5.54E-011	
171	3191.5	5.77E-010	

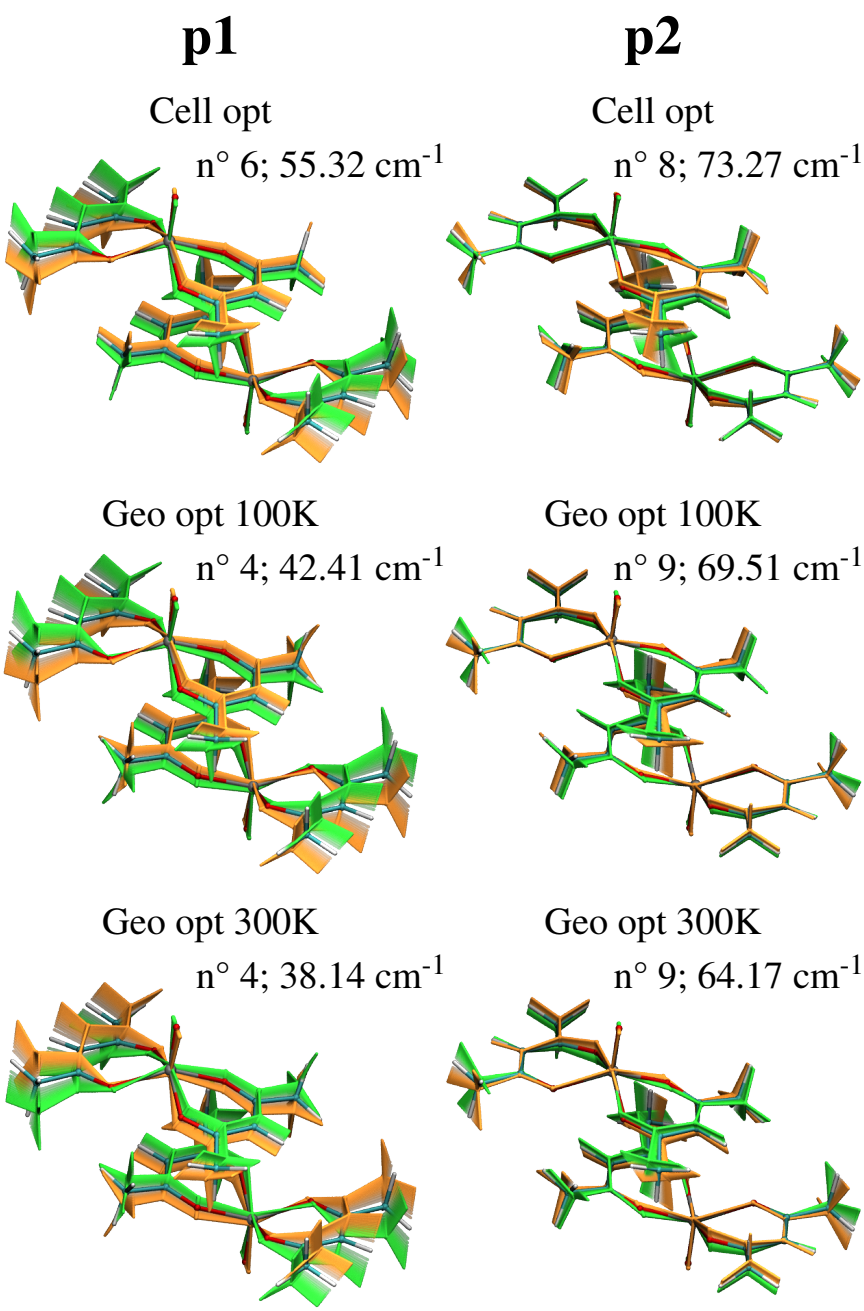

Figure A.6: Normal modes composition in IR peaks 1 and 2 (see Fig. 3.28).

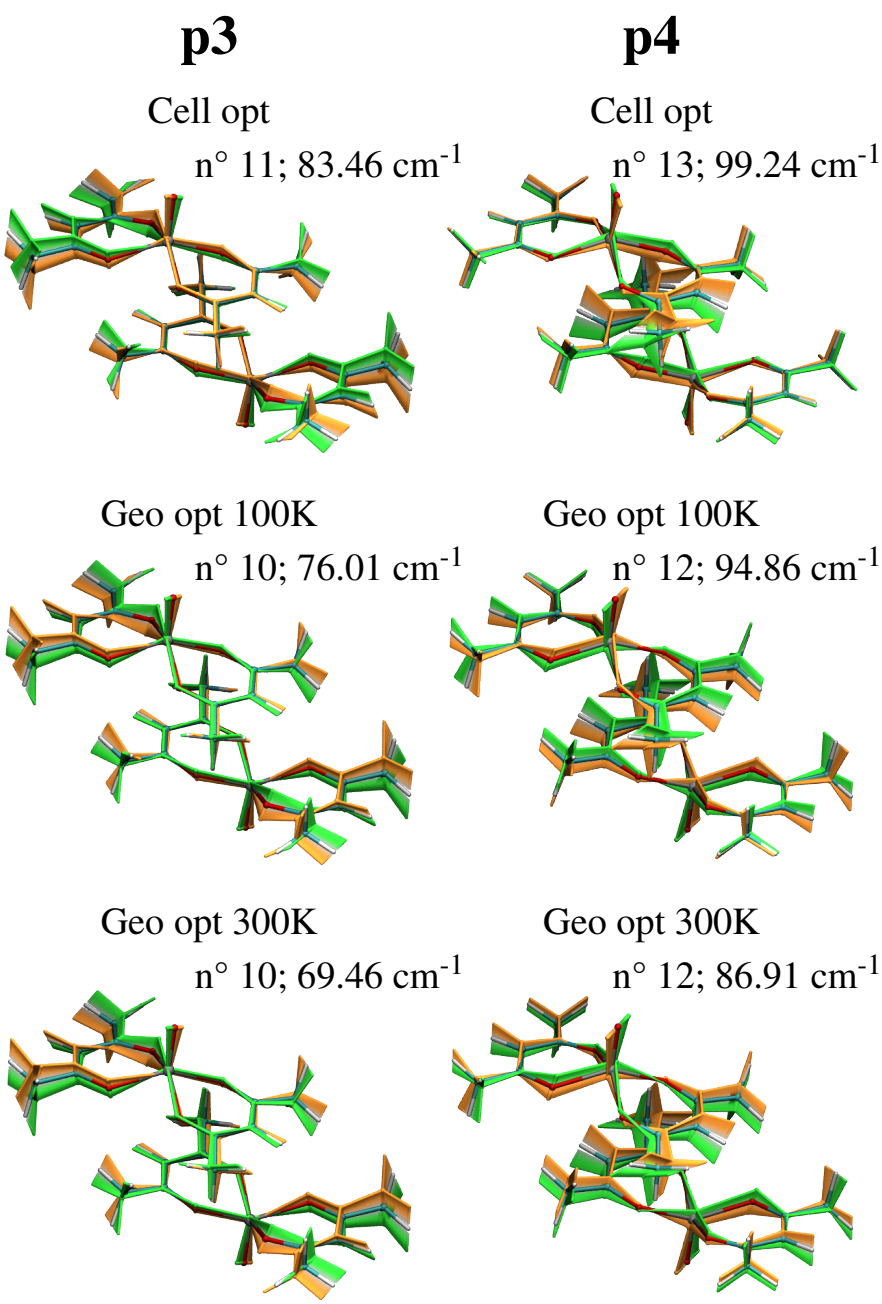

Figure A.7: Normal modes composition in IR peaks 3 and 4 (see Fig. 3.28).

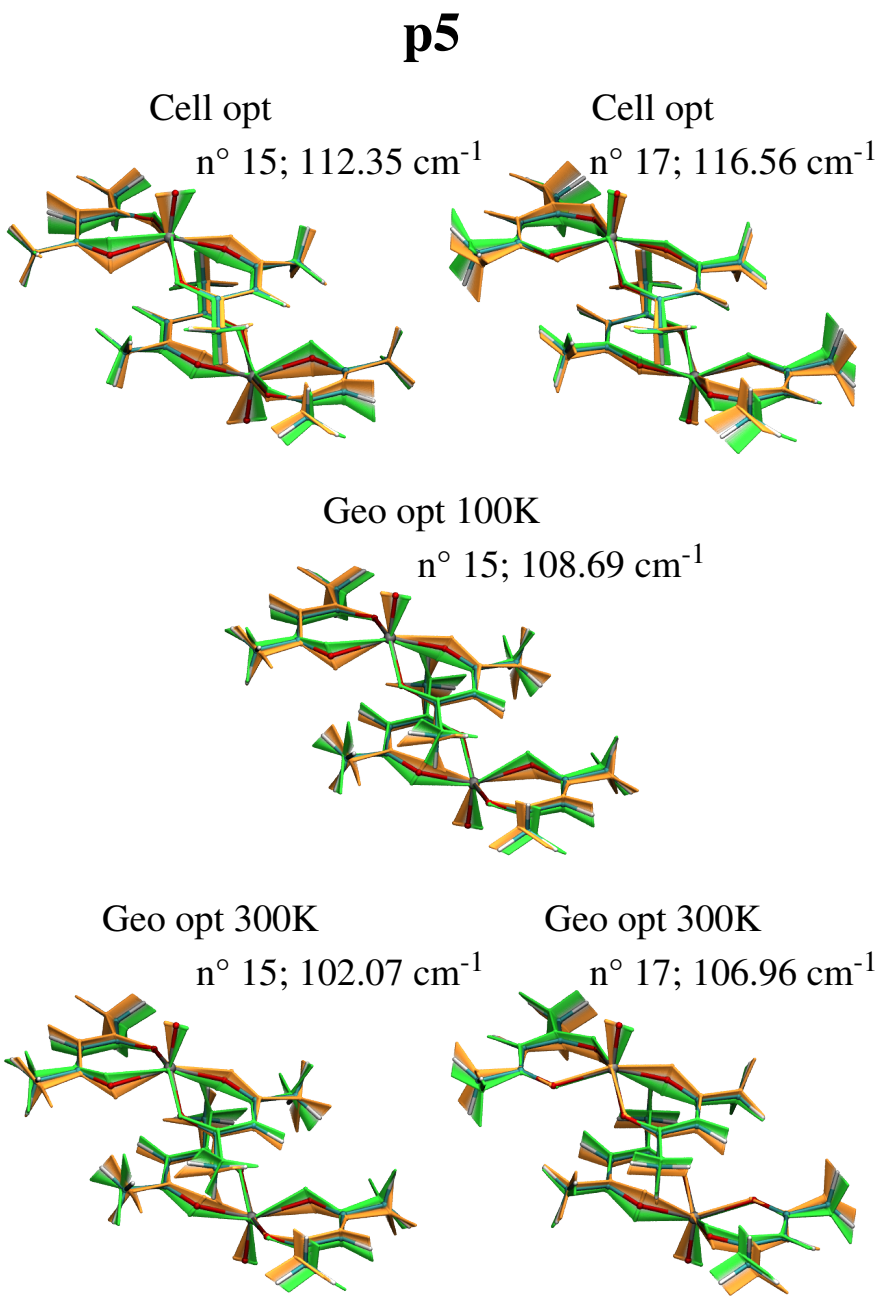

Figure A.8: Normal modes composition in IR peaks 5 (see Fig. 3.28).

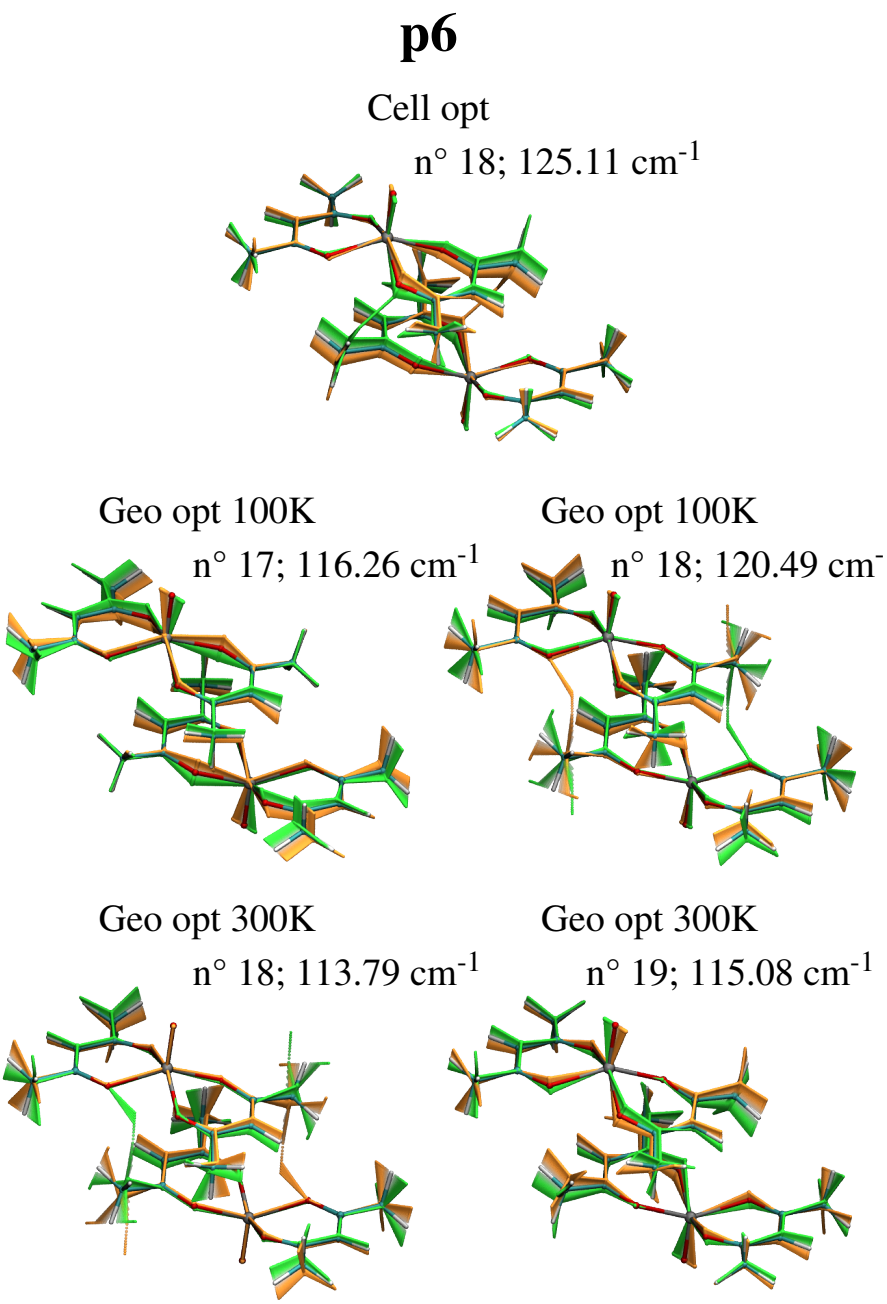

Figure A.9: Normal modes composition in IR peaks 6 (see Fig. 3.28).

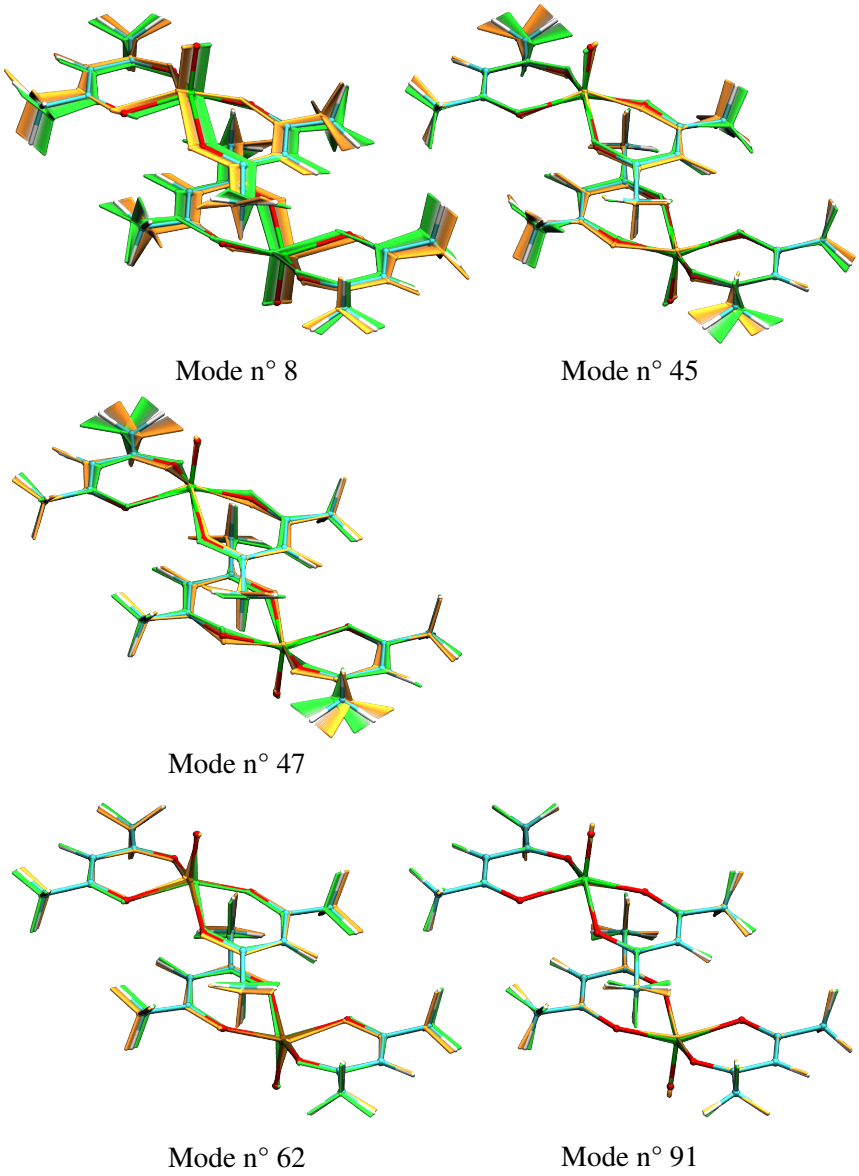

Figure A.10: Normal modes 8, 45, 62, and 91 from $\mathbf{1}_{\mathbf{100K,opt}}$ structure are depicted. 45, 62, and 91 show the largest charges variation and the largest Sp-Ph coupling (see Fig. 3.33).

BIBLIOGRAPHY

[1] T. Sonar. *The History of the Priority Di∫pute between Newton and Leibniz*. Springer International Publishing. Basel: Birkhäuser, **2018**. DOI: 10.1007/978-3-319-72563-5 (cit. on p. v).

[2] C. Benelli and D. Gatteschi. "Magnetism in florence." In: *Coordination Chemistry Reviews* 120.C (**1992**), pp. 137–161. DOI: 10.1016/0010-8545(92)80049-W (cit. on p. 1).

[3] D. N. Hendrickson, W. Wernsdorfer, N. Aliaga-Alcalde, D. N. Hendrickson, and G. Christou. "Exchange-biased quantum tunnelling in a supramolecular dimer of single-molecule magnets." In: *Nature* 416.6879 (**2002**), pp. 406–409. DOI: 10.1038/416406a (cit. on p. 1).

[4] D. Gatteschi, R. Sessoli, and J. Villain. *Molecular Nanomagnets*. Oxford: Oxford University Press, **2006**. DOI: 10.1093/acprof:oso/9780198567530.001.0001 (cit. on pp. 1, 11, 22).

[5] E. J. McInnes. "Spectroscopy of Single-Molecule Magnets." In: *Single-Molecule Magnets and Related Phenomena*. Ed. by R. Winpenny. Berlin, Heidelberg: Springer Berlin Heidelberg, **2006**. DOI: 10.1007/430_034 (cit. on p. 1).

[6] D. Gatteschi, A. Caneschi, and R. Sessoli. *Inorganic and Organometallic Polymers with Special Properties*. Ed. by D. Springer. NATD ASI s. **1992**, pp. 147–160. DOI: 10.1007/978-94-011-2612-0 (cit. on p. 1).

[7] A. Caneschi, D. Gatteschi, R. Sessoli, and P. Rey. "Toward Molecular Magnets: The Metal–Radical Approach." In: *Accounts of Chemical Research* 22.11 (**1989**), pp. 392–398. DOI: 10.1021/ar00167a004 (cit. on p. 1).

[8] O. Kahn. *Molecular Magnetism*. New York: Wiley-VCH, **1993** (cit. on p. 1).

[9] M. Shatruk, S. Gómez-Coca, and K. R. Dunbar. "Molecular Magnetism." In: *Molecular Magnetic Materials: Concepts and Applications; Edited by: Barbara Sieklucka and Dawid Pinkowicz*. Weinheim, Germany: Wiley-vch, **2017** (cit. on p. 1).

[10] D. Gatteschi and R. Sessoli. "Quantum tunneling of magnetization and related phenomena in molecular materials." In: *Angewandte Chemie - International Edition* 42.3 (**2003**), pp. 268–297. DOI: 10.1002/anie.200390099 (cit. on p. 1).

[11] M. Mannini, F. Pineider, P. Sainctavit, C. Danieli, E. Otero, C. Sciancalepore, A. M. Talarico, M. A. Arrio, A. Cornia, D. Gatteschi, and R. Sessoli. "Magnetic memory of a single-molecule quantum magnet wired to a gold surface." In: *Nature Materials* 8.3 (**2009**), pp. 194–197. DOI: 10.1038/nmat2374 (cit. on p. 1).

[12] M. Mannini, F. Pineider, C. Danieli, F. Totti, L. Sorace, P. Sainctavit, M. A. Arrio, E. Otero, L. Joly, J. C. Cezar, A. Cornia, and R. Sessoli. "Quantum tunnelling of the magnetization in a monolayer of oriented single-molecule magnets." In: *Nature* 468.7322 (**2010**), pp. 417–421. DOI: 10.1038/nature09478 (cit. on p. 1).

[13] R. Sessoli. "Materials science: Magnetic molecules back in the race." In: *Nature* 548.7668 (**2017**), pp. 400–401. DOI: 10.1038/548400a (cit. on p. 1).

[14] R. Sessoli, D. Gatteschi, A. Caneschi, and M. A. Novak. "Magnetic bistability in a metal-ion cluster." In: *Nature* 365.6442 (**1993**), pp. 141–143. DOI: 10.1038/365141a0 (cit. on p. 1).

[15] G. Christou, D. Gatteschi, D. N. Hendrickson, and R. Sessoli. "Single-Molecule Magnets." In: *MRS Bulletin* 25.11 (**2000**), pp. 66–71. DOI: 10.1557/mrs2000.226 (cit. on p. 1).

[16] S. Hill, R. S. Edwards, N. Aliaga-Alcalde, and G. Christou. "Quantum Coherence in an Exchange-Couped Dimer of Single-Molecule Magnets." In: *Science* 302.5647 (**2003**), pp. 1015–1018. DOI: 10.1126/science.1090082 (cit. on p. 1).

[17] C. Schlegel, J. Van Slageren, M. Manoli, E. K. Brechin, and M. Dressel. "Direct observation of quantum coherence in single-molecule magnets." In: *Physical Review Letters* 101.14 (**2008**), pp. 1–4. DOI: 10.1103/PhysRevLett.101.147203 (cit. on p. 1).

[18] S. Takahashi, J. Van Tol, C. C. Beedle, D. N. Hendrickson, L. C. Brunel, and M. S. Sherwin. "Coherent manipulation and decoherence of S=10 single-molecule magnets." In: *Physical Review Letters* 102.8 (**2009**), pp. 1–4. DOI: 10.1103/PhysRevLett.102.087603 (cit. on p. 1).

[19] M. Atzori, L. Tesi, E. Morra, M. Chiesa, L. Sorace, and R. Sessoli. "Room-Temperature Quantum Coherence and Rabi Oscillations in Vanadyl Phthalocyanine: Toward Multifunctional Molecular Spin Qubits." In: *Journal of the American Chemical Society* 138.7 (**2016**), pp. 2154–2157. DOI: 10.1021/jacs.5b13408 (cit. on pp. 1, 8, 10, 35, 54).

[20] M. Warner, S. Din, I. S. Tupitsyn, G. W. Morley, A. M. Stoneham, J. A. Gardener, Z. Wu, A. J. Fisher, S. Heutz, C. W. Kay, and G. Aeppli. "Potential for spin-based information processing in a thin-film molecular semiconductor." In: *Nature* 503.7477 (**2013**), pp. 504–508. DOI: 10.1038/nature12597 (cit. on pp. 1, 9, 52, 53, 163).

[21] K. Bader, M. Winkler, and J. Van Slageren. "Tuning of molecular qubits: Very long coherence and spin-lattice relaxation times." In: *Chemical Communications* 52.18 (**2016**), pp. 3623–3626. DOI: 10.1039/c6cc00300a (cit. on pp. 1, 9, 52).

[22] J. M. Zadrozny, J. Niklas, O. G. Poluektov, and D. E. Freedman. "Millisecond coherence time in a tunable molecular electronic spin qubit." In: *ACS Central Science* 1.9 (**2015**), pp. 488–492. DOI: 10.1021/acscentsci.5b00338 (cit. on pp. 1, 35).

[23] L. Tesi, E. Lucaccini, I. Cimatti, M. Perfetti, M. Mannini, M. Atzori, E. Morra, M. Chiesa, A. Caneschi, L. Sorace, and R. Sessoli. "Quantum coherence in a processable vanadyl complex: New tools for the search of molecular spin qubits." In: *Chemical Science* 7.3 (**2016**), pp. 2074–2083 (cit. on p. 1).

[24] H. Li and T. J. Meade. "Molecular Magnetic Resonance Imaging with Gd(III)-Based Contrast Agents: Challenges and Key Advances." In: *Journal of the American Chemical Society* 141.43 (**2019**), pp. 17025–17041. DOI: 10.1021/jacs.9b09149 (cit. on p. 2).

[25] R. Mirzoyan, N. P. Kazmierczak, and R. G. Hadt. "Deconvolving Contributions to Decoherence in Molecular Electron Spin Qubits: A Dynamic Ligand Field Approach." In: *Chemistry – A European Journal* (**2021**), pp. 1–14. DOI: 10.1002/chem.202100845 (cit. on pp. 3, 36, 85).

[26] M. R. Wasielewski, M. D. Forbes, N. L. Frank, K. Kowalski, G. D. Scholes, J. Yuen-Zhou, M. A. Baldo, D. E. Freedman, R. H. Goldsmith, T. Goodson, M. L. Kirk, J. K. McCusker, J. P. Ogilvie, D. A. Shultz, S. Stoll, and K. B. Whaley. "Exploiting chemistry and molecular systems for quantum information science." In: *Nature Reviews Chemistry* 4.9 (**2020**), pp. 490–504. DOI: 10.1038/s41570-020-0200-5 (cit. on p. 3).

[27] L. Escalera-Moreno, J. J. Baldoví, A. Gaita-Ariño, and E. Coronado. "Spin states, vibrations and spin relaxation in molecular nanomagnets and spin qubits: A critical perspective." In: *Chemical Science* 9.13 (**2018**), pp. 3265–3275. DOI: 10.1039/c7sc05464e (cit. on pp. 3, 42).

[28] R. Hoffmann. "How Chemistry and Physics Meet in the Solid State." In: *Angewandte Chemie International Edition in English* 26.9 (**1987**), pp. 846–878. DOI: 10.1002/anie.198708461 (cit. on p. 3).

[29] N. D. Mermin and N. W. Ashcroft. *Solid State Physics*. **1976**, p. 826 (cit. on p. 3).

[30] P. W. Shor. "Algorithms for quantum computation: discrete logarithms and factoring." In: *Proceedings 35th Annual Symposium on Foundations of Computer Science* (**1994**), pp. 124–134. DOI: 10.1109/SFCS.1994.365700 (cit. on p. 5).

[31] A. Acín, I. Bloch, H. Buhrman, T. Calarco, C. Eichler, J. Eisert, D. Esteve, N. Gisin, S. J. Glaser, F. Jelezko, S. Kuhr, M. Lewenstein, M. F. Riedel, P. O. Schmidt, R. Thew, A. Wallraff, I. Walmsley, and F. K. Wilhelm. "The quantum technologies roadmap: A European community view." In: *New Journal of Physics* 20.8 (**2018**), p. 080201. DOI: 10.1088/1367-2630/aad1ea (cit. on pp. 5, 8).

[32] J. J. Pla, K. Y. Tan, J. P. Dehollain, W. H. Lim, J. J. Morton, D. N. Jamieson, A. S. Dzurak, and A. Morello. "A single-atom electron spin qubit in silicon." In: *Nature* 489.7417 (**2012**), pp. 541–545. DOI: 10.1038/nature11449 (cit. on p. 5).

[33] S. Asaad, V. Mourik, B. Joecker, M. A. Johnson, A. D. Baczewski, H. R. Firgau, M. T. Mądzik, V. Schmitt, J. J. Pla, F. E. Hudson, K. M. Itoh, J. C. McCallum, A. S. Dzurak, A. Laucht, and A. Morello. "Coherent electrical control of a single high-spin nucleus in silicon." In: *Nature* 579.7798 (**2020**), pp. 205–209. DOI: 10.1038/s41586-020-2057-7 (cit. on p. 5).

[34] S. Ebadi, T. T. Wang, H. Levine, A. Keesling, G. Semeghini, A. Omran, D. Bluvstein, R. Samajdar, H. Pichler, W. W. Ho, S. Choi, S. Sachdev, M. Greiner, V. Vuletic, and M. D. Lukin. "Quantum Phases of Matter on a 256-Atom Programmable Quantum Simulator." In: *Nature* 595.December 2020 (**2020**). DOI: 10.1038/s41586-021-03582-4 (cit. on p. 5).

[35] A. Chiesa, F. Tacchino, M. Grossi, P. Santini, I. Tavernelli, D. Gerace, and S. Carretta. "Quantum hardware simulating four-dimensional inelastic neutron scattering." In: *Nature Physics* 15.5 (**2019**), pp. 455–459. DOI: 10.1038/s41567-019-0437-4 (cit. on p. 5).

[36] F. Tacchino, A. Chiesa, R. Sessoli, I. Tavernelli, and S. Carretta. "A proposal for using molecular spin qudits as quantum simulators of light–matter interactions." In: *Journal of Materials Chemistry C* 9.32 (**2021**), pp. 10266–10275. DOI: 10.1039/d1tc00851j (cit. on p. 5).

[37] L. Crippa, F. Tacchino, M. Chizzini, A. Aita, M. Grossi, A. Chiesa, P. Santini, I. Tavernelli, and S. Carretta. "Simulating Static and Dynamic Properties of Magnetic Molecules with Prototype Quantum Computers." In: *Magnetochemistry* 7.8 (**2021**), p. 117. DOI: 10.3390/magnetochemistry7080117 (cit. on p. 5).

[38] A. W. Harrow and A. Montanaro. "Quantum computational supremacy." In: *Nature* 549.7671 (**2017**), pp. 203–209. DOI: 10.1038/nature23458 (cit. on p. 5).

[39] F. Arute, K. Arya, R. Babbush, D. Bacon, J. C. Bardin, R. Barends, R. Biswas, S. Boixo, F. G. Brandao, D. A. Buell, B. Burkett, Y. Chen, Z. Chen, B. Chiaro, R. Collins, W. Courtney, A. Dunsworth, E. Farhi, B. Foxen, A. Fowler, C. Gidney, M. Giustina, R. Graff, K. Guerin, S. Habegger, M. P. Harrigan, M. J. Hartmann, A. Ho, M. Hoffmann, T. Huang, T. S. Humble, S. V. Isakov, E. Jeffrey, Z. Jiang, D. Kafri, K. Kechedzhi, J. Kelly, P. V. Klimov, S. Knysh, A. Korotkov, F. Kostritsa, D. Landhuis, M. Lindmark, E. Lucero, D. Lyakh, S. Mandrà, J. R. McClean, M. McEwen, A. Megrant, X. Mi, K. Michielsen, M. Mohseni, J. Mutus, O. Naaman, M. Neeley, C. Neill, M. Y. Niu, E. Ostby, A. Petukhov, J. C. Platt, C. Quintana, E. G. Rieffel, P. Roushan, N. C. Rubin, D. Sank, K. J. Satzinger, V. Smelyanskiy, K. J. Sung, M. D. Trevithick, A. Vainsencher, B. Villalonga, T. White, Z. J. Yao, P. Yeh, A. Zalcman, H. Neven, and J. M. Martinis. "Quantum supremacy using a programmable superconducting processor." In: *Nature* 574.7779 (**2019**), pp. 505–510. DOI: 10.1038/s41586-019-1666-5 (cit. on p. 5).

[40] M. A. Nielsen and I. L. Chuang. *Quantum Computation and Quantum Information*. Cambridge University Press, **2010** (cit. on pp. 5, 6, 15).

[41] F. Petruccione and H. Breuer. *The Theory of Open Quantum System*. Oxford University Press, **2002** (cit. on pp. 5, 17, 39).

[42] M. Le Bellac. *A Short Introduction to Quantum Information and Quantum Computation*. **2006**, pp. 1–179. DOI: 10.1017/CBO9780511755361 (cit. on p. 5).

[43] D. P. DiVincenzo. "The Physical Implementation of Quantum Computing." In: *Fortschr. Phys.* 48.9-11 (**2000**), pp. 771–783. DOI: doi.org/10.1002/1521-3978 (cit. on pp. 5, 16).

[44] C. E. Shannon. "A Mathematical Theory of Communication." In: *Bell System Technical Journal* 27.4 (**1948**), pp. 623–656. DOI: 10.1002/j.1538-7305.1948.tb00917.x (cit. on p. 6).

[45] F. Bloch. "Nuclear Induction." In: *Physical Review* 70.1946 (**1946**), pp. 460–473. DOI: http://dx.doi.org/10.1103/PhysRev.70.460 (cit. on pp. 6, 13, 15, 16).

[46] E. Majorana. "Atomi orientati in campo magnetico variabile." In: *Ettore Majorana Scientific Papers: On occasion of the centenary of his birth* 2 (**2006**), pp. 113–136. DOI: 10.1007/978-3-540-48095-2_7 (cit. on pp. 6, 15).

[47] C. Bonizzoni, A. Ghirri, F. Santanni, M. Atzori, L. Sorace, R. Sessoli, and M. Affronte. "Storage and retrieval of microwave pulses with molecular spin ensembles." In: *npj Quantum Information* 6.1 (**2020**). DOI: 10.1038/s41534-020-00296-9 (cit. on p. 7).

[48] A. Chiesa, E. Macaluso, F. Petiziol, S. Wimberger, P. Santini, and S. Carretta. "Molecular Nanomagnets as Qubits with Embedded Quantum-Error Correction." In: *Journal of Physical Chemistry Letters* 11.20 (**2020**), pp. 8610–8615. DOI: 10.1021/acs.jpclett.0c02213 (cit. on pp. 7, 9, 10).

[49] A. Schweiger and G. Jeschke. *Principles of Pulse Electron Paramagnetic Resonance*. Oxford: Oxford University Press, **2001** (cit. on pp. 7, 12, 14, 19).

[50] D. G. Cory, A. F. Fahmy, and T. F. Havel. "Ensemble quantum computing by NMR spectroscopy." In: *Proceedings of the National Academy of Sciences of the United States of America* 94.5 (**1997**), pp. 1634–1639. DOI: 10.1073/pnas.94.5.1634 (cit. on pp. 7, 8).

[51] S. Sproules. "Molecules as electron spin qubits." In: *Electron Paramagnetic Resonance: Volume 25*. Vol. 25. The Royal Society of Chemistry, **2017**, pp. 61–97. DOI: 10.1039/9781782629436-00061. URL: http://dx.doi.org/10.1039/9781782629436-00061 (cit. on p. 8).

[52] J. I. Cirac and P. Zoller. "Quantum computations with cold trapped ions." In: *Physical Review Letters* 74.20 (**1995**), pp. 4091–4094. DOI: 10.1103/PhysRevLett.74.4091 (cit. on pp. 8, 129).

[53] M. H. Devoret and R. J. Schoelkopf. *Superconducting circuits for quantum information: An outlook*. **2013**. DOI: 10.1126/science.1231930 (cit. on p. 8).

[54] E. Knill, R. Laflamme, and G. J. Milburn. "A scheme for efficient quantum computation with linear optics." In: *Nature* 409.6816 (**2001**), pp. 46–52. DOI: 10.1038/35051009 (cit. on p. 8).

[55] L. M. K. Vandersypen, M. Steffen, G. Breyta, C. S. Yannoni, M. H. Sherwood, and I. L. Chuang. "Experimental realization of Shor's quantum factoring algorithm using nuclear magnetic resonance." In: *Nature* 414.1976 (**2001**), pp. 883–887 (cit. on p. 8).

[56] Z. L. Xiang, S. Ashhab, J. Q. You, and F. Nori. "Hybrid quantum circuits: Superconducting circuits interacting with other quantum systems." In: *Reviews of Modern Physics* 85.2 (**2013**), pp. 623–653. DOI: 10.1103/RevModPhys.85.623 (cit. on p. 8).

[57] C. Bonizzoni, A. Ghirri, and M. Affronte. "Coherent coupling of molecular spins with microwave photons in planar superconducting resonators." In: *Advances in Physics: X* 3.1 (**2018**). DOI: 10.1080/23746149.2018.1435305 (cit. on p. 8).

[58] H. Bernien, B. Hensen, W. Pfaff, G. Koolstra, M. S. Blok, L. Robledo, T. H. Taminiau, M. Markham, D. J. Twitchen, L. Childress, and R. Hanson. "Heralded entanglement between solid-state qubits separated by three metres." In: *Nature* 497.7447 (**2013**), pp. 86–90. DOI: 10.1038/nature12016 (cit. on p. 8).

[59] L. Li, T. Schroder, E. H. Chen, M. Walsh, I. Bayn, J. Goldstein, O. Gaathon, M. E. Trusheim, M. Lu, J. Mower, M. Cotlet, M. L. Markham, D. J. Twitchen, and D. Englund. "Coherent spin control of a nanocavity-enhanced qubit in diamond." In: *Nature Communications* 6 (**2015**). DOI: 10.1038/ncomms7173 (cit. on p. 8).

[60] R. Hanson and D. D. Awschalom. "Coherent manipulation of single spins in semiconductors." In: *Nature* 453.7198 (**2008**), pp. 1043–1049. DOI: 10.1038/nature07129 (cit. on p. 8).

[61] D. Loss and D. P. DiVincenzo. "Quantum computation with quantum dots." In: *Physical Review A* 57.1 (**1998**), pp. 120–126. DOI: 10.1103/PhysRevA.57.120 (cit. on p. 8).

[62] A. Imamoglu, D. D. Awschalom, G. Burkard, D. P. DiVincenzo, D. Loss, M. Sherwin, and A. Small. "Quantum Information Processing Using Quantum Dot Spins and Cavity QED." In: *Phys. Rev. Lett.* 83 (20 **1999**), pp. 4204–4207. DOI: 10.1103/PhysRevLett.83.4204 (cit. on p. 8).

[63] F. Meier, J. Levy, and D. Loss. "Quantum Computing with Spin Cluster Qubits." In: *Physical Review Letters* 90.4 (**2003**), p. 4. DOI: 10.1103/PhysRevLett.90.047901 (cit. on p. 8).

[64] F. Meier, J. Levy, and D. Loss. "Quantum computing with antiferromagnetic spin clusters." In: *Physical Review B - Condensed Matter and Materials Physics* 68.13 (**2003**), pp. 1–15. DOI: 10.1103/PhysRevB.68.134417 (cit. on p. 8).

[65] P. Santini, S. Carretta, and G. Amoretti. “Magnetic Molecules as Spin Qubits.” In: *Molecular Magnetic Materials: Concepts and Applications; Edited by: Barbara Sieklucka and Dawid Pinkowicz*. Weinheim, Germany: Wiley-vch, **2017** (cit. on pp. 8, 9, 15).

[66] A. Gaita-Ariño, F. Luis, S. Hill, and E. Coronado. “Molecular spins for quantum computation.” In: *Nature Chemistry* 11.4 (**2019**), pp. 301–309. DOI: 10.1038/s41557-019-0232-y (cit. on p. 8).

[67] A. Ardavan, O. Rival, J. J. Morton, S. J. Blundell, A. M. Tyryshkin, G. A. Timco, and R. E. Winpenny. “Will spin-relaxation times in molecular magnets permit quantum information processing?” In: *Physical Review Letters* 98.5 (**2007**), pp. 1–4. DOI: 10.1103/PhysRevLett.98.057201 (cit. on p. 9).

[68] M. N. Leuenberger and D. Loss. “Quantum computing in molecular magnets.” In: *Nature* 410.6830 (**2001**), pp. 789–793. DOI: 10.1038/35071024 (cit. on p. 9).

[69] A. Gaita-Ariño, H. Prima-García, S. Cardona-Serra, L. Escalera-Moreno, L. E. Rosaleny, and J. J. Baldoví. “Coherence and organisation in lanthanoid complexes: From single ion magnets to spin qubits.” In: *Inorganic Chemistry Frontiers* 3.5 (**2016**), pp. 568–577. DOI: 10.1039/c5qi00296f (cit. on p. 9).

[70] F. Troiani and M. Affronte. “Molecular spins for quantum information technologies.” In: *Chemical Society Reviews* 40.6 (**2011**), pp. 3119–3129. DOI: 10.1039/c0cs00158a (cit. on pp. 9, 35).

[71] M. Atzori, E. Morra, L. Tesi, A. Albino, M. Chiesa, L. Sorace, and R. Sessoli. “Quantum Coherence Times Enhancement in Vanadium(IV)-based Potential Molecular Qubits: The Key Role of the Vanadyl Moiety.” In: *Journal of the American Chemical Society* 138.35 (**2016**), pp. 11234–11244. DOI: 10.1021/jacs.6b05574 (cit. on pp. 9, 10, 22, 35, 44, 46, 49, 54).

[72] J. J. Baldoví, S. Cardona-Serra, J. M. Clemente-Juan, L. Escalera-Moreno, A. Gaita-Ariño, and G. Mínguez Espallargas. “Quantum Error Correction with magnetic molecules.” In: *Epl* 110.3 (**2015**). DOI: 10.1209/0295-5075/110/33001 (cit. on p. 10).

[73] W. Wernsdorfer and M. Ruben. “Synthetic Hilbert Space Engineering of Molecular Qudits: Isotopologue Chemistry.” In: *Advanced Materials* 31.26 (**2019**). DOI: 10.1002/adma.201806687 (cit. on p. 10).

[74] A. H. Morrish. *The Physical Principles of Magnetism*. Vol. 1. 1. **1965**, p. 88. DOI: 10.1002/9780470546581 (cit. on p. 11).

[75] A. J. Leggett, S Chakravarty, A. T. Dorsey, M. P. A. Fisher, A. Garg, and W Zwerger. “Dynamics of the dissipative two-state system.” In: *Rev. Mod. Phys.* 59.1 (**1987**), pp. 1–85. DOI: 10.1103/RevModPhys.59.1 (cit. on p. 12).

[76] J. Standley and R. A. Vaughan. *Electron Spin Relaxation Phenomena in Solids*. springer, **1969** (cit. on pp. 12, 37).

[77] M. Bustolon and E. Giamello. *Electron Paramagnetic Resonance. A Pratictioner Toolkit*. John Wiley and Sons, Ltd, **2009**. DOI: https://doi.org/10.1002/9780470432235.fmatter (cit. on p. 12).

[78] A. Abragam. *The Principles of Nuclear Magnetism*. London: Clarendon Press, **1961** (cit. on p. 12).

[79] J. H. Van Vleck. “Paramagnetic relaxation times for titanium and chrome alum.” In: *Physical Review* 57.5 (**1940**), pp. 426–447. DOI: 10.1103/PhysRev.57.426 (cit. on p. 12).

[80] N. Bloembergen, E. M. Purcell, and R. V. Pound. “Relaxation effects in nuclear magnetic resonance absorption.” In: *Physical Review* 73.7 (**1948**), pp. 679–712. DOI: 10.1103/PhysRev.73.679 (cit. on p. 12).

[81] N. Bloembergen. “On the interaction of nuclear spins in a crystalline lattice.” In: *Physica* 15.3-4 (**1949**), pp. 386–426. DOI: 10.1016/0031-8914(49)90114-7 (cit. on p. 12).

[82] R. K. Wangness and F. Bloch. “The Dynamical Theory of Nuclear Induction.” In: *Phys. Rev.* 89.4 (**1953**), pp. 728–739. DOI: doi.org/10.1103/PhysRev.89.728 (cit. on p. 12).

[83] I. Solomon. “Relaxation Processes in a System of Two Spins.” In: *Physical Review* 99.2 (**1955**), pp. 559–565. DOI: doi.org/10.1103/PhysRev.99.559 (cit. on p. 12).

[84] R. Orbach. “Spin-Lattice Relaxation in Rare-Earth Salts.” In: *Proceedings of the Royal Society A: Mathematical, Physical and Engineering Sciences* 264.1319 (**1961**), pp. 458–484. DOI: 10.1098/rspa.1961.0211 (cit. on p. 12).

[85] M. Goldman. “Advances in magnetic resonance: Formal theory of spin-lattice relaxation.” In: *Journal of Magnetic Resonance* 149.2 (**2001**), pp. 160–187. DOI: 10.1006/jmre.2000.2239 (cit. on p. 12).

[86] S. S. Eaton and G. R. Eaton. “Relaxation mechanisms.” In: *eMagRes* 5.4 (**2016**), pp. 1543–1556. DOI: 10.1002/9780470034590.emrstm1507 (cit. on p. 12).

[87] F. Marquardt and A. Püttmann. “Introduction to dissipation and decoherence in quantum systems.” In: (**2008**), pp. 1–21 (cit. on p. 13).

[88] F Troiani, V Bellini, and M Affronte. “Decoherence induced by hyperfine interactions with nuclear spins in antiferromagnetic molecular rings.” In: *Phys. Rev. B* 77.5 (**2008**), p. 54428. DOI: 10.1103/PhysRevB.77.054428 (cit. on p. 15).

[89] A. Morello, P. C. Stamp, and I. S. Tupitsyn. “Pairwise decoherence in coupled spin qubit networks.” In: *Physical Review Letters* 97.20 (**2006**), pp. 1–4. DOI: 10.1103/PhysRevLett.97.207206 (cit. on p. 15).

[90] A. Lunghi and S. Sanvito. “How do phonons relax molecular spins?” In: *Science Advances* 5.9 (**2019**), eaax7163. DOI: 10.1126/sciadv.aax7163 (cit. on pp. 15, 31, 46, 78).

[91] R. Righini. “Handout of "Spectroscopic Methods for the structural and dynamic investigation" class.” In: (**2016**) (cit. on p. 15).

[92] M. H. Levitt. *Spin Dynamics: Basics of Nuclear Magnetic Resonance.* 2nd ed. Chichester, England; Hoboken, N.J.: John Wiley & Sons Ltd, **2008** (cit. on p. 16).

[93] K. T. McDonald. *Density-Matrix Description of the EPR “Paradox”*. **Apr. 2013**. URL: https://www.physics.princeton.edu/mcdonald/examples/density.pdf (cit. on p. 16).

[94] P. C. Stamp and A. Gaita-Ariño. “Spin-based quantum computers made by chemistry: Hows and whys.” In: *Journal of Materials Chemistry* 19.12 (**2009**), pp. 1718–1730. DOI: 10.1039/b811778k (cit. on p. 17).

[95] A. Lunghi and S. Sanvito. “Electronic spin-spin decoherence contribution in molecular qubits by quantum unitary spin dynamics.” In: *Journal of Magnetism and Magnetic Materials* 487.April (**2019**), p. 165325. DOI: 10.1016/j.jmmm.2019.165325 (cit. on pp. 17, 101).

[96] W. H. Zurek. "Decoherence, einselection, and the quantum origins of the classical." In: *Reviews of Modern Physics* 75.3 (**2003**), pp. 715–775. DOI: 10.1103/RevModPhys.75.715 (cit. on p. 18).

[97] D. Aravena and E. Ruiz. "Spin dynamics in single-molecule magnets and molecular qubits." In: *Dalton Transactions* 49.29 (**2020**), pp. 9916–9928. DOI: 10.1039/d0dt01414a (cit. on pp. 18, 43).

[98] R. McWeeny. *Spins in Chemistry*. Advances in Magnetic and Optical Resonance. New York: Academic Press, **1970** (cit. on p. 19).

[99] K. M. Salikhov and N. E. Zavoiskaya. "Zavoisky and the discovery of EPR." In: *Resonance* 20.11 (**2015**), pp. 963–968. DOI: 10.1007/s12045-015-0264-6 (cit. on p. 19).

[100] D. A. Hall, D. C. Maus, G. J. Gerfen, S. J. Inati, L. R. Becerra, F. W. Dahlquist, and R. G. Griffin. "Polarization-enhanced NMR spectroscopy of biomolecules in frozen solution." In: *Science* 276.5314 (**1997**), pp. 930–932. DOI: 10.1126/science.276.5314.930 (cit. on p. 19).

[101] J. H. Ardenkjær-Larsen, B. Fridlund, A. Gram, G. Hansson, L. Hansson, M. H. Lerche, R. Servin, M. Thaning, and K. Golman. "Increase in signal-to-noise ratio of >10,000 times in liquid-state NMR." In: *Proceedings of the National Academy of Sciences of the United States of America* 100.18 (**2003**), pp. 10158–10163. DOI: 10.1073/pnas.1733835100 (cit. on p. 19).

[102] P. Carretta and A. Lascialfari. *NMR-MRI, μSR and Mössbauer Spectroscopies in Molecular Magnets*. Milano: Springer, **2007**. DOI: https://doi.org/10.1007/978-88-470-0532-7 (cit. on p. 19).

[103] B. C. Gilbert, D. M. Murphy, and V Chechik. *Electron Paramagnetic Resonance, Volume 23*. Vol. 1. **2012**, p. 311. URL: https://books.google.com/books?id=Sk-Nw5GXO6ACpgis=1 (cit. on p. 19).

[104] G. Mathies, M. A. Caporini, V. K. Michaelis, Y. Liu, K. N. Hu, D. Mance, J. L. Zweier, M. Rosay, M. Baldus, and R. G. Griffin. "Efficient Dynamic Nuclear Polarization at 800 MHz/527 GHz with Trityl-Nitroxide Biradicals." In: *Angewandte Chemie - International Edition* 54.40 (**2015**), pp. 11770–11774. DOI: 10.1002/anie.201504292 (cit. on p. 19).

[105] L. Tesi, D. Bloos, M. Hrtoň, A. Beneš, M. Hentschel, M. Kern, A. Leavesley, R. Hillenbrand, V. Křápek, T. Šikola, and J. V. Slageren. "Plasmonic Metasurface Resonators to Enhance Terahertz Magnetic Fields for High-Frequency Electron Paramagnetic Resonance." In: *Small Methods* (**2021**), p. 2100376. DOI: 10.1002/smtd.202100376 (cit. on p. 19).

[106] P. Neugebauer, D. Bloos, R. Marx, P. Lutz, M. Kern, D. Aguilà, J. Vaverka, O. Laguta, C. Dietrich, R. Clérac, and J. Van Slageren. "Ultra-broadband EPR spectroscopy in field and frequency domains." In: *Physical Chemistry Chemical Physics* 20.22 (**2018**), pp. 15528–15534. DOI: 10.1039/c7cp07443c (cit. on p. 19).

[107] O. Laguta, M. Tuček, J. van Slageren, and P. Neugebauer. "Multi-frequency rapid-scan HFEPR." In: *Journal of Magnetic Resonance* 296.September (**2018**), pp. 138–142. DOI: 10.1016/j.jmr.2018.09.005 (cit. on p. 19).

[108] A. Bencini and D. Gatteschi. "Electron Paramagnetic Resonance Spectroscopy." In: *Inorganic Electronic Structure and Spectroscopy, Volume I. Edited by: E. I. Solomon, A. B. P. Lever*. Hoboken, New Jersey: John Wiley & Sons, **2006** (cit. on p. 19).

[109] S. S. Eaton and G. R. Eaton. "The world as viewed by and with unpaired electrons." In: *Journal of Magnetic Resonance* 223 (**2012**), pp. 151–163. DOI: 10.1016/j.jmr.2012.07.025 (cit. on p. 19).

[110] C. Corvaja. *Introduction to Electron Paramagnetic Resonance*. Hoboken, New Jersey: John Wiley and Sons, Ltd, **2009**. Chap. 1, pp. 1–36. DOI: https://doi.org/10.1002/9780470432235.ch1 (cit. on p. 19).

[111] J. A. Weil and J. R. Bolton. *Electron Paramagnetic Resonance*. Hoboken, New Jersey: John Wiley and Sons, Ltd, **2006**. DOI: https://doi.org/10.1002/9780470084984.fmatter. URL: https://onlinelibrary.wiley.com/doi/abs/10.1002/9780470084984.fmatter (cit. on pp. 19, 24).

[112] L. J. Berliner, S. S. Eaton, and G. R. Eaton. New York: Springer US, **2000** (cit. on pp. 19, 53, 54, 103).

[113] H. C. Torrey. "Transient Nutations in Nuclear Magnetic Resonance." In: *Phys. Rev.* 76 (8 **1949**), pp. 1059–1068. DOI: 10.1103/PhysRev.76.1059 (cit. on p. 19).

[114] E. L. Hahn. "Spin Echoes." In: *Phys. Rev.* 80 (4 **1950**), pp. 580–594. DOI: 10.1103/PhysRev.80.580 (cit. on p. 19).

[115] M. H. Pryce. "A modified perturbation procedure for a problem in paramagnetism." In: *Proceedings of the Physical Society. Section A* 63.1 (**1950**), pp. 25–29. DOI: 10.1088/0370-1298/63/1/304 (cit. on p. 20).

[116] A. Abragam and M. H. L. Pryce. "Theory of the nuclear hyperfine structure of paramagnetic resonance spectra in crystals." In: *Proceedings of the Royal Society of London. Series A. Mathematical and Physical Sciences* 205.1080 (**1951**), pp. 135–153. DOI: 10.1098/rspa.1951.0022 (cit. on p. 20).

[117] J. S. Griffith. London, New York: Cambridge University Press, **1961** (cit. on p. 20).

[118] In: *Theoretical Foundations of Electron Spin Resonance*. Ed. by J. E. Harriman and E. M. Loebl. Vol. 37. Physical Chemistry: A Series of Monographs. New York: Academic Press, **1978**. DOI: https://doi.org/10.1016/B978-0-12-326350-6.50004-8 (cit. on pp. 20, 22).

[119] G. H. Lushington. "The Effective Spin Hamiltonian Concept from a Quantum Chemical Perspective." In: *Calculation of NMR and EPR Parameters. Theory and Applications. Edited by Martin Kaupp, Michael Bühl, Vladimir G. Malkin*. Weinheim, Germany: John Wiley and Sons, Ltd, **2004**. Chap. 4, pp. 33–41. DOI: https://doi.org/10.1002/3527601678.ch4. URL: https://onlinelibrary.wiley.com/doi/abs/10.1002/3527601678.ch4 (cit. on p. 20).

[120] A. Abragam and B. Bleaney. *Electron Paramagnetic Resonance of Transition Ions*. Oxford: Clarendon Press, **1970**. DOI: 10.1017/CBO9781107415324.004 (cit. on pp. 20, 21, 39).

[121] URL: https://easyspin.org/easyspin/documentation/spinoperators.html (cit. on p. 21).

[122] I. Konstantin. "Lecture by Konstantin Ivanov at Roshchino Magnetic Resonance School 2020." In: (**2020**) (cit. on p. 21).

[123] A. Yurkovskaya and G. Bodenhausen. “In memoriam Konstantin L’vovich Ivanov.” In: *Magnetic Resonance* 2.1 (**2021**), pp. 341–342. DOI: 10.5194/mr-2-341-2021 (cit. on p. 21).

[124] J. S. Griffith. “Some investigations in the theory of open-shell ions Part I. The spin-Hamiltonian.” In: *Molecular Physics: An International Journal at the Interface Between Chemistry and Physics* (**1960**), pp. 79–89. DOI: 10.1080/00268976000100091 (cit. on p. 22).

[125] S. Stoll and A. Schweiger. “EasySpin, a comprehensive software package for spectral simulation and analysis in EPR.” In: *Journal of Magnetic Resonance* 178.1 (**2006**), pp. 42–55. DOI: 10.1016/j.jmr.2005.08.013 (cit. on pp. 22, 24).

[126] C. E. Soliverez. “The contact hyperfine interaction: An ill-defined problem.” In: *Journal of Physics C: Solid State Physics* 13.34 (**1980**). DOI: 10.1088/0022-3719/13/34/002 (cit. on p. 22).

[127] D. Gatteschi and L. Sorace. “Hints for the control of magnetic anisotropy in molecular materials.” In: *Journal of Solid State Chemistry* 159.2 (**2001**), pp. 253–261. DOI: 10.1006/jssc.2001.9154 (cit. on p. 23).

[128] W. Heisenberg. “Zur Theorie des Ferromagnetismus.” In: *Zeitschrift für Physik* 49.9 (**2008**), pp. 619–636. DOI: 10.1007/BF01328601 (cit. on p. 23).

[129] A. Bencini and D. Gatteschi. *Electron Paramagnetic Resonance of Exchange Coupled Systems*. Berlin Heidelberg: Springer Verlag, **1990**. DOI: 10.1007/978-3-642-74599-7 (cit. on p. 23).

[130] F. Neese and M. L. Munzarová. “Historical Aspects of EPR Parameter Calculations.” In: *Calculation of NMR and EPR Parameters. Theory and Applications. Edited by Martin Kaupp, Michael Bühl, Vladimir G. Malkin*. Weinheim, Germany: John Wiley and Sons, Ltd, **2004**. Chap. 4, pp. 33–41. DOI: https://doi.org/10.1002/3527601678.ch4. URL: https://onlinelibrary.wiley.com/doi/abs/10.1002/3527601678.ch4 (cit. on p. 24).

[131] L. Lang and F. Neese. “Spin-dependent properties in the framework of the dynamic correlation dressed complete active space method.” In: *Journal of Chemical Physics* 150.10 (**2019**). DOI: 10.1063/1.5085203 (cit. on p. 24).

[132] F. Neese. “Quantum chemistry and EPR parameters.” In: *eMagRes* 6.1 (**2017**), pp. 1–22. DOI: 10.1002/9780470034590.emrstm1505 (cit. on p. 24).

[133] Y. Cao, J. Romero, J. P. Olson, M. Degroote, P. D. Johnson, M. Kieferová, I. D. Kivlichan, T. Menke, B. Peropadre, N. P. Sawaya, S. Sim, L. Veis, and A. Aspuru-Guzik. “Quantum Chemistry in the Age of Quantum Computing.” In: *Chemical Reviews* 119.19 (**2019**), pp. 10856–10915. DOI: 10.1021/acs.chemrev.8b00803 (cit. on p. 24).

[134] K. Möbius, A. Savitsky, A. Schnegg, M. Plato, and M. Fuchs. “High-field EPR spectroscopy applied to biological systems: Characterization of molecular switches for electron and ion transfer.” In: *Physical Chemistry Chemical Physics* 7.1 (**2005**), pp. 19–42. DOI: 10.1039/b412180e (cit. on p. 24).

[135] C. Vallance. *Linear Variational Method and the Secular Determinant*. **Mar. 2020**. URL: https://chem.libretexts.org/@go/page/210833 (cit. on p. 24).

[136] D. Ghosh. “Advances and Applications of Static and Dynamic Correlation Methods in Ab-Initio Quantum Chemistry.” PhD thesis. **2010** (cit. on p. 25).

[137] P. Hohenberg and W. Kohn. "Inhomogeneous Electron Gas." In: *Physical Review B* 36,3B (**1964**), B864–B871. DOI: 10.1103/PhysRevB.7.1912 (cit. on p. 25).

[138] W. Kohn and L. J. Sham. "Self-consistent equations including exchange and correlation effects." In: *Physical Review* 140.4A (**1965**). DOI: 10.1103/PhysRev.140.A1133 (cit. on p. 25).

[139] R. G. Parr and W. Yang. *Density Functional Theory of Atoms and Molecules*. New York, Oxford: Oxford University Press, **1989** (cit. on p. 25).

[140] C. Møller and M. S. Plesset. "Note on an Approximation Treatment for Many-Electron Systems." In: *Phys. Rev.* 46 (7 **1934**), pp. 618–622. DOI: 10.1103/PhysRev.46.618 (cit. on p. 25).

[141] M. Briganti, E. Lucaccini, L. Chelazzi, S. Ciattini, L. Sorace, R. Sessoli, F. Totti, and M. Perfetti. "Magnetic Anisotropy Trends along a Full 4f-Series: The fn+7 Effect." In: *Journal of the American Chemical Society* 143.21 (**2021**), pp. 8108–8115. DOI: 10.1021/jacs.1c02502 (cit. on pp. 25, 84).

[142] A. Szabo and N. Ostlund. *Modern quantum chemistry: introduction to advanced electronic structure theory*. New York: Dover Publications, **1996** (cit. on p. 25).

[143] A. A. Patrascu, M. Briganti, S. Soriano, S. Calancea, R. A. Allão Cassaro, F. Totti, M. G. Vaz, and M. Andruh. "SMM Behavior Tuned by an Exchange Coupling LEGO Approach for Chimeric Compounds: First 2p-3d-4f Heterotrispin Complexes with Different Metal Ions Bridged by One Aminoxyl Group." In: *Inorganic Chemistry* 58.19 (**2019**), pp. 13090–13101. DOI: 10.1021/acs.inorgchem.9b01998 (cit. on p. 26).

[144] J. Paulovič, F. Cimpoesu, M. Ferbinteanu, and K. Hirao. "Mechanism of Ferromagnetic Coupling in Copper(II)-Gadolinium(III) Complexes." In: *Journal of the American Chemical Society* 126.10 (**2004**), pp. 3321–3331. DOI: 10.1021/ja030628k (cit. on p. 26).

[145] A. H. Castro Neto, F. Guinea, N. M. Peres, K. S. Novoselov, and A. K. Geim. "The electronic properties of graphene." In: *Reviews of Modern Physics* 81.1 (**2009**), pp. 109–162. DOI: 10.1103/RevModPhys.81.109 (cit. on pp. 26, 116, 128).

[146] K. Parlinski. "Phonons calculated from first-principles." In: *JDN* 12 (**2011**), pp. 161–166. DOI: 10.1051/sfn/201112008 (cit. on p. 28).

[147] S. Califano, V. Schettino, and N. Neto. *Lattice Dynamics of Molecular Crystals*. Berlin Heidelberg: Springer-Verlag, **1981** (cit. on pp. 28, 48, 71, 75, 76).

[148] Y. Wang, S. L. Shang, H. Fang, Z. K. Liu, and L. Q. Chen. "First-principles calculations of lattice dynamics and thermal properties of polar solids." In: *npj Computational Materials* 2.December 2015 (**2016**). DOI: 10.1038/npjcompumats.2016.6 (cit. on pp. 28, 31).

[149] S. Nudleman and S. S. Mitra, eds. *Optical Properties of Solids*. New York: Springer Science, **1969**. Chap. 14. DOI: 10.1016/B978-0-444-99523-0.50010-6 (cit. on p. 29).

[150] J Kalus, I Natkaniec, and G. S. Pawley. "The 12 external and the 4 lowest internal phonon dispersion branches in d10-anthracene at 12K." In: *Journal of Physics C: ...* 15 (**1982**), pp. 2353–2365. DOI: 10.1088/0022-3719/15/11/016 (cit. on p. 29).

[151] A. Lunghi, F. Totti, R. Sessoli, and S. Sanvito. "The role of anharmonic phonons in under-barrier spin relaxation of single molecule magnets." In: *Nature Communications* 8 (**2017**), pp. 1–7. DOI: 10.1038/ncomms14620 (cit. on pp. 29, 80, 108).

[152] I Natkanie, E. L. Bokhenkov, B. Dorner, J. Kalus, G. A. Mackenzie, G. S. Pawley, U. Schmelzer, and E. F. Sheka. "Phonon dispersion in d8-naphthalene crystal at 6K." In: *J. Phys. C: Solid State Phys.* 13 (**1980**), pp. 4265–4283. DOI: 10.1088/0022-3719/13/23/014 (cit. on p. 30).

[153] M. Yin and M. Cohen. "Calculation of the lattice dynamical properties of Ge." In: *Solid State Communications* 43.5 (**1982**), pp. 391–393. DOI: https://doi.org/10.1016/0038-1098(82)90501-4 (cit. on p. 30).

[154] K. Kunc and R. M. Martin. "Ab initio force constants of GaAs: A new approach to calculation of phonons and dielectric properties." In: *Physical Review Letters* 48.6 (**1982**), pp. 406–409. DOI: 10.1103/PhysRevLett.48.406 (cit. on p. 30).

[155] S. Baroni, S. de Gironcoli, and A. Dal Corso. "Phonons and related crystal properties from density-functional perturbation theory." In: *Reviews of Modern Physics* 73 (**2001**), pp. 515–567. DOI: 10.1103/RevModPhys.73.515 (cit. on p. 30).

[156] P. Kratzer and J. Neugebauer. "The basics of electronic structure theory for periodic systems." In: *Frontiers in Chemistry* 7 (**2019**), pp. 1–18. DOI: 10.3389/fchem.2019.00106 (cit. on pp. 30, 120).

[157] L. Tesi, A. Lunghi, M. Atzori, E. Lucaccini, L. Sorace, F. Totti, and R. Sessoli. "Giant spin–phonon bottleneck effects in evaporable vanadyl-based molecules with long spin coherence." In: *Dalton Trans.* 45.42 (**2016**), pp. 16635–16643. DOI: 10.1039/C6DT02559E (cit. on pp. 31, 36, 41, 68, 78, 82, 87, 88).

[158] F. Neese. "Software update: the ORCA program system, version 4.0." In: *Wiley Interdisciplinary Reviews: Computational Molecular Science* 8.1 (**2018**), pp. 1–6. DOI: 10.1002/wcms.1327 (cit. on pp. 32, 40).

[159] J. P. Perdew. "Jacob's ladder of density functional approximations for the exchange-correlation energy." In: *AIP Conference Proceedings* 577.2001 (**2001**), pp. 1–20. DOI: 10.1063/1.1390175 (cit. on p. 32).

[160] J VandeVondele, M Krack, F Mohamed, M Parrinello, T Chassaing, and J Hutter. "QUICKSTEP: Fast and accurate density functional calculations using a mixed Gaussian and plane waves approach." In: *Comput. Phys. Commun.* 167.2 (**2005**), pp. 103–128. DOI: 10.1016/j.cpc.2004.12.014 (cit. on pp. 32, 120).

[161] J. Hutter, M. Iannuzzi, F. Schiffmann, and J. Vandevondele. "Cp2k: Atomistic simulations of condensed matter systems." In: *Wiley Interdisciplinary Reviews: Computational Molecular Science* 4.1 (**2014**), pp. 15–25. DOI: 10.1002/wcms.1159 (cit. on pp. 32, 120).

[162] T. D. Kühne, M. Iannuzzi, M. Del Ben, V. V. Rybkin, P. Seewald, F. Stein, T. Laino, R. Z. Khaliullin, O. Schütt, F. Schiffmann, D. Golze, J. Wilhelm, S. Chulkov, M. H. Bani-Hashemian, V. Weber, U. Borštnik, M. Taillefumier, A. S. Jakobovits, A. Lazzaro, H. Pabst, T. Müller, R. Schade, M. Guidon, S. Andermatt, N. Holmberg, G. K. Schenter, A. Hehn, A. Bussy, F. Belleflamme, G. Tabacchi, A. Glöß, M. Lass, I. Bethune, C. J. Mundy, C. Plessl, M. Watkins, J. VandeVondele, M. Krack, and J. Hutter. "CP2K: An electronic structure and molecular dynamics software package -Quickstep: Efficient and accurate electronic structure calculations." In: *J. Chem. Phys.* 152.19 (**2020**), p. 194103. DOI: 10.1063/5.0007045 (cit. on pp. 32, 120).

[163] S. Goedecker, M. Teter, and J. Hutter. "Separable dual-space Gaussian pseudopotentials." In: *Phys. Rev. B* 54 (3 **1996**), pp. 1703–1710. DOI: 10.1103/PhysRevB.54.1703 (cit. on pp. 32, 120).

[164] C. Hartwigsen, S. Goedecker, and J. Hutter. "Relativistic separable dual-space Gaussian pseudopotentials from H to Rn." In: *Phys. Rev. B* 58 (7 **1998**), pp. 3641–3662. DOI: 10.1103/PhysRevB.58.3641 (cit. on pp. 32, 120).

[165] M Krack. "Pseudopotentials for H to Kr optimized for gradient-corrected exchange-correlation functionals." In: *Theor. Chem. Acc.* 114.1 (**2005**), pp. 145–152. DOI: 10.1007/s00214-005-0655-y (cit. on pp. 32, 120).

[166] J. P. Perdew, K. Burke, and M. Ernzerhof. "Generalized gradient approximation made simple." In: *Phys. Rev. Lett.* 77.3 (**1996**), p. 3865. DOI: 10.1103/PhysRevLett.77.3865 (cit. on pp. 32, 120).

[167] S. Grimme. "Accurate description of van der Waals complexes by density functional theory including empirical corrections." In: *J. Comput. Chem.* 25.12 (**2004**), pp. 1463–1473. DOI: https://doi.org/10.1002/jcc.20078 (cit. on p. 32).

[168] S. Grimme. "Semiempirical GGA-type density functional constructed with a long-range dispersion correction." In: *J. Comput. Chem.* 27.15 (**2006**), pp. 1787–1799. DOI: https://doi.org/10.1002/jcc.20495 (cit. on p. 32).

[169] S. Grimme, J. Antony, S. Ehrlich, and H. Krieg. "A consistent and accurate ab initio parametrization of density functional dispersion correction (DFT-D) for the 94 elements H-Pu." In: *J. Chem. Phys.* 132.15 (**2010**), p. 154104. DOI: 10.1063/1.3382344 (cit. on p. 32).

[170] S. Grimme. "Supramolecular binding thermodynamics by dispersion-corrected density functional theory." In: *Chemistry - A European Journal* 18.32 (**2012**), pp. 9955–9964. DOI: 10.1002/chem.201200497 (cit. on pp. 32, 89, 91).

[171] D. F. Shanno. "Conjugate Gradient Methods with Inexact Searches." In: *Math. Oper. Res.* 3.3 (**1978**), pp. 244–256. DOI: 10.1287/moor.3.3.244 (cit. on p. 32).

[172] B. G. Pfrommer, M. Cote, S. G. Louie, and M. L. Cohen. "Relaxation of Crystals with the Quasi-Newton Method." In: *J. Comput. Phys.* 131 (**1997**), pp. 233–240 (cit. on p. 32).

[173] M. P. Teter, M. C. Payne, and D. C. Allan. "Solution of Schrödingers equation for large systems." In: *Physical Review B* 40.18 (**1989**), pp. 12255–12263. DOI: 10.1103/PhysRevB.40.12255 (cit. on pp. 32, 120).

[174] A. Albino, S. Benci, L. Tesi, M. Atzori, R. Torre, S. Sanvito, R. Sessoli, and A. Lunghi. "First-Principles Investigation of Spin–Phonon Coupling in Vanadium-Based Molecular Spin Quantum Bits." In: *Inorganic Chemistry* 58.15 (**2019**), pp. 10260–10268. DOI: 10.1021/acs.inorgchem.9b01407 (cit. on pp. 35, 41, 44).

[175] T. Yamabayashi, M. Atzori, L. Tesi, G. Cosquer, F. Santanni, M. E. Boulon, E. Morra, S. Benci, R. Torre, M. Chiesa, L. Sorace, R. Sessoli, and M. Yamashita. "Scaling Up Electronic Spin Qubits into a Three-Dimensional Metal-Organic Framework." In: *Journal of the American Chemical Society* 140.38 (**2018**), pp. 12090–12101. DOI: 10.1021/jacs.8b06733 (cit. on pp. 35, 54, 86, 94, 108).

[176] M. Sato and T. Kwan. "Electron spin resonance study of vanadyl phthalocyanine." In: *The Journal of Chemical Physics* 50.1 (**1965**), pp. 558–559. DOI: 10.1063/1.1696446 (cit. on p. 35).

[177] S. Chicco, A. Chiesa, G. Allodi, E. Garlatti, M. Atzori, L. Sorace, R. De Renzi, R. Sessoli, and S. Carretta. "Controlled coherent dynamics of [VO(TPP)], a prototype molecular nuclear qudit with an electronic ancilla." In: *Chem. Sci.* 12 (36 **2021**), pp. 12046–12055. DOI: 10.1039/D1SC01358K (cit. on p. 35).

[178] R. Orbach. "On the theory of spin-lattice relaxation in paramagnetic salts." In: *Proceedings of the Physical Society* 77.4 (**1961**), pp. 821–826. DOI: 10.1088/0370-1328/77/4/301 (cit. on p. 36).

[179] S. T. Liddle and J. Van Slageren. "Improving f-element single molecule magnets." In: *Chemical Society Reviews* 44.19 (**2015**), pp. 6655–6669. DOI: 10.1039/c5cs00222b (cit. on p. 36).

[180] A. M. Ariciu, D. H. Woen, D. N. Huh, L. E. Nodaraki, A. K. Kostopoulos, C. A. Goodwin, N. F. Chilton, E. J. McInnes, R. E. Winpenny, W. J. Evans, and F. Tuna. "Engineering electronic structure to prolong relaxation times in molecular qubits by minimising orbital angular momentum." In: *Nature Communications* 10.1 (**2019**), pp. 1–8. DOI: 10.1038/s41467-019-11309-3 (cit. on p. 36).

[181] L. Gu and R. Wu. "Origin of the anomalously low Raman exponents in single molecule magnets." In: *Physical Review B* 103.1 (**2021**), pp. 1–24. DOI: 10.1103/PhysRevB.103.014401 (cit. on p. 36).

[182] C. Cohen-Tannoudji, J. Dupont-Roc, and G. Grynberg. *Atom-Photon Interactions*. John Wiley and Sons, Ltd, **1998**. DOI: https://doi.org/10.1002/9783527617197.fmatter (cit. on pp. 38, 100).

[183] S. K. Hoffmann and S. Lijewski. "Phonon spectrum, electron spin-lattice relaxation and spin-phonon coupling of Cu2+ ions in BaF2 crystal." In: *Journal of Magnetic Resonance* 252 (**2015**), pp. 49–54. DOI: 10.1016/j.jmr.2014.12.015 (cit. on p. 38).

[184] Y. P. Kalmykov, W. T. Coffey, and S. V. Titov. *Spin Relaxation In Phase Space*. Vol. 161. John Wiley & Sons, **2016**, pp. 41–275. DOI: 10.1002/9781119290971.ch2 (cit. on p. 39).

[185] J. Villain, F. Hartman-Boutron, R. Sessoli, and A. Rettori. "Magnetic relaxation in big magnetic molecules." In: *Epl* 27.2 (**1994**), pp. 159–164. DOI: 10.1209/0295-5075/27/2/014 (cit. on p. 40).

[186] A. Lunghi and S. Sanvito. "Multiple spin-phonon relaxation pathways in a Kramer single-ion magnet." In: *Journal of Chemical Physics* 153.17 (**2020**). DOI: 10.1063/5.0017118 (cit. on p. 41).

[187] S. D. Jiang, B. W. Wang, G. Su, Z. M. Wang, and S. Gao. "A mononuclear dysprosium complex featuring single-molecule-magnet behavior." In: *Angewandte Chemie - International Edition* 49.41 (**2010**), pp. 7448–7451. DOI: 10.1002/anie.201004027 (cit. on p. 41).

[188] Y. Rechkemmer, F. D. Breitgoff, M. Van Der Meer, M. Atanasov, M. Hakl, M. Orlita, P. Neugebauer, F. Neese, B. Sarkar, and J. Van Slageren. "A four-coordinate cobalt(II) single-ion magnet with coercivity and a very high energy barrier." In: *Nature Communications* 7.Ii (**2016**), pp. 1–8. DOI: 10.1038/ncomms10467 (cit. on p. 41).

[189] L. Escalera-Moreno, J. J. Baldoví, A. Gaita-Ariño, and E. Coronado. "Design of high-temperature: F -block molecular nanomagnets through the control of vibration-induced spin relaxation." In: *Chemical Science* 11.6 (**2020**), pp. 1593–1598. DOI: 10.1039/c9sc03133b (cit. on p. 42).

[190] A. Ullah, J. Cerdá, J. J. Baldoví, S. A. Varganov, J. Aragó, and A. Gaita-Ariño. "In Silico Molecular Engineering of Dysprosocenium-Based Complexes to Decouple Spin Energy Levels from Molecular Vibrations." In: *Journal of Physical Chemistry Letters* 10.24 (**2019**), pp. 7678–7683. DOI: 10.1021/acs.jpclett.9b02982 (cit. on p. 42).

[191] J. Chen, C. Hu, J. F. Stanton, S. Hill, H. P. Cheng, and X. G. Zhang. "Decoherence in Molecular Electron Spin Qubits: Insights from Quantum Many-Body Simulations." In: *Journal of Physical Chemistry Letters* 11.6 (**2020**), pp. 2074–2078. DOI: 10.1021/acs.jpclett.0c00193 (cit. on p. 42).

[192] M. Atzori, S. Benci, E. Morra, L. Tesi, M. Chiesa, R. Torre, L. Sorace, and R. Sessoli. "Structural Effects on the Spin Dynamics of Potential Molecular Qubits." In: *Inorganic Chemistry* (**2017**), acs.inorgchem.7b02616. DOI: 10.1021/acs.inorgchem.7b02616 (cit. on pp. 44, 46, 49, 70).

[193] L. Escalera-Moreno, N. Suaud, A. Gaita-Ariño, and E. Coronado. "Determining Key Local Vibrations in the Relaxation of Molecular Spin Qubits and Single-Molecule Magnets." In: *Journal of Physical Chemistry Letters* 8.7 (**2017**), pp. 1695–1700. DOI: 10.1021/acs.jpclett.7b00479 (cit. on p. 45).

[194] N. Neto and L. Bellucci. "A new algorithm for rigid body molecular dynamics." In: *Chem. Phys.* 328.1-3 (**2006**), pp. 259–268. DOI: 10.1016/j.chemphys.2006.07.009 (cit. on pp. 48, 80).

[195] A. B. P. Lever and E. I. Solomon. *Inorganic Electronic Structure and Spectroscopy, Methodology*. Vol. 1. New Jersey: John Wiley & Sons., **1999**, p. 32 (cit. on pp. 49, 50).

[196] F. Santanni, A. Albino, M. Atzori, D. Ranieri, E. Salvadori, M. Chiesa, A. Lunghi, A. Bencini, L. Sorace, F. Totti, and R. Sessoli. "Probing Vibrational Symmetry Effects and Nuclear Spin Economy Principles in Molecular Spin Qubits." In: *Inorg. Chem.* 60.1 (**2021**), pp. 140–151. DOI: 10.1021/acs.inorgchem.0c02573 (cit. on pp. 52, 60, 83, 103, 108).

[197] A. Lunghi and S. Sanvito. "The limit of spin lifetime in solid-state electronic spins." In: *Journal of Physical Chemistry Letters* 11.15 (**2020**), pp. 1–20. DOI: 10.1021/acs.jpclett.0c01681 (cit. on pp. 52, 54, 67, 165).

[198] Y. Suzuki, M. Fujimori, H. Yoshikawa, and K. Awaga. "Packing motifs and magneto-structural correlations in crystal structures of metallo-tetrakis(1,2,5-thiadiazole)porphyrazine series, MTTDPz (M=H2, Fe, Co, Ni, Cu, Zn)." eng. In: *Chemistry (Weinheim an der Bergstrasse, Germany)* 10.20 (**2004**), pp. 5158–5164. DOI: 10.1002/chem.200400394 (cit. on p. 52).

[199] A. Hoshino, Y. Takenaka, and H. Miyaji. "Redetermination of the crystal structure of α-copper phthalocyanine grown on KCl." In: *Acta Crystallographica Section B* 59.3 (**2003**), pp. 393–403. DOI: 10.1107/S010876810300942X (cit. on p. 52).

[200] C. Y. Lin, T. Ngendahimana, G. R. Eaton, S. S. Eaton, and J. M. Zadrozny. "Counterion influence on dynamic spin properties in a V(iv) complex." In: *Chemical Science* 10.2 (**2019**), pp. 548–555. DOI: 10.1039/c8sc04122a (cit. on p. 53).

[201] M. Atzori, S. Benci, E. Morra, L. Tesi, M. Chiesa, R. Torre, L. Sorace, and R. Sessoli. "Structural Effects on the Spin Dynamics of Potential Molecular Qubits." In: *Inorganic Chemistry* 57.2 (**2018**), pp. 731–740. DOI: 10.1021/acs.inorgchem.7b02616 (cit. on p. 54).

[202] D. Penchoff. “Group Theory: An Application of Discrete Groups.” In: (**2008**). URL: http://sces.phys.utk.edu/~moreo/mm08/penchoïňĂ.pdf (cit. on pp. 60, 61).

[203] N. P. Kazmierczak, R. Mirzoyan, and R. G. Hadt. “The Impact of Ligand Field Symmetry on Molecular Qubit Coherence.” In: *J. Am. Chem. Soc.* (**2021**), pp. 1–27. DOI: 10.1021/jacs.1c04605 (cit. on pp. 60, 110).

[204] A. Albino, S. Benci, M. Atzori, L. Chelazzi, S. Ciattini, A. Taschin, P. Bartolini, A. Lunghi, R. Righini, R. Torre, F. Totti, and R. Sessoli. “Temperature Dependence of Spin–Phonon Coupling in [VO(acac)2]: A Computational and Spectroscopic Study.” In: *The Journal of Physical Chemistry C* 125.40 (**2021**), pp. 22100–22110. DOI: 10.1021/acs.jpcc.1c06916 (cit. on p. 67).

[205] E. Garlatti, L. Tesi, A. Lunghi, M. Atzori, D. J. Voneshen, P. Santini, S. Sanvito, T. Guidi, R. Sessoli, and S. Carretta. “Unveiling phonons in a molecular qubit with four-dimensional inelastic neutron scattering and density functional theory.” In: *Nat. Commun.* 11.1 (**2020**), p. 1751. DOI: 10.1038/s41467-020-15475-7 (cit. on pp. 67, 78, 88).

[206] A. Taschin, P. Bartolini, J. Tasseva, and R. Torre. “THz time-domain spectroscopic investigations of thin films.” In: *J. Measurement* 118 (**2018**), pp. 282–288. DOI: 10.1016/j.measurement.2017.05.074 (cit. on p. 67).

[207] J. Tasseva, A. Taschin, P. Bartolini, J. Striova, R. Fontana, and R. Torre. “Thin layered drawing media probed by THz time-domain spectroscopy.” In: *Analyst* 142.1 (**2017**), pp. 42–47. DOI: 10.1039/c6an02113a (cit. on p. 67).

[208] A. Taschin, P. Bartolini, J. Tasseva, J. Striova, R. Fontana, C. Riminesi, and R. Torre. “Drawing materials studied by THz spectroscopy.” In: *Acta Imeko* 6.3 (**2017**), pp. 12–17 (cit. on p. 67).

[209] E. Shuter, S. J. Rettig, and C. Orvig. “Oxobis(2,4-pentanedionato)vanadium(IV), a Redetermination.” In: *Acta Crystallogr., Sect. C: Cryst. Struct. Commun.* 51.1 (**1995**), pp. 12–14. DOI: 10.1107/s0108270194010462 (cit. on p. 68).

[210] W. Withayachumnankul and M. Naftaly. “Fundamentals of Measurement in Terahertz Time-Domain Spectroscopy.” In: *J. Infrared Milli. Terahz. Waves* 35.8 (**2014**), pp. 610–637. DOI: 10.1007/s10762-013-0042-z (cit. on p. 72).

[211] S. Califano and V. Schettino. “Vibrational relaxation in molecular crystals.” In: *Int. Rev. Phys. Chem.* 7.1 (**1988**), pp. 19–57. DOI: 10.1080/01442358809353204 (cit. on p. 77).

[212] R. Bini, P. Foggi, P. R. Salvi, and V. Schettino. “FTIR study of vibrational relaxation in potassium perchlorate crystal.” In: *J. Phys. Chem.* 94.17 (**1990**), pp. 6653–6658. DOI: 10.1021/j100380a025 (cit. on p. 77).

[213] M. D. King and T. M. Korter. “Application of London-type dispersion corrections in solid-state density functional theory for predicting the temperature-dependence of crystal structures and terahertz spectra.” In: *Cryst. Growth Des.* 11.5 (**2011**), pp. 2006–2010. DOI: 10.1021/cg200211x (cit. on p. 77).

[214] K. N. Shrivastava. “Theory of Spin–Lattice Relaxation.” In: *Phys. Status Solidi B* 117.2 (**1983**), pp. 437–458. DOI: 10.1002/pssb.2221170202 (cit. on p. 85).

[215] URL: https://www.esrf.fr/home.html (cit. on p. 87).

[216] URL: https://www.esrf.fr/UsersAndScience/Experiments/DynExtrCond/ID28/Characteristics (cit. on p. 87).

[217] M. L. Baker, T. Guidi, S. Carretta, J. Ollivier, H. Mutka, H. U. Güdel, G. A. Timco, E. J. Mcinnes, G. Amoretti, R. E. Winpenny, and P. Santini. "Spin dynamics of molecular nanomagnets unravelled at atomic scale by four-dimensional inelastic neutron scattering." In: *Nature Physics* 8.12 (**2012**), pp. 906–911. DOI: 10.1038/nphys2431 (cit. on p. 88).

[218] S. Ansbro, E. Moreno-Pineda, W. Yu, J. Ollivier, H. Mutka, M. Ruben, and A. Chiesa. "Magnetic properties of transition metal dimers probed by inelastic neutron scattering." In: *Dalton Transactions* 47.34 (**2018**), pp. 11953–11959. DOI: 10.1039/c8dt02570c (cit. on p. 88).

[219] C. J. Bradley and A. P. Cracknell. *The Mathematical Theory of Symmetry in Solids Representation Theory for Point Groups and Space Groups*. Oxford: Clarendon Press, **1972**. DOI: 10.5840/bradley19984110 (cit. on p. 89).

[220] B. Alfred Q. R. "Introduction to High-Resolution Inelastic X-Ray Scattering." In: (**2020**) (cit. on p. 88).

[221] X. Gonze and C. Lee. "Dynamical matrices, Born effective charges, dielectric permittivity tensors, and interatomic force constants from density-functional perturbation theory." In: *Physical Review B - Condensed Matter and Materials Physics* 55.16 (**1997**), pp. 10355–10368. DOI: 10.1103/PhysRevB.55.10355 (cit. on p. 91).

[222] M. Bal, J. R. Friedman, Y. Suzuki, E. M. Rumberger, D. N. Hendrickson, N. Avraham, Y. Myasoedov, H. Shtrikman, E. Zeldov, D. O. C. M. Physics, and T. W. I. O. Science. "Non-equilibrium magnetization dynamics in the Fe8 single-molecule magnet induced by high-intensity microwave radiation." In: *Europhysics Letters* 71.1 (**2005**), pp. 110–116. DOI: 10.1209/epl/i2005-10069-3 (cit. on p. 94).

[223] M. Bal, J. R. Friedman, Y. Suzuki, K. M. Mertes, E. M. Rumberger, D. N. Hendrickson, Y. Myasoedov, H. Shtrikman, N. Avraham, and E. Zeldov. "Photon-induced magnetization reversal in the Fe8 single-molecule magnet." In: *Physical Review B - Condensed Matter and Materials Physics* 70.10 (**2004**), pp. 1–4. DOI: 10.1103/PhysRevB.70.100408 (cit. on p. 94).

[224] M. Bal, J. R. Friedman, M. T. Tuominen, E. M. Rumberger, and D. N. Hendrickson. "Measurement of magnetization dynamics in single-molecule magnets induced by pulsed millimeter-wave radiation." In: *Journal of Applied Physics* 99.8 (**2006**). DOI: 10.1063/1.2173215 (cit. on p. 94).

[225] K. Petukhov, S. Bahr, W. Wernsdorfer, A. L. Barra, and V. Mosser. "Magnetization dynamics in the single-molecule magnet Fe8 under pulsed microwave irradiation." In: *Physical Review B - Condensed Matter and Materials Physics* 75.6 (**2007**), pp. 1–12. DOI: 10.1103/PhysRevB.75.064408 (cit. on p. 94).

[226] J. H. Quilter, A. J. Brash, F. Liu, M. Glässl, A. M. Barth, V. M. Axt, A. J. Ramsay, M. S. Skolnick, and A. M. Fox. "Phonon-Assisted Population Inversion of a Single InGaAs/GaAs Quantum Dot by Pulsed Laser Excitation." In: *Physical Review Letters* 114.13 (**2015**), pp. 1–5. DOI: 10.1103/PhysRevLett.114.137401 (cit. on p. 94).

[227] O. A. Shevchenko, V. S. Arbuzov, N. A. Vinokurov, P. D. Vobly, V. N. Volkov, Y. V. Getmanov, Y. I. Gorbachev, I. V. Davidyuk, O. I. Deychuly, E. N. Dementyev, B. A. Dovzhenko, B. A. Knyazev, E. I. Kolobanov, A. A. Kondakov, V. R. Kozak, E. V. Kozyrev, V. V. Kubarev, G. N. Kulipanov, E. A. Kuper, I. V. Kuptsov, G. Y. Kurkin, S. A. Krutikhin, L. E. Medvedev, S. V. Motygin, V. K. Ovchar, V. N. Osipov, V. M. Petrov, A. M. Pilan, V. M. Popik, V. V. Repkov, T. V. Salikova, I. K. Sedlyarov, S. S. Serednyakov, A. N. Skrinsky, S. V. Tararyshkin, A. G. Tribendis, V. G. Tcheskidov, K. N. Chernov, and M. A. Scheglov. "The Novosibirsk Free Electron Laser - Unique Source of Terahertz and Infrared Coherent Radiation." In: *Physics Procedia* 84.July (**2016**), pp. 13–18. DOI: 10.1016/j.phpro.2016.11.004 (cit. on p. 95).

[228] S. L. Veber, S. V. Tumanov, E. Y. Fursova, O. A. Shevchenko, Y. V. Getmanov, M. A. Scheglov, V. V. Kubarev, D. A. Shevchenko, I. I. Gorbachev, T. V. Salikova, G. N. Kulipanov, V. I. Ovcharenko, and M. V. Fedin. "X-band EPR setup with THz light excitation of Novosibirsk Free Electron Laser: Goals, means, useful extras." In: *Journal of Magnetic Resonance* 288 (**2018**), pp. 11–22. DOI: 10.1016/j.jmr.2018.01.009 (cit. on pp. 95, 96).

[229] G. N. Kulipanov, E. G. Bagryanskaya, E. N. Chesnokov, Y. Y. Choporova, V. V. Gerasimov, Y. V. Getmanov, S. L. Kiselev, B. A. Knyazev, V. V. Kubarev, S. E. Peltek, V. M. Popik, T. V. Salikova, M. A. Scheglov, S. S. Seredniakov, O. A. Shevchenko, A. N. Skrinsky, S. L. Veber, and N. A. Vinokurov. "Novosibirsk Free Electron Laser-Facility Description and Recent Experiments." In: *IEEE Transactions on Terahertz Science and Technology* 5.5 (**2015**), pp. 798–809. DOI: 10.1109/TTHZ.2015.2453121 (cit. on p. 96).

[230] S. Benci. *PhD Thesis*. **2020**. URL: https://flore.unifi.it/retrieve/handle/2158/1234475/591177/PhD_Thesis_Benci_Stefano.pdf (cit. on p. 96).

[231] R. Zwanzig. "On the identity of three generalized master equations." In: *Physica* 30.6 (**1964**), pp. 1109–1123. DOI: https://doi.org/10.1016/0031-8914(64)90102-8 (cit. on p. 98).

[232] D. Manzano. "A short introduction to the Lindblad master equation." In: *AIP Advances* 10.2 (**2020**). DOI: 10.1063/1.5115323 (cit. on p. 98).

[233] M. Berman and R. Kosloff. "Time-dependent solution of the Liouville-von Neumann equation: non-dissipative evolution." In: *Computer Physics Communications* 63.1-3 (**1991**), pp. 1–20. DOI: 10.1016/0010-4655(91)90233-B (cit. on p. 99).

[234] B. Di Bartolo and R. C. Powell. *Crystal symmetry, lattice vibrations, and optical spectroscopy of solids: A group theoretical approach*. **2014**, pp. 1–515. DOI: 10.1142/9052 (cit. on p. 100).

[235] J. Sólyom. "The Quantum Theory of Lattice Vibrations." In: *Fundamentals of the Physics of Solids: Volume I Structure and Dynamics*. Berlin, Heidelberg: Springer Berlin Heidelberg, **2007**, pp. 413–418. DOI: 10.1007/978-3-540-72600-5_8. URL: https://doi.org/10.1007/978-3-540-72600-5_8 (cit. on p. 104).

[236] A. Ishizaki and G. R. Fleming. "On the adequacy of the Redfield equation and related approaches to the study of quantum dynamics in electronic energy transfer." In: *Journal of Chemical Physics* 130.23 (**2009**). DOI: 10.1063/1.3155214 (cit. on p. 108).

[237] I. Zutic, J. Fabian, and S. Das Sarma. "Spintronics: Fundamentals and applications." In: *Rev. Mod. Phys* 76 (**2004**), pp. 323–386. DOI: doi.org/10.1103/RevModPhys.76.323 (cit. on p. 115).

[238] E. Coronado. "Molecular magnetism: from chemical design to spin control in molecules, materials and devices." In: *Nature Reviews Materials* 5.2 (**2020**), pp. 87–104. DOI: 10.1038/s41578-019-0146-8 (cit. on p. 115).

[239] Z. Zanolli. "Graphene-multiferroic interfaces for spintronics applications." In: *Scientific Reports* 6.August (**2016**), pp. 1–6. DOI: 10.1038/srep31346 (cit. on p. 115).

[240] S. Roche, J. Åkerman, B. Beschoten, J. C. Charlier, M. Chshiev, S. P. Dash, B. Dlubak, J. Fabian, A. Fert, M. Guimarães, F. Guinea, I. Grigorieva, C. Schönenberger, P. Seneor, C. Stampfer, S. O. Valenzuela, X. Waintal, and B. Van Wees. "Graphene spintronics: The European Flagship perspective." In: *2D Materials* 2.3 (**2015**). DOI: 10.1088/2053-1583/2/3/030202 (cit. on p. 115).

[241] B. Dieny, V. S. Speriosu, S. S. Parkin, B. A. Gurney, D. R. Wilhoit, and D. Mauri. "Giant magnetoresistive in soft ferromagnetic multilayers." In: *Physical Review B* 43.1 (**1991**), pp. 1297–1300. DOI: 10.1103/PhysRevB.43.1297 (cit. on p. 115).

[242] R Jansen. "The spin-valve transistor : a review and outlook." In: *Journal of Physics D: Applied Physics* 36 (**2003**), pp. 289–308. DOI: 10.1088/0022-3727/36/19/R01 (cit. on p. 115).

[243] L. Poggini, G. Cucinotta, A. M. Pradipto, M. Scarrozza, P. Barone, A. Caneschi, P. Graziosi, M. Calbucci, R. Cecchini, V. A. Dediu, S. Picozzi, M. Mannini, and R. Sessoli. "An Organic Spin Valve Embedding a Self-Assembled Monolayer of Organic Radicals." In: *Advanced Materials Interfaces* 3.14 (**2016**). DOI: 10.1002/admi.201500855 (cit. on p. 116).

[244] M. Z. Iqbal, M. W. Iqbal, J. H. Lee, Y. S. Kim, S. H. Chun, and J. Eom. "Spin valve effect of NiFe/graphene/NiFe junctions." In: *Nano Research* 6.5 (**2013**), pp. 373–380. DOI: 10.1007/s12274-013-0314-x (cit. on p. 116).

[245] M. Z. Iqbal, M. W. Iqbal, X. Jin, C. Hwang, and J. Eom. "Interlayer dependent polarity of magnetoresistance in graphene spin valves." In: *Journal of Materials Chemistry C* 3.2 (**2015**), pp. 298–302. DOI: 10.1039/c4tc02389g (cit. on p. 116).

[246] S. Sanvito. "Molecular spintronics: The rise of spinterface science." In: *Nature Physics* 6.8 (**2010**), pp. 562–564. DOI: 10.1038/nphys1714 (cit. on p. 116).

[247] D. Pesin and A. H. MacDonald. "Spintronics and pseudospintronics in graphene and topological insulators." In: *Nature Materials* 11.5 (**2012**), pp. 409–416. DOI: 10.1038/nmat3305 (cit. on p. 116).

[248] C. C. Lin, A. V. Penumatcha, Y. Gao, V. Q. Diep, J. Appenzeller, and Z. Chen. "Spin transfer torque in a graphene lateral spin valve assisted by an external magnetic field." In: *Nano Letters* 13.11 (**2013**), pp. 5177–5181. DOI: 10.1021/nl402547m (cit. on p. 116).

[249] M. Z. Iqbal, G. Hussain, S. Siddique, and M. W. Iqbal. "Graphene spin valve: An angle sensor." In: *Journal of Magnetism and Magnetic Materials* 432 (**2017**), pp. 135–139. DOI: 10.1016/j.jmmm.2017.02.004 (cit. on p. 116).

[250] A. Candini, S. Klyatskaya, M. Ruben, W. Wernsdorfer, and M. Affronte. "Graphene spintronic devices with molecular nanomagnets." In: *Nano Letters* 11.7 (**2011**), pp. 2634–2639. DOI: 10.1021/nl2006142 (cit. on p. 116).

[251] Y.-W. Son, M. L. Cohen, and S. G. Louie. "Half-metallic graphene nanoribbon." In: *Nature* 444.7117 (**2006**), pp. 347–349. DOI: 10.1038/nature05180 (cit. on p. 116).

[252] K. S. Novoselov, A. K. Geim, S. V. Morozov, D. Jiang, Y. Zhang, S. V. Dubonos, I. V. Grigorieva, and A. A. Firsov. "Electric Field Effect in Atomically Thin Carbon Films." In: *Science* 306.5696 (**2004**), pp. 666–669. DOI: 10.1126/science.1102896 (cit. on p. 116).

[253] K. S. Kim, Y. Zhao, H. Jang, S. Y. Lee, J. M. Kim, K. S. Kim, J. H. Ahn, P. Kim, J. Y. Choi, and B. H. Hong. "Large-scale pattern growth of graphene films for stretchable transparent electrodes." In: *Nature* 457.7230 (**2009**), pp. 706–710. DOI: 10.1038/nature07719 (cit. on p. 116).

[254] K. S. Novoselov, A. K. Geim, S. V. Morozov, D. Jiang, M. I. Katsnelson, I. V. Grigorieva, S. V. Dubonos, and A. A. Firsov. "Two-dimensional gas of massless Dirac fermions in graphene." In: *Nature* 438.7065 (**2005**), pp. 197–200. DOI: 10.1038/nature04233 (cit. on p. 116).

[255] Y. Zhang, Y. W. Tan, H. L. Stormer, and P. Kim. "Experimental observation of the quantum Hall effect and Berry's phase in graphene." In: *Nature* 438.7065 (**2005**), pp. 201–204. DOI: 10.1038/nature04235 (cit. on p. 116).

[256] N. M. Peres, F. Guinea, and A. H. Castro Neto. "Electronic properties of disordered two-dimensional carbon." In: *Physical Review B - Condensed Matter and Materials Physics* 73.12 (**2006**), pp. 1–23. DOI: 10.1103/PhysRevB.73.125411 (cit. on p. 116).

[257] P. R. Wallace. "The Band Theory of Graphite." In: *Phys. Rev.* 71.9 (**1947**), pp. 622–634. DOI: 10.1103/PhysRev.71.622 (cit. on pp. 116, 121, 124).

[258] M. Y. Han, B. Özyilmaz, Y. Zhang, and P. Kim. "Energy band-gap engineering of graphene nanoribbons." In: *Physical Review Letters* 98.20 (**2007**), pp. 1–4. DOI: 10.1103/PhysRevLett.98.206805 (cit. on p. 117).

[259] T. Ohta, A. Bostwick, T. Seyller, K. Horn, and E. Rotenberg. "Controlling the electronic structure of bilayer graphene." In: *Science* 313.5789 (**2006**), pp. 951–954. DOI: 10.1126/science.1130681 (cit. on p. 117).

[260] H. Lee, K. Paeng, and I. S. Kim. "A review of doping modulation in graphene." In: *Synthetic Metals* 244.May (**2018**), pp. 36–47. DOI: 10.1016/j.synthmet.2018.07.001 (cit. on p. 117).

[261] M. Pumera and Z. Sofer. "Towards stoichiometric analogues of graphene: Graphane, fluorographene, graphol, graphene acid and others." In: *Chemical Society Reviews* 46.15 (**2017**), pp. 4450–4463. DOI: 10.1039/c7cs00215g (cit. on p. 117).

[262] L. Liao, H. Peng, and Z. Liu. "Chemistry makes graphene beyond graphene." In: *Journal of the American Chemical Society* 136.35 (**2014**), pp. 12194–12200. DOI: 10.1021/ja5048297 (cit. on p. 117).

[263] J. Wang, Y. Zhang, M. P. Sahoo, T. Shimada, T. Kitamura, P. Ghosez, and T. Y. Zhang. "Giant magnetoelectric effect at the graphone/ferroelectric interface." In: *Scientific Reports* 8.12448 (**2018**), pp. 1–9. DOI: 10.1038/s41598-018-30010-x (cit. on p. 117).

[264] S. Agnoli and G. Granozzi. "Second generation graphene: Opportunities and challenges for surface science." In: *Surface Science* 609 (**2013**), pp. 1–5. DOI: 10.1016/j.susc.2012.11.016 (cit. on p. 117).

[265] J. Hong, S. Niyogi, E. Bekyarova, M. E. Itkis, P. Ramesh, N. Amos, D. Litvinov, C. Berger, W. A. De Heer, S. Khizroev, and R. C. Haddon. "Effect of nitrophenyl functionalization on the magnetic properties of epitaxial graphene." In: *Small* 7.9 (**2011**), pp. 1175–1180. DOI: 10.1002/smll.201002244 (cit. on p. 117).

[266] E. J. Duplock, M. Scheffler, and P. J. Lindan. "Hallmark of perfect graphene." In: *Physical Review Letters* 92.22 (**2004**), pp. 1–4. DOI: 10.1103/PhysRevLett.92.225502 (cit. on p. 117).

[267] L. Xie, X. Wang, J. Lu, Z. Ni, Z. Luo, H. Mao, R. Wang, Y. Wang, H. Huang, D. Qi, R. Liu, T. Yu, Z. Shen, T. Wu, H. Peng, B. Özyilmaz, K. Loh, A. T. Wee, Ariando, and W. Chen. "Room temperature ferromagnetism in partially hydrogenated epitaxial graphene." In: *Applied Physics Letters* 98.193113 (**2011**), pp. 1–4. DOI: 10.1063/1.3589970 (cit. on pp. 117, 118, 132, 144).

[268] W. Han, R. K. Kawakami, M. Gmitra, and J. Fabian. "Graphene spintronics." In: *Nature Nanotechnology* 9.10 (**2014**), pp. 794–807. DOI: 10.1038/nnano.2014.214 (cit. on p. 118).

[269] Y. Fei, S. Fang, and Y. H. Hu. "Synthesis, properties and potential applications of hydrogenated graphene." In: *Chemical Engineering Journal* 397.125408 (**2020**), pp. 1–12. DOI: 10.1016/j.cej.2020.125408 (cit. on p. 118).

[270] D. K. Samarakoon and X. Q. Wang. "Tunable band gap in hydrogenated bilayer graphene." In: *ACS Nano* 4.7 (**2010**), pp. 4126–4130. DOI: 10.1021/nn1007868 (cit. on p. 118).

[271] D. C. Elias, R. R. Nair, T. M. G. Mohiuddin, S. V. Morozov, P Blake, M. P. Halsall, A. C. Ferrari, D. W. Boukhvalov, M. I. Katsnelson, A. K. Geim, and K. S. Novoselov. "Control of Graphene's Properties by Reversible Hydrogenation: Evidence for Graphane." In: *Science* 323.5914 (**2009**), pp. 610–613. DOI: 10.1126/science.1167130 (cit. on p. 118).

[272] J. D. Jones, K. K. Mahajan, W. H. Williams, P. A. Ecton, Y. Mo, and J. M. Perez. "Formation of graphane and partially hydrogenated graphene by electron irradiation of adsorbates on graphene." In: *Carbon* 48.8 (**2010**), pp. 2335–2340. DOI: 10.1016/j.carbon.2010.03.010 (cit. on p. 118).

[273] S. Ryu, M. Y. Han, J. Maultzsch, T. F. Heinz, P. Kim, M. L. Steigerwald, and L. E. Brus. "Reversible basal plane hydrogenation of graphene." In: *Nano Letters* 8.12 (**2008**), pp. 4597–4602. DOI: 10.1021/nl802940s (cit. on p. 118).

[274] J. S. Bunch, S. S. Verbridge, J. S. Alden, A. M. Van Der Zande, J. M. Parpia, H. G. Craighead, and P. L. McEuen. "Impermeable atomic membranes from graphene sheets." In: *Nano Letters* 8.8 (**2008**), pp. 2458–2462. DOI: 10.1021/nl801457b (cit. on p. 118).

[275] M. H. Sluiter and Y. Kawazoe. "Cluster expansion method for adsorption: Application to hydrogen chemisorption on graphene." In: *Physical Review B - Condensed Matter and Materials Physics* 68.085410 (**2003**), pp. 1–7. DOI: 10.1103/PhysRevB.68.085410 (cit. on pp. 118, 140).

[276] J. O. Sofo, A. S. Chaudhari, and G. D. Barber. "Graphane: A two-dimensional hydrocarbon." In: *Physical Review B - Condensed Matter and Materials Physics* 75.153401 (**2007**), pp. 1–4. DOI: 10.1103/PhysRevB.75.153401 (cit. on pp. 118, 124, 127, 140).

[277] O. Leenaerts, H. Peelaers, A. D. Hernández-Nieves, B. Partoens, and F. M. Peeters. "First-principles investigation of graphene fluoride and graphane." In: *Physical Review B - Condensed Matter and Materials Physics* 82.195436 (**2010**), pp. 1–6. DOI: 10.1103/PhysRevB.82.195436 (cit. on pp. 118, 130).

[278] M. Pumera and C. H. An Wong. "Graphane and hydrogenated graphene." In: *Chemical Society Reviews* 42.14 (**2013**), pp. 5987–5995. DOI: 10.1039/c3cs60132c (cit. on p. 118).

[279] F. Buonocore, A. Mosca Conte, and N. Lisi. "Effects of the substrate on graphone magnetism: A density functional theory study." In: *Physica E: Low-Dimensional Systems and Nanostructures* 78 (**2016**), pp. 65–72. DOI: 10.1016/j.physe.2015.11.032 (cit. on pp. 118, 124, 133).

[280] L. Feng and W. X. Zhang. "The structure and magnetism of graphone." In: *AIP Advances* 2.042138 (**2012**), pp. 1–6. DOI: 10.1063/1.4766937 (cit. on pp. 118, 124, 127, 128).

[281] A. J. Giesbers, K. Uhlírová, M. Konečný, E. C. Peters, M. Burghard, J. Aarts, and C. F. Flipse. "Interface-induced room-temperature ferromagnetism in hydrogenated epitaxial graphene." In: *Physical Review Letters* 111.166101 (**2013**), pp. 1–5. DOI: 10.1103/PhysRevLett.111.166101 (cit. on pp. 118, 132, 144).

[282] R. R. Nair, M. Sepioni, I. L. Tsai, O. Lehtinen, J. Keinonen, A. V. Krasheninnikov, T. Thomson, A. K. Geim, and I. V. Grigorieva. "Spin-half paramagnetism in graphene induced by point defects." In: *Nature Physics* 8.3 (**2012**), pp. 199–202. DOI: 10.1038/nphys2183 (cit. on pp. 118, 132).

[283] J. Berashevich and T. Chakraborty. "Sustained ferromagnetism induced by H-vacancies in graphane." In: *Nanotechnology* 21.355201 (**2010**), pp. 1–5. DOI: 10.1088/0957-4484/21/35/355201 (cit. on pp. 118, 128, 132, 138).

[284] J. Zhou, Q. Wang, Q. Sun, X. S. Chen, Y. Kawazoe, and P. Jena. "Ferromagnetism in semihydrogenated graphene sheet." In: *Nano Letters* 9.11 (**2009**), pp. 3867–3870. DOI: 10.1021/nl9020733 (cit. on pp. 118, 124, 128).

[285] B. Li, L. Zhou, D. Wu, H. Peng, K. Yan, Y. Zhou, and Z. Liu. "Photochemical chlorination of graphene." In: *ACS Nano* 5.7 (**2011**), pp. 5957–5961. DOI: 10.1021/nn201731t (cit. on p. 118).

[286] N. Watanabe, T. Nakajima, and N. Ohsawa. "Surface Free Energies of Two Kinds of Graphite Fluorides, (CF)n and (C2F)n." In: *Bulletin of the Chemical Society of Japan* 55.7 (**1982**), pp. 2029–2033. DOI: 10.1246/bcsj.55.2029 (cit. on pp. 118, 124).

[287] D. K. Samarakoon and X.-Q. Wang. "Chair and Twist-Boat Membranes in Hydrogenated Graphene." In: *ACS Nano* 3.12 (**2009**), pp. 4017–4022. DOI: 10.1021/nn901317d (cit. on pp. 118, 126, 142).

[288] C. Zhou, S. Chen, J. Lou, J. Wang, Q. Yang, C. Liu, D. Huang, and T. Zhu. "Graphene's cousin: The present and future of graphane." In: *Nanoscale Research Letters* 9.1 (**2014**), pp. 1–9. DOI: 10.1186/1556-276X-9-26 (cit. on pp. 118, 140).

[289] R. Hoffmann. "A chemical and theoretical way to look at bonding on surfaces." In: *Reviews of Modern Physics* 60.3 (**1988**), pp. 601–628. DOI: 10.1103/RevModPhys.60.601 (cit. on p. 120).

[290] A. Caneschi, D. Gatteschi, and F. Totti. "Molecular magnets and surfaces: A promising marriage. A DFT insight." In: *Coordination Chemistry Reviews* 289-290.1 (**2015**), pp. 357–378. DOI: 10.1016/j.ccr.2014.11.016 (cit. on p. 120).

[291] Y. Zhang and W. Yang. "Comment on "generalized gradient approximation made simple"." In: *Physical Review Letters* 80.4 (**1998**), p. 890. DOI: 10.1103/PhysRevLett.80.890 (cit. on p. 120).

[292] R. Sabatini, T. Gorni, and S. De Gironcoli. "Nonlocal van der Waals density functional made simple and efficient." In: *Physical Review B - Condensed Matter and Materials Physics* 87.4 (**2013**). DOI: 10.1103/PhysRevB.87.041108 (cit. on p. 120).

[293] G. Santarossa, A. Vargas, M. Iannuzzi, C. A. Pignedoli, D. Passerone, and A. Baiker. "Modeling bulk and surface Pt using the "gaussian and plane wave" density functional theory formalism: Validation and comparison to k-point plane wave calculations." In: *Journal of Chemical Physics* 129.23 (**2008**). DOI: 10.1063/1.3037227 (cit. on p. 120).

[294] G. Lippert, J. Hutter, and M. Parrinello. "A hybrid Gaussian and plane wave density functional scheme." In: *Molecular Physics* 92.3 (**1997**), pp. 477–487. DOI: 10.1080/00268979709482119 (cit. on p. 120).

[295] G. Lippert, J. J. Hutter, and M. Parrinello. "The Gaussian and augmented-plane-wave density functional method for ab initio molecular dynamics simulations." In: *Theoretical Chemistry Accounts* 103.2 (**1999**), pp. 124–140. DOI: 10.1007/s002140050523 (cit. on p. 120).

[296] F. Neese. "Prediction of molecular properties and molecular spectroscopy with density functional theory: From fundamental theory to exchange-coupling." In: *Coordination Chemistry Reviews* 253.5-6 (**2009**), pp. 526–563. DOI: 10.1016/j.ccr.2008.05.014 (cit. on p. 122).

[297] L. Noodleman, C. Y. Peng, D. A. Case, and J. M. Mouesca. "Orbital interactions, electron delocalization and spin coupling in iron-sulfur clusters." In: *Coordination Chemistry Reviews* 144 (**1995**), pp. 199–244. DOI: 10.1016/0010-8545(95)07011-L (cit. on p. 122).

[298] A. Bencini, F. Totti, C. A. Daul, K. Doclo, P. Fantucci, and V. Barone. "Density Functional Calculations of Magnetic Exchange Interactions in Polynuclear Transition Metal Complexes." In: *Inorganic Chemistry* 36.22 (**1997**), pp. 5022–5030. DOI: 10.1021/ic961448x (cit. on p. 122).

[299] A. Bencini and F. Totti. "A few comments on the application of density functional theory to the calculation of the magnetic structure of oligo-nuclear transition metal clusters." In: *Journal of Chemical Theory and Computation* 5 (**2009**), pp. 144–154. DOI: 10.1021/ct800361x (cit. on pp. 122, 129).

[300] D. W. Boukhvalov. "Stable antiferromagnetic graphone." In: *Physica E: Low-Dimensional Systems and Nanostructures* 43.1 (**2010**), pp. 199–201. DOI: 10.1016/j.physe.2010.07.015 (cit. on pp. 124, 131).

[301] A. N. Rudenko, F. J. Keil, M. I. Katsnelson, and A. I. Lichtenstein. "Exchange interactions and frustrated magnetism in single-side hydrogenated and fluorinated graphene." In: *Physical Review B - Condensed Matter and Materials Physics* 88.081405 (**2013**), pp. 1–4. DOI: 10.1103/PhysRevB.88.081405 (cit. on pp. 124, 129–131).

[302] J. Nakamura, N. Arimura, M. Hirayama, and A. Natori. "Structural and electronic properties of the planar C-skeleton polymers." In: *Applied Physics Letters* 94.22 (**2009**), pp. 1–4. DOI: 10.1063/1.3148722 (cit. on p. 124).

[303] L. Zhang, N. Schwertfager, T. Cheiwchanchamnangij, X. Lin, P. A. Glans-Suzuki, L. F. Piper, S. Limpijumnong, Y. Luo, J. F. Zhu, W. R. Lambrecht, and J. H. Guo. "Electronic band structure of graphene from resonant soft x-ray spectroscopy: The role of core-hole effects." In: *Physical Review B - Condensed Matter and Materials Physics* 86.245430 (**2012**), pp. 1–5. DOI: 10.1103/PhysRevB.86.245430 (cit. on pp. 123, 125).

[304] D. W. Boukhvalov, M. I. Katsnelson, and A. I. Lichtenstein. "Hydrogen on graphene: Electronic structure, total energy, structural distortions and magnetism from first-principles calculations." In: *Physical Review B - Condensed Matter and Materials Physics* 77.035427 (**2008**), pp. 1–7. DOI: 10.1103/PhysRevB.77.035427 (cit. on p. 124).

[305] B. Uchoa, V. N. Kotov, N. M. Peres, and A. H. Castro Neto. "Localized magnetic states in graphene." In: *Physical Review Letters* 101.2 (**2008**), pp. 1–4. DOI: 10.1103/PhysRevLett.101.026805 (cit. on p. 124).

[306] S. Casolo, O. M. Løvvik, R. Martinazzo, and G. F. Tantardini. "Understanding adsorption of hydrogen atoms on graphene." In: *Journal of Chemical Physics* 130.054704 (**2009**), pp. 1–10. DOI: 10.1063/1.3072333 (cit. on pp. 126, 140).

[307] T. Rangel, M. Del Ben, D. Varsano, G. Antonius, F. Bruneval, F. H. da Jornada, M. J. van Setten, O. K. Orhan, D. D. O'Regan, A. Canning, A. Ferretti, A. Marini, G. M. Rignanese, J. Deslippe, S. G. Louie, and J. B. Neaton. "Reproducibility in G0W0 calculations for solids." In: *Computer Physics Communications* 255 (**2020**), p. 107242. DOI: 10.1016/j.cpc.2020.107242 (cit. on p. 127).

[308] S. Lebègue, M. Klintenberg, O. Eriksson, and M. I. Katsnelson. "Accurate electronic band gap of pure and functionalized graphane from GW calculations." In: *Physical Review B - Condensed Matter and Materials Physics* 79.24 (**2009**), pp. 3–7. DOI: 10.1103/PhysRevB.79.245117 (cit. on p. 127).

[309] E. H. Lieb. "Two theorems on the Hubbard model." In: *Physical Review Letters* 62.10 (**1989**), pp. 1201–1204. DOI: 10.1103/PhysRevLett.62.1201 (cit. on p. 128).

[310] J. Berashevich and T. Chakraborty. "Magnetic properties of hydrogenated bilayer graphene flakes." In: *Epl* 93.47007 (**2011**), pp. 1–6. DOI: 10.1209/0295-5075/93/47007 (cit. on pp. 128, 138).

[311] R. R. Nair, W. Ren, R. Jalil, I. Riaz, V. G. Kravets, L. Britnell, P. Blake, F. Schedin, A. S. Mayorov, S. Yuan, M. I. Katsnelson, H. M. Cheng, W. Strupinski, L. G. Bulusheva, A. V. Okotrub, I. V. Grigorieva, A. N. Grigorenko, K. S. Novoselov, and A. K. Geim. "Fluorographene: A two-dimensional counterpart of Teflon." In: *Small* 6.24 (**2010**), pp. 2877–2884. DOI: 10.1002/smll.201001555 (cit. on p. 130).

[312] J. C. Charlier, X. Gonze, and J. P. Michenaud. "First-principles study of graphite monofluoride (CF)n." In: *Physical Review B* 47.24 (**1993**), pp. 16162–16168. DOI: 10.1103/PhysRevB.47.16162 (cit. on p. 130).

[313] K. E. Whitener. "Review Article: Hydrogenated graphene: A user's guide." In: *Journal of Vacuum Science and Technology A* 36.5 (**2018**), 05G401. DOI: 10.1116/1.5034433 (cit. on pp. 130, 132).

[314] W. K. Lee, K. E. Whitener, J. T. Robinson, and P. E. Sheehan. "Patterning magnetic regions in hydrogenated graphene via E-Beam Irradiation." In: *Advanced Materials* 27.10 (**2015**), pp. 1774–1778. DOI: 10.1002/adma.201404144 (cit. on pp. 130, 132, 139).

[315] M. Wojtaszek, N. Tombros, A. Caretta, P. H. Van Loosdrecht, and B. J. Van Wees. "A road to hydrogenating graphene by a reactive ion etching plasma." In: *Journal of Applied Physics* 110.6 (**2011**), pp. 1–7. DOI: 10.1063/1.3638696 (cit. on p. 132).

[316] Y. Song, K. Qian, L. Tao, Z. Wang, H. Guo, H. Chen, S. Zhang, Y.-Y. Zhang, X. Lin, S. T. Pantelides, S. Du, and H.-J. Gao. "Intrinsically Honeycomb-patterned Hydrogenated Graphene with Spin Polarized Edge-states." In: (**2021**) (cit. on p. 132).

[317] R. Balog, B. Jørgensen, L. Nilsson, M. Andersen, E. Rienks, M. Bianchi, M. Fanetti, E. Lægsgaard, A. Baraldi, S. Lizzit, Z. Sljivancanin, F. Besenbacher, B. Hammer, T. G. Pedersen, P. Hofmann, and L. Hornekær. "Bandgap opening in graphene induced by patterned hydrogen adsorption." In: *Nature Materials* 9.4 (**2010**), pp. 315–319. DOI: 10.1038/nmat2710 (cit. on pp. 132, 133).

[318] J. Son, S. Lee, S. J. Kim, B. C. Park, H. K. Lee, S. Kim, J. H. Kim, B. H. Hong, and J. Hong. "Hydrogenated monolayer graphene with reversible and tunable wide band gap and its field-effect transistor." In: *Nature Communications* 7.13261 (**2016**), pp. 1–7. DOI: 10.1038/ncomms13261 (cit. on p. 132).

[319] J. Tuček, K. Holá, A. B. Bourlinos, P. Błoński, A. Bakandritsos, J. Ugolotti, M. Dubecký, F. Karlický, V. Ranc, K. Čépe, M. Otyepka, and R. Zbořil. "Room temperature organic magnets derived from sp3 functionalized graphene." In: *Nature Communications* 8.14525 (**2017**), pp. 1–12. DOI: 10.1038/ncomms14525 (cit. on p. 132).

[320] A. Ney, P. Papakonstantinou, A. Kumar, N. G. Shang, and N. Peng. "Irradiation enhanced paramagnetism on graphene nanoflakes." In: *Applied Physics Letters* 99.10 (**2011**), pp. 2–5. DOI: 10.1063/1.3628245 (cit. on p. 132).

[321] M. Birowska, M. E. Marchwiany, C. Draxl, and J. A. Majewski. "Assessment of approaches for dispersive forces employing semihydrogenated graphene as a case study." In: *Computational Materials Science* 186 (**2021**), p. 109940. DOI: https://doi.org/10.1016/j.commatsci.2020.109940 (cit. on p. 133).

[322] M. Birowska, K. Milowska, and J. A. Majewski. "Van der Waals density functionals for graphene layers and graphite." In: *Acta Physica Polonica A* 120.5 (**2011**), pp. 845–848. DOI: 10.12693/APhysPolA.120.845 (cit. on p. 136).

[323] M. J. Schmidt and D. Loss. "Tunable edge magnetism at graphene/graphane interfaces." In: *Physical Review B - Condensed Matter and Materials Physics* 82.8 (**2010**), pp. 1–13. DOI: 10.1103/PhysRevB.82.085422 (cit. on pp. 138–140).

[324] M. Wu, X. Wu, Y. Gao, and X. C. Zeng. "Patterned hydrogenation of graphene: Magnetic quantum dot array." In: *Journal of Physical Chemistry C* 114.1 (**2010**), pp. 139–142. DOI: 10.1021/jp9086128 (cit. on p. 138).

[325] M. Terrones, A. R. Botello-Méndez, J. Campos-Delgado, F. López-Urías, Y. I. Vega-Cantú, F. J. Rodríguez-Macías, A. L. Elías, E. Muñoz-Sandoval, A. G. Cano-Márquez, J. C. Charlier, and H. Terrones. "Graphene and graphite nanoribbons: Morphology, properties, synthesis, defects and applications." In: *Nano Today* 5.4 (**2010**), pp. 351–372. DOI: 10.1016/j.nantod.2010.06.010 (cit. on p. 138).

[326] Q. Peng, A. K. Dearden, J. Crean, L. Han, S. Liu, X. Wen, and S. De. "New materials graphyne, graphdiyne, graphone, and graphane: Review of properties, synthesis, and application in nanotechnology." In: *Nanotechnology, Science and Applications* 7.2 (**2014**), pp. 1–29. DOI: 10.2147/NSA.S40324 (cit. on p. 138).

[327] T. Giovannini, L. Bonatti, M. Polini, and C. Cappelli. "Graphene Plasmonics: Fully Atomistic Approach for Realistic Structures." In: *Journal of Physical Chemistry Letters* 11.18 (**2020**), pp. 7595–7602. DOI: 10.1021/acs.jpclett.0c02051 (cit. on p. 138).

[328] V. Barone, O. Hod, and G. E. Scuseria. "Electronic structure and stability of semiconducting graphene nanoribbons." In: *Nano Letters* 6.12 (**2006**), pp. 2748–2754. DOI: 10.1021/nl0617033 (cit. on p. 138).

[329] X. Jia, M. Hofmann, V. Meunier, B. G. Sumpter, J. Campos-Delgado, J. M. Romo-Herrera, H. Son, Y.-P. Hsieh, A. Reina, J. Kong, M. Terrones, and M. S. Dresselhaus. "Controlled formation of sharp zigzag and armchair edges in graphitic nanoribbons." In: *Science* 323.5922 (**2009**), pp. 1701–1705 (cit. on p. 138).

[330] L. Pisani, J. A. Chan, B. Montanari, and N. M. Harrison. "Electronic structure and magnetic properties of graphitic ribbons." In: *Physical Review B - Condensed Matter and Materials Physics* 75.6 (**2007**), pp. 1–9. DOI: 10.1103/PhysRevB.75.064418 (cit. on p. 139).

[331] P. Koskinen, S. Malola, and H. Häkkinen. "Evidence for graphene edges beyond zigzag and armchair." In: *Physical Review B - Condensed Matter and Materials Physics* 80.7 (**2009**), pp. 16–18. DOI: 10.1103/PhysRevB.80.073401 (cit. on pp. 139, 140, 142).

[332] H. Şahin, C. Ataca, and S. Ciraci. "Magnetization of graphane by dehydrogenation." In: *Applied Physics Letters* 95.222510 (**2009**), pp. 1–3. DOI: 10.1063/1.3268792 (cit. on p. 139).

[333] A. I. Podlivaev and L. A. Openov. "On the thermal stability of graphone." In: *Semiconductors* 45.7 (**2011**), pp. 958–961. DOI: 10.1134/S1063782611070177 (cit. on p. 139).

[334] L. A. Openov and A. I. Podlivaev. "Spontaneous regeneration of an atomically sharp graphene/graphane interface under thermal disordering." In: *JETP Letters* 90.6 (**2009**), pp. 459–463. DOI: 10.1134/S002136400918012X (cit. on p. 139).

[335] V. Tozzini and V. Pellegrini. "Electronic structure and Peierls instability in graphene nanoribbons sculpted in graphane." In: *Physical Review B - Condensed Matter and Materials Physics* 81.11 (**2010**), pp. 22–25. DOI: 10.1103/PhysRevB.81.113404 (cit. on pp. 139, 142).

[336] M. Z. Flores, P. A. Autreto, S. B. Legoas, and D. S. Galvao. "Graphene to graphane: A theoretical study." In: *Nanotechnology* 20.465704 (**2009**), pp. 1–6. DOI: 10.1088/0957-4484/20/46/465704 (cit. on p. 139).

[337] A. G. Villalba. "Single shot ablation of monolayer graphene by spatially shaped femtosecond laser pulses." PhD thesis. Université Bourgogne Franche-Comté, **2017**. URL: https://tel.archives-ouvertes.fr/tel-01816952/document (cit. on p. 139).

[338] A. D. Hernández-Nieves, B. Partoens, and F. M. Peeters. "Electronic and magnetic properties of superlattices of graphene/graphane nanoribbons with different edge hydrogenation." In: *Physical Review B - Condensed Matter and Materials Physics* 82.16 (**2010**), pp. 1–9. DOI: 10.1103/PhysRevB.82.165412 (cit. on pp. 139, 142).

[339] J. H. Lee and J. C. Grossman. "Magnetic properties in graphene-graphane superlattices." In: *Applied Physics Letters* 97.13 (**2010**), pp. 19–22. DOI: 10.1063/1.3495771 (cit. on pp. 139, 144, 147, 151).

[340] S. Okada. "Energetics of nanoscale graphene ribbons: Edge geometries and electronic structures." In: *Physical Review B - Condensed Matter and Materials Physics* 77.4 (**2008**), pp. 1–4. DOI: 10.1103/PhysRevB.77.041408 (cit. on p. 140).

[341] V. Georgakilas, J. A. Perman, J. Tucek, and R. Zboril. "Broad Family of Carbon Nanoallotropes: Classification, Chemistry, and Applications of Fullerenes, Carbon Dots, Nanotubes, Graphene, Nanodiamonds, and Combined Superstructures." In: *Chemical Reviews* 115.11 (**2015**), pp. 4744–4822. DOI: 10.1021/cr500304f (cit. on p. 142).

[342] A. Miede. "Theses and other Beautiful Documents with `classicthesis`." In: *TUGboat – The Communications of the TEX Users Group* 31.1 (**2010**), pp. 18–20 (cit. on p. 201).

[343] URL: https://www.latex-project.org/ (cit. on p. 201).

[344] T. Williams, C. Kelley, and many others. *Gnuplot: an interactive plotting program*. Version 5.2. **2019**. URL: http://gnuplot.sourceforge.net/ (cit. on p. 201).

[345] W. Humphrey, A. Dalke, and K. Schulten. "VMD – Visual Molecular Dynamics." In: *Journal of Molecular Graphics* 14 (**1996**), pp. 33–38 (cit. on p. 201).

[346] J. Stone. "*An Efficient Library for Parallel Ray Tracing and Animation*." MA thesis. Computer Science Department, University of Missouri-Rolla, **1998** (cit. on p. 201).

[347] The ImageMagick Development Team. *ImageMagick*. Version 7.0.10. **2021**. URL: https://imagemagick.org (cit. on p. 201).

[348] The GIMP Development Team. *GIMP*. Version 2.10. **2019**. URL: https://www.gimp.org (cit. on p. 201).

This document was typeset using the typographical package `classicthesis` [342], in the LaTeX environment [343]. The plotting software used is `gnuplot` [344]. Molecular visualization is accomplished with VMD [345], with Tachyon rendering [346]. The entire image editing is carried out with LaTeX, ImageMagick [347], and Gimp [348].